

# Structural Disorder and Magnetic Order in Atomically Thin Crystals

Présentée le 24 avril 2020

à la Faculté des sciences de base  
Chaire de physique numérique de la matière condensée  
Programme doctoral en physique

pour l'obtention du grade de Docteur ès Sciences

par

**Michele PIZZOCHERO**

Acceptée sur proposition du jury

Prof. H. M. Rønnow, président du jury  
Prof. O. Yazyev, directeur de thèse  
Prof. A. Krasheninnikov, rapporteur  
Prof. M. Luisier, rapporteur  
Prof. A. Kis, rapporteur



(a) Sometimes dreams can be very realistic so that *during* the dream it is indistinguishable from everyday life.

(b) If you cannot distinguish being awake from dreaming,  
then it is possible that you are dreaming now.

(c) If you cannot eliminate the possibility that you are dreaming now,  
then you don't know that you are not dreaming now.

Therefore you don't know you are not dreaming now.

— James Ladyman, *Understanding Philosophy of Science*





# Abstract

This Thesis is mainly devoted to the exploration of the structural disorder and magnetic order in two-dimensional crystals by means of first-principles methodologies.

Firstly, we present a comparative study of defect formation in the semiconducting  $2H$  and semi-metallic  $1T'$  phases of  $\text{MoS}_2$ , the most representative member of transition metal dichalcogenides. We assess the thermodynamic stability of a broad set of point defects, along with their effect on the electronic structure and magnetic properties. We further investigate the response of  $1T'$ - $\text{MoS}_2$  to the electron beam irradiation. The energy range of the electron beam which is necessary to conduct sample imaging without inducing knock-on damage, as well as to intentionally create vacancy defects in  $1T'$ - $\text{MoS}_2$  is discussed. Next, we show how native defects can be exploited to induce magnetism in otherwise non-magnetic ultrathin  $\text{PtSe}_2$  by providing a theoretical model which explains magneto-resistance measurements. We reveal an antiferro- and ferro-magnetic ordering in semiconducting mono- and bi-layers, respectively, together with a layer-dependent RKKY interaction in thicker metallic films.

Secondly, we focus on magnetic interactions in monolayer  $\text{CrI}_3$  by determining the strength of both intra- and inter-site magnetic exchange interactions. We find that inter-site exchange interactions are primarily dominated by the ferromagnetic isotropic Heisenberg coupling, being inter-site anisotropic terms substantially weaker. Also, this system features a single-ion anisotropy pointing along the out-of-plane direction. Then, we show that Heisenberg exchange interactions can be effectively modulated through mild lattice deformations. In fact, depending on the magnitude and direction along which the strain is exerted, monolayer  $\text{CrI}_3$  undergoes a transition from the ferromagnetic phase to either Néel antiferromagnetic or ferrimagnetic phase. Additionally, we briefly examine the role point defects on monolayer  $\text{CrI}_3$ , and point out an interplay between lattice disorder and local magnetic moments in this system.

Thirdly, we revisit two fundamental yet poorly understood problems in physical chemistry. These include the hydration dynamics of the excess electrons in liquid water, a species relevant to many biological and chemical processes, and the nature of double bonds between higher main group elements, with a particular emphasis on the comparison between the properties of  $\text{C}=\text{C}$  vs  $\text{Si}=\text{Si}$ , an issue which is crucial to understand the structural dissimilarities between graphene and silicene.

**Keywords:** Two-dimensional Materials, Point Defects, Transition Metal Dichalcogenides, 2D Magnets, Quantum Magnetism, Heisenberg Spin Hamiltonian, Liquid Water, Theory of Chemical Bonding, First Principles



# Résumé

Cette thèse est principalement consacrée à l'exploration du désordre structural et de l'ordre magnétique dans les cristaux bidimensionnels au moyen de méthodes de premiers principes. Premièrement, nous présentons une étude comparative de la formation de défauts dans les phases semi-conductrice  $2H$  et semi-métallique  $1T'$  de  $\text{MoS}_2$ , le membre le plus représentatif des dichalcogénures de métaux de transition. Nous évaluons la stabilité thermodynamique d'un large éventail de défauts ponctuels et leur effet sur la structure électronique et les propriétés magnétiques. Nous étudions en outre la réponse de  $1T'$ - $\text{MoS}_2$  à l'irradiation par faisceau d'électrons. La gamme d'énergie du faisceau d'électrons qui est nécessaire pour effectuer l'imagerie de l'échantillon sans induire de dommages, ainsi que pour créer intentionnellement des défauts de type lacune dans  $1T'$ - $\text{MoS}_2$  est discutée. Ensuite, nous montrons comment les défauts natifs peuvent être exploités pour induire le magnétisme dans des films ultraminces de  $\text{PtSe}_2$  en fournissant un modèle théorique qui explique les mesures de magnétorésistance. Nous révélons un ordre antiferro- et ferro-magnétique dans les monocouches et les bi-couches semi-conductrices, respectivement, ainsi qu'une interaction RKKY en fonction du nombre de couches dans les films métalliques plus épais.

Deuxièmement, nous nous concentrons sur les interactions magnétiques dans la monocouche de  $\text{CrI}_3$  en déterminant la force des interactions d'échange magnétique. Nous constatons que les interactions d'échange entre les sites sont principalement dominées par le couplage ferromagnétique isotrope de Heisenberg, étant donné que les termes anisotropes sont sensiblement plus faibles. De plus, ce système présente une anisotropie mono-ionique pointant dans la direction hors du plan. En second lieu, nous montrons que les interactions d'échange de Heisenberg peuvent être efficacement modulées par de légères déformations du réseau. En fait, en fonction de l'amplitude et de la direction dans lesquelles s'exerce la déformation, la monocouche de  $\text{CrI}_3$  subit une transition de la phase ferromagnétique à la phase antiferromagnétique ou ferrimagnétique. De plus, nous examinons brièvement le rôle des défauts ponctuels sur la monocouche de  $\text{CrI}_3$ , et mettons en valeur une interaction entre les lacunes dans le réseau et le changement de moments magnétiques locaux dans ce système.

Troisièmement, nous revisitons deux problèmes fondamentaux mais très peu compris en chimie physique. Ceux-ci incluent la dynamique d'hydratation des électrons en excès dans l'eau liquide, une espèce pertinente pour de nombreux processus biologiques et chimiques, et la nature des liaisons doubles entre les éléments supérieur du groupe principal, avec un accent particulier sur la comparaison entre les propriétés de  $\text{C}=\text{C}$  vs  $\text{Si}=\text{Si}$ , une question cruciale pour comprendre les dissemblances structurales entre le graphène et le silicène.

## Résumé

---

Mots-clés : Matériaux Bidimensionnels, Défauts Ponctuels, Dichalcogénures de Métaux de Transition, Aimants Bidimensionnels, Magnétisme Quantique, Hamiltonien de Heisenberg, Eau Liquide, Théorie de la Liaison Chimique, Premiers Principes

# Sommario

Questa tesi è principalmente dedicata all'esplorazione del disordine strutturale e dell'ordine magnetico in cristalli bidimensionali per mezzo di metodologie sviluppate da principi primi.

In primo luogo, viene presentato uno studio comparativo della formazione dei difetti nella fase semiconduttrice  $2H$  e nella fase semimetallica  $1T'$  di  $\text{MoS}_2$ , il più rappresentativo tra i dicalcogenuri dei metalli di transizione. Viene quindi valutata la stabilità termodinamica dei difetti puntuali, insieme al loro effetto sulla struttura elettronica e le proprietà magnetiche. Inoltre, si indaga la risposta di  $1T'$ - $\text{MoS}_2$  all'irradiazione con fasci elettronici. Gli intervalli di energia del fascio elettronico necessari per visualizzare il campione senza introdurre ulteriore disordine e per creare intenzionalmente difetti di vacanza sono discussi in dettaglio. Successivamente, viene mostrato come i difetti puntuali offrono nuove opportunità per introdurre il magnetismo in film ultra-sottili di  $\text{PtSe}_2$  attraverso lo sviluppo di un modello teorico in grado di spiegare recenti misure di magnetoresistenza. In particolare, viene rivelato un ordine antiferro- e ferro-magnetico in film semiconduttori a singolo e doppio strato, rispettivamente, mentre la risposta magnetica nei film metallici di maggior spessore atomico è attribuita all'interazione RKKY.

In secondo luogo, sono state determinate le interazioni magnetiche di scambio nel singolo strato di  $\text{CrI}_3$ . Le interazioni di scambio tra i siti magnetici sono primariamente dominate dall'accoppiamento di Heisenberg ferromagnetico, essendo gli accoppiamenti anisotropi significativamente più deboli. Questo sistema presenta una anisotropia di singolo ione lungo la direzione perpendicolare al piano. Viene quindi dimostrato come le interazioni di scambio di Heisenberg possano essere efficacemente modulate attraverso leggere deformazioni del reticolo cristallino. Dipendentemente dall'intensità e la direzione lungo la quale le deformazioni sono esercitate, infatti, il singolo strato di  $\text{CrI}_3$  subisce una transizione dalla fase ferromagnetica a quella antiferromagnetica o ferrimagnetica. Inoltre, viene brevemente esaminato il ruolo dei difetti di punto in  $\text{CrI}_3$  e sottolineata una connessione tra disordine strutturale e cambiamento dei momenti magnetici locali.

Infine, sono stati rivisitati due problemi fondamentali e ancora ampiamente poco compresi in chimica fisica. Da una parte, la dinamica di idratazione di un elettrone in eccesso in acqua, un fenomeno rilevante in diversi processi chimici e biologici. Dall'altra parte, la natura dei doppi legami tra gli elementi del terzo periodo e oltre della tavola periodica, con un particolare accento tra il confronto tra  $\text{C}=\text{C}$  e  $\text{Si}=\text{Si}$ , un aspetto cruciale per cogliere l'origine delle differenze strutturali tra il grafene e il silicene.

## Sommario

---

Parole chiave: Materiali Bidimensionali, Difetti di Punto, Dicalcogenuri dei Metalli di Transizione, Magneti Bidimensionali, Magnetismo Quantistico, Hamiltoniana di Heisenberg, Acqua, Teoria del Legame Chimico, Principi Primi

# List of Publications

## Publications relevant to this Thesis

15. A. Avsar, C.-C. Yeon, M. Pizzochero, M. Tripathi, A. Ciarrocchi, O. V. Yazyev, and A. Kis  
*Probing magnetism in atomically thin semiconducting PtSe<sub>2</sub>*  
Nature Communications, submitted (2020)
14. M. Pizzochero  
*Atomic-scale defects in the two-dimensional ferromagnet CrI<sub>3</sub> from first principles*  
Journal of Physics D: Applied Physics, in press (2020)
13. M. Pizzochero and O. V. Yazyev  
*Inducing magnetic phase transitions in monolayer CrI<sub>3</sub> via lattice deformations*  
The Journal of Physical Chemistry C 124, 7585 (2020)
12. M. Pizzochero, R. Yadav, and O. V. Yazyev  
*Magnetic exchange interactions in monolayer CrI<sub>3</sub> from many-body wavefunction calculations*  
2D Materials, in press (2020)
11. M. Pizzochero, M. Bonfanti, and R. Martinazzo  
*To bend or not to bend, the dilemma of multiple bonds*  
Physical Chemistry Chemical Physics 21, 26342 (2019)
10. M. Pizzochero, F. Ambrosio, and A. Pasquarello  
*Picture of the wet electron: A localized transient state in liquid water*  
Chemical Science 10, 7442 (2019)
9. A. Avsar, A. Ciarrocchi, M. Pizzochero, D. Unuchek, O. V. Yazyev, and A. Kis  
*Defect induced, layer-modulated magnetism in ultrathin metallic PtSe<sub>2</sub>*  
Nature Nanotechnology 14, 674 (2019)
8. M. Pizzochero and O. V. Yazyev  
*Single-layer 1T'-MoS<sub>2</sub> under electron irradiation from ab initio molecular dynamics*  
2D Materials 5, 025022 (2018)

## List of Publications

---

7. M. Pizzochero and O. V. Yazyev  
*Point defects in the 1T' and 2H phases of single-layer MoS<sub>2</sub>: A comparative first-principles study*  
Physical Review B 96, 245402 (2017)

## Other publications

6. E. Martino, D. Santos-Cottin, F. Le Martelé, K. Semeniuk, M. Pizzochero, K. Cernevics, S. Klotz, L. Delbes, B. Baptiste, F. Capitani, H. Berger, O.V. Yazyev, A. Akrap  
*Pressure-driven structural phase transition and band-gap collapse in layered semiconductors 1T-ZrX<sub>2</sub> (X=S, Se)*  
In preparation
5. Z. Pedramrazi, C. Herbig, A. Pulkin, S. Tang, M. Philips, D. Wong, H. Ryu, M. Pizzochero, Y. Chen, F. Wang, E. J. Mele, Z. X. Shen, S.-K. Mo, O. V. Yazyev, and M. F. Crommie  
*Manipulating topological domain boundaries in the single-layer quantum spin Hall insulator 1T'-WSe<sub>2</sub>*  
Nano Letters 19, 5634 (2019)
4. M. W. Chen, H. K. Kim, C. Bernard, M. Pizzochero, J. Zaldivar Fernandez, J. I. Pascual, M. M. Ugeda, O. V. Yazyev, T. Greber, J. Osterwalder, O. Renault, and A. Kis  
*Electronic properties of transferable atomically-thin MoSe<sub>2</sub>/h-BN heterostructures grown on Rh(111)*  
ACS Nano 12, 11161 (2018)
3. M. W. Chen, D. Ovchinnikov, S. Lazar, M. Pizzochero, M. B. Whitwick, A. Surrente, M. Baranowski, O. Lopez-Sanchez, P. Gillet, P. Plochocka, O. V. Yazyev, and A. Kis  
*Highly-oriented atomically thin ambipolar MoSe<sub>2</sub> grown by molecular beam epitaxy*  
ACS Nano 11, 6355 (2017)
2. M. Pizzochero, M. Bonfanti, and R. Martinazzo  
*Hydrogen on silicene: like or unlike graphene?*  
Physical Chemistry Chemical Physics 18, 15654 (2016)
1. M. Pizzochero, O. Leenaerts, B. Partoens, R. Martinazzo, and F. M. Peeters  
*Hydrogen adsorption on boron and nitrogen doped graphene*  
Journal of Physics: Condensed Matter 27, 425502 (2015)



# Contents

<b>Abstract (English/Français/Italiano)</b>	<b>iv</b>
<b>List of Publications</b>	<b>xi</b>
<b>1 Introduction</b>	<b>1</b>
1.1 Transition metal dichalcogenides . . . . .	1
1.1.1 Molybdenum disulfide ( $\text{MoS}_2$ ) . . . . .	1
1.1.2 Platinum diselenide ( $\text{PtSe}_2$ ) . . . . .	6
1.2 Chromium triiodide ( $\text{CrI}_3$ ) . . . . .	7
1.3 Outline of the Thesis . . . . .	10
<b>2 Methodology</b>	<b>13</b>
2.1 The many-electron problem . . . . .	13
2.2 Kohn-Sham density-functional theory . . . . .	15
2.3 <i>Ab initio</i> molecular dynamics . . . . .	17
2.3.1 Microcanonical ensemble ( $NVE$ ) . . . . .	18
2.3.2 Canonical ensemble ( $NVT$ ) . . . . .	19
2.4 Practical aspects of first-principles calculations . . . . .	19
2.4.1 Pseudopotentials . . . . .	19
2.4.2 Basis sets . . . . .	20
<b>I Intrinsic and Engineered Defects in Transition Metal Dichalcogenides</b>	<b>23</b>
<b>3 Point Defects in the <math>1T'</math> and <math>2H</math> Phases of Single-Layer <math>\text{MoS}_2</math>: A Comparative First-Principles Study</b>	<b>25</b>
3.1 Motivation . . . . .	26
3.2 Methodology . . . . .	27
3.2.1 First-principles calculations . . . . .	27
3.2.2 Formation energies . . . . .	27
3.3 Results and discussion . . . . .	28
3.3.1 Pristine $\text{MoS}_2$ . . . . .	28
3.3.2 Vacancy defects . . . . .	30
3.3.3 Adatom defects . . . . .	33
3.3.4 Antisite defects . . . . .	36

3.4	Conclusion . . . . .	39
<b>4</b>	<b>Single-Layer 1T'-MoS<sub>2</sub> Under Electron Irradiation from <i>Ab Initio</i> Molecular Dynamics</b>	<b>41</b>
4.1	Motivation . . . . .	42
4.2	Methodology . . . . .	42
4.3	Results and discussion . . . . .	45
4.3.1	Electron irradiation of pristine 1T'-MoS <sub>2</sub> . . . . .	45
4.3.2	Electron irradiation of defective 1T'-MoS <sub>2</sub> . . . . .	48
4.4	Conclusion . . . . .	51
<b>5</b>	<b>Defect-Induced Magnetism in Metallic and Semiconducting 2D-PtSe<sub>2</sub></b>	<b>53</b>
5.1	Motivation . . . . .	54
5.2	Defect-induced, layer modulated magnetism in ultrathin metallic PtSe <sub>2</sub> . . . .	54
5.2.1	Experimental results . . . . .	54
5.2.2	Theoretical results . . . . .	58
5.2.3	Methodology . . . . .	60
5.3	Probing magnetism in atomically thin semiconducting PtSe <sub>2</sub> . . . . .	60
5.3.1	Experimental results . . . . .	60
5.3.2	Theoretical results . . . . .	64
5.3.3	Methodology . . . . .	66
5.4	Conclusion . . . . .	66
<b>II</b>	<b>Understanding and Manipulating Magnetism in Monolayer CrI<sub>3</sub></b>	<b>69</b>
<b>6</b>	<b>Magnetic Exchange Interactions in Monolayer CrI<sub>3</sub> from Many-Body Wavefunction Calculations</b>	<b>71</b>
6.1	Motivation . . . . .	72
6.2	Results and dicussion . . . . .	73
6.2.1	Spin Hamiltonian from many-body wavefunctions . . . . .	73
6.2.2	Magnetic interactions from density functional theory . . . . .	76
6.3	Conclusion . . . . .	79
6.4	Methodology . . . . .	79
<b>7</b>	<b>Inducing Magnetic Phase Transitions in Monolayer CrI<sub>3</sub> <i>via</i> Lattice Deformations</b>	<b>81</b>
7.1	Motivation . . . . .	82
7.2	Methodology . . . . .	82
7.3	Results and discussion . . . . .	83
7.4	Conclusion . . . . .	87
<b>8</b>	<b>Atomic-Scale Defects in the Two-Dimensional Ferromagnet CrI<sub>3</sub> from First Principles</b>	<b>89</b>
8.1	Motivation . . . . .	90

8.2	Methodology . . . . .	90
8.3	Results and discussion . . . . .	91
8.4	Conclusion . . . . .	96
<b>III Revisiting Two <i>Classics</i> in Chemistry</b>		<b>99</b>
<b>9</b>	<b>Picture of the Wet Electron: A Localized Transient State in Liquid Water</b>	<b>101</b>
9.1	Motivation . . . . .	102
9.2	Computational model . . . . .	103
9.3	Results . . . . .	103
9.3.1	Energetics and dynamics of excess electrons . . . . .	103
9.3.2	Atomic structure of the wet electron . . . . .	107
9.4	Discussion and conclusion . . . . .	109
9.5	Methodology . . . . .	110
<b>10</b>	<b>To Bend or Not to Bend, the Dilemma of Multiple Bonds</b>	<b>113</b>
10.1	Motivation . . . . .	114
10.2	Methodology . . . . .	116
10.3	Results and discussion . . . . .	116
10.3.1	A simple $\sigma + \pi$ model . . . . .	116
10.3.2	Influence of the bond length . . . . .	119
10.3.3	Substituent effects . . . . .	120
10.3.4	Elemental 2D and layered crystals . . . . .	121
10.4	Conclusion . . . . .	124
<b>11</b>	<b>Concluding Remarks</b>	<b>125</b>
	<b>Bibliography</b>	<b>129</b>
	<b>Curriculum Vitæ</b>	<b>157</b>



# 1 Introduction

The first isolation of graphene back in 2004 represented a paradigm shift in condensed matter physics. This discovery sparked a wealth of unexplored research directions, most notably the search for novel two-dimensional crystals, together with their controlled stacking for the assembling of van der Waals heterostructures in a layer-by-layer fashion. Since then, the library of atomically thin materials is rapidly expanding, first starting from those parent 3D crystals which can be peeled off to the 2D limit (*e.g.* transition metal dichalcogenides or hexagonal boron nitride) and subsequently evolving into the synthesis of artificial monolayers (*e.g.* silicene or its heavier group IV analogs), eventually spanning a wide range of properties, including metals, semi- and super-conductors, trivial or topological insulators, as well as non-magnetic or magnetically ordered systems. In this Chapter, we introduce the salient physical properties and potential applications of the 2D materials which are the focus of this work – *i.e.* molybdenum disulfide ( $\text{MoS}_2$ ), platinum diselenide ( $\text{PtSe}_2$ ), and chromium triiodide ( $\text{CrI}_3$ ) – and presents the outline of this Thesis.

## 1.1 Transition metal dichalcogenides

### 1.1.1 Molybdenum disulfide ( $\text{MoS}_2$ )

Since the very first isolation of graphene [Novoselov et al., 2004], a constantly growing effort has been devoted to the search of novel atomically thin crystals [Novoselov et al., 2005]. In addition to the fundamental interest in expanding the library of 2D materials and their accompanying physical properties, this search has largely been fueled by the need for overcoming some of the well-known limitations of graphene in achieving prospective technological applications. For instance, the semi-metallic character of graphene stemming from a pair of Dirac cones crossing at the corners of its Brillouin zone [Castro Neto et al., 2009] prevents the realization of switchable electronic devices. Although a number of strategies has been proposed to induce a band-gap opening in graphene (see *e.g.* [Balog et al., 2010, Bostwick et al., 2009, Elias et al., 2009, Martinazzo et al., 2010]), a feature which is instrumental in achieving a non-vanishing on-off current ratio, they were also invariably found to deteriorate the carrier mobility. In this vein, monolayers of transition metal dichalcogenides (TMDs) are promising candidates for next-generation technologies [Chhowalla et al., 2013]. TMDs are a class of layered crystals

with general formula  $\text{MX}_2$ , with M being a transition metal atom ( $\text{M} = \text{Mo}, \text{W}, \text{Nb}, \text{Ta}, \text{Ti}, \text{Re}, \dots$ ) and X a chalcogen atom ( $\text{S}, \text{Se}$  or  $\text{Te}$ ). The most representative member of this novel class of systems is undoubtedly  $\text{MoS}_2$ . Similarly to graphene, monolayers of  $\text{MoS}_2$  can be obtained throughout micromechanical or chemical exfoliation from molybdenite, a naturally occurring layered mineral well-known in the lubricant industry, as well as *via* chemical vapor deposition or chemical vapor transport techniques [Yazyev and Kis, 2015]. Contrary to graphene, however, monolayer  $\text{MoS}_2$  (and, in general, all atomically thin group VI dichalcogenides) admits several polymorphs with distinct electronic properties, namely the stable and semiconducting  $2H$  along with the metastable and semimetallic  $1T'$  phases [Calandra, 2013], which will be presented in the following.

### The $2H$ crystalline phase

Molybdenite [see Fig. 1.1(a)], the bulk  $\text{MoS}_2$  crystal, consists of vertical stacking of two-dimensional layers which are separated by  $\sim 6.5 \text{ \AA}$  and weakly interact through van der Waals forces, thereby enabling their exfoliation to the few- and eventually single-layer regime of thickness. The  $2H$  phase of  $\text{MoS}_2$  displays an atomic plane of Mo atoms sandwiched between a pair of S planes in an ABA-stacking fashion, giving rise to the honeycomb-like lattice shown in Figs. 1.1(b) and (c). The first isolation of atomically thin layers of  $2H\text{-MoS}_2$  traces back to the 1960s [Frindt, 1966], largely motivated by progress in the low-friction coatings industry. It is only with the appearance of graphene about thirty years later – along with the important recognition that 2D materials may host strikingly different properties with respect to their 3D parent counterparts – that the interest in transition metal dichalcogenides has experienced a renaissance. In Fig. 1.1(d), we compare the electronic band structures of bulk and monolayer  $\text{MoS}_2$ , where distinct features can be appreciated [Yazyev and Kis, 2015]. Bulk  $\text{MoS}_2$  is an indirect-gap ( $\sim 1.2 \text{ eV}$ ) semiconductor, being the valence band maximum located at the origin of the Brillouin zone and the conduction band minimum in an off-symmetry point located between  $K$  and  $\Gamma$ . In the single-layer limit, however, several changes in the shape of the bands are observed. These include a transition from indirect-to-direct gap semiconductor, an increase of the gap width by  $\sim 0.7 \text{ eV}$  with both band edges shifted at the  $K$  point, as well as the lifting of the band-degeneracy ensuing from the broken inversion-symmetry of the crystal structure in the monolayer. The combination of the reduced dimensionality with the presence of a direct band gap [Mak et al., 2010, Splendiani et al., 2010] of  $\sim 1.9 \text{ eV}$  renders monolayer  $\text{MoS}_2$  an appealing material for the design and realization of novel electronic devices [Lu et al., 2017, Wang et al., 2012, Szabò et al., 2015]

2D semiconductors are suitable platforms to foster innovations in digital electronics, given their lack of short-channel effect, relatively easy processability, as well as scaling to smaller dimensions [Xie et al., 2017]. Motivated by these considerations, in 2011 the first realization of single-layer  $\text{MoS}_2$  field-effect transistor (FET) was reported [Radisavljevic et al., 2011a], the schematics of which is shown in Fig. 1.1(e). Following the usual basic FET structure, it consists of monolayer  $\text{MoS}_2$  acting as a semiconducting channel, contacted by source and drain Au electrodes, and separated from a gate electrode by a high- $k$  dielectric. Such a  $\text{MoS}_2$ -based

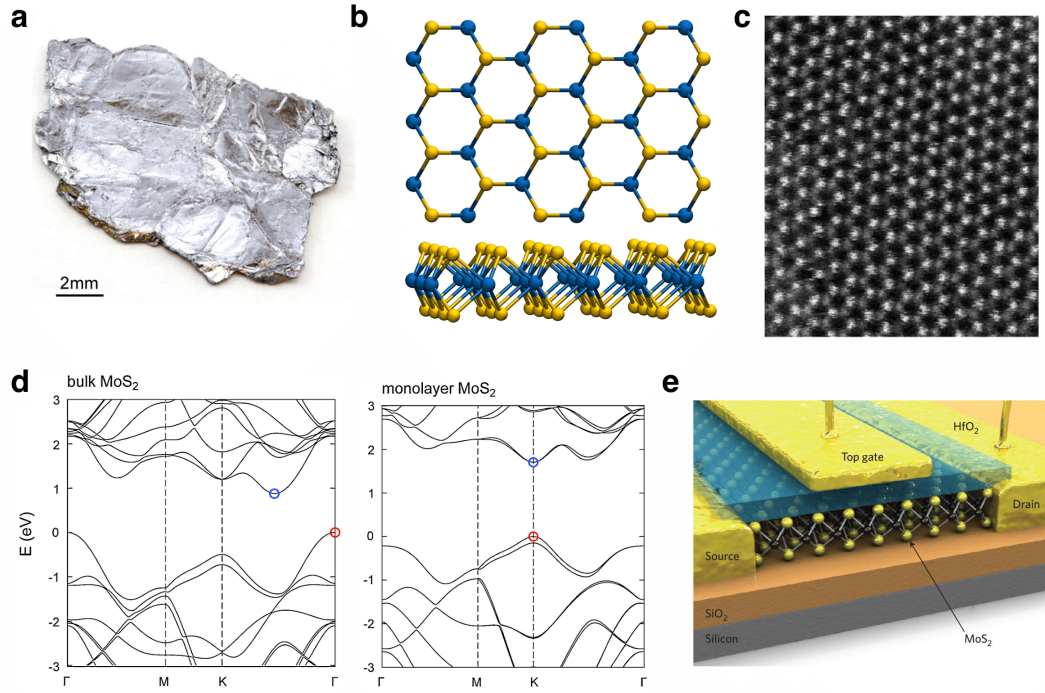


Figure 1.1 – (a) Picture of molybdenite, a naturally occurring crystal consisting of van der Waals-stacked  $\text{MoS}_2$  layers. (b) Top- and side-view of the atomic structure of monolayer  $2H\text{-MoS}_2$ . Blue (orange) balls represent Mo (S) atoms. (c) Atomic resolution transmission electron microscopy (HAADF) image of monolayer  $2H\text{-MoS}_2$ . (d) Electronic band structure of bulk and monolayer  $\text{MoS}_2$  obtained at the semilocal density-functional theory level. (e) Schematics of the first monolayer  $\text{MoS}_2$ -based transistor. Panels (a) and (d) are adapted from [Yazyev and Kis, 2015]. Panel (c) is adapted from [Zan et al., 2013]. Panel (e) is adapted with permission from [Wang et al., 2012], Springer Nature.

transistor meets many of the requirements which are necessary for practical applications in electronics, including a high on-off current ratio exceeding  $10^8$  at room temperature and a carrier mobility of  $\sim 200 \text{ cm}^2 \text{ V}^{-1} \text{ s}^{-1}$ , comparable to that of silicon films [Wang et al., 2012]. Such transistors have later been later exploited as building blocks for the realization of more complex applications in the context of both electronics, *e.g.* integrated circuits operating at room temperature and capable of performing logic operations [Radisavljevic et al., 2011b], and optoelectronics, like ultrasensitive photodetecting devices [Lopez-Sanchez et al., 2013]. In addition to conventional electronics, unconventional device concepts have been introduced on the basis of the peculiar properties of two-dimensional  $\text{MoS}_2$ , depending on the nature of the degree of freedom exploited [Yazyev and Kis, 2015, Pulkin and Yazyev, 2016]. For instance, the strong-spin orbit interactions observed in the valence band of monolayer  $\text{MoS}_2$  [see Fig. 1.1(d)] may be used in *spintronics*, where spin is employed for the storage and processing of the information. In addition, band edges in monolayer  $\text{MoS}_2$  occurs at two inequivalent valleys located at the corners of the Brillouin zone, thereby suggesting that the valley degree of freedom of the charge carriers may also be manipulated, an emerging field

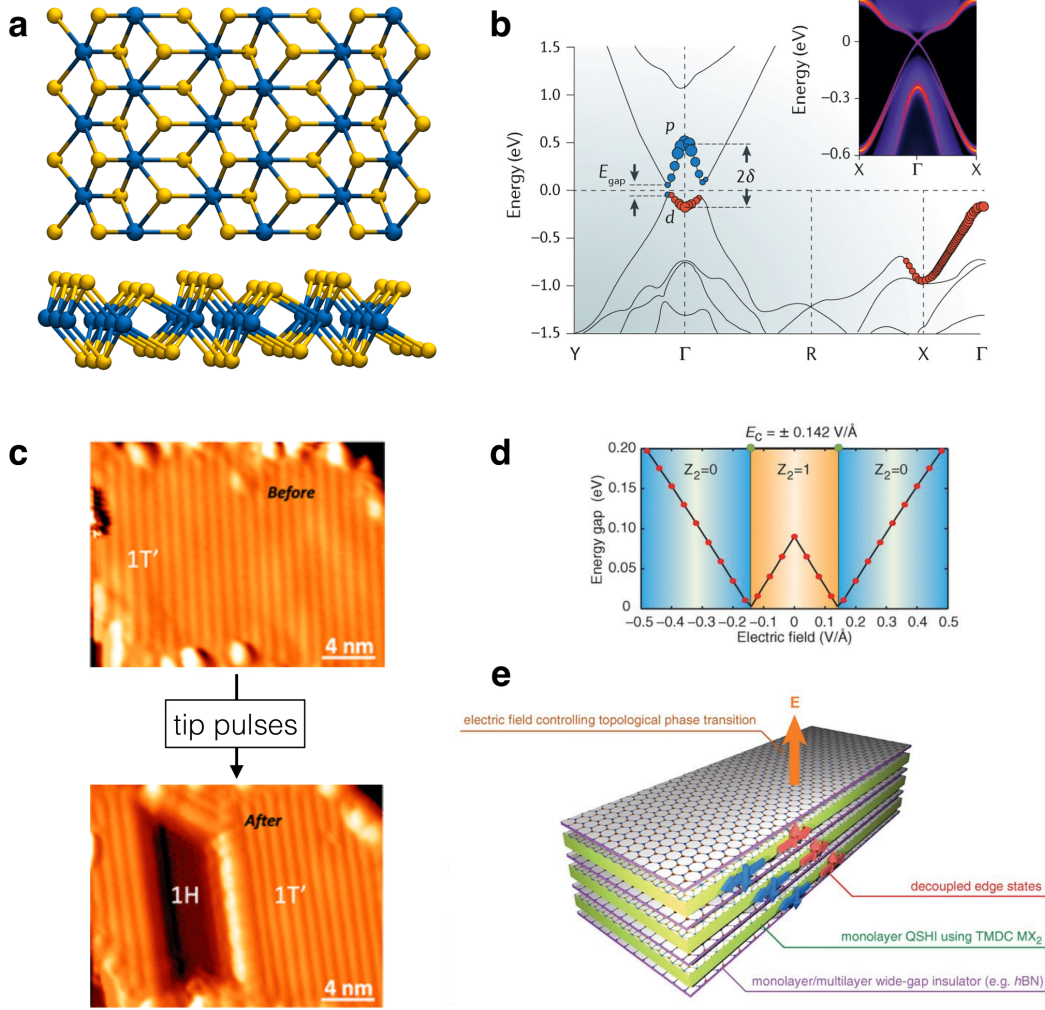


Figure 1.2 – (a) Top- and side-view of the atomic structure of monolayer 1T'-MoS<sub>2</sub>. Blue (orange) balls represent Mo (S) atoms. (b) Electronic band structure of 1T'-MoS<sub>2</sub> along with the topologically protected surface states, as obtained from first-principles calculations. (c) Creation of semiconducting 2H-WSe<sub>2</sub> islands embedded in semi-metallic 1T'-WSe<sub>2</sub> upon STM tip pulses. (d) Evolution of the band gap and topological invariant with the application of an external electric field in 1T'-MoS<sub>2</sub>. (e) Schematics of the proposed "topological" field effect transistor. Panel (b) is adapted with permission from [Manzeli et al., 2017], Springer Nature. Panel (c) is adapted from [Pedramrazi et al., 2019]. Panels (d) and (e) are adapted with permission from [Qian et al., 2014], AAAS.

dubbed *valleytronics*.

### The 1T' crystalline phase

When thinned down to the atomically thin limit, MoS<sub>2</sub> and group VI dichalcogenides display a metastable polymorph, in addition to the thermodynamically stable 2H phase. This corresponds to the 1T' phase (sometimes referred to as distorted 1T), which lies 0.53 eV per



formula unit higher in energy than the  $2H$  [Kretschmer et al., 2017]. As shown in Fig. 1.2(a), this polymorph exhibits a rather complex crystal structure, which is characterized by parallel zigzag chains of metal atoms sandwiched between two chalcogen layers. While semiconducting  $2H$ -MoS<sub>2</sub> holds great promise in next-generation devices, the exploration of the  $1T'$  phase is still in its infancy. To date, the interest in the metastable  $1T'$  phase of group VI TMDs has mainly originated from its peculiar electronic properties, where the combination of a  $p$ - $d$  band inversion along with a small band gap stemming from spin-orbit interactions was predicted to drive the system into a quantum spin Hall insulator [Qian et al., 2014], where topologically protected edge states develop at the interface between phases with different topological invariants, see Fig. 1.2(b). Such predictions have later been confirmed in the  $1T'$  phases of WTe<sub>2</sub> [Tang et al., 2017, Fei et al., 2017], WSe<sub>2</sub> [Ugeda et al., 2018] and eventually inferred for MoS<sub>2</sub> [Xu et al., 2018b]. Switching between topological and trivial phases in  $1T'$ -TMDs can be achieved with the application on external electric field as well as lattice strain [Qian et al., 2014, Pulkin and Yazyev, 2017], as shown in Fig. 1.2(d). These findings pave the way for new concepts of low-power field-effect transistors based on topological  $1T'$ -MoS<sub>2</sub> [Qian et al., 2014, Liu and Guo, 2015] of the kind presented in Figs. 1.2(d) and (e), where the on-off current states are controlled by quenching the topological phase through the application of a vertical electric field. Furthermore, it has been shown that  $1T'$ -TMDs display superior catalytic activity in hydrogen evolution reaction as compared to the  $2H$  phase [Gao et al., 2015, Seok et al., 2017], and their peculiar crystal structure biases the accommodation of organic cations towards specific lattice sites, with potential applications in sensors based on  $1T'$ -TMDs [Goloveshkin et al., 2015].

Several techniques have been theoretically and experimentally introduced in order to promote a transition between the  $2H$  and  $1T'$  crystalline phases of group VI dichalcogenides [Voiry et al., 2015], including lattice strain [Duerloo et al., 2014], lithiation or alkali metal intercalation [Esfahani et al., 2015, Bunjaku and Luisier, 2019], mild annealing [Eda et al., 2011], alloying [Raffone et al., 2016], scanning tunneling microscope tip pulses [see Fig. 1.2(c), [Pedramrazi et al., 2019]] and electrostatic gating [Li et al., 2016b], with the aim of exploiting complementary functionalities within the same nominal stoichiometry. Among the many strategies which have been proposed in the context of crystalline-phase engineering of MoS<sub>2</sub>, the opportunity of achieving a local structural transformation in MoS<sub>2</sub> upon exposure to the electron beam is of particular interest [Lin et al., 2014]. In fact, the coexistence of the two phases in the same monolayer yields the formation of a lateral metal-semiconductor heterojunction. Given that the  $1T'$  polymorph is a (topological) semimetal and the  $2H$  a (trivial) semiconductor, such heterojunctions can conceivably be exploited for the realization of novel electronic nanodevices [Eda et al., 2012] in the ultimate limit of atomic thickness. A recent theoretical work has proposed a detailed mechanism underlying this beam-driven crystalline phase transition [Kretschmer et al., 2017]. In particular, it associates the initial stabilization of the  $1T'$  polymorph to the creation of the local strain induced by vacancy line defects which form upon known-on damage, along with charge transfers and electron excitation effects. Subsequently, the emerging  $1T'$  polymorph remains stable even in the absence of the electron beam due to the large energy barrier separating the two phases. Overall, these findings highlight an

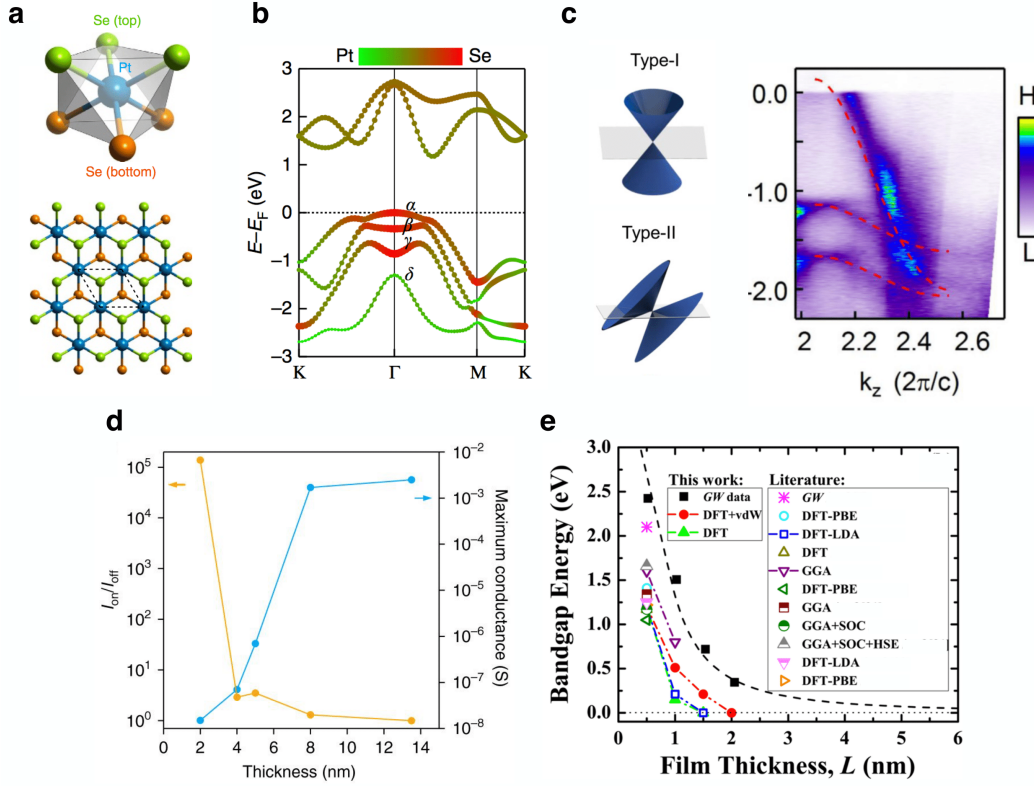


Figure 1.3 – (a) Top- and side-view of the atomic structure of monolayer PtSe<sub>2</sub>. (b) Band structure of monolayer PtSe<sub>2</sub> obtained from first-principles calculations. (c) Representation of the band crossing in type-I and type-II Dirac semi-metals, along with the tilted Dirac cone observed in angle-resolved photoemission spectroscopy in bulk PtSe<sub>2</sub>. (d) on-off current ratio and conductance of PtSe<sub>2</sub> as a function of the sample thickness. (e) First-principles calculations at several levels of theory showing the evolution of the band gap with the film thickness in PtSe<sub>2</sub>. Panels (a) and (b) are adapted from [Yao et al., 2017]. Panel (c) is adapted with permission from [Zhang et al., 2017], APS. Panel (d) is adapted from [Ciarrocchi et al., 2018]. Panel (e) is adapted from [Ansari et al., 2019].

intimate correlation between disorder and phase-engineering in two-dimensional transition metal dichalcogenides.

### 1.1.2 Platinum diselenide (PtSe<sub>2</sub>)

Noble-transition metal dichalcogenides ( $M = \text{Pt}$  or  $\text{Pd}$ ) exhibit rather unique properties emerging from the abnormally strong coupling between layers [Pi et al., 2019]. As compared to group VI dichalcogenides discussed in the previous Section,  $\text{PtX}_2$  or  $\text{PdX}_2$  ( $X = \text{S}, \text{Se}, \text{Te}$ ) feature different crystal structures, namely either an unusual orthorhombic structure consisting of puckered pentagonal rings (not shown here) and the  $1T$  structure shown in Fig. 1.3(a) [Pi et al., 2019]. In this latter case, the transition metal resides in an octahedral environment, accompanied by an ABC-stacking pattern of the chalcogen-metal-chalcogen planes. In the following,

we will focus mainly on  $\text{PtSe}_2$ , the most well-studied member among noble-transition metal dichalcogenides. Quantum confinement effects play a crucial role in ruling the electronic properties of 1T- $\text{PtSe}_2$  [Clark et al., 2019, Ciarrocchi et al., 2018]. In the monolayer limit, this system displays a semiconducting character [Fig. 1.3(b), [Yao et al., 2017, Wang et al., 2015a]], with an indirect band gap whose width is theoretically estimated to be in the order of 1.5 – 2.5 eV depending on the level of theory adopted, see Fig. 1.3(e). The orbital character of the valence band maximum, which is located at the  $\Gamma$  point, is mainly due to the  $p$  states of Se, whereas both the  $d$  states of Pt and the  $p$  states of Se contribute to the orbital character of the conduction band minimum. In bulk, on the other hand,  $\text{PtSe}_2$  is found to possess a metallic nature and to host type-II Dirac fermions [Zhang et al., 2017], as shown by first-principles calculations and angle-resolved photoemission spectroscopy measurements, see Fig. 1.3(c).

This strikingly different electronic structure between monolayer and bulk  $\text{PtSe}_2$  makes this material stand out from other transition metal dichalcogenides, where typically only moderate dependence of the band gap on the number of layers is observed. The evolution of the electronic and transport properties of  $\text{PtSe}_2$  with the atomic thickness has been investigated in recent experiments [Fig. 1.3(d), [Ciarrocchi et al., 2018]], where a semiconducting-to-metal transition has been observed at a thickness of  $\sim 8$  nm. This, in turn, leads to a suppression of the on-off current ratio along with a substantial increase of the conductance when increasing the sample thickness from 2 to 8 nm, as further confirmed by the theoretical investigations performed under the  $GW$  formalism [Fig. 1.3(e), [Clark et al., 2019]]. This layer-dependent electronic structure originates from the unique interlayer interaction in  $\text{PtSe}_2$  [Zhao et al., 2016]. Unlike  $\text{MoS}_2$  and many transition metal dichalcogenides, the low-lying  $d$  orbitals of  $\text{PtSe}_2$ , and noble-transition metal dichalcogenides in general, are fully occupied. This promotes a dominant role of the out-of-plane  $p_z$  states of the chalcogen atoms belonging to adjacent layers, which are found to be hybridized to an extent that largely exceeds the strength of ordinary van der Waals interactions in layered crystals. Indeed, such a strong hybridization between chalcogen atoms is responsible for the vanishing band gap in thicker  $\text{PtSe}_2$  films [Zhao et al., 2016]. Overall, the peculiar electronic structure of  $\text{PtSe}_2$  opens up new opportunities in nano-circuitry, where the transport characteristics of the individual components may be modulated through the atomic thickness [Zhao et al., 2017b, Yim et al., 2016, Ciarrocchi et al., 2018]

## 1.2 Chromium triiodide ( $\text{CrI}_3$ )

Within the family of atomically thin crystals, the emergence of correlated electronic phases, including superconductivity, Mott-insulating phases, or charge density waves [Castro Neto, 2001, Cao et al., 2018b, Cao et al., 2018a, Manzeli et al., 2017], has culminated in the discovery of intrinsic magnetism in certain 2D materials [Burch et al., 2018, Gong and Zhang, 2019]. Indeed, while magnetism in lattices of reduced dimensionality has hitherto been ascribed to native or engineered impurities [Yazyev and Helm, 2007, Nair et al., 2012, Pizzochero and Yazyev, 2017, Karthikeyan et al., 2019], the groundbreaking isolation and characterization of atomically thin metallic  $\text{Cr}_2\text{Ge}_2\text{Te}_6$  and semiconducting  $\text{CrI}_3$  in 2017 have unambiguously

## Chapter 1. Introduction

Table 1.1 – List of some representative magnetic van der Waals crystals grouped by the sign of their intra-layer ( $J_{\parallel}$ ) and inter-layer ( $J_{\perp}$ ) magnetic exchange interaction [Gibertini et al., 2019].

Magnetic Interactions	Materials
$J_{\parallel} < 0; J_{\perp} > 0$	CoPS <sub>3</sub> ; MnPS <sub>3</sub> ; NiPS <sub>3</sub>
$J_{\parallel} > 0; J_{\perp} > 0$	bulk CrI <sub>3</sub> ; CrBr <sub>3</sub> , Cr <sub>2</sub> Ge <sub>2</sub> Te <sub>6</sub>
$J_{\parallel} < 0; J_{\perp} < 0$	FePS <sub>3</sub> ; MnPSe <sub>3</sub>
$J_{\parallel} > 0; J_{\perp} < 0$	few-layer CrI <sub>3</sub> ; bulk CrCl <sub>3</sub>

demonstrated the possibility of a long-range, intrinsic magnetism in low dimensions [Huang et al., 2017, Burch et al., 2018, Gibertini et al., 2019, Gong and Zhang, 2019, Mak et al., 2019]. Although van der Waals crystals hosting a magnetic order have been known for quite a long time, whether such order is retained in the ultimate limit of vertical miniaturization remained an elusive question. On the theoretical side, the Mermin-Wagner theorem [Mermin and Wagner, 1966], which relies on the *isotropic* Heisenberg spin Hamiltonian, indicates that no magnetic order at all can be preserved against thermal fluctuations when moving from three to two dimensions. However, this restriction is lifted when the single-ion anisotropy comes into play, thereby making this physical quantity essential to realize truly 2D magnets with non-vanishing critical temperatures. So far, several intrinsically magnetic, atomically thin crystals have been isolated [Gibertini et al., 2019], with many more theoretically predicted and currently awaiting experimental confirmation [Torelli et al., 2019, Mounet et al., 2018]. Their magnetism is often found to be ruled by the competition between the in-plane and out-of-plane magnetic exchange interactions; a non-exhaustive list of ultrathin layered magnets is presented in Table 1.1.

Among the 2D magnets, the most prototypical member is certainly CrI<sub>3</sub>, the atomic structure of which is shown in Fig. 1.4(a). It consists of Cr atoms located on the corners of a honeycomb network, each of them six-fold coordinated by I ligands, giving rise to a Cr-I-Cr angle close to 90° [McGuire et al., 2015]. This indicates that Cr<sup>3+</sup> ions are spin-3/2 centers, which couple through the I-mediated super-exchange channels [Lado and Fernández-Rossier, 2017]. In bulk, this semiconducting crystal exhibits a ferromagnetic order up to 61 K [McGuire et al., 2015]. This is not surprising, as such a magnetic order has to be expected based on the rule proposed by Goodenough [Goodenough, 1958] and Kanamori [Kanamori, 1959]. A more complex scenario emerges when moving from the parent bulk crystal to the two-dimensional limit. In Fig. 1.4(b), we show the results of magneto-optical Kerr effect (MOKE) measurements performed on mono-, bi-, and tri-layers of CrI<sub>3</sub>, proving that magnetically ordered phases do persist in two dimensions [Huang et al., 2017]. It can be clearly noticed that mono- and tri-layer CrI<sub>3</sub> behave similarly to each other, and both very differently from the bilayer system. In mono- and tri-layer, hysteretic features appear at about  $\pm 0.1$  T, which eventually reach a plateau upon the application of higher magnetic fields. This observation is the hallmark of ferromagnetic order. In the case of the bilayer, conversely, one can notice a vanishing net magnetization at zero field, which acquires a non-vanishing character at magnetic fields of approximately  $\pm 0.65$

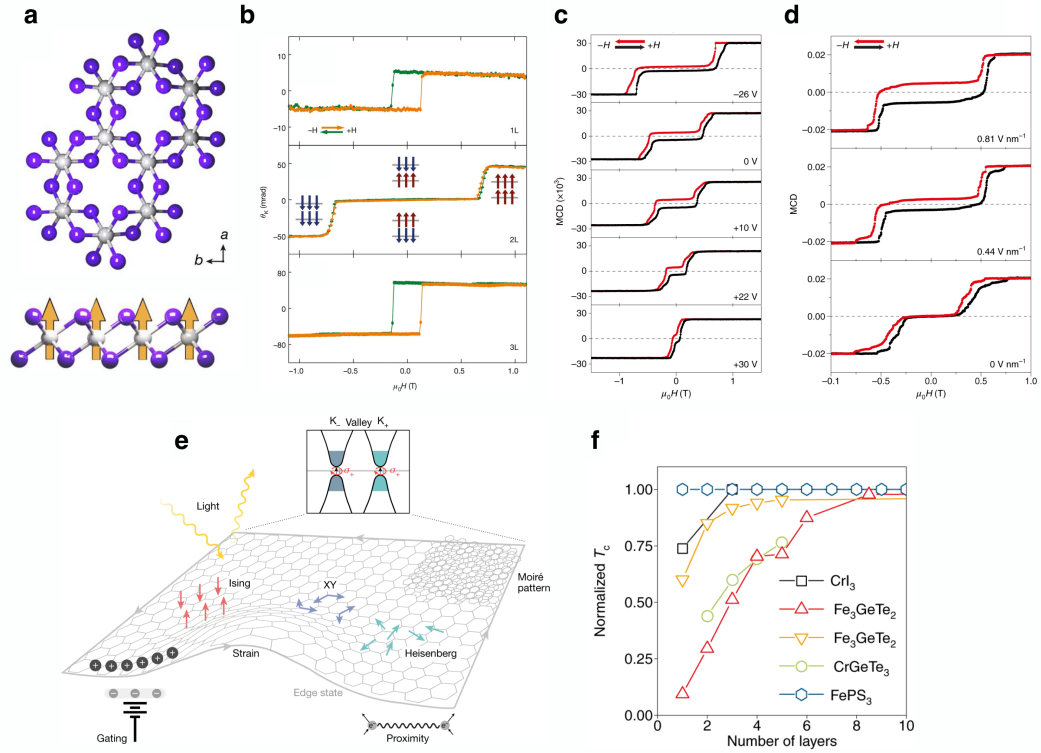


Figure 1.4 – (a) Top- and side-view of the atomic structure of monolayer CrI<sub>3</sub>. Grey (violet) balls represent Cr (I) atoms. (b) MOKE response of mono-, bi-, and tri-layer CrI<sub>3</sub>. Effect of (c) voltage and (d) electric field on the magnetic circular dichroism of bilayer CrI<sub>3</sub>. (e) Overview of some novel physical effects and device concepts based on two-dimensional magnets. (f) Evolution of the normalized critical temperature with the atomic thickness of several 2D magnets. Panels (a) and (b) are adapted with permission from [Huang et al., 2017], Springer Nature. Panels (c), (d) and (f) are adapted with permission from [Gibertini et al., 2019], Springer Nature. Panel (e) is adapted with permission from [Burch et al., 2018], Springer Nature.

T. This, on the other hand, is the signature of antiferromagnetic order. The observed thickness-dependent magnetic response suggests that, in the two-dimensional limit, CrI<sub>3</sub> possesses in-plane ferromagnetic and off-plane antiferromagnetic magnetic exchange interactions. Reconciling the out-of-plane interactions observed in the bilayer with the ferromagnetic order in bulk remains an open question. It has been suggested that the reason for this discrepancy may be traced back to the structural phase transition which CrI<sub>3</sub> undergoes when thinned down to few-layers [Ubrig et al., 2019]. Furthermore, the critical temperature of ultrathin CrI<sub>3</sub> is 45 K [Huang et al., 2017] (to be compared to 65 K for bulk CrI<sub>3</sub> [McGuire et al., 2015]), thereby indicating that this quantity is quite insensitive to interlayer interactions.

The competition between ferromagnetic and antiferromagnetic exchange couplings in bilayer CrI<sub>3</sub> is appealing for engineering the magnetic interactions in this system. Notably, it has been shown through magnetic circular dichroism measurements that the magnetic response of CrI<sub>3</sub>

can be largely controlled, *e.g.* through electrostatic doping [Fig. 1.4(c), [Jiang et al., 2018a]] or the applied electric field in the direction perpendicular to the layers [Fig. 1.4(d), [Jiang et al., 2018b]]. The application of external voltage modulates the magnitude of the magnetic field which is required to switch bilayer CrI<sub>3</sub> from the antiferromagnetic state (that is, a vanishing net spin polarization) at zero field into the ferromagnetic (that is, a full spin polarization) at higher fields. Specifically, such magnitude is found to increase (decrease) upon the application of positive (negative) voltages. The main effect arising from the application of an external electric field consists in the introduction of a hysteresis loop located at zero field, thereby signaling the appearance of a net spin polarization in the otherwise antiferromagnetic system. In addition to these strategies, many other techniques have been introduced to tailor the magnetism of atomically thin CrI<sub>3</sub>, including the application of an external pressure [Song et al., 2019, Li et al., 2019], off-plane lattice deformations [Thiel et al., 2019], or a careful adjustment of the stacking pattern [Sivadas et al., 2018, Ubrig et al., 2019]. An overview of potential routes towards the engineering of magnetism in 2D crystals is presented in Fig. 1.4(e) [Burch et al., 2018].

The emergence of magnetic orders in low dimensions, along with their large degree of tunability, is of great interest in the design of a number of potential technologies, including the realization of heterostructures with specific functionalities achieved by exploiting interface effects, magnetic sensors, spintronic devices which can be modulated by *e.g.* lattice strain and gating, as well as innovative concepts in information technology like topological quantum computing [Burch et al., 2018, Gong and Zhang, 2019]. In order to translate these novel physical phenomena into prospective device applications, however, several issues need to be settled. For instance, to date atomically thin magnets have been obtained by mechanical exfoliation in an inert atmosphere due to their lack of air stability. Hence, developing novel synthetic paths toward air-stable 2D magnets of large area is of primary importance. Also, the critical temperature in van der Waals magnets is often small, and most likely further reduces when the crystal is peeled off to few layers, as shown in Fig. 1.4(f). Devising effective approaches to stabilize the magnetism against thermal fluctuations by strengthening both the exchange interactions and magnetic anisotropies would be therefore desirable for room-temperature applications [Torelli and Olsen, 2018].

### 1.3 Outline of the Thesis

The rest of this Thesis is organized as follows:

- Chapter 2 overviews the main ideas underlying the computational methodologies adopted throughout this work, including Kohn-Sham density-functional theory and its approximations, *ab initio* molecular dynamics, and some practical aspects of first-principles calculations.
- Part I (Chapters 3, 4, 5) reports on the investigation of native and electron beam-driven defects in transition metal dichalcogenides. We start by conducting a comparative study of the thermodynamic stability, electronic and magnetic properties of point defects in

the  $2H$  and  $1T'$  phases of monolayer  $\text{MoS}_2$  by means of first-principles calculations [Pizzochero and Yazyev, 2017]. Next, we examine the response of  $1T'$ - $\text{MoS}_2$  to the electron irradiation with the help of *ab initio* molecular dynamics simulations and formulate guidelines for the intentional creation of engineered defects in the electron microscope [Pizzochero and Yazyev, 2018]. Finally, we present a joint experimental and theoretical study of defect-induced magnetism in both semiconducting and metallic ultrathin films of  $\text{PtSe}_2$  [Avsar et al., 2019, Avsar et al., 2020].

- Part II (Chapters 6, 7, 8) covers the theoretical investigation of magnetic exchange interactions in monolayer  $\text{CrI}_3$  through a combination of model spin Hamiltonians, density functional, and quantum chemistry calculations. We first provide an unprecedentedly accurate determination of magnetic couplings in  $\text{CrI}_3$  and establish a firm theoretical ground to recent experimental observations [Pizzochero et al., 2020]. We further show how such couplings can be engineered through lattice deformations, thereby promoting a series of strain-induced magnetic phase transitions [Pizzochero and Yazyev, 2020]. Finally, we present the very first investigation of defects formation in monolayer  $\text{CrI}_3$ , along with their mobility, aggregation tendency, and defect-induced local magnetic moments [Pizzochero, 2020].
- Part III (Chapters 9, 10) sheds fresh light on two long-standing yet poorly understood issues in physical chemistry. These comprise (i) the hydration dynamics of an excess electron in liquid water – a process which is relevant *e.g.* to DNA damage in living organisms – from hybrid-functional molecular dynamics [Pizzochero et al., 2019a], and (ii) the development of a unified picture of the (seemingly different) nature of double bonds between C atoms as compared to higher group elements [Pizzochero et al., 2019b], with important consequences in the otherwise elusive comprehension of the structural dissimilarities between graphene *vs* silicene and germanene.
- Finally, Chapter 11 summarizes the main findings of this Thesis and concludes this work.





## 2 Methodology

This Chapter illustrates the main ideas underlying the computational techniques adopted throughout this work. Our goal here is not to give a detailed derivation of the first-principles approaches used in this Thesis, rather to recall the fundamental expressions. We start with the non-relativistic time-independent Schrödinger equation under the Born-Oppenheimer scheme. Next, we introduce Kohn-Sham density-functional theory along with popular approximations to the universal density functional. We then discuss *ab initio* molecular dynamics in the microcanonical and canonical ensembles, and finally conclude with some practical aspects of first-principles calculations.

### 2.1 The many-electron problem

We start by considering the Hamiltonian  $\mathcal{H}$  describing an arbitrary system consisting of  $n$  electrons and  $N$  nuclei [Szabo and Ostlund, 1996]. For the sake of simplicity, we neglect both relativistic effects and assume a vanishing magnetic field. Hence, the resulting Hamiltonian encodes the kinetic terms of both nuclei ( $T_n$ ) and electrons ( $T_e$ ), along with pair-wise interaction terms ( $V_{ee}$ ,  $V_{en}$ ,  $V_{nn}$ ), thereby reading

$$\mathcal{H} = T_e + T_n + V_{ee} + V_{en} + V_{nn} \quad (2.1)$$

with  $V_{ee}$ ,  $V_{en}$ ,  $V_{nn}$  being the electron-electron, electron-nucleus, nucleus-nucleus Coulomb interaction, respectively. More explicitly, the five terms appearing in the Hamiltonian above take the form

$$T_e = \sum_i \frac{\vec{p}_i^2}{2m_e} \quad (2.2)$$

$$T_n = \sum_I \frac{\vec{P}_I^2}{2M_I} \quad (2.3)$$

$$V_{ee} = \frac{1}{2} \sum_{i \neq j} \frac{e^2}{|\vec{r}_i - \vec{r}_j|} \quad (2.4)$$

$$V_{en} = - \sum_{i,I} \frac{e^2 Z_I}{|\vec{r}_i - \vec{R}_I|} \quad (2.5)$$

$$V_{nn} = \frac{1}{2} \sum_{I \neq J} \frac{e^2 Z_I Z_J}{|\vec{R}_I - \vec{R}_J|} \quad (2.6)$$

where the  $i$ -th ( $I$ -th) electron (nucleus) has charge  $e$  ( $eZ_I$ ), mass  $m_e$  ( $M_I$ ), momentum  $\vec{p}_i$  ( $\vec{P}_I$ ), and spatial coordinates  $\vec{r}_i$  ( $\vec{R}_I$ ). Next, we introduce the Born-Oppenheimer (or adiabatic) approximation [Born and Oppenheimer, 1927]. This approximation decouples the electronic and nuclear degrees of freedom, on the basis that the former evolve much faster in time than the latter, and at each instant electrons can reasonably be considered at thermal equilibrium for a given (frozen) nuclear configuration. This approach is well-justified by the heavier mass of nuclei ( $\sim 10^{-27}$  kg) as compared to that of electrons ( $\sim 10^{-31}$  kg). In practice, this approximation involves the separation of the  $N$  nucleus  $[\chi(\vec{R}_1, \vec{R}_2, \dots, \vec{R}_N)]$  and the  $n$  electrons  $[\psi(\vec{r}_1, \vec{r}_2, \dots, \vec{r}_n)]$  wavefunctions in the overall wavefunction  $\Psi(\vec{r}_1, \vec{r}_2, \dots, \vec{r}_n; \vec{R}_1, \vec{R}_2, \dots, \vec{R}_N)$  according to the following ansatz

$$\Psi(\vec{r}_1, \vec{r}_2, \dots, \vec{r}_n; \vec{R}_1, \vec{R}_2, \dots, \vec{R}_N) = \psi(\vec{r}_1, \vec{r}_2, \dots, \vec{r}_n) \chi(\vec{R}_1, \vec{R}_2, \dots, \vec{R}_N) \quad (2.7)$$

Keeping nuclear coordinates  $R_I$  as parameters, the Hamiltonian of Eq. (2.1) hence reduces to the electronic Hamiltonian  $\mathcal{H}_{\text{el}}$  as

$$\mathcal{H}_{\text{el}} = T_e + V_{ee} + V_{ne} \quad (2.8)$$

the corresponding eigenvalues ( $E$ ) and eigenvectors  $[\psi(\vec{r}_1, \vec{r}_2, \dots, \vec{r}_n)]$  of which can be obtained by solving the usual non-relativistic time-independent Schrödinger equation at a fixed nuclear configuration

$$\left[ \sum_i \frac{\vec{p}_i^2}{2m_e} + \frac{1}{2} \sum_{i \neq j} \frac{e^2}{|\vec{r}_i - \vec{r}_j|} - \sum_{i,I} \frac{e^2 Z_I}{|\vec{r}_i - \vec{R}_I|} \right] \psi(\vec{r}) = E \psi(\vec{r}) \quad (2.9)$$

Because electrons are fermions, the electronic wavefunction must satisfy the antisymmetry principle, according to which it has to change sign upon exchanging a pair of electrons [Pauli, 1925]. This is typically accomplished by expressing the  $n$ -electron wavefunction as a Slater determinant of the constituent single-particle wavefunctions  $\phi_i(\vec{r})$ . For instance, in the case two-electron system  $[\phi_i$  (with  $i = 1, 2$ )], the Slater determinant reads

$$\psi(\vec{r}_1, \vec{r}_2) = \frac{1}{\sqrt{2}} \det \begin{vmatrix} \phi_1(\vec{r}_1) & \phi_2(\vec{r}_1) \\ \phi_1(\vec{r}_2) & \phi_2(\vec{r}_2) \end{vmatrix} = \frac{1}{\sqrt{2}} [\phi_1(\vec{r}_1)\phi_2(\vec{r}_2) - \phi_1(\vec{r}_2)\phi_2(\vec{r}_1)] \quad (2.10)$$

where the coefficient  $\frac{1}{\sqrt{2}}$  is a normalization factor. The advantage of such expression is two-fold. On the one hand, it assures that the sign is reverted if a pair of electrons is swapped,

i.e.  $\psi(\vec{r}_1, \vec{r}_2) = -\psi(\vec{r}_2, \vec{r}_1)$ . On the other hand, it vanishes if a pair of electrons either has either the same coordinates (that is, if  $\vec{r}_1 = \vec{r}_2$ ) or the same wavefunction (that is,  $\phi_j = \phi_i$ ), hence inherently complying with Pauli exclusion principle. Eqn. (2.10) can readily be extended to an  $n$ -electron system as

$$\psi(\vec{r}_1, \vec{r}_2, \dots, \vec{r}_n) = \frac{1}{\sqrt{n!}} \det \begin{vmatrix} \phi_1(\vec{r}_1) & \phi_2(\vec{r}_1) & \dots & \phi_n(\vec{r}_1) \\ \phi_1(\vec{r}_2) & \phi_2(\vec{r}_2) & \dots & \phi_n(\vec{r}_2) \\ \vdots & \vdots & \ddots & \vdots \\ \phi_1(\vec{r}_n) & \phi_2(\vec{r}_n) & \dots & \phi_n(\vec{r}_n) \end{vmatrix} \quad (2.11)$$

Unfortunately, Eqn. (2.9) presents a complexity that grows exponentially with the number of electrons in the system, thereby making it possible to access its solutions only for a relatively small number of electronic degrees of freedom. For realistic systems, however,  $n$  is often in the order of  $\sim 10^{23}$ , hence requiring the introduction of methodologies capable of coping with the many-body problem at a reasonable computational effort.

## 2.2 Kohn-Sham density-functional theory

Among the many strategies which have been devised to find approximate solutions to the time-independent Schrödinger equations, density-functional theory [Hohenberg and Kohn, 1964] under the Kohn-Sham formalism [Kohn and Sham, 1965] is certainly the most widely used, as it allows to achieve a quantum mechanical description of molecules and solids at a favorable compromise between accuracy and computational cost [Parr and Yang, 1994]. On a fundamental level, density-functional theory is rooted in the two theorems introduced by Hohenberg and Kohn [Hohenberg and Kohn, 1964], which can be summarized as follows

1. The ground state density of an arbitrary system of interacting particles is uniquely determined by an external potential  $v(\vec{r})$  exerted on the particles (which, for our purposes, corresponds to the potential generated by nuclei), except for a constant shift.
2. There exists a universal functional of the electron density, such that the electron density  $n(\vec{r})$  of the ground state corresponds to the minimum of that functional. Hence, the search for the ground state density boils down to a variational problem.

Overall, these two theorems ensure that, when examining the ground state of a system, one can replace the complex many-body wavefunction  $\psi(\vec{r}_1, \vec{r}_2, \dots, \vec{r}_n)$  with the relatively simpler electron density  $n(\vec{r})$ . Remarkably, density-functional theory is, in principle, an *exact* reformulation of quantum mechanics, as far as the ground state properties are concerned. An exact expression of the density functional was found for the limiting case of a nearly constant electron density [Hohenberg and Kohn, 1964]. However, such a limiting case leads to an unrealistic description of actual electronic systems.

Thus, approximations to the universal density functional need to be developed [Jones, 2015]. In this regard, substantial progress has been made by Kohn and Sham [Kohn and Sham,

1965], who proposed to introduce an auxiliary system consisting of non-interacting particles – each of them described by a single-particle orbital  $\psi_i(\vec{r})$  – yielding the same ground state density of the system under investigation (this, of course, requires the external potential  $v(\vec{r})$  to be different). For an  $n$ -electron system, the universal functional of the electron density  $n(\vec{r}) = \sum_i \psi_i^*(\vec{r})\psi_i(\vec{r})$  can be written as

$$E_v[n(\vec{r})] = T_n[n(\vec{r})] + E_H[n(\vec{r})] + E_{xc}[n(\vec{r})] + \int d\vec{r} v(\vec{r})n(\vec{r}) \quad (2.12)$$

with  $T_n[n(\vec{r})]$  being the kinetic energy

$$T_n[n(\vec{r})] = -\frac{1}{2} \sum_i \int d\vec{r} \nabla \psi_i^*(\vec{r}) \nabla \psi_i(\vec{r}), \quad (2.13)$$

$E_H[n(\vec{r})]$  the Hartree potential

$$E_H[n(\vec{r})] = \frac{1}{2} \int d\vec{r} d\vec{r}' \frac{n(\vec{r})n(\vec{r}')}{|\vec{r} - \vec{r}'|}, \quad (2.14)$$

and  $E_{xc}[n(\vec{r})]$  the exchange and correlation functional, which accounts for the remaining electron-electron interactions. With these quantities at hand, one can write the Kohn-Sham (KS) Hamiltonian

$$\mathcal{H}_{\text{KS}} = -\frac{1}{2} \nabla^2 + v(\vec{r}) + v_H(\vec{r}) + v_{xc}(\vec{r}) \quad (2.15)$$

leading to a set of  $n$  Schrödinger-like equations for the single-particle Kohn-Sham orbitals

$$\mathcal{H}_{\text{KS}}\phi_i(\vec{r}) = \epsilon_i\phi_i(\vec{r}) \quad (2.16)$$

which are solved in a self-consistent manner. In practice, one (i) starts with an educated guess of the electron density  $n_k(\vec{r})$  to (ii) construct the Kohn-Sham Hamiltonian  $\mathcal{H}_{\text{KS}}$ , (iii) finds upon diagonalization the corresponding eigenvalues  $\epsilon_i$  and eigenvectors, which are then used to (iv) obtain the new density  $n_{k+1}(\vec{r})$ , until the difference between  $n_{k+1}(\vec{r})$  and  $n_k(\vec{r})$  does not exceed a given tolerance.

The theoretical framework presented so far is an exact description of the electronic Hamiltonian. Although the Hohenberg-Kohn theorems guarantee the existence of the exchange and correlation functional  $E_{xc}[n(\vec{r})]$ , which embodies all the many-body physics, the exact expression of this quantity remains unknown. Several approximations at different levels of complexity have been devised for different purposes [Sholl and Steckel, 2009, Parr and Yang, 1994], most notably

- the Local Density Approximation (LDA), in which one assumes that the electron density locally corresponds to that of the uniform electron gas. The resulting exchange-correlation energy is therefore the sum of an analytically exact exchange energy con-

tribution and the correlation energy contribution, with this latter being derived from accurate Monte Carlo results [Ceperley and Alder, 1980];

- the Generalized Gradient Approximation (GGA) under different parametrizations, including PBE [Perdew et al., 1996a], PW91 [Perdew and Wang, 1992], PBEsol [Perdew et al., 2008], revPBE [Zhang and Yang, 1998], which expands the LDA through the introduction of the gradient of the density;
- Meta-Generalized Gradient Approximations (meta-GGA), including TPSS, RTPSS [Sun et al., 2011] and SCAN [Sun et al., 2015], in which further accuracy is reached by introducing the Laplacian of the electron density;
- Hubbard-corrected density functionals (DFT+ $U$ ) [Anisimov et al., 1997], where an energy penalty to the double occupancy of a given set of orbitals, as quantified by a Hubbard  $U$  of arbitrary magnitude, is introduced to describe the Mott-insulating character of  $d$ - and  $f$ -electron systems;
- Hybrid Functionals, including PBE0 [Perdew et al., 1996b], HSE03 [Heyd et al., 2003] and HSE06 [Krukau et al., 2006], in which a certain fraction of the orbital-dependent Fock exchange is included in the otherwise bare exchange and correlation GGA functional.

We remark that, among the current approximations to the time-independent Schrödinger equation that partly account for electron correlation effects, Kohn-Sham density-functional methods are probably the most computationally efficient, thereby allowing for the simulation of a relatively large number of atoms. Currently, calculations involving tens of atoms are routine, those involving hundreds of atoms are, though challenging, certainly feasible, while calculations involving several thousands of atoms are restricted to a quite narrow community engaged in the development of highly scalable methods. From the physical point of view, a droplet of water having radius of 1  $\mu\text{m}$  comprises  $\sim 10^{11}$  atoms. To date, there is no evidence that any conceivable advances in either hardware or software technology will enable the investigation of systems of this size from first principles. Hence, translating the results of a calculation on a model-system composed of a tiny number of atoms into the actual physical reality is a challenge that only the individual physical intuition can overcome [Sholl and Steckel, 2009].

## 2.3 *Ab initio* molecular dynamics

The discussion presented so far concerned the calculation of the electronic structure of an arbitrary system for a *fixed* nuclear configuration. Yet, for many purposes, considering the time evolution of the nuclei is essential to achieve a physically meaningful description of the system under investigation, *e.g.* in the case of liquid or amorphous phases. In the following, we present the main equations involved in *ab initio* molecular dynamics [Tuckerman, 2002, Sholl and Steckel, 2009], in which the nuclei evolve within the framework of classical mechanics and, at each instant, the quantum mechanical  $n$ -electron problem is solved under the desired approximation.

### 2.3.1 Microcanonical ensemble ( $NVE$ )

According to classical mechanics, the configuration of a set of  $N$  nuclei of masses  $M_I$  in a volume  $V$  is, at each instant, fully defined by the spatial coordinates  $(\vec{R}_1, \vec{R}_1, \dots, \vec{R}_N)$  together with the velocities  $(\vec{v}_1, \vec{v}_1, \dots, \vec{v}_N)$ . The two quantities of main interests are the kinetic energy

$$T = \frac{1}{2} \sum_I M_I \vec{v}_I^2 \quad (2.17)$$

and the potential energy

$$U = U(\vec{R}_1, \vec{R}_1, \dots, \vec{R}_N) \quad (2.18)$$

One then treats the motion of the  $I$ -th nucleus according to the Newton equation

$$F_I = - \frac{\partial U(\vec{R}_1, \vec{R}_1, \dots, \vec{R}_N)}{\partial \vec{R}_I} = M_I \frac{d\vec{v}_I}{dt} \quad (2.19)$$

with  $F_I$  being the force acting on the  $I$ -th nucleus at time  $t$ . This expression leads to a set of equations of motion for the nuclei, which can be given as a system of first-order differential equations

$$\begin{aligned} \frac{d\vec{R}_I}{dt} &= \vec{v}_I \\ \frac{d\vec{v}_I}{dt} &= - \frac{1}{M_I} \frac{\partial U(\vec{R}_1, \vec{R}_1, \dots, \vec{R}_N)}{\partial \vec{R}_I} \end{aligned} \quad (2.20)$$

Several approaches have been proposed to integrate numerically the above equations by discretizing the time over a grid with spacing  $\Delta t$ . In this Thesis, we rely on the commonly used Verlet algorithm [Verlet, 1967], according to which the nuclear coordinates  $\vec{R}_I$  at the instant  $t + \Delta t$  read

$$\vec{R}_I(t + \Delta t) = 2\vec{R}_I(t) - \vec{R}_I(t - \Delta t) + \frac{F_I(t)}{M_I} \Delta t^2 \quad (2.21)$$

We remark that one of the important property of Eqn. (2.24) is that the total energy (that is, the sum of the kinetic and the potential energies) is conserved over the trajectory, *i.e.* the system evolves within the *microcanonical* ensemble ( $NVE$ ). This implies that, during the molecular dynamics, no control over the temperature  $T_{MD}$  is achieved. Hence,  $T_{MD}$  fluctuates in time according to the Maxwell-Boltzmann distribution (which, in turn, is often used to define  $T_{MD}$ )

$$k_B T_{MD} = \frac{1}{3N} \sum_I M_I \vec{v}_I^2 \quad (2.22)$$

where  $k_B$  is the Boltzmann constant.

### 2.3.2 Canonical ensemble ( $NVT$ )

In many practical applications, however, the results of molecular dynamics simulations have to be compared with actual experiments, in which nuclei are thermalized at a given temperature. Hence, one has to adapt the microcanonical ensemble to the *canonical* ensemble, where  $T$  is maintained constant at a target value throughout the dynamics. The most commonly used thermostat is probably the one introduced by Nosé [Nosé, 1984] and Hoover [Hoover, 1985], who expanded the  $NVE$  Lagrangian in an *extended* Lagrangian of the form

$$L = \frac{1}{2} \sum_I M_I s^2 \vec{v}_I^2 - U(\vec{R}_1, \vec{R}_1, \dots, \vec{R}_N) + \frac{Q}{2} \left( \frac{ds}{dt} \right)^2 + g k_B \ln s \quad (2.23)$$

where  $s$  is an extra degree of freedom,  $Q$  is an imaginary mass, and  $g$  is the number of degrees of freedom of the extended system. The extended Lagrangian reduces to the usual Lagrangian  $L = T - U$  when  $s$  takes a unitary value. The equations of motion stemming from the extended Lagrangian are

$$\begin{aligned} \frac{d\vec{R}_I}{dt} &= \vec{v}_I \\ \frac{d\vec{v}_I}{dt} &= -\frac{1}{M_I} \frac{\partial U(\vec{R}_1, \vec{R}_1, \dots, \vec{R}_N)}{\partial \vec{R}_I} - \frac{\xi}{M_I} \vec{v}_I \\ \frac{d\xi}{dt} &= \frac{1}{Q} \left( \sum_I M_I \vec{v}_I^2 - 3N k_B T \right) \\ \frac{d \ln s}{dt} &= \xi \end{aligned} \quad (2.24)$$

where the first and the second equations are the same as in Eqn. (2.24), apart from the fact that the second one is supplemented with a friction term  $\xi$  which yields an increase or decrease of the velocity, depending on its sign. The third and fourth equations control the magnitude of  $\xi$ , which in turn tunes the temperature of the system. In fact, if *e.g.* the instantaneous temperature is higher than the target temperature,  $\xi$  adjusts the velocities and eventually the kinetic energies of the nuclei correspondingly, with the parameter  $Q$  determining how rapidly the temperature renormalization takes place.

## 2.4 Practical aspects of first-principles calculations

### 2.4.1 Pseudopotentials

The computational burden associated with the (approximate) solution of Eqn. (2.9) for an  $n$ -electron system is dramatically mitigated by the introduction of pseudopotentials. Core electrons are largely unaffected by their chemical environment, and they do not participate in most of the physico-chemical processes, *e.g.* chemical bonds or low-energy excitations. Hence, one can replace an explicit single-particle description of core electrons with an effective

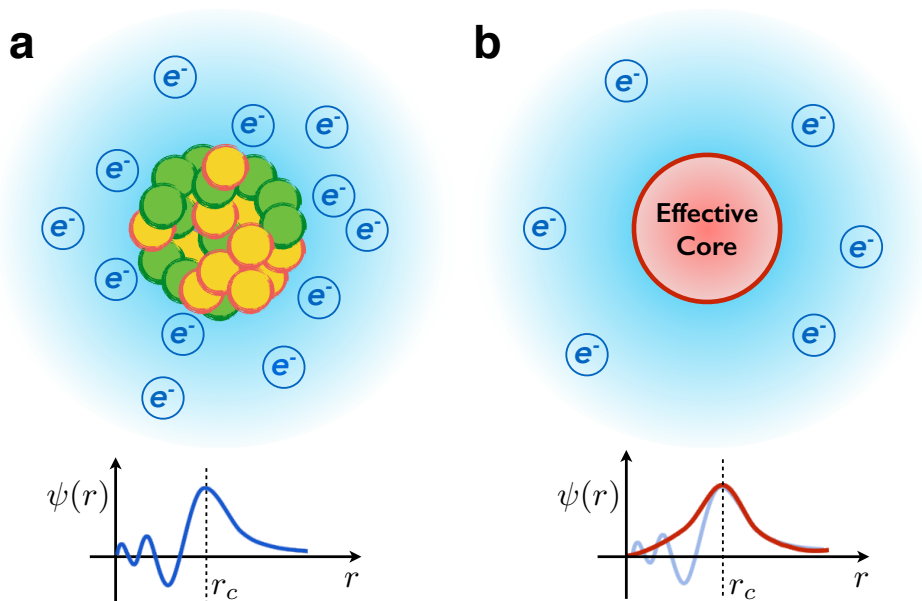


Figure 2.1 – Illustration of the (a) all-electron and (b) pseudopotential approaches.

Coulomb potential, as sketched in Fig. 2.1. The quality of a pseudopotential is typically related to its transferability, that is, its ability to accurately describe the core electrons of a given chemical element when embedded in different chemical environments and examining different physical properties. In order to construct a pseudopotential of a chemical element, one has to

1. Perform an all-electron calculation of the isolated atom and separate the resulting energy levels in core and valence levels according to an (arbitrary) threshold. Notice that the choice of a large numbers of valence electrons converges to the (exact) all-electron limit thereby increasing the computational effort, whereas the choice of a large number of core electrons is typically detrimental to the resulting transferability;
2. Select a core radius,  $r_c$ , such that the valence electron wavefunction of the pseudopotential wavefunction under construction matches the all-electron wavefunction previously calculated beyond  $r_c$ ;
3. Construct pseudo-wavefunction inside the core region. Several methods leading to several flavors of pseudopotentials have been introduced, for instance ultrasoft [Vanderbilt, 1990] or norm-conserving [Hamann et al., 1979] pseudopotentials.

### 2.4.2 Basis sets

When core electrons are described through pseudopotentials, one is left with valence electrons, the wavefunctions  $\psi(\vec{r})$  of which are expanded on a finite basis. In the choice of the basis set, under periodic boundary conditions like in the case of solids, one can take advantage of the



Bloch theorem

$$\psi(\vec{r}) = \sum_{\vec{G}} c_{\vec{G}+\vec{k}} \exp[i(\vec{k} + \vec{G}) \cdot \vec{r}] \quad (2.25)$$

with  $\vec{G}$  being a vector in the reciprocal space. Hence, we notice that plane waves are the most natural basis set for periodic systems. According to Eqn. (2.25), however, the evaluation of the solution at a single point requires the summation over an infinite number of  $\vec{G}$  vectors. In practice, this indicates that the expansion has to be truncated up to an energy cutoff,  $E_{\text{cut}}$ . This implies that only solutions of kinetic energy

$$\frac{h^2}{2m_e} |\vec{k} + \vec{G}|^2 < E_{\text{cut}} \quad (2.26)$$

are evaluated. Delocalized plane waves further offer the advantage of completeness, and the convergence of the calculated properties can be systematically improved by increasing the energy cutoff. In addition to plane waves, localized basis sets have found a widespread use – especially in the computational chemistry community – and typically consist of atomic-like (*e.g.* Gaussian- or Slater-type) orbitals. In contrast to plane waves, fewer basis functions are often needed to achieve a reasonable accuracy, hence substantially decreasing the computational effort required and, additionally, offering a simple intuition for chemical analysis. However, localized basis sets are controlled by many parameters beside the energy cutoff, in a way that no systematic convergence can be achieved. Also, many resulting properties are affected by the basis set superposition error [Boys and Bernardi, 1970] stemming from the incompleteness of the adopted basis functions.



# **Intrinsic and Engineered Defects in Transition Metal Dichalcogenides**

## **Part I**



### 3 Point Defects in the $1T'$ and $2H$ Phases of Single-Layer $\text{MoS}_2$ : A Comparative First-Principles Study

The metastable  $1T'$  polymorph of layered transition metal dichalcogenides has recently attracted considerable interest due to its electronic properties, possible topological phases, and catalytic activity. Here, we report a comprehensive theoretical investigation of intrinsic point defects in  $1T'$ - $\text{MoS}_2$ , and draw a comparison with the well-studied semiconducting  $2H$  phase. Based on density functional theory calculations, we explore a large number of configurations of vacancy, adatom and antisite defects and analyze their atomic structure, thermodynamic stability, electronic and magnetic properties. The emerging picture suggests that, under thermodynamic equilibrium,  $1T'$ - $\text{MoS}_2$  is more prone to host lattice imperfections than the  $2H$  phase. Specifically, our findings reveal that the S atoms that are closer to the Mo atomic plane are the most reactive sites. Similarly to the  $2H$  phase, S vacancies and adatoms in  $1T'$ - $\text{MoS}_2$  are very likely to occur, while Mo adatoms and antisites induce local magnetic moments. Contrary to the  $2H$  phase, however, Mo vacancies in  $1T'$ - $\text{MoS}_2$  are expected to be abundant defects due to the structural relaxation that plays a major role in lowering their formation energy. Overall, our study predicts that the realization of high-quality flakes of  $1T'$ - $\text{MoS}_2$  should be carried out under careful laboratory conditions, but at the same time the facile defects introduction can be exploited to tailor the physical and chemical properties of this polymorph.

This Chapter is adapted from:

M. Pizzochero & O. V. Yazyev

*Point Defects in the  $1T'$  and  $2H$  Phases of Single-Layer  $\text{MoS}_2$ : A Comparative First-Principles Study*

Physical Review B 96, 245402 (2017) [pre-print: arXiv:1804.04575]

My contribution to this work has been performing all first-principles calculations, analyzing the data, and writing the paper.

### **3.1 Motivation**

The presence of certain amount of defects in crystalline materials is unavoidable, and in this respect TMDs are no exceptions. On the one hand, crystalline disorder is typically detrimental to various material's properties. On the other hand, defects can be deliberately introduced, thus offering novel opportunities for tailoring the properties of the system. Defects in TMDs can be created in different ways, *e.g.* by means of electron beam irradiation [Komsa et al., 2012, Komsa et al., 2013], argon plasma treatment [Chow et al., 2015], thermal annealing [Donarelli et al., 2013] and  $\alpha$ -particle or ion bombardment [Mathew et al., 2012]. In the  $2H$  phase of  $\text{MoS}_2$ , point and extended defects have been extensively studied both theoretically [Komsa and Krasheninnikov, 2015, Noh et al., 2014, KC et al., 2014, González et al., 2016] and experimentally [Hong et al., 2015, Zhou et al., 2013, Liu et al., 2016b, Najmaei et al., 2015]. Beside the fundamental interest in exploring lattice disorder in  $\text{MoS}_2$ , the introduction of lattice imperfections can be used to tune several properties of this system [Lin et al., 2016]. For instance, the abundant sulfur vacancies were shown to induce localized states [Pandey et al., 2016] that enhance optical absorption [Shu et al., 2016], lead to electronic transport *via* hopping in the low carrier density regime [Qiu et al., 2013], promote catalytic activity [Li et al., 2016a] and degrade thermal conductivity [Wang et al., 2016b]. Under lattice strain, both Mo and S vacancies are expected to induce magnetism [Tao et al., 2014] and similar predictions were also reported for metal adatoms and antisite defects [Ataca and Ciraci, 2011, Zheng et al., 2015, Cao et al., 2016], whereas a proper vacancy functionalization can lead to giant magnetocrystalline anisotropy [Sivek et al., 2016]. Magnetic ordering was also experimentally observed in  $\text{MoS}_2$  at room temperature upon proton irradiation, and its origin attributed to structural disorder [Sivek et al., 2016]. Additionally, both vacancies and adatoms were used to tailor the electric properties of  $\text{MoS}_2$  by engineering the band gap width [Wang et al., 2016a].

So far, this large body of works focusing on various types of imperfections was restricted to the stable  $2H$  phase only, while the impact of intrinsic point defects on the properties of the  $1T'$  phase of TMDs has not been covered yet, although samples of this metastable polymorph have been widely characterized by microscopy techniques [Wang et al., 2016b]. It is therefore important to address this issue in order to portray a wide-angle view of the effect of intrinsic atomic-scale defects on the properties of  $\text{MoS}_2$ . In this Chapter, we report on the atomic structure and thermodynamic stability of vacancy, antisite and adatom defects in single-layer  $1T'$ - $\text{MoS}_2$  investigated by means of first-principles calculations. Throughout this work, we systematically compare defects in the  $1T'$ -phase of monolayer  $\text{MoS}_2$  with those in the  $2H$  polymorph. Even though we focus on  $\text{MoS}_2$ , we remark that the main results of our study can reasonably be extended to other group VI disulfides and diselenides (that is,  $\text{MoSe}_2$ ,  $\text{WS}_2$  and  $\text{WSe}_2$ ), where a similar physics of defects is expected.

## 3.2 Methodology

### 3.2.1 First-principles calculations

Our first-principles calculations are performed within the Density Functional Theory (DFT) formalism [Jones, 2015] as implemented in the SIESTA code [Soler et al., 2002]. The exchange and correlation effects are treated within the semilocal density functional of Perdew, Burke and Ernzerhof [Perdew et al., 1996a]. Core electrons are replaced by norm-conserving pseudopotentials [Hamann et al., 1979] generated within the Troullier-Martins approach [Troullier and Martins, 1991], whereas Kohn-Sham wavefunctions for valence electrons are expanded in a linear combination of double- $\zeta$  plus polarization (DZP) basis set in conjunction with a mesh cutoff of 250 Ry. Throughout this work, we neglect spin-orbit interaction as its contribution to the formation energies of defects is negligible, but systematically include spin-polarization in order to unravel possible defect-induced magnetism and correctly treat its substantial contribution to the formation energies. However, spin-orbit interaction is considered when addressing the magnetic anisotropy of defects that give rise local magnetic moments. To this end, we perform calculations of total energies by initializing the resulting magnetic moment in the in-plane direction ( $E_{\parallel}$ ) and in the out-of-plane direction ( $E_{\perp}$ ). The magnetocrystalline anisotropy energy (MAE) is then calculated as the energy difference between the two configurations ( $E_{\text{MAE}} = E_{\parallel} - E_{\perp}$ ) and assumes negative (positive) values when the magnetic moment has lower energy in the case of in-plane (out-of-plane) orientation.

In order to model isolated point defects, we consider rectangular  $3 \times 6$  supercells of monolayer  $\text{MoS}_2$  containing 108 atoms. This corresponds to supercell dimensions of  $17.24 \text{ \AA} \times 19.15 \text{ \AA}$  for the  $1T'$  phase and  $16.61 \text{ \AA} \times 19.21 \text{ \AA}$  for the  $2H$  phase. The periodic replicas are separated by a vacuum region  $16 \text{ \AA}$  thick in the out-of-plane direction. The integration over the first Brillouin zone is performed with a  $\Gamma$ -centered grid following the scheme devised by Monkhorst and Pack [Monkhorst and Pack, 1976]. Specifically, we use the equivalent of  $12 \times 18 \times 1$   $k$ -points for geometry optimization and a five times denser mesh of  $60 \times 90 \times 1$   $k$ -points per rectangular 6-atoms unit cell for the calculation of the electronic density of states (DOS), where a broadening of 0.03 eV was employed. The number of  $k$ -points is properly reduced for the above mentioned supercell in order to preserve the grid density. Geometries are considered relaxed when the maximum force component acting on each atom is lower than  $0.01 \text{ eV/\AA}$ . During the structural optimization of the defect models, the supercell dimensions are kept fixed to the values of the pristine system, according to the recommendation of Ref. [Van de Walle and Neugebauer, 2004]. We include the slab-dipole correction [Bengtsson, 1999] in order to eliminate the effect of possible artificial electric fields.

### 3.2.2 Formation energies

The formation energy of defects is the primary property that allows understanding their relative stability under thermodynamic equilibrium conditions. Since  $\text{MoS}_2$  is a binary system, in most cases point defects result in the deviation from nominal stoichiometry, which makes their formation energies dependent on chemical potentials  $\mu$  of the constituent elements. At

### Chapter 3. Point Defects in the 1T' and 2H Phases of Single-Layer MoS<sub>2</sub>: A Comparative First-Principles Study

---

charge neutrality, the formation energy  $E_{\text{form}}(\mu)$  is defined as

$$E_{\text{form}}(\mu) = E_{\text{def}} - E_{\text{clean}} - \Delta N\mu, \quad (3.1)$$

with  $E_{\text{def}}$  and  $E_{\text{clean}}$  being the total energies of the defect model and pristine materials, respectively, while  $\Delta N$  is the change of the number of atoms upon introducing the defect and  $\mu$  the chemical potential of one of the chemical elements. The calculation of the formation energy requires the choice of the reference elemental system for the determination of the chemical potential. In our work, as a reference system we choose bulk sulfur, obtaining its total energy upon relaxation of the  $\alpha$  phase [Rettig and Trotter, 1987] crystal structure, which consists of S<sub>8</sub> puckered rings packed in a orthorhombic lattice, with a intramolecular S–S bond length of 2.13 Å.

The boundaries of the relevant range of the chemical potential of sulfur  $\mu_{\text{S}}$  are defined by the conditions at which the precipitation of one of the chemical elements takes place. The upper boundary, corresponding to S-rich condition, is given by  $\mu_{\text{S}}^{\text{max}} = E_{\text{S}}$  with  $E_{\text{S}}$  being the energy per atom in the  $\alpha$  phase of bulk sulfur. The lower boundary, that corresponds to Mo-rich conditions, is defined as  $\mu_{\text{S}}^{\text{min}} = (E_{\text{clean}} - E_{\text{Mo}})/2$ , where  $E_{\text{Mo}}$  is the total energy per atom in the bcc crystal structure of bulk molybdenum. Specifically, the ranges of stability of the monolayers are  $-1.25 < \mu_{\text{S}} < 0$  eV for 1T'-MoS<sub>2</sub> and  $-1.54 < \mu_{\text{S}} < 0$  eV for 2H-MoS<sub>2</sub>. Such a difference in the boundaries of  $\mu_{\text{S}}$  implies the existence of a chemical potential window of 0.29 eV in the Mo-rich conditions, where the most stable phase is preferred against bulk Mo precipitation.

## 3.3 Results and discussion

### 3.3.1 Pristine MoS<sub>2</sub>

Before presenting the results for defect models, we overview our calculations on pristine MoS<sub>2</sub> monolayers in the different crystalline phases. The atomic structures are shown in Fig. 3.1. All polymorphs of monolayer MoS<sub>2</sub> consists of a Mo atoms plane sandwiched between two planes of S atoms. The stable polymorph is the 2H phase [Fig. 3.1(a)], in which the S/Mo/S atomic planes are arranged to form an ABA stacking order, with a Mo–S interatomic distance of 2.44 Å and a trigonal prismatic coordination of each Mo atom. As shown in Fig. 3.2(a), this phase is semiconducting with a direct band gap of ~1.7 eV at the adopted PBE level and band edges mostly composed of Mo *4d* atomic orbitals and S *3p* atomic orbitals.

A rhombohedral ABC stacking order of the S/Mo/S atomic planes corresponds to the 1T phase, where the Mo atom exhibits a distorted octahedral coordination [Fig. 3.1(b)]. In agreement with previous calculations [Enyashin et al., 2011], this structure is found to be 0.82 eV/f.u. less stable than the 2H phase and presents a longer Mo–S interatomic distance of 2.46 Å. The different stacking order has important consequences on the electronic structure around the Fermi level, being this phase metallic, as shown in Fig. 3.2(b). As pointed out by earlier works, this system is dynamically unstable in its free-standing form, as large imaginary branches



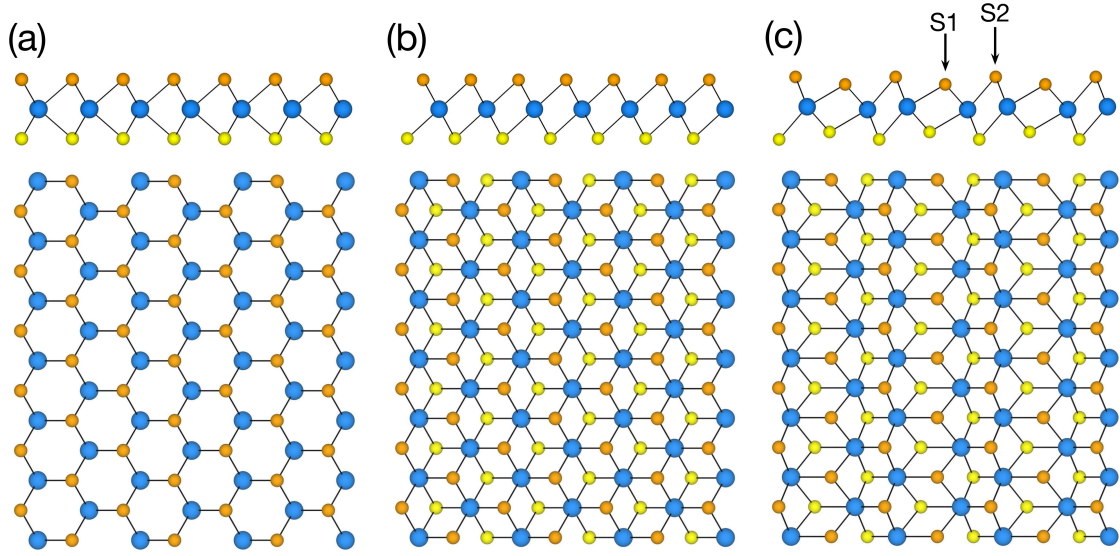


Figure 3.1 – Side- (upper panels) and top- (lower panels) views of the atomic structures of (a)  $2H$ , (b)  $1T$  and (c)  $1T'$  crystalline phases of monolayer  $\text{MoS}_2$ . Blue balls represent Mo atoms, whereas orange (yellow) balls represent S atoms belonging to the top (bottom) atomic planes.

throughout the first Brillouin zone appear in its phonon dispersion [Shirodkar and Waghmare, 2014, Calandra, 2013]. In fact,  $1T$ - $\text{MoS}_2$  undergoes a dimerization distortion resulting in the so-called  $1T'$  phase [Fig. 3.1(c)]. Though 0.57 eV/f.u. less stable than  $2H$ - $\text{MoS}_2$ , the metastable  $1T'$  phase is a local minimum on the Born-Oppenheimer surface, as supported by the absence of imaginary frequencies in the phonon spectrum reported by several authors [Fan et al., 2014, Calandra, 2013]. Contrary to the other phases, in the  $1T'$  phase there exist two symmetry inequivalent sulfur atoms, with Mo-S interatomic distances equal to 2.50 Å and 2.42 Å. To distinguish these S atoms, throughout this work we label S1 (S2) the sulfur atom which is closer to (farther from) the Mo atomic plane, as shown in Fig. 3.1(c). The longer Mo-S1 bond, as opposed to Mo-S2 bond length, clearly signals an inhomogeneity in the bond strength, thereby suggesting that the bond involving the S atom that is closer to the Mo plane (the S1 lattice site) is weaker than the other one. Contrary to the  $2H$  phase, single-layer  $1T'$ - $\text{MoS}_2$  has a practically semi-metallic band structure, where the band degeneracy at the Fermi level is lifted by the spin-orbit interaction [Fig. 3.2(c)].

Despite the considerable differences in the properties of the three polymorphs, one can still recognize some common features in their electronic density of states, see Fig. 3.2. For all the phases, we observe a sharp peak due to the Mo  $d$  atomic orbitals at  $\sim 2$  eV as well as a peak corresponding to the  $p$  and  $d$  atomic orbitals of S and Mo, respectively, at about  $-1$  eV. Comparing the electronic structure of the  $2H$  phase with the  $1T'$  phase, some analogies in the shape and composition in the energy range between  $-1$  eV and 2 eV are apparent; the main difference is due to the population of the band-gap region of  $2H$ - $\text{MoS}_2$  by the  $4d$  states of Mo in the  $1T'$  polymorph, which confers a semi-metallic nature to the latter phase. Throughout the rest of this Chapter, we analyze the structure, energetics and electronic properties of point

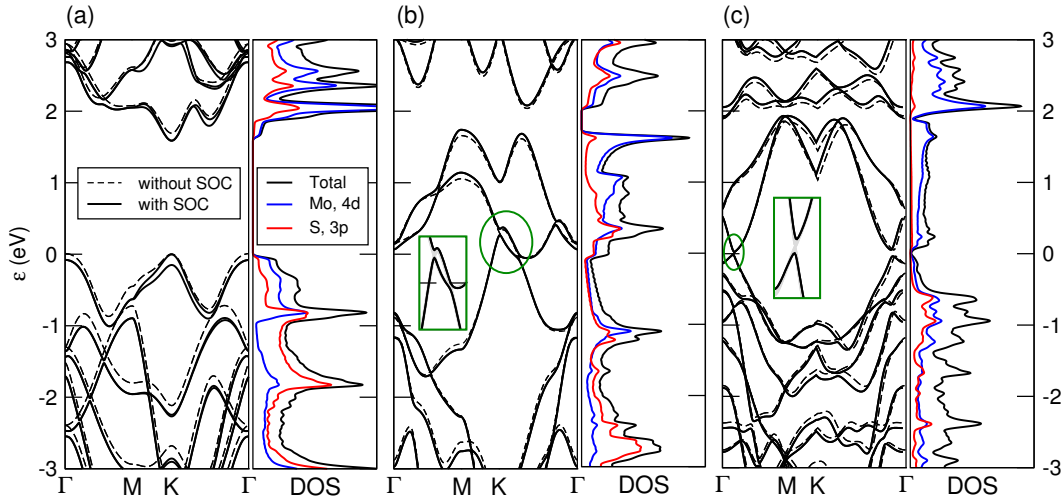


Figure 3.2 – Electronic band structures with and without spin-orbit coupling (SOC) (left) and density of states (DOS) plots (right) for the (a)  $2H$ , (b)  $1T$  and (c)  $1T'$  crystalline phases of single-layer  $\text{MoS}_2$ . Band structures have been obtained using a hexagonal  $1 \times 1$  supercell for  $2H$ - and  $1T$ - $\text{MoS}_2$  and a  $2 \times 1$  supercell for  $1T'$ - $\text{MoS}_2$  along high-symmetry points  $\Gamma(0;0)$ ,  $M(\frac{1}{2};0)$  and  $K(\frac{1}{3};\frac{1}{3})$ . Green circles in (b) and (c) indicate the band crossing at the Fermi level and the insets are their magnified views. Valence band maximum of the  $2H$ - and Fermi levels in  $1T$ - and  $1T'$ - $\text{MoS}_2$  band structures are set to zero.

defects in the crystalline phases of single-layer  $\text{MoS}_2$ . We restrict our further investigations to the dynamically stable  $2H$  and  $1T'$  polymorphs, and systematically discuss the similarities and differences of their defect physics.

### 3.3.2 Vacancy defects

We start with vacancy defects, the atomic structures of which is presented in Fig. 3.3. For both the  $1T'$  and  $2H$  polymorphs, the formation energies as a function of the chemical potential of sulfur  $\mu_S$  are given in Fig. 3.4. As expected, the formation of a S (Mo) vacancy is more likely to occur within a Mo-rich (S-rich) environment.

Upon the introduction of a  $V_S$  defect in the  $2H$  phase, the Mo–Mo interatomic distance between the three metal atoms in the vicinity of the missing atom is reduced from 3.20 Å to 3.09 Å. This latter value is in excellent agreement with experiments, where aberration-corrected transmission electron microscopy (AC-TEM) revealed such a distance to be equal to 3.10 Å [Wang et al., 2016a]. In the  $1T'$  polymorph, because of the presence of the inequivalent S1 and S2 atoms, two distinct S vacancy configurations can be realized, namely  $1T'$ - $V_{S1}$  and  $1T'$ - $V_{S2}$ . In both configurations, the formation of a single vacancy largely affects the average distance between Mo atoms surrounding the defective site. Specifically, for  $1T'$ - $V_{S1}$  ( $1T'$ - $V_{S2}$ ), these average distances increase from 3.61 Å (2.92 Å) in the pristine monolayer to 3.78 Å (3.20 Å) upon vacancy formation. Importantly, the inequivalence of the two S atoms is strongly reflected in the relative stability of vacancy defects, where the formation energy of the  $1T'$ - $V_{S1}$

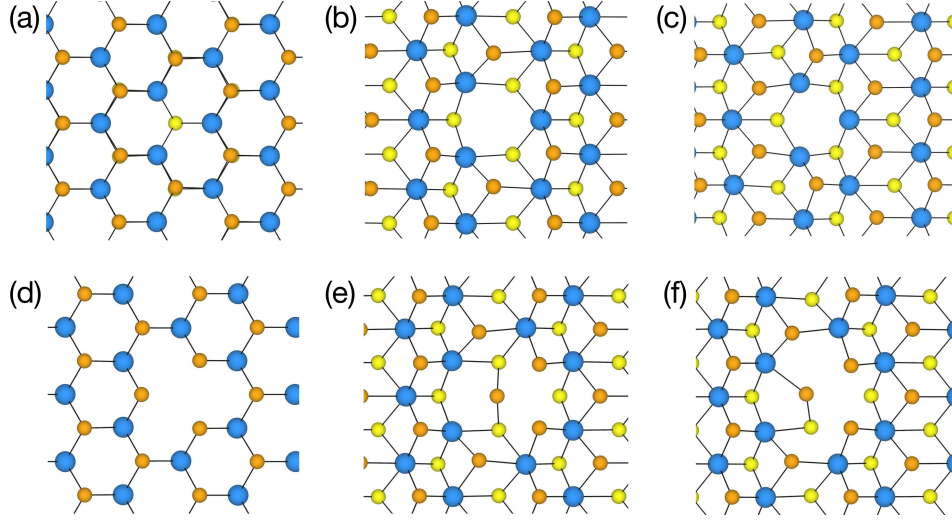


Figure 3.3 – Atomic structures of vacancy defects: (a)  $2H-V_S$  (b)  $1T'-V_{S1}$ , (c)  $1T'-V_{S2}$  (d)  $2H-V_{Mo}$ , (e)  $1T'-V_{Mo}$  and (f)  $1T'-V_{MoS}$ .

defect is 0.85 eV lower in energy than that of the  $1T'-V_{S2}$  one. This agrees with the fact that the Mo–S1 bond is weaker than the Mo–S2 bond, as explained in the previous Section. In general, as reported in Fig. 3.4, S vacancies form easier in the  $1T'$  phase than in the  $2H$  phase, as a consequence of the lower stability of the former polymorph with respect to the latter (by 0.57 eV/f.u). In line with previous reports [Pandey et al., 2016], a chalcogen vacancy defect in the  $2H$  phase leads to the formation of a pair of mid-gap states in the electronic density of states, one located very close to the valence band edge and the other  $\sim 1$  eV higher in energy, deep in the gap [see Fig. 3.5(b)]. Since a missing sulfur atom affects only the coordination sphere of a Mo atom, these electronic states originate from the Mo  $4d$  atomic orbitals. In the  $1T'$  phase, on the other hand, the vacancy-induced states are hybridized with the bulk states due to the nearly gapless character of  $1T'$ -MoS<sub>2</sub>, and characterized both by S- and Mo- atomic orbitals contributions. However, they can still be distinguished, mostly within 0.5 eV below the Fermi level, as shown in Fig. 3.5(a).

We next consider Mo vacancy defects. For the  $2H$  phase, this defect is characterized by a relatively large formation energy, as the removal of the metal atom affects the coordination sphere of a large number of S atoms. This is in line with experimental observations, where Mo vacancies are only rarely found [Hong et al., 2015]. A very different situation emerges for the  $1T'$  phase, where in the S-rich conditions of Fig. 3.4 the formation energy of  $V_{Mo}$  is about half of that calculated for the semiconducting  $2H$  phase, despite the same coordination number around associated with the Mo atom. We suggest that the reason for this is twofold. On the one hand, similarly to S vacancies, atoms can be more readily removed from the  $1T'$  phase than the  $2H$  due to the smaller cohesive energy of the former phase as compared to the latter. On the other hand, removing a Mo atom from  $1T'$  lattice induces a strong reconstruction [see Fig. 3.3(e)], in which one S atom displaces towards the vacant site and establishes covalent bonds with a pair of S atoms belonging to different chalcogen layers. This bond is 2.13 Å long,

### Chapter 3. Point Defects in the $1T'$ and $2H$ Phases of Single-Layer $\text{MoS}_2$ : A Comparative First-Principles Study

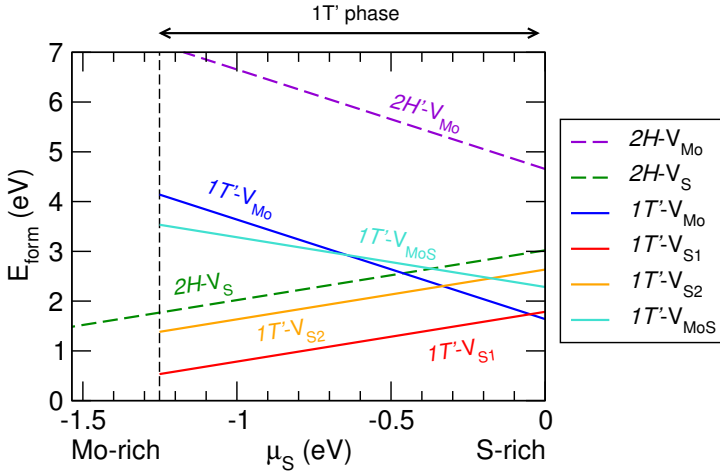


Figure 3.4 – Formation energies of vacancy defects as a function of the chemical potential of sulfur  $\mu_S$ . Vertical dashed line indicates the range of stability of  $1T'$ - $\text{MoS}_2$ . Colored solid (dashed) lines represent the formation energies of defects in the  $1T'$  ( $2H$ ) phase. See text for details on the chemical potential ranges.

very close to the value observed in the puckered  $\text{S}_8$  rings, as mentioned in the previous Section. We suggest that the formation of this chemical bond compensates for the dangling bonds otherwise formed, *i.e.* the main origin of the large formation energy of the  $2H\text{-V}_{\text{Mo}}$  defect. Indeed, in this latter phase, no significant structural relaxation is observed [Fig. 3.3(d)], and the removal of the metal atom leaves the defective lattice almost unperturbed. To gain further insight into the role of S–S bonds forming upon defect reconstruction, we consider a defect complex  $1T'\text{-V}_{\text{MoS}}$  in which the central S atom is removed. Its atomic structure is shown in Fig. 3.3(f), and presents a new bond between S atoms belonging to different sulfur atomic planes. It is worth noting that the formation energy of  $1T'\text{-V}_{\text{MoS}}$  defect (Fig. 3.4) is lower than the sum of formation energies of single Mo and S vacancies by 1.14 eV. This suggests that it is more likely to form a S vacancy within the coordination network of a Mo vacancy than in the clean area of the monolayer. In Figs. 3.5(c) and (d), we show the density of states of  $\text{MoS}_2$  hosting Mo vacancy defects. In the  $2H$  phase,  $2H\text{-V}_{\text{Mo}}$  leads to the formation of three deep levels, two of them due to the sulfur orbitals and one composed of Mo orbitals, whereas in  $1T'$ - $\text{MoS}_2$  one can recognize defect-induced states approximately 0.1 eV and 0.5 eV below the Fermi level.

In general, from Fig. 3.4, one can notice a sharp contrast between the stability of monovacancies in the two crystalline phases. In the  $2H$  phase, the sulfur vacancy is the most stable defect across the entire range of chemical potential. Conversely, in the  $1T'$  phase, under extreme S-rich conditions (*i.e.*  $\mu_S = -1.25$  eV),  $1T'\text{-V}_{\text{Mo}}$  is more stable than  $1T'\text{-V}_{\text{S1}}$  by 0.15 eV. Overall, the lower formation energy of the  $1T'\text{-V}_{\text{Mo}}$  defect in the  $1T'$  phase compared to the  $2H$  phase indicates that Mo vacancies in the semi-metallic phase are more abundant than in the semiconducting one. We remark that, in the present work, all calculations are performed on charge-neutral defects. Previous theoretical works addressed the charged defects in semiconducting  $2H\text{-MoS}_2$  and found that both  $2H\text{-V}_\text{S}$  and  $2H\text{-V}_{\text{Mo}}$  are likely to assume negative charge states when the Fermi level is close to the conduction band (*i.e.*,  $n$ -type doping) [Komsa and Krasheninnikov, 2015, Noh et al., 2014]. However, because of the semi-metallic character of  $1T'\text{-MoS}_2$ , defects in this material have been considered only in their neutral state and, for

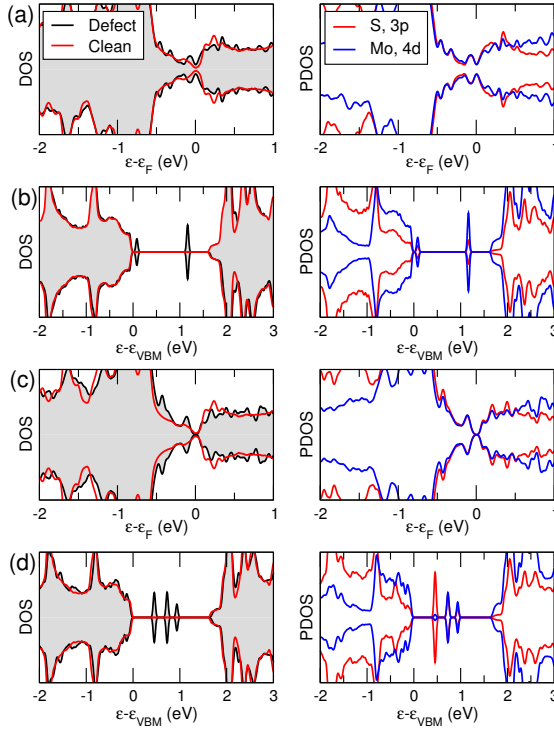


Figure 3.5 – Total (left) and projected (right) electronic density of states plots of (a)  $1T'$ - $V_{S1}$ , (b)  $2H$ - $V_S$ , (c)  $1T'$ - $V_{Mo}$  and (d)  $2H$ - $V_{Mo}$  defects. The total DOS of the pristine (red lines) and the defective (black lines)  $MoS_2$  monolayers are shown.

consistency when comparing the two phases, equivalent defects in the  $2H$ - $MoS_2$  are considered neutral as well. For a detailed discussion of charge transition levels in semiconducting  $MoS_2$ , the reader is referred to Refs. [Komsa and Krasheninnikov, 2015, Noh et al., 2014].

### 3.3.3 Adatom defects

Next, we examine the formation of S and Mo adatom defects on monolayers of  $MoS_2$  along with their effect on the electronic and magnetic properties. The chemisorption of a Mo (S) atom is thermodynamically more favorable in a Mo-rich (S-rich) conditions, as displayed in Fig. 3.6(a). For S adatoms in the  $2H$  phase, we inspect three different adsorption sites, namely (i) on top of a Mo atom, (ii) on top of a S atom and (iii) on the hollow site. The S adatom is found to be stable only when bound on top of a S atom ( $2H$ - $S^S$ ) and to form a S–S bond 1.96 Å long, in excellent agreement with previous works [Komsa and Krasheninnikov, 2015, Cao et al., 2016]. Such an interatomic distance, very close to the one of 1.94 Å calculated for the  $S_2$  molecule, clearly signals the formation of a strong covalent bond. This is corroborated by the low formation energy, among the lowest for all impurities here considered in the  $2H$  phase [Noh et al., 2014]. In the case of  $1T'$  polymorph, we consider the adsorption of S adatom on top of either the S1 ( $1T'$ - $S^{S1}$ ) or S2 ( $1T'$ - $S^{S2}$ ) site. The resulting S–S bond lengths are 1.98 Å and 1.95 Å for  $1T'$ - $S^{S1}$  and  $1T'$ - $S^{S2}$ , respectively, very similar to those observed for adsorption on the  $2H$  phase. Remarkably, the defect formation energy for S adatom on top of the S1 site is 0.49 eV lower in energy than on the S2 site. Hence, our calculations indicate that the S1 site is not only the most prone lattice site to forming vacancies, but also the most reactive towards chemisorption, whereas the S2 site in the  $1T'$  phase behaves more similarly to the S atom in

### Chapter 3. Point Defects in the $1T'$ and $2H$ Phases of Single-Layer $\text{MoS}_2$ : A Comparative First-Principles Study

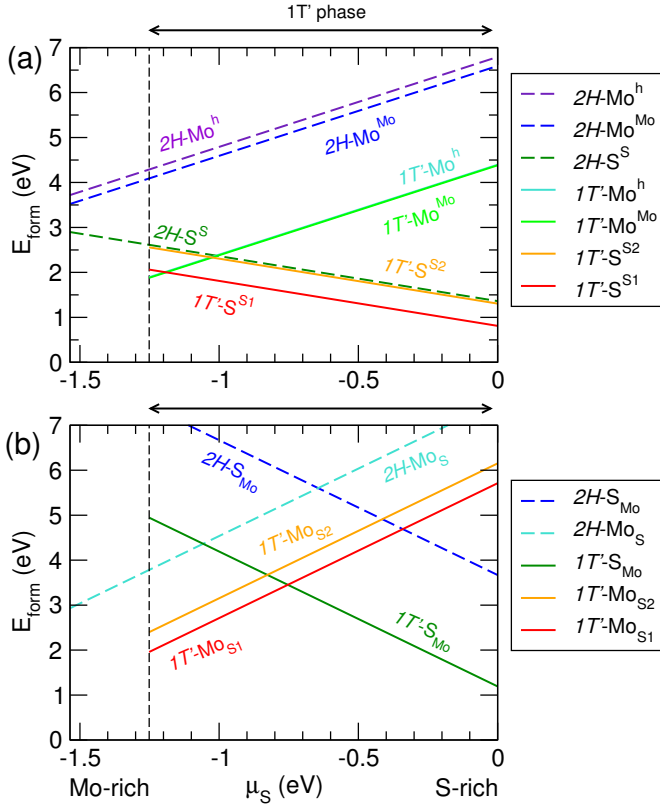


Figure 3.6 – Formation energies of (a) adatom and (b) antisite defects as a function of the chemical potential of sulfur  $\mu_S$ . Vertical dashed line indicates the range of stability of  $1T'$ - $\text{MoS}_2$ . Colored solid (dashed) lines represent the formation energies of defects in the  $1T'$  ( $2H$ ) phase.

the  $2H$  in terms of defect energetics. Despite the dissimilarities in the thermodynamic stability and electronic structure of the pristine monolayers, as well as in the energetics involved in the S adsorption presented above, comparable changes in the density of states upon the formation of this impurity are found. Specifically, from Fig. 3.7(a) and (b), in both phases we observe that the adatom-induced states are composed of the sulfur  $3p$  atomic orbitals. For the  $2H$  phase, two localized states emerge in the band gap, one very close to the valence band edge and the other close to the conduction band edge, indicating that S adatom acts as a shallow defect. In the  $1T'$  phase, the chalcogen chemisorption leads to a sharp peak located at *ca.* 0.5 eV below the Fermi level.

We then assess the stability of Mo adatom located on top of a Mo lattice site ( $\text{Mo}^{\text{Mo}}$ ) as well as at the hollow site ( $\text{Mo}^{\text{h}}$ ). In the case of  $2H$  phase, these configurations differ by 0.20 eV and in general represent the most energetically unfavorable defects among those presented in Fig. 3.6(a) [Komsa et al., 2013]. In the  $2H\text{-Mo}^{\text{Mo}}$  configuration, the adatom is located 3.06 Å above the Mo atomic plane, with an average distance with the three neighboring S atoms equals to 2.46 Å, very close to the interatomic distances observed in the  $2H\text{-Mo}^{\text{h}}$  configuration (2.45 Å) [Ataca and Ciraci, 2011]. The adsorption of Mo atoms on the  $1T'$  phase is more energetically favorable as compared to the  $2H$  phase by  $\sim 2$  eV, hence suggesting that the incorporation of excess Mo atoms is more likely to occur in the former polymorph compared to the latter. Additionally, adsorption on top of the Mo site is only slightly more stable than at the hollow site (by 13 meV), although the corresponding bond lengths are overall similar to the one observed



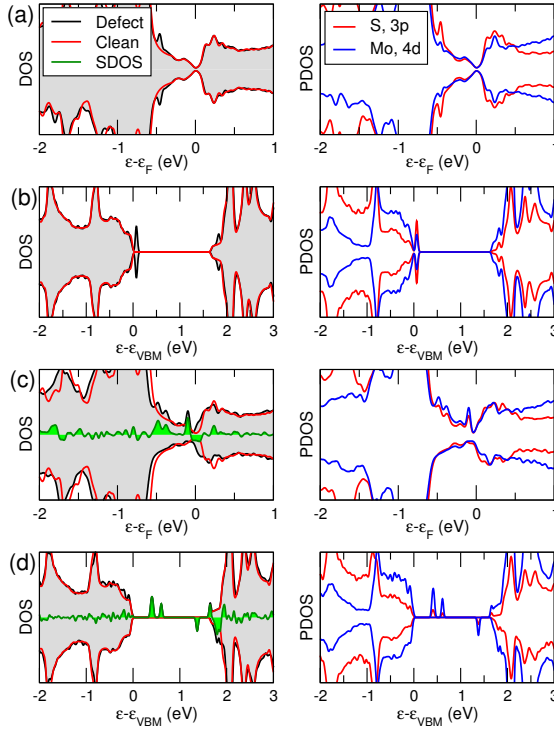


Figure 3.7 – Total (left) and projected (right) electronic density of states plots of (a)  $1T'$ -S<sup>S1</sup>, (b)  $2H$ -S<sup>S</sup>, (c)  $1T'$ -Mo<sup>Mo</sup> and (d)  $2H$ -Mo<sup>Mo</sup> defects. The total DOS of the pristine (red lines) and the defective (black lines) monolayers are superimposed. Green shaded area indicates the net spin-polarization (SDOS), defined as the difference between spin-majority and spin-minority DOS.

for Mo adsorbed on  $2H$ -MoS<sub>2</sub>. Contrary to the  $2H$  phase, where the S adatom is the most stable defect across the entire range of stability of the monolayer, in the  $1T'$  phase extreme Mo-rich conditions promote the formation of Mo adatoms, both on top of a Mo atom as well as on the hollow site (by 0.18 eV and 0.17 eV, respectively), as it can be noticed at  $\mu_S = -1.25$  eV in Fig. 3.6(a). Figs. 3.7(c) and (d) show the density of states of Mo adatom defects. In the  $2H$  phase, it is found to induce three states in the band gap: one close to the conduction band edge and two located at  $\sim 0.5$  eV above the valence band maximum. This is in contrast to what is observed for Mo adatoms in  $1T'$ -MoS<sub>2</sub>, where they are seen to give rise to a single localized state located at the Fermi energy.

As far as the defect-induced magnetic properties are concerned, the adsorption of Mo atoms leads to a large magnetic moment  $\mu = 4 \mu_B$  in the lattice, irrespective of the crystalline phase and defect configuration considered [Cao et al., 2016, Komsa and Krashenninnikov, 2015]. We address the spatial distribution of this local magnetic moment in Figs. 3.8(a) and (b), where the spin densities in the vicinity of the Mo adatom are shown for the two polymorphs. In the  $2H$  phase, the spin density is seen to be strongly localized around the defect, whereas in the  $1T'$  phase appears to be more extended, likely due to the hybridization of the defect-induced, spin-polarized states with the underlying delocalized electrons. This can be observed also from the green shaded area of Figs. 3.7(c) and (d), where, contrary to  $1T'$ -MoS<sub>2</sub>, in the semiconducting phase the magnetism is mainly due to the mid-gap states. Because of the relative low formation energy necessary to host a Mo adatom in the  $1T'$  polymorph and its stability in Mo-rich conditions, Mo adsorption may offer a suitable avenue towards magnetism in monolayers of MoS<sub>2</sub>, with potential applications in spintronics. Furthermore, we determine

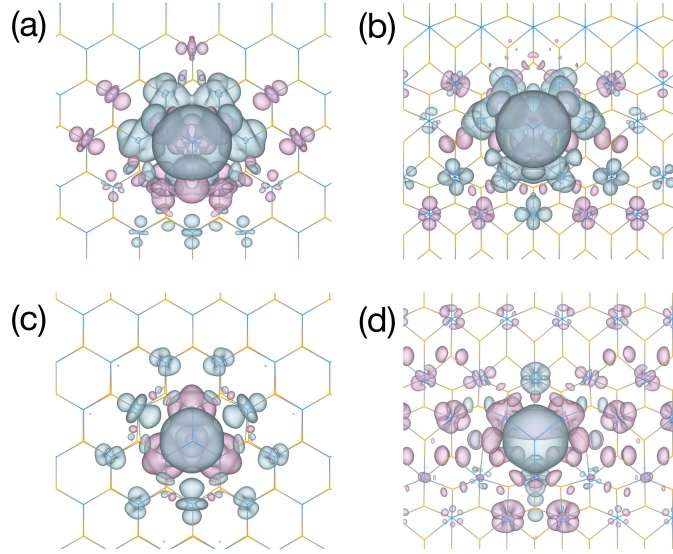


Figure 3.8 – Spin densities upon (a)  $2H\text{-Mo}^{\text{Mo}}$ , (b)  $1T'\text{-Mo}^{\text{Mo}}$ , (c)  $2H\text{-MoS}$  and (d)  $1T'\text{-MoS}$  defects formation. Grey (pink) clouds represent spin-majority (spin-minority) isosurfaces, with isocontours of  $\pm 0.003$  ( $0.008$ )  $e \text{ \AA}^{-3}$  for adatom (antisite) defects.

the magnetocrystalline anisotropy energies ( $E_{\text{MAE}}$ ) of the stable configurations of Mo adatom defects, which turn out to be  $-0.85$  meV and  $0.11$  meV for  $2H\text{-Mo}^{\text{Mo}}$  and  $1T'\text{-Mo}^{\text{Mo}}$  defects, respectively. This implies that the easy axis of the magnetic moment lies along the in-plane (out-of-plane) direction for adatom defects in single-layer  $2H$ - ( $1T'$ -)  $\text{MoS}_2$ .

### 3.3.4 Antisite defects

As a final subject of investigation, we discuss the formation antisite defects, which are realized upon the replacement of a Mo (S) atom with a S (Mo) atom. Thus, in order to rationalize our results, we decompose the antisite defect formation into a hypothetical two-step process, namely (i) the vacancy formation and (ii) the subsequent addition of an adatom of the element complementary to the removed atom. Following this argument, we can understand our results in the light of the formation energies presented in the previous Sections. In fact, one expects that the more likely the vacancy and adatom formation, the more likely the antisite defect. As pointed out in Fig. 3.6(b), Mo-rich conditions stabilize both S vacancies and Mo adatoms, and therefore would favor the formation of  $\text{MoS}$  antisites. Reciprocally, S-rich conditions favor both the formation of Mo vacancies and S adatoms, hence  $\text{S}_{\text{Mo}}$  antisite defects are stabilized.

In both phases, upon the  $\text{S}_{\text{Mo}}$  formation, the substituting S atom is surrounded by six sulfur atoms, owing to the trigonal prismatic coordination of the Mo atom in the pristine lattice. In the  $2H$  phase, the bond distance of the impurity with the neighboring atoms is  $2.40 \text{ \AA}$ , slightly shorter than the Mo–S bond length observed in the pristine crystal. Similarly, in  $1T'$ - $\text{MoS}_2$ , the same average bond length is  $2.32 \text{ \AA}$ , even shorter than typical Mo–S distances in this polymorph. Such a bond contraction at the impurity site can be interpreted in term of covalent radii. In fact, as the S atom is smaller ( $1.05 \text{ \AA}$ ) than the Mo atom ( $1.54 \text{ \AA}$ ), the sites



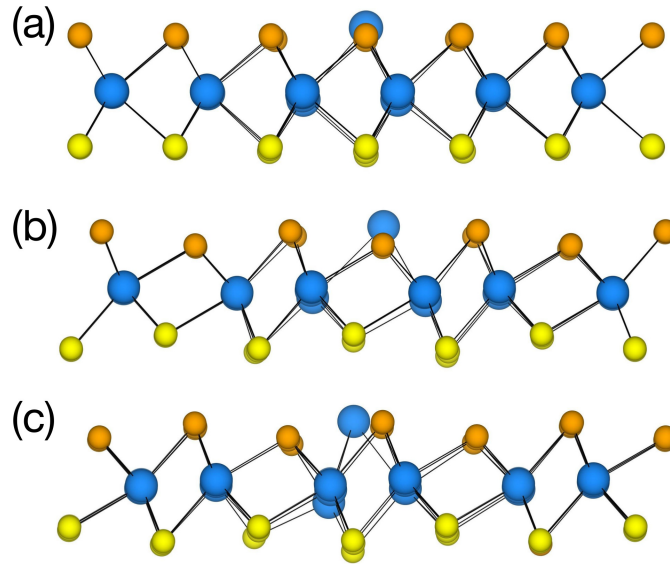


Figure 3.9 – Atomic structures of (a)  $2H$ -MoS<sub>2</sub>, (b)  $1T'$ -MoS<sub>1</sub> and (c)  $1T'$ -MoS<sub>2</sub> defects.

surrounding the imperfection move towards the defective site in order to accommodate the chalcogen impurity, thus locally shortening the bond distances.  $S_{Mo}$  antisites show a very different formation energy in the two crystalline phases, being about 2 eV more favorable in the  $1T'$  phase as compared to the  $2H$  phase at the same value of chemical potential  $\mu_S$ . This is not surprising, as both the formation of a Mo vacancy and the adsorption of a S adatom are more favorable in the  $1T'$  phase compared to the  $2H$  phase. Comparing the formation energy of  $S_{Mo}$  antisites with the sum of the formation energies of isolated Mo vacancy and S adatom, it is found that such an antisite defect is more stable by 2.35 eV in the  $2H$  phase and 1.26 eV in the  $1T'$  phase. This indicates a remarkable reactivity of the Mo vacant site. The  $S_{Mo}$  antisites affects the electronic structure [see Figs. 3.10(a) and (b)] by introducing three distinct electronic states. In the case of  $2H$  phase, two of these peaks are located close to the band edges, whereas the third one is in the middle of the band-gap. In  $1T'$  phase, the three impurity states are occupied and form around the Fermi level. Similarly to  $2H$ -MoS<sub>2</sub>, their composition is mainly due to the  $4d$  Mo states, as a consequence of the change in the Mo–Mo interaction that occurs when the substitution of the metal with the chalcogen atom takes place. As we already observed for Mo-vacancies and S-adatoms described above,  $S_{Mo}$  defect does not lead to any spin-polarization [Cao et al., 2016].

Finally, we study the formation of the MoS antisites shown in Fig. 3.6(b). In the  $2H$  phase, only one distinct configuration for this defect exists, whereas two inequivalent configurations can be achieved in the  $1T'$  polymorph, depending on whether the substitution takes place in position S1 (yielding  $1T'$ -MoS<sub>1</sub> defect) or position S2 (yielding  $1T'$ -MoS<sub>2</sub> defect). The atomic structures presented in Fig. 3.9 show that the substitution of a S atom with a Mo atom leads to a distortion in the lattice due to the larger atomic radius of Mo atom compared to the S atom. The distortion is more pronounced for the  $1T'$  phase, in particular in the  $1T'$ -MoS<sub>2</sub> configuration shown in Fig. 3.9(c), where the larger metal atom can barely be accommodated

### Chapter 3. Point Defects in the $1T'$ and $2H$ Phases of Single-Layer $\text{MoS}_2$ : A Comparative First-Principles Study

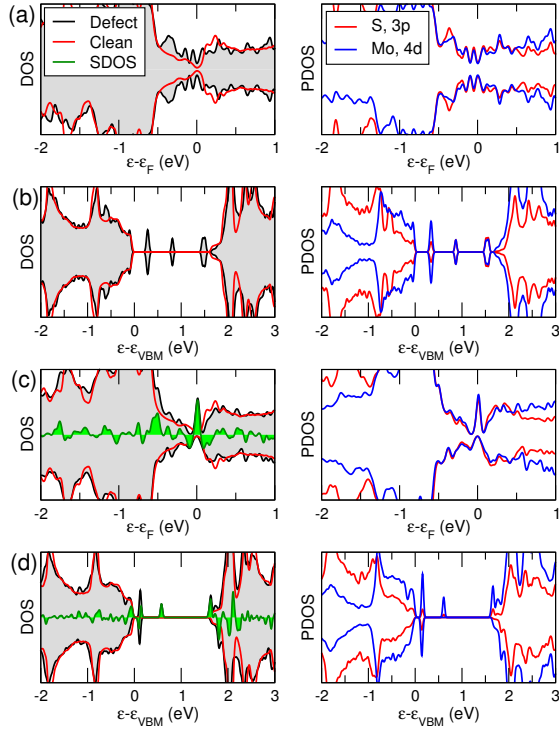


Figure 3.10 – Total (left) and projected (right) electronic density of states plots of (a)  $1T'$ - $\text{S1}_{\text{Mo}}$ , (b)  $2H$ - $\text{S}_{\text{Mo}}$ , (c)  $1T'$ - $\text{Mo}_{\text{S1}}$  and (d)  $2H$ - $\text{Mo}_{\text{S}}$  defects. The total DOS of the pristine (red lines) and the defective (black lines) monolayers are superimposed. Green shaded area indicates the net spin-polarization (SDOS), defined as the difference between spin-majority and spin-minority DOS.

between a pair of Mo atoms, the average distance of which in the pristine system is only 2.92 Å. In the  $2H$  phase, the resulting bond lengths between the substitutional Mo at the defective site and the three surroundings Mo are equal to 2.75 Å. In the  $1T'$  phase, the same three bond lengths are 3.05 Å for  $1T'$ - $\text{Mo}_{\text{S1}}$ , whereas in  $1T'$ - $\text{Mo}_{\text{S2}}$  two of these bond lengths are equal to 3.01 Å and the other to 2.56 Å. The formation energies of these antisites are shown in Fig. 3.6(b). Similarly to all the defects discussed above,  $\text{Mo}_{\text{S}}$  defects preferentially form in the  $1T'$  phase than in the  $2H$ , and, again, defects involving S1 sites (that is,  $1T'$ - $\text{Mo}_{\text{S1}}$ ) are more stable than the one involving S2 (that is,  $1T'$ - $\text{Mo}_{\text{S2}}$ ), with an energy difference of 0.44 eV. This is consistent with our initial assumption based on the fact that both vacancies and adatoms have lower formation energies in position S1 rather than in position S2. In analogy with the  $\text{S}_{\text{Mo}}$  defect,  $2H$ - $\text{Mo}_{\text{S}}$  antisite is more stable than isolated Mo adatom and S vacancy by 2.08 eV, while in  $1T'$  phase this value is found to be 1.31 eV and 2.11 eV for  $1T'$ - $\text{Mo}_{\text{S1}}$  and  $1T'$ - $\text{Mo}_{\text{S2}}$ , respectively. The effect of  $\text{Mo}_{\text{S}}$  antisites on the density of states is shown in Figs. 3.10(c) and (d). Similarly to the  $\text{S}_{\text{Mo}}$  defect previously discussed, the formation of this antisite defect in the semiconducting phase leads to the formation of three mid-gap states, two closer to the band edges and one deep the gap. In the  $1T'$  phase, though, the main consequence of such impurity is a sharp level located around the Fermi level, similarly to the case of Mo adatoms.

A further similarity with Mo adatoms is the emergence of magnetism induced by  $\text{Mo}_{\text{S}}$  antisite in both crystalline phases [Cao et al., 2016]. Contrary to adatoms, however, the resulting magnetic moment reduces to  $\mu = 2 \mu_{\text{B}}$ . The net spin-polarization is shown as green shaded area in Figs. 3.10(c) and (d), where it can be noticed that in both phases the origin of the magnetism is due to the defect states, but in the  $1T'$  such impurity levels appear hybridized

with the bulk electronic states of the monolayer. This can also be observed in Figs. 3.8(c) and (d), in which the spin density is more spatially confined around the imperfection in the semiconducting phase as compared to the semi-metallic phase. In addition, we find  $E_{\text{MAE}}$  equal to  $-1.31$  meV and  $0.53$  meV for antisite defects in  $2H\text{-MoS}$  and  $1T'\text{-MoS}_1$ , respectively, thereby suggesting that, similarly to what we observed for Mo adatoms, the easy axis is located in the in-plane (out-of-plane) direction for such antisite defects in the  $2H$  ( $1T'$ ) phase.

### 3.4 Conclusion

We performed a comprehensive first-principles investigation of the atomic structure and thermodynamic stability of intrinsic point defects in the semi-metallic  $1T'$  phase of single-layer  $\text{MoS}_2$ , and carried out a thorough comparison with equivalent defects in the semiconducting  $2H$  phase. We explored a large number of defects among vacancies, adatoms as well as antisites and examined their effect on the electronic and magnetic properties of the two crystalline phases. Our simulations clearly indicate that all considered defects present lower formation energies in the metastable  $1T'$  phase compared to the  $2H$ . Therefore, under thermodynamic equilibrium, the  $1T'$  polymorph is expected to be more susceptible to the structural disorder. The reason for this traces back to the lower cohesive energy of the  $1T'$  phase with respect to  $2H$ . Also, our findings suggest that impurities preferentially form at the S atom closer to the Mo atomic plane. Comparing the formation energy of all investigated point defects in the  $1T'$  phase, we conclude that similarly to the  $2H$  phase the most stable impurities are sulfur vacancy defect ( $1T'\text{-V}_{\text{S}1}$ ) in Mo-rich conditions and sulfur adatom defect ( $1T'\text{-S}^{\text{S}1}$ ) in S-rich conditions. Overall, we suggest that our conclusions can qualitatively be extended to other group VI disulfides and diselenides, where a similar relative stability and electronic structure of the two crystalline phases are observed.



## 4 Single-Layer 1T'-MoS<sub>2</sub> Under Electron Irradiation from *Ab Initio* Molecular Dynamics

Irradiation with high-energy particles has recently emerged as an effective tool for tailoring the properties of two-dimensional transition metal dichalcogenides. In order to carry out an atomically precise manipulation of the lattice, a detailed understanding of the beam-induced events occurring at the atomic scale is necessary. Here, we investigate the response of 1T'-MoS<sub>2</sub> to the electron irradiation by means of *ab initio* molecular dynamics. Our simulations indicate that an electron beam with energy smaller than 75 keV does not result in any knock-on damage. The displacement threshold energies are different for the two inequivalent sulfur atoms in 1T'-MoS<sub>2</sub>, and strongly depend on whether the top or bottom chalcogen layer is considered. As a result, we suggest that a careful tuning of the beam energy can promote the formation of ordered defects in the sample. We further discuss the effect of the electron irradiation on the lattice sites in the vicinity of a vacancy defect, the mobility of the sulfur vacancies created, and their tendency to aggregate. Overall, our work establishes practical guidelines for the imaging and the defect engineering of 1T'-MoS<sub>2</sub> in the electron microscope.

This Chapter is adapted from:

M. Pizzochero & O. V. Yazyev

*Single-Layer 1T'-MoS<sub>2</sub> Under Electron Irradiation from Ab Initio Molecular Dynamics*

2D Materials 5, 025022 (2018) [pre-print: arXiv:1804.04599]

My contribution to this work has been designing the project, performing all first-principles and molecular dynamics calculations, analyzing the data, and writing the paper.

### 4.1 Motivation

Among all transition metal dichalcogenides, MoS<sub>2</sub> is considered the most representative example. It is well-established that a controlled introduction of defects in its 2H phase can tailor many chemical and physical properties of the material [Lin et al., 2016]. For instance, it has been shown that the thermodynamically stable sulfur vacancy defects act as a catalytic centers for the hydrogen evolution reaction [Li et al., 2016a, Ye et al., 2016], affect thermal [Wang et al., 2016b] and electron transport [Qiu et al., 2013, Pulkin and Yazyev, 2016], lead to magnetism when strained [Tao et al., 2014] or passivated with metal elements [Sivek et al., 2016], form ordered one-dimensional defects [Wang et al., 2016a, Komsa et al., 2012] and offer a reactive site for the insertion of dopant species [Komsa et al., 2012]. In addition, the introduction of defects can be carried out in a controlled manner when the sample is exposed to an electron irradiation, thereby turning electron microscopy from a tool for material imaging to an effective strategy for an *in situ* defects creation [Komsa et al., 2012, Komsa et al., 2013, Krashenninnikov and Nordlund, 2010, Susi et al., 2017, Zhao et al., 2017a]. Remarkably, it has been experimentally shown that the exposure to an electron beam is able to promote a crystalline phase transition from the stable 2H structure to the otherwise metastable 1T', yielding the realization of lateral semiconductor-semimetallic heterostructures between different polymorphs [Lin et al., 2014, Katagiri et al., 2016]. First-principles simulations have suggested that this transformation is triggered by the disorder in the sample [Kretschmer et al., 2017], highlighting once more the importance of lattice imperfections in 2H-MoS<sub>2</sub>.

While the electron irradiation of the 2H-phase MoS<sub>2</sub> has widely been investigated, the response of 1T' phase to the electron beam remains unexplored to date. In this Chapter, we fill this gap in knowledge on the basis of *ab initio* molecular dynamics simulations. We discuss the atomic structure of the defects which form upon electron irradiation at increasing beam energies, their mobility through the lattice, and their tendency to aggregate. Furthermore, we conduct a comparison between the displacement threshold energy (the key quantity that governs the knock-on damage under the beam) and the formation energy (that accounts for the relative stability of defects under thermodynamic equilibrium conditions). Our findings offer an important insight to experimental researchers by identifying the range of beam energies needed to carry out imaging of 1T'-MoS<sub>2</sub> without inducing any radiation damage in the sample, as well as guidelines for the controlled introduction of defects in the electron microscope.

### 4.2 Methodology

The exposure of a solid to the irradiation with high-energy electrons leads to beam-induced electron-electron and electron-nucleus scattering events. Primarily, the former events result in electronic excitations and the latter in both phonon generation and possible ballistic displacement of atoms from their equilibrium position. While in insulating media the effect of electronic excitations can be substantial, in 1T'-MoS<sub>2</sub> they are expected to be quenched due to the metallic character of the system. Furthermore, the energy scales of phonon modes

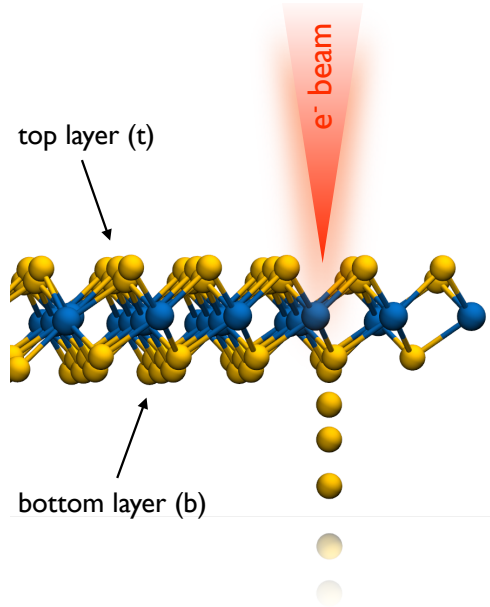


Figure 4.1 – Sketch of the knock-on damage process on  $1T'$ -MoS<sub>2</sub> upon electron beam irradiation, as modelled in this work. The electron beam transfers a certain amount of kinetic energy to one atom in the lattice, which may eventually be sputtered to the gas phase. The top (t) and bottom (b) layers are those which are closer to or further from the electron beam source, respectively.

(meV) are much smaller compared to those of atomic displacements (eV), and usually are not responsible for any beam-driven damage in the irradiated samples. As a consequence, in this work we restrict our investigation to atoms displacements – with a particular emphasis on knock-on damage – that are the relevant events in the defect-engineering of materials [Banhart, 1999, Krasheninnikov and Nordlund, 2010]. Ballistic displacement of atoms takes place *via* elastic electron-nucleus scattering, a process that occurs instantaneously ( $\sim 10^{-21}$  s) and results in an energy transfer from the incoming beam to the sample, within a focus area which can be narrowed down to the same order of magnitude of the interatomic distances [Krasheninnikov and Nordlund, 2010]. We model this process by assigning to one sulfur atom in  $1T'$ -MoS<sub>2</sub> an initial momentum, which corresponds to kinetic energy  $T$  along the direction normal to the monolayer (see Fig. 4.1), as such orientation maximizes the transferred energy [Banhart, 1999]. We then let the lattice evolve in time performing *ab initio* molecular dynamics (AIMD) simulations in the microcanonical ensemble within the Born-Oppenheimer scheme. The displacement threshold energy  $T_d$  is defined to be the minimum amount of transferred energy which is necessary to permanently create a defect in the lattice upon irradiation. This well-established methodology has been already successfully adopted to model the experimentally observed behavior of  $2H$ -MoS<sub>2</sub> [Komsa et al., 2012] as well as carbon nanostructures [Yazyev et al., 2007] under irradiation.

Taking into account relativistic effects, the maximum energy  $T_{\max}$  that can be transferred from an incident beam of energy  $E_{\text{beam}}$  to a nucleus of atomic mass  $M$  as a result of the collision reads as [Garcia et al., 2014]:

$$T_{\max} = \frac{E_{\text{beam}}(E_{\text{beam}} + 2m_e c^2)}{E_{\text{beam}} + \frac{Mc^2}{2}(1 + \frac{m_e}{M})} \quad (4.1)$$

with  $m_e$  and  $c$  being the mass of the electron at rest and the speed of light, respectively. When

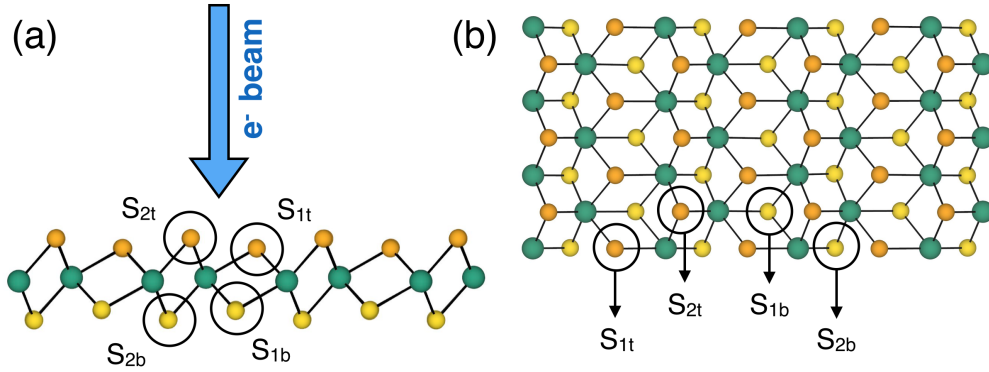


Figure 4.2 – (a) Side-view and (b) top-view of the atomic structure of single-layer 1T'-MoS<sub>2</sub>. Molybdenum atoms are shown in green, while sulfur atoms belonging to the top and bottom chalcogen layers are orange and yellow, respectively. The direction of the electron beam and the labels of the inequivalent sulfur lattice sites are shown.

the maximum energy is equal to or larger than the displacement energy of a given defect (*i.e.*  $T_{\max} \geq T_d$ ), then that defect is likely to form at the corresponding electron beam energy  $E_{\text{beam}}$ . This allows one to give an estimate of the electron energy at which certain structural defects form – based on the determination of  $T_d$  solely – under the assumption of a static lattice. Furthermore, we investigate the relative stability of the sulfur vacancy defects along with their complexes through the determination of their formation energies  $E_f$  defined as

$$E_f = E_{\text{defect}} - E_{\text{pristine}} + N \times \mu_S \quad (4.2)$$

with  $E_{\text{defect}}$  and  $E_{\text{pristine}}$  being the total energies of our models with and without the defect, respectively,  $N$  the number of removed sulfur atoms and  $\mu_S$  their chemical potential, taken as the energy of the isolated sulfur atom. Notice that this is not the conventional thermodynamic formation energy (that should instead be defined with respect to elemental sulfur), rather an operative definition that allows us to quantify the energetics of sulfur atoms sputtering from the lattice far to the gas phase, as it typically occurs during the electron beam irradiation (see Fig. 4.1).

Our periodic model system of single-layer 1T'-MoS<sub>2</sub> consists of a rectangular  $6 \times 3$  supercell containing 108 atoms, separated by its periodic replica by a vacuum region of 15 Å. All our calculations are performed within the Density Functional Theory (DFT) framework [Jones, 2015] relying on the generalized gradient approximation of Perdew, Burke and Ernzerhof [Perdew et al., 1996a], as implemented in the Vienna *ab initio* simulation package (VASP) [Kresse and Hafner, 1993, Kresse and Furthmüller, 1996]. The electron-core interaction is described through the projector-augmented wave (PAW) method [Kresse and Joubert, 1999] while a plane-wave basis is used for valence electrons. Integration over the first Brillouin zone is carried out using a Monkhorst-Pack  $k$ -grid. In molecular dynamics simulations, classical equations of motion are integrated with the Verlet algorithm and a timestep of 0.5 fs. Trajectories of 1–2 ps are found to be sufficiently long for our purposes. In order to accurately



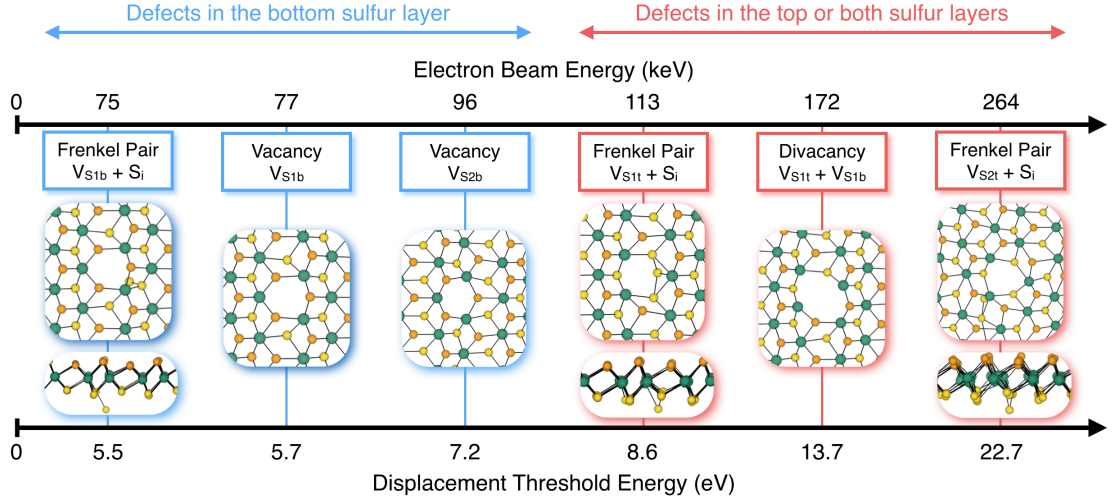


Figure 4.3 – Overview of the atomic defects observed in our molecular dynamics simulations, as obtained on pristine single-layer  $1T'$ -MoS<sub>2</sub>, along with their displacement threshold energies and corresponding electron beam energies. Lattice sites at which defects form are labelled according to Fig. 4.2. Blue (red) boxes correspond to defects forming at the bottom (top or both) chalcogen layer(s).

trace the  $T_d$ , for each lattice site we scan values of initial momenta ranging from 0 to 25 eV, with an energy resolution of 0.1 eV. Kinetic energy cutoff is set to 300 eV and only the  $\Gamma$  point is sampled during AIMD runs while geometry relaxations were performed with a larger cutoff of 500 eV, a denser mesh of  $4 \times 3 \times 1$   $k$ -points and a tolerance on Hellmann-Feynman forces of 0.01 eV/Å. Diffusion energy barriers are computed with the climbing-image nudged elastic band method [Henkelman et al., 2000] relaxing three intermediate images between the initial and final states until the residual force on each atom converges to 0.04 eV/Å.

## 4.3 Results and discussion

### 4.3.1 Electron irradiation of pristine $1T'$ -MoS<sub>2</sub>

The structure of  $1T'$ -MoS<sub>2</sub> consists of one layer of Mo atoms sandwiched between two layers of S atoms. As we pointed out in our previous work [Pizzochero and Yazyev, 2017], this lattice features two symmetry inequivalent sulfur atoms per chalcogen layer. In order to distinguish these two positions, we refer to the sulfur layer closer to (farther from) the molybdenum layer as  $S_1$  ( $S_2$ ). In addition, we label  $S_{1t}$  or  $S_{2t}$  and  $S_{1b}$  or  $S_{2b}$  the chalcogen atoms belonging to the top (t) or bottom (b) layer, respectively, where the top layer is the one which is the closest to the electron beam source (Fig. 4.1). Hence, there exist four inequivalent sulfur sites from the point of view of the head-on collision process, as we summarize for clarity in Fig. 4.2.

As a first step, we consider pristine  $1T'$ -MoS<sub>2</sub> and determine the different events that take place when an increasing amount of energy is transferred from the electron beam to each of the four inequivalent sulfur atoms. An overview of our results is presented in Fig. 4.3. It

## Chapter 4. Single-Layer 1T'-MoS<sub>2</sub> Under Electron Irradiation from *Ab Initio* Molecular Dynamics

---

is found that defects at the bottom chalcogen layer require lower threshold energies to form ( $5.5 \text{ eV} < T_d < 7.2 \text{ eV}$ ) compared to those at top or both chalcogen layers ( $8.6 \text{ eV} < T_d < 22.7 \text{ eV}$ ). In fact, when a chalcogen atom in the top layer ( $S_{1t}$  and  $S_{2t}$ ) is displaced downwards, it is "stopped" and kicked back by the underlying Mo layer. This is not the case of S atom in the bottom layer ( $S_{1b}$  and  $S_{2b}$ ), where atoms can therefore be sputtered at lower energies. Specifically, our simulations suggest that a Frenkel pair forming at the  $S_{1b}$  site – in which one atom is removed from its equilibrium lattice site and is located in an interstitial position – is characterized by a  $T_d$  of 5.5 eV. However, when the energy transferred to the  $S_{1b}$  atom is slightly increased by 0.2 eV, a  $V_{S1b}$  defect forms. It is worth noting that the  $V_{S1b}$  defect presents lower displacement energy than the  $V_{S2b}$  by 1.5 eV. The reason for this traces back to the weaker Mo– $S_{1b}$  (or, equivalently, Mo– $S_{1t}$ ) bond compared to the Mo– $S_{2b}$  (or Mo– $S_{2t}$ ) bond, as it can also be inferred from the longer interatomic distance of the former (2.48 Å) when compared to the latter (2.39 Å) [Pizzochero and Yazyev, 2017]. For the purpose of comparison, we also determine the displacement threshold energy of a single sulfur vacancy in the bottom layer of the semiconducting 2H-MoS<sub>2</sub>. In excellent agreement with previous works [Komsa et al., 2012, Garcia et al., 2014], we obtain a value of 7.0 eV, hence suggesting that the 1T' phase is more susceptible to knock-on damage than the 2H phase, when the same electron energy is used.

It has been previously shown that in the 2H phase of single-layer transition metal dichalcogenides the displacement threshold energy to form a sulfur vacancy in the bottom layer is very similar to the formation energy calculated in the unrelaxed lattice [Komsa et al., 2012]. This is indeed the case also for 1T'-MoS<sub>2</sub>, where we found formation energies in unrelaxed lattices of 5.97 eV and 6.98 eV for  $V_{S1b}$  and  $V_{S2b}$  defects, respectively, to be compared with their  $T_d$  of 5.70 eV and 7.20 eV. This agreement deteriorates when the lattice is allowed to relax, lowering the formation energies to 5.35 eV and 6.42 eV. We explain this effect in terms of time-scales at which vacancy defects form during the irradiation process. The sputtering of a sulfur atom upon electron-nucleus scattering occurs within a few tens of femtoseconds, a time-scale that allows only a little amount of energy to be dissipated at the neighboring lattice sites. Therefore, the energy which is necessary to remove one sulfur atom from the frozen lattice can be considered a good approximation to the displacement threshold energy. The difference between the formation energies calculated in the frozen and relaxed lattices is 0.62 eV and 0.56 eV for  $V_{S1b}$  and  $V_{S2b}$  defects, respectively, and quantifies the energy that is accommodated in 1T'-MoS<sub>2</sub> upon defect formation. This suggests that a similar structural relaxation takes place at the two different sulfur vacancies, and the larger formation energy of the  $V_{S2b}$  defect compared to  $V_{S1b}$  only stems from the stronger bond of  $S_{2b}$  compared to  $S_{1b}$ , as we mentioned above.

Contrary to the bottom layer, we do not observe any single vacancy formation when sulfur atoms in the top layer undergo knock-on collision events. We found that Frenkel pairs forming at  $S_{1t}$  and  $S_{2t}$  sites are characterized by threshold energies of 8.6 eV and 22.7 eV, again a remarkable difference between the two inequivalent sulfur atoms. A divacancy composed of  $V_{S1t}$  and  $V_{S2b}$  defects can form in the lattice when an energy of 13.7 eV is transferred to

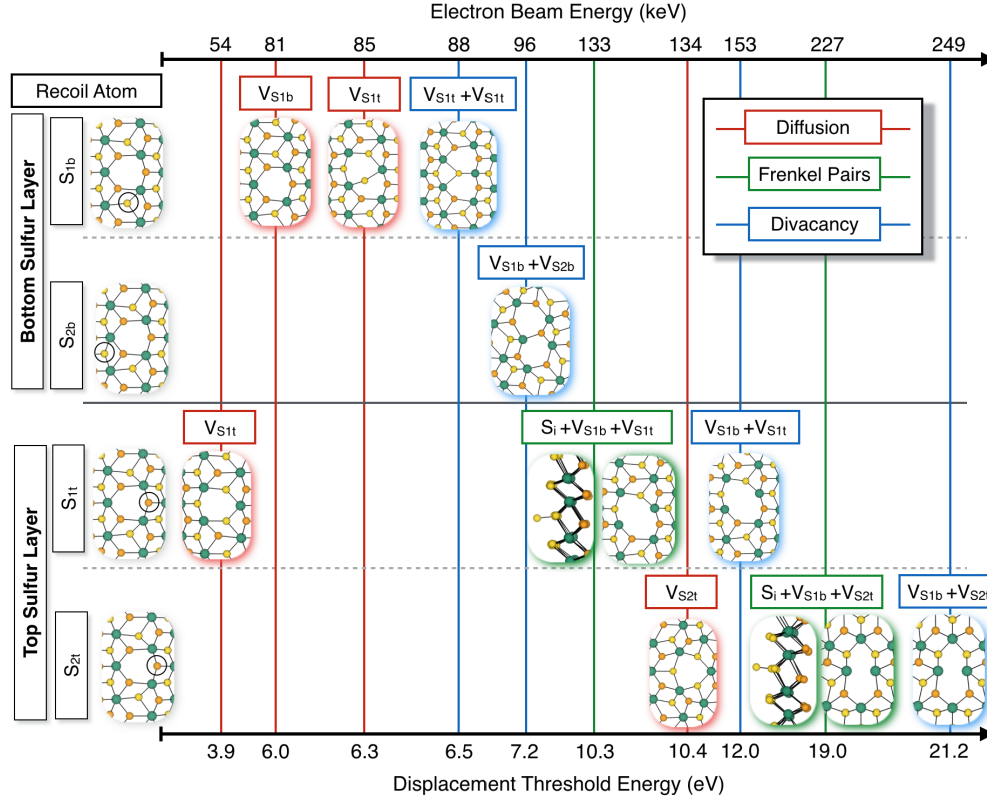


Figure 4.4 – Overview of the atomic defects that emerge in the vicinity of a  $V_{S1b}$  defect as a function of the displacement threshold energies and corresponding electron beam energies. For each row, the initial recoil atom is shown in the black circle in the left column. According to the legend, red, green and blue boxes correspond to diffusion events, Frenkel pairs and divacancies formation, respectively. Lattice sites are labelled according to Fig. 4.2.

the  $S_{1t}$  lattice site. Our molecular dynamics simulations provide a detailed explanation of the mechanism underlying the origin of this divacancy defect, which turns out to involve the formation of a diatomic  $S_2$  molecule. Specifically, the recoil atom  $S_{1t}$  is knocked downwards, being displaced by the electron beam, and further transfers momentum to the underlying  $S_{1b}$  atom leading to the formation of the  $S_2$  molecule that is eventually sputtered, leaving a divacancy in the lattice. Importantly, within the investigated range of  $T_d$ , we do not observe any vacancy defect involving the  $S_{2t}$  sites, thereby suggesting that this sulfur atom can be displaced only for  $T_d > 25$  eV.

In order to provide an useful insight to experimentalists, we now turn our attention to the electron beam energies necessary to create the atomic defects described above, that we show in Fig. 4.3. When the pristine lattice of  $1T'$ -MoS<sub>2</sub> is considered as a model of the crystal, no defects is predicted to be produced for electron energies which are smaller than 75 keV. This is the larger beam energy at which imaging in the transmission electron microscope can be carried out without leading to any substantial radiation-induced damage in the sample. Above this value, in fact, vacancies at the bottom layer should start forming. In the  $2H$  crystalline

phase, within the same static lattice approximation used here, vacancies are introduced when electron beam energy larger than 92 keV are employed. Such a remarkable difference stems from the lower cohesive energy of 1T'-MoS<sub>2</sub> as compared to 2H-MoS<sub>2</sub> [Pizzochero and Yazyev, 2017]. Interestingly, the electron energy to form the V<sub>S1b</sub> defect (77 keV) is significantly lower compared to the one necessary to create the V<sub>S2b</sub> defect (96 keV). This indicates that an electron beam of energy equal to or larger than 77 keV, but smaller than 96 keV, can be used to *selectively* create vacancies at the S<sub>1b</sub> sites while keeping the S<sub>2b</sub> sublattice intact, thereby promoting the formation of *ordered* vacancy defects. Furthermore, we note that only electron energies larger than 113 keV induce major damage in both sulfur layers. Importantly, we remark that the above mentioned values of electron beam energies do not account for lattice thermal motion and zero-point vibrations. As a consequence, the static beam energies mentioned above have to be regarded as an upper limit of the actual beam energies to induce knock-on damages in the sample, when a finite temperature is considered. In a recent work [Komsa et al., 2012], it has been found that lattice vibrations at room temperature lowers the electron beam energy to remove a sulfur atom in 2H-MoS<sub>2</sub> by ~10 keV, and we suggest that a similar estimate should hold also for irradiated 1T'-MoS<sub>2</sub>.

#### 4.3.2 Electron irradiation of defective 1T'-MoS<sub>2</sub>

Next, we investigate 1T'-MoS<sub>2</sub> under the electron beam in the vicinity of a sulfur vacancy. Specifically, we introduce the V<sub>S1b</sub> defect in the otherwise pristine monolayer. The reason for this choice is twofold. On the one hand, the V<sub>S1b</sub> defect presents the lowest displacement threshold energy and therefore it can readily form during the irradiation, see Fig. 4.3. On the other hand, in our previous work [Pizzochero and Yazyev, 2017], we have found that this defect is characterized by a very low formation energies – ~1 eV lower than the frequently observed sulfur vacancy in the stable 2H phase of MoS<sub>2</sub> – thereby suggesting that it is likely to be the most common native impurity when thermodynamic equilibrium prevails. In the following, we focus on the response of each of the four inequivalent sulfur atoms closest to the V<sub>S1b</sub> defect to the electron beam. Our results are presented in Fig. 4.4. Depending on the magnitude of the transferred momentum during the irradiation, two different types of events take place around the impurity, namely (i) the sulfur vacancy diffusion and (ii) the Frenkel pair formation followed by the formation of divacancy defects.

Under irradiation, the diffusion of atoms around a vacancy defect is very favorable in the bottom chalcogen layer. In particular, we found that a transferred momentum as low as 3.9 eV can result in diffusion of V<sub>S1b</sub> defect in the out-of-plane direction, leading to the V<sub>S1t</sub> defect. This suggests that an electron beam energy of 54 keV, though not sufficient for inducing any additional atom sputtering, is nevertheless large enough to promote the diffusion of vacancy defects, if present in the monolayer. Furthermore, when the S<sub>1b</sub> lattice site acts as a recoil atom, both in-plane and out-of-plane diffusion paths are observed with corresponding  $T_d$  of 6.0 and 6.3 eV (or, equivalently, electron beam energies of 81 keV and 85 keV), respectively. The mobility of the sulfur vacancy V<sub>S2t</sub> belonging to the top sulfur layer is observed only at a larger transferred momentum of 10.4 eV (or beam energy of 134 keV) to in-plane diffusion

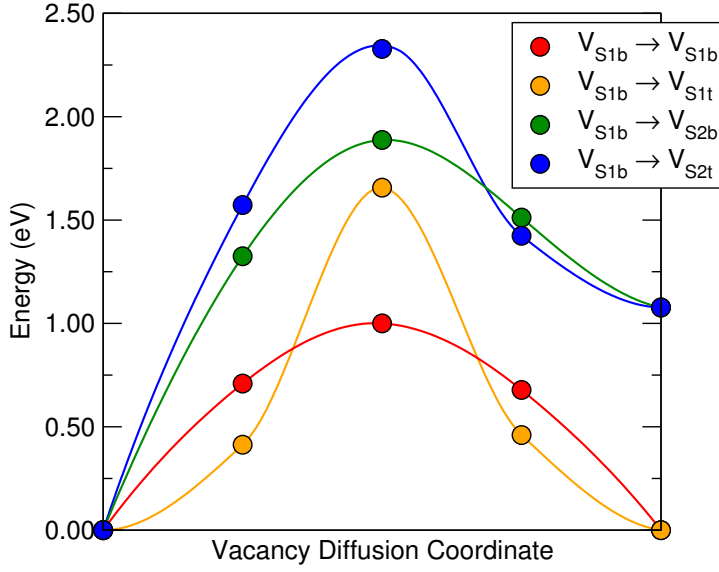


Figure 4.5 – Energy profiles for the stable  $V_{S1b}$  defect to diffuse to symmetry-inequivalent neighboring sulfur sites in single-layer  $1T'$ -MoS<sub>2</sub>, as calculated through the climbing-image nudged elastic band method. Lattice sites at which the vacancy defects form are labelled according to Fig. 4.2. Calculated points are interpolated with splines to guide the eye.

to a neighboring equivalent site. Overall, diffusion processes involving  $S_{1b}$  and  $S_{1t}$  sites are achieved at lower beam energies than those involving the  $S_{2t}$ , further highlighting the different bond strength between the inequivalent sulfur atoms in the  $1T'$ -MoS<sub>2</sub> lattice. We extend our investigation of the mobility of the stable  $V_{S1b}$  defect by computing its energy barriers to diffuse to all possible neighboring sites, *i.e.* the  $S_{1b}$ ,  $S_{1t}$ ,  $S_{2b}$  and  $S_{2t}$  sites. Our results are given in Fig. 4.5. It is found that the lowest barrier path involves the in-plane diffusion of the  $V_{S1b}$  defect to an equivalent  $S_{1b}$  site with a barrier equals to 1.00 eV, while the out-of-plane diffusion to the  $S_{1t}$  site requires a larger barrier of 1.66 eV to occur. These latter paths are likely to take place at room temperature and above, and are overall the most energetically favorable ones. This is consistent with our molecular dynamics simulations reported in Fig. 4.4, where we found that the diffusion along the above mentioned paths occurs at the lowest electron beam energies. On the other hand, diffusion processes of the  $V_{S1b}$  defect to the  $S_{2b}$  and  $S_{2t}$  sites are characterized by larger energy barriers of 1.89 eV and 2.33 eV, respectively. While we observe the latter diffusive event in AIMD simulations at a beam energy of 134 keV, we do not observe the former, despite the accompanying barrier is lower in energy by 0.44 eV. We suggest that the reason for this is possibly due to the direction of the incoming beam: given that the electron beam is incident along the direction normal to the monolayer (head-on collision), it is unlikely to observe in-plane diffusions requiring larger activation barriers to take place.

It is an interesting question whether a single sulfur vacancy defect promotes or not the formation of a second vacancy at its neighboring sites under electron irradiation. In order to address this issue, we identify the displacement threshold energies of the  $S_{1b}$ ,  $S_{2b}$ ,  $S_{1t}$ , and  $S_{2t}$  sites which are the closest to the vacant site (Fig. 4.4). As far as the bottom chalcogen layer is concerned, we found that divacancy defects are characterized by  $T_d$  of 6.5 and 7.2 eV, depending on whether the  $S_{1b}$  or  $S_{2b}$  site is considered as a recoil atom, respectively. When comparing those threshold energies with the ones of the single vacancy reported in Fig. 4.3, we find that that the sulfur vacancy does not play any significant role in affecting the threshold

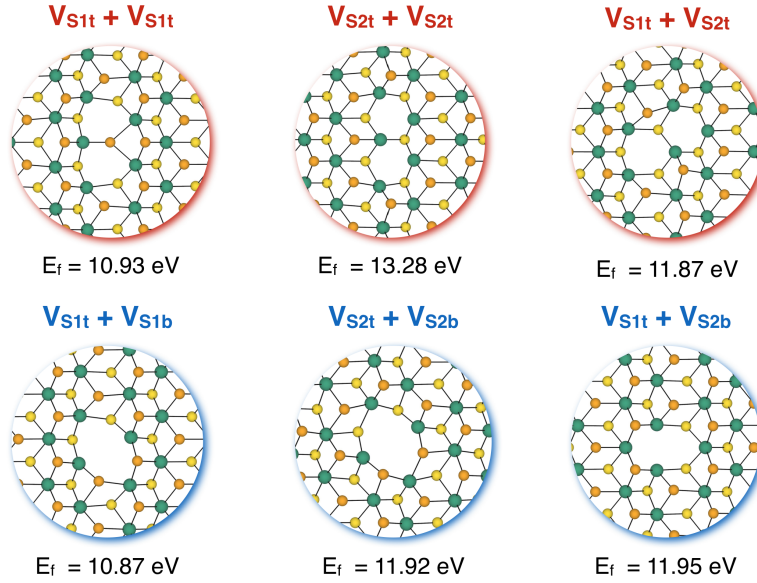


Figure 4.6 – Atomic structures and formation energies ( $E_f$ ) of all possible configurations of sulfur divacancy defects in 1T'-MoS<sub>2</sub>. Blue (red) color indicates divacancies forming at the same (opposite) chalcogen layers. Lattice sites are labeled according to Fig. 4.2

energies (or electron beam energy) of the nearest S<sub>2b</sub> lattice site – that thus remains unchanged – while it slightly increases the  $T_d$  of S<sub>1b</sub> sites in the bottom layer by 0.7 eV. Hence, the presence of V<sub>S1b</sub> does not promote the formation of a second vacancy in its neighborhood in the bottom layer. Then, we inspect the response of the S sites in the vicinity of the V<sub>S1b</sub> defect belonging to the bottom layer (that is, S<sub>1t</sub> and S<sub>2t</sub>). First, we observe that similarly to the pristine lattice, the electron beam energy necessary to create defects in the top layer of defective lattice is larger than in the bottom layer. Second, Frenkel pairs form at threshold energies of 10.3 eV and 19.0 eV at S<sub>1t</sub> and S<sub>2t</sub> sites, respectively, and precede in energy the formation of divacancies by ~2 eV. Furthermore, we note that such divacancies have lower threshold energies (12.0 eV and 21.2 eV) than the corresponding ones forming in the same layer of pristine lattice (13.7 eV and >25 eV). We also observe that V<sub>S1b</sub>+V<sub>S1t</sub> and V<sub>S1b</sub>+V<sub>S2t</sub> divacancies should form under beams of energies at least equal to 134 keV and 249 keV, respectively. To summarize, our simulations suggest that the presence of the V<sub>S1b</sub> defect lowers the displacement threshold energies for the formation of a second vacancy only in the top layer but not in the bottom one. In the case of pristine lattice, the bottom layer is intact and therefore it stops the recoil atom when displaced downwards upon the irradiation. However, when V<sub>S1b</sub> is introduced, this stopping effect is of minor extent because of the missing atom, thereby lowering the displacement threshold energies of the sulfur atoms in the top layer.

Finally, we focus on the stability of divacancy defects in 1T'-MoS<sub>2</sub> through the determination of their formation energies (see Fig. 4.6). Again, we stress that formation energies account for the stability of defect under thermodynamic equilibrium, while electron beam irradiation is a non-equilibrium process. Nevertheless, it is possible to draw some qualitative connection between

$E_f$  and  $T_d$ . Specifically, it is found that the most stable divacancies configurations are those involving the  $S_{1t}$  and/or  $S_{1b}$  lattice sites, namely  $V_{S1t}+V_{S1t}$  and  $V_{S1t}+V_{S1b}$ . These configurations also emerge from our molecular dynamics simulations at electron beam energies of 88 keV and 134 keV, respectively. On the other hand, the  $V_{S2t}+V_{S2t}$  divacancy presents the largest formation energies, and consistently it does not appear as a result of the AIMD calculations. Further, we note that  $V_{S1t}+V_{S2t}$ ,  $V_{S1t}+V_{S2b}$  and  $V_{S2t}+V_{S2b}$  divacancies show very similar formation energies that only differ by few tens meV. Despite this, only the former configurations are observed as a result of the dynamics while the latter is not, thereby indicating a competition between equilibrium and non-equilibrium processes during the electron beam irradiation.

## 4.4 Conclusion

Motivated by the recent progress in defect-engineering of transition metal dichalcogenides in the electron microscope, we have theoretically investigated for the first time the response of  $1T'$ -MoS<sub>2</sub> to the electron irradiation. We have found that an electron beam energy below 75 keV has to be employed to acquire images of the  $1T'$ -MoS<sub>2</sub> samples in the microscope without yielding any substantial knock-on damage. Sulfur atoms belonging to the bottom layer present lower displacement threshold energies compared to those in the top layer. As a consequence, an electron beam of energy up to 113 keV can selectively create vacancy defects in the bottom layer while preserving the top one intact. Furthermore, in the bottom layer, the sulfur atoms closer to the Mo plane have the lowest displacement threshold energies among all lattice sites. This implies that, when a proper tuning of the beam energy ( $77 \text{ keV} < E_{\text{beam}} < 96 \text{ keV}$ ) is employed, they can be selectively sputtered from the lattice, leading to the formation of ordered defects. In addition, the created vacancies are mobile under the electron beam. Depending on the specific path considered, the calculated barriers to diffuse range from 1.00 to 2.33 eV, suggesting that these defects can acquire mobility at room temperature and above. We also found that the presence of a single vacancy lowers the displacement threshold energies of sulfur atoms at certain neighboring sites. Finally, we have discussed the most stable configurations of divacancy defects when thermodynamic equilibrium prevails and provided a comparison with those that are expected to be observed during the electron irradiation.

Overall, our simulations suggest that the metastable  $1T'$  phase of single-layer MoS<sub>2</sub> is more susceptible to knock-on damage compared to the thermodynamically stable  $2H$  when the same electron beam energy is adopted. Recently, it has been theoretically shown that the introduction of sulfur vacancy defects and the accompanying lattice strain are able to reduce the difference in energy between the  $2H$  phase and the  $1T'$  polymorphs of MoS<sub>2</sub> [Kretschmer et al., 2017]. As vacancies can be created easier in  $1T'$ -MoS<sub>2</sub> compared to  $2H$ -MoS<sub>2</sub>, our results suggest that, once the  $1T'$  phase is formed, the subsequent introduction of defects through electron irradiation should further stabilize it over the otherwise thermodynamically stable  $2H$  phase. In conclusion, our findings provide useful insights to the imaging of  $1T'$ -MoS<sub>2</sub> in the electron microscope along with important guidelines for the defect engineering.





## 5 Defect-Induced Magnetism in Metallic and Semiconducting 2D-PtSe<sub>2</sub>

One of the opportunities offered by crystal imperfections is the introduction of a long-range magnetic ordering, a long-time subject of theoretical investigations. Intrinsically magnetic two-dimensional materials are attracting increasing attention thanks to their unique properties, which include layer-dependent magnetism and electric-field modulation. Yet, inducing magnetism in non-magnetic 2D crystals remains a challenge. Here, we reveal an unexpected magnetic response of both metallic and semiconducting ultrathin films of PtSe<sub>2</sub> by means of magneto-transport measurements. Our first-principles calculations, supported by transmission electron microscope imaging, indicate that Pt vacancy defects are at the origin of the observed magnetism in otherwise non-magnetic PtSe<sub>2</sub>. Our work ignites the potential of atomic-scale defects for driving non-magnetic atomically thin crystals into magnetic phases, thereby opening new directions for expanding the library of two-dimensional magnets.

This Chapter is adapted from:

A. Avsar, A. Ciarrocchi, M. Pizzochero, D. Unuchek, O. V. Yazyev and A. Kis  
*Defect Induced, Layer-Modulated Magnetism in Ultrathin Metallic PtSe<sub>2</sub>*  
Nature Nanotechnology 14, 674 (2019)

A. Avsar,\* C. Y. Cheon,\* M. Pizzochero,\* M. Tripathi, A. Ciarrocchi, O. V. Yazyev and A. Kis  
*Probing Magnetism in Atomically Thin Semiconducting PtSe<sub>2</sub>*  
Nature Communications, submitted (2020)

\*these authors contributed equally

My contribution to these works has been devising theoretical models and performing all first-principles calculations.

## **5.1 Motivation**

While intrinsically magnetic materials are rare in nature, long-range magnetism can be introduced into non-magnetic 2D materials through the intercalation of excess atoms [Hardy et al., 2015], proximity effects [Wang et al., 2015b], and defect engineering [Guguchia et al., 2018], owing to their large surface area-to-volume ratio. The latter strategy has been predicted for several 2D materials including graphene [Yazyev and Helm, 2007], but has not been experimentally accomplished yet. Among the rapidly expanding family of 2D materials, layered platinum diselenide (PtSe<sub>2</sub>) is a relatively new and interesting member due to its unique thickness-dependent electronic structure [Ciarrocchi et al., 2018, Wang et al., 2015a, Zhao et al., 2017b, Yim et al., 2016]. While multilayer films exhibit metallic character, this crystal undergoes a metal-to-semiconductor transition when thinned down to mono- and bi-layers. Recent experimental investigations highlighted a broad variety of intrinsic point defects in PtSe<sub>2</sub> [Zheng et al., 2019], thereby rendering this system an ideal platform for investigating defect-induced magnetization. Indeed, earlier first-principles calculations showed that Pt vacancies in monolayer PtSe<sub>2</sub> have a strong influence on the magnetic properties, being the introduction of these defects accompanied by a large local magnetic moment [Gao et al., 2017, Zhang et al., 2016]. Vacancy defects in 2D materials can either form naturally during the growth/annealing processes [Zhou et al., 2013] or be intentionally created post-synthesis, *e.g.* under high-energy particles irradiation [Krashennnikov and Nordlund, 2010]. Recently, they have been observed at the topmost layers in chemical vapor transport-grown PtSe<sub>2</sub> [Zheng et al., 2019].

This Chapter presents a joint experimental<sup>1</sup> and theoretical investigation of defect-induced magnetism in PtSe<sub>2</sub>. Considering the existence of unavoidable growth-related defects in 2D materials [Zhou et al., 2013, Zheng et al., 2019], our findings expand the range of 2D magnets into materials that would otherwise be overlooked, and further lay the foundation for an atom-by-atom engineering of magnetism of non-magnetic systems in the ultimate limit of atomic thickness. The rest of this Chapter is organized as follows. In Section 5.2, we present the results on metallic PtSe<sub>2</sub>, while in Section 5.3 we discuss our findings in mono- and bilayer semiconducting PtSe<sub>2</sub>. Finally, Section 5.4 summarizes and concludes our work.

## **5.2 Defect-induced, layer modulated magnetism in ultrathin metallic PtSe<sub>2</sub>**

### **5.2.1 Experimental results**

We obtain thin, ribbon-shaped PtSe<sub>2</sub> flakes by mechanical exfoliation from chemical vapor transport-grown bulk crystals (HQ Graphene) onto a Si/SiO<sub>2</sub> (270 nm) substrate. In total, ten devices were characterized with PtSe<sub>2</sub> thickness varying in the ~4.15 – 14 nm range, as determined by atomic force microscopy (AFM), allowing us to study the thickness dependence

---

<sup>1</sup>The experimental results presented in this Chapter have been achieved in the Laboratory of Nanoscale Electronics and Structures (LANES) at EPFL led by Prof. Andras Kis.

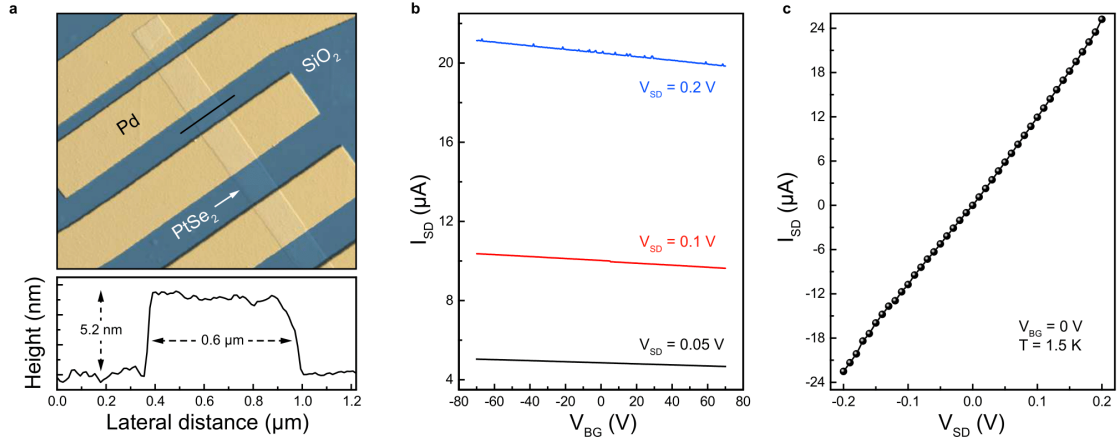


Figure 5.1 – (a) An AFM image of the device A. Height scale bar is  $\pm 40$  nm. Following the black dashed line, we measure a height of 5.2 nm and a width of  $0.6 \mu\text{m}$  for this device. (b)  $V_{BG}$  dependence of  $I_{SD}$  measured at fixed  $V_{BG} = 0.05$  V, 0.1 V and 0.2 V. (c) Output characteristics of the device as a function of  $V_{BG}$  at fixed  $V_{BG} = 0$  V. All charge transport measurements were performed at 1.5 K.

of the magnetism. Non-magnetic metallic palladium (Pd) contacts (80 nm thick) were formed using electron beam lithography and electron beam evaporation techniques. These non-magnetic Pd contacts were fabricated to exclude any influence of the contact on the magnetic response of the device. Due to the ribbon-like shape of our crystals, devices were fabricated in the two-terminal geometry. An AFM image of a completed device is shown in Fig. 5.1(a). Longitudinal device resistance was characterized as a function of back-gate voltage ( $V_{BG}$ ), source-drain bias ( $V_{SD}$ ), magnetic field ( $B$ ) and temperature ( $T$ ). We first discuss the charge transport properties of a device based on a 5.2 nm thick PtSe<sub>2</sub> crystal (device A). Fig. 5.1(b) shows the gate-voltage dependence of source-drain current ( $I_{SD}$ ) at fixed bias-voltage values of 50, 100 and 200 mV, where we observe nearly gate-independent transport characteristics. This indicates that PtSe<sub>2</sub> with a thickness of 5.2 nm is metallic.

We utilize magnetoresistance measurements as a sensing tool to characterize the magnetism of PtSe<sub>2</sub>. To this end, we sweep an out-of-plane magnetic field while recording the device resistance. As shown in Fig. 5.2(a), we observe a hysteresis loop with minima at  $\pm 25$  mT under backward and forward scans. The hysteretic behavior and the presence of a minor loop are the hallmarks of ferromagnetism. We extract a coercive field of  $\sim 25$  mT. We also note that, just like the total device resistance, the change in the device resistance under a magnetic field is almost insensitive to the  $V_{BG}$ . Next, we study the dependence of the change of device resistance ( $\Delta R$ ) on the bias voltage and the temperature. Fig. 5.2(b) shows the  $V_{SD}$  dependence on  $\Delta R$ , as measured at 1.6 K. The signal increases from  $\Delta R = 30 \Omega$  to  $400 \Omega$  as the bias is reduced from 50 mV to 1 mV. The extracted MR relative variation is 5% at low biases. As shown in Fig. 5.2(b), the dependencies of both  $\Delta R$  and  $R$  on  $V_{SD}$  are similar, and may be due to slightly non-linear charge injection at low biases, though its physical origin needs further investigation. Following, we present the temperature dependence of the magnetoresistance

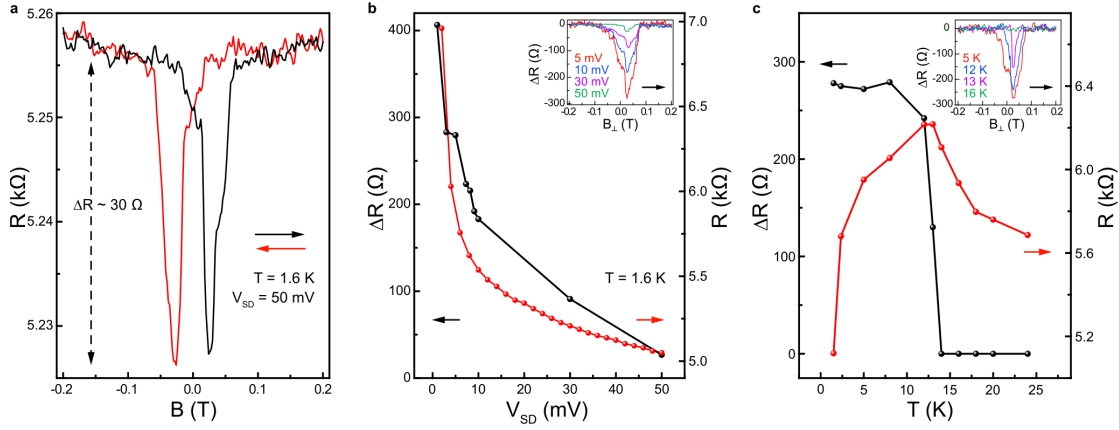


Figure 5.2 – (a) Magnetic field dependence of the device resistance measured at  $T = 1.6$  K. The red (black) arrow represents sweep direction from 0.2 T (–0.2 T) to –0.2 T (0.2 T). (b) Source-drain bias ( $V_{BG}$ ) dependences of the change in the device resistance under the magnetic field ( $\Delta R$ ) and the longitudinal device resistance ( $R$ ). Inset shows the resistance change under magnetic field acquired at fixed biases of  $V_{BG} = 1$  mV, 3 mV and 50 mV.  $\Delta R$  is calculated by subtracting a polynomial fitting from the device resistance. (c) Temperature dependence of  $\Delta R$  and  $R$ . Inset shows the magnetic field dependence of the resistance change measured at  $T = 1.5$  K, 13 K and 16 K.

measured at a fixed bias  $V_{SD} = 5$  mV [Fig. 2(c)].  $\Delta R$  has a very weak temperature dependence in the  $1.5 \text{ K} < T < 13 \text{ K}$  range. Raising the temperature just slightly over 13 K quickly suppresses the magnetic response of the device. The temperature dependence of device resistance also shows a similar drop when  $T$  is raised above 13 K, which could be related to the suppression of spin-dependent scattering. The resistance keeps increasing as the temperature is further increased, due to the metallic nature of PtSe<sub>2</sub>.

In contrast to this hysteretic magneto-transport response, another subset containing five out of ten characterized devices shows different characteristics. In Fig. 5.3(a), we show the magnetic field dependence (forward and backward sweep directions) of the device resistance for one of these devices (device B), which exhibits plateaus with two different values. Here, we observe the lower plateau at low fields in the  $-30 \text{ mT} < B < 30 \text{ mT}$  range, whereas a sharp jump to the high plateau is observed for fields above 30 mT. The height of the jump in this device is  $\Delta R \approx 2$   $\Omega$  and depends on the  $V_{SD}$ , as shown in Fig. 5.3(b). The width and height of this plateau are also strongly sensitive to the temperature, as the signal is completely quenched above 5 K [Fig. 5.3(c)]. Here, we are confident that the transition between these plateaus is a result of the switching between antiferromagnetic ordering at low fields into a fully spin polarized state at higher fields due to the metamagnetic effect [Huang et al., 1994]. Such magneto-transport response with two plateaus was previously observed in semiconducting bilayer CrI<sub>3</sub>-based tunneling devices [Song et al., 2018, Klein et al., 2018]. It was shown that each CrI<sub>3</sub> layer has initially opposite spin polarization at low fields and that the application of a field above the coercive field reverses the magnetization of one of CrI<sub>3</sub> layers causing both layers to have the same spin polarization. Additionally, the observation of very sharp switching between low and

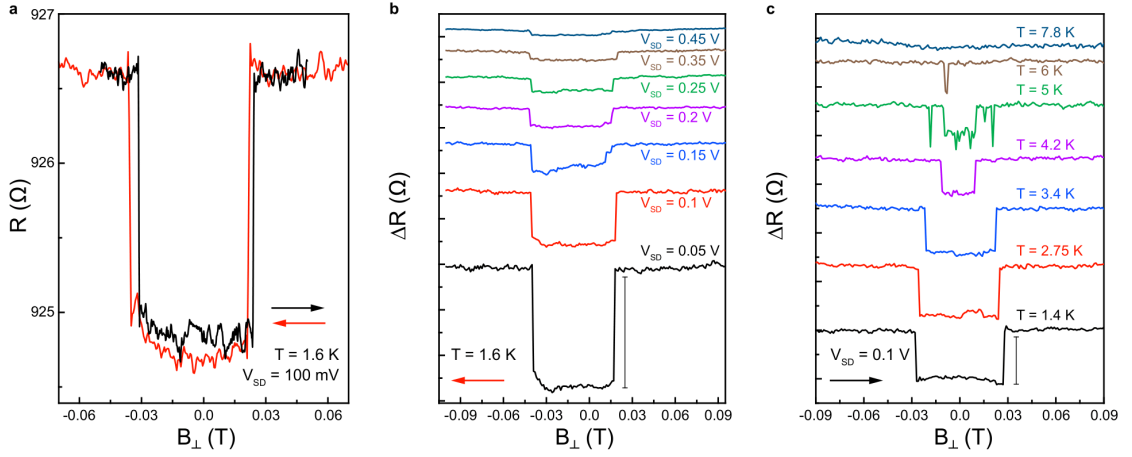


Figure 5.3 – (a) Magnetic field dependence of the device resistance. The red (black) arrow represents the sweep direction from positive (negative) to negative (positive) values. (b)  $V_{BG}$  dependence of the magneto-resistance change measured at  $T = 1.5$  K. Scale bar is  $5 \Omega$ . Curves shown for sweeps at  $0.1 \text{ V} \leq V_{BG} \leq 0.45 \text{ V}$  are shifted for clarity. (c) Temperature dependence of  $\Delta R$  measured at fixed bias of  $V_{BG} = 0.1 \text{ V}$ . Scale bar is  $2 \Omega$ . Curves shown for sweeps at  $2.75 \text{ K} \leq T \leq 7.8 \text{ K}$  are offset for clarity.

high plateaus indicates the out-of-plane direction magneto-crystalline anisotropy of PtSe<sub>2</sub>, in line with recent predictions [Zhang et al., 2016]. If the anisotropy had in-plane components, the switching would occur gradually with the field.

After presenting the existence of both ferromagnetic and antiferromagnetic ordering in metallic PtSe<sub>2</sub>, we next assess if there is a layer dependent magnetization. We have characterized two adjacent devices prepared under identical conditions. As confirmed by the AFM scan, thickness of PtSe<sub>2</sub> crystals in these devices differs by only one layer [as shown in Figs. 5.4(a) and (b)], allowing us to investigate layer-dependent magnetism. While the device with a thickness of 6.45 nm (device C) PtSe<sub>2</sub> shows the characteristic response with two plateaus [Fig. 5.4(c)], the device with an additional layer and resulting thickness of 7.05 nm (device D) shows a ferromagnetic response [Fig. 5.4(d)]. This observation pinpoints the emergence of a layer-dependent magnetism in atomically thin PtSe<sub>2</sub>. To further investigate this effect, we prepared another PtSe<sub>2</sub> device (device E) containing additional one-layer thick fragments on the channel surface, as revealed by AFM imaging [Fig. 5.4(e)]. Magneto-transport response of this sample is very intriguing: both ferromagnetic and antiferromagnetic ordering coexist [Fig. 5.4(f)]. This measurement also allows us to directly conclude that the switching fields for these two contrasting magnetic orderings are different. Here, the strong layer-dependent relationship between different mechanisms could be stabilizing magnetic ordering differently and hence results in different switching fields.

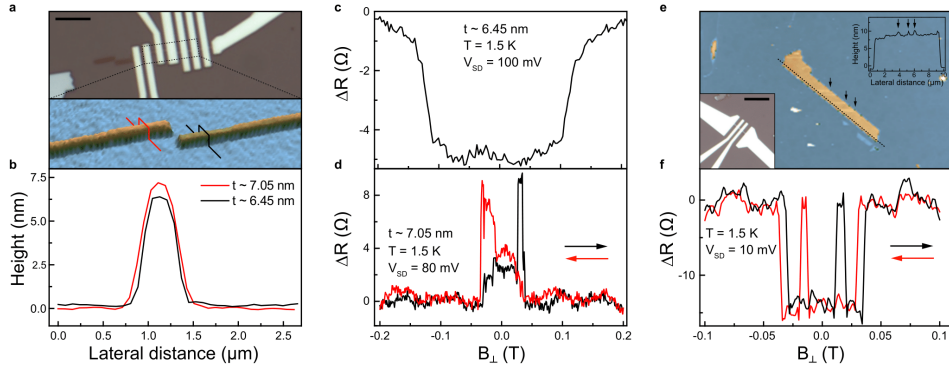


Figure 5.4 – (a) Optical and AFM images of a completed PtSe<sub>2</sub> device and its crystal, respectively. Dashed area represents the scanned AFM region. (b) Cross-sectional plots along the red and black lines in (a). AFM scans show that crystals used in device C and device D has one-layer difference ( $\sim 0.6$  nm) in their heights. (c) Magnetic field dependence of  $\Delta R$  measured from the device C (6.45 nm thick). (d) Magnetic field dependence of  $\Delta R$  measured from device D ( $\sim 7.05$  nm thick). (e) AFM image of a PtSe<sub>2</sub> crystal having multiple one-layer thick fragments on its surface. Top inset shows the cross-sectional plots along the black line in (e). Black color arrows in (e) and top-inset e indicate the one-layer thick fragments. Bottom-inset e shows the optical image of the corresponding device. Black solid line represents the scale bar ( $5 \mu\text{m}$ ). (f) Magnetic field dependence of  $\Delta R$  measured from the device E shown in (e). We would like to note that the change in device resistance in these samples has opposite sign compared to the thinner devices shown in Fig. 5.2(a).

### 5.2.2 Theoretical results

In the following, we propose a theoretical picture to interpret the observed effects. According to a purely ionic argument, Pt atoms in PtSe<sub>2</sub> exhibit a formal oxidation state of +4 and a resulting valence electron configuration  $5d^6 6s^0$ . On the basis of the crystal and ligand fields associated with the octahedral environment in which each Pt atom resides, a splitting of the  $d$  orbitals into a pair of empty  $e_{2g}$  states and fully occupied  $t_{2g}$  states is expected. Such a full occupation of the  $t_{2g}$  manifold prevents any intrinsic magnetism in PtSe<sub>2</sub> at all possible thicknesses – from monolayer to bulk – as further confirmed by our explicit density-functional calculations. As pristine PtSe<sub>2</sub> does not present any intrinsic spin-polarization, we suggest that the observed magnetism originates from lattice imperfections. The appropriate model describing the interaction between magnetic impurities mediated by conduction electrons is the well-established Ruderman-Kittel-Kasuya-Yosida (RKKY) model [Ruderman and Kittel, 1954, Kasuya, 1956, Yosida, 1957]. According to this, the dependence of magnetic exchange coupling  $J$  on the distance  $r$  reads as

$$J(r) \approx \cos \frac{2k_F r}{r^\alpha} \quad (5.1)$$

with  $k_F$  being the Fermi wavevector of the metal hosting the magnetic impurities and  $\alpha$  a constant which reflects the dimensionality of the system. Earlier theoretical and experimental investigations indicated that the Fermi surface of metallic PtSe<sub>2</sub> is composed of closed electron

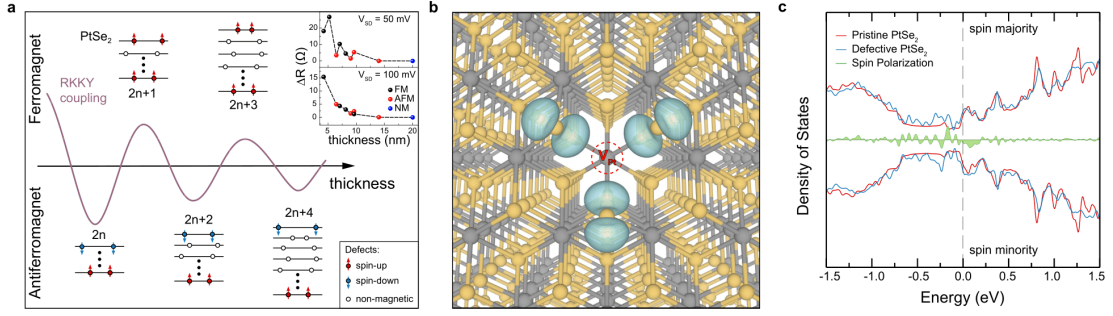


Figure 5.5 – (a) Schematic illustration showing the oscillating RKKY interaction across the PtSe<sub>2</sub> slab and the corresponding ground-state magnetic configurations. Inset plot shows the thickness dependence of MR curves for studied samples at fixed  $V_{BG}$  of 50 mV and 100 mV. (b) Atomic structure and spin density (turquoise) around a surface  $V_{Pt}$  defect (red, dotted circle) in multilayer PtSe<sub>2</sub>. Grey (orange) balls represent Pt (Se) atoms. Isosurfaces contour is set to  $0.003 e \text{ \AA}^{-3}$ . (c) Electronic density of states of multilayer PtSe<sub>2</sub> with (blue) and without (red) a surface Pt vacancy defect. In green, the difference between spin majority and spin minority states. Fermi level is set to zero (vertical dashed line).

and hole pockets located at  $k_z = 0$  and electron pockets at  $k_z = \pm 0.6 \pi/c$  [Zhang et al., 2017, Clark et al., 2019]. The latter give rise to an oscillating and power-law decaying contribution to  $J(r)$  in the direction normal to the PtSe<sub>2</sub> layers, with a period of approximately two layers, as we schematically show in Fig. 5.5(a). Hence, we see that adding or removing one layer from metallic PtSe<sub>2</sub> is sufficient to revert the sign of the magnetic exchange coupling, thereby realizing a thickness-dependent ferro- or anti-ferromagnetic configuration. This observation is also in a good agreement with the summary of devices measured at fixed bias of  $V_{SD} = 50$  mV and 100 mV. As shown in the inset of Fig. 5.5(a), we observe that the MR decreases as crystal thickness increases, layer-dependent magnetism exist and magnetism is not detectable in thicker crystals.

Next, we step from model interactions to first-principles calculations performed on realistic models in order to suggest which type of defect may actually be responsible for the magnetic response observed in our samples. Previous experimental investigations revealed the abundance of vacancy point defects in PtSe<sub>2</sub> film [Zheng et al., 2019]. Motivated by this observation, we assess the effects of such defects on the magnetic properties of PtSe<sub>2</sub> by introducing Se ( $V_{Se}$ ) and Pt ( $V_{Pt}$ ) vacancy in both metallic multilayer and bulk PtSe<sub>2</sub> models. In analogy with other transition metal dichalcogenides [Pizzochero and Yazyev, 2017], we find that the  $V_{Se}$  defect does not lead to magnetism. On the other hand, the introduction of the  $V_{Pt}$  defect located at the surface of the multilayer model induces a local magnetic moment of  $\sim 1.2 \mu_B$  per defect. We further observe that the spin density around the  $V_{Pt}$  defect mostly localizes on the neighboring selenium atoms within its first coordination shell, as shown in Fig. 5.5(b). Additionally, the investigation of the electronic density of states reported in Fig. 5.5(c) indicates that the local magnetic moments stem from defect-induced spin-split states that emerge around the Fermi level. Remarkably, we find that the same defect does *not* lead to a local magnetic moment



when forming in the bulk, hence indicating a surface-magnetism scenario. It is worth noting in this context that PtSe<sub>2</sub> is more prone to hosting metal atom vacancies than conventional, group VI dichalcogenides (*e.g.* MoS<sub>2</sub>) as a consequence of the substantially lower formation energy that this defect exhibits in the former material as compared to the latter, as reported by earlier calculations [Zheng et al., 2019, Pizzochero and Yazyev, 2017].

### 5.2.3 Methodology

First-principles calculations have been performed within the generalized gradient approximation to density functional theory devised by Perdew, Burke and Ernzerhof [Perdew et al., 1996a]. Geometry optimizations have been carried out with the VASP code [Kresse and Hafner, 1993, Kresse and Furthmüller, 1996] using a kinetic energy cutoff of 400 eV and  $k$ -meshes equivalent to 18  $k$ -points per unit cell along each periodic direction. During geometry optimizations, lattice constants and interlayer spacing were constrained to their experimental values of 3.73 Å and 5.08 Å, respectively, while the tolerance on atomic forces was set to 0.02 eV/Å. The electronic density of states has been calculated with the SIESTA code,<sup>40</sup> using a fine mesh equivalent to 120  $k$ -points and a smearing of 0.02 eV. The adopted multilayer and bulk PtSe<sub>2</sub> models consist of a 6-layer thick  $3 \times 3$  supercell and a periodic  $3 \times 3 \times 2$  supercell, respectively. In the case of multilayer models, the defects are placed in the topmost layer and a vacuum region of 15 Å was introduced to separate periodic images.

## 5.3 Probing magnetism in atomically thin semiconducting PtSe<sub>2</sub>

### 5.3.1 Experimental results

Our ultra-thin PtSe<sub>2</sub> flakes were obtained by mechanical exfoliation from CVT-grown bulk crystals (HQ Graphene), and their thickness is determined by atomic force microscopy (AFM). As shown in Fig. 5.6(a), the thickness of a monolayer is found to be  $\sim 0.6$  nm. The monolayer was transferred onto a monolayer graphene ribbon which was initially deposited onto a Si/SiO<sub>2</sub> (270 nm) substrate. Graphene is utilized as a bottom electrode, thereby taking advantage of its electrostatic transparency. This enables gate-tunable vertical and lateral transport operations, as the screening length exceeds its monolayer thickness [Avsar et al., 2018]. By employing electron beam lithography and electron beam evaporation techniques, non-magnetic metallic Palladium (Pd) contacts (80 nm thick) were formed on top of PtSe<sub>2</sub> and graphene. The schematics of the resulting device geometry is shown in Fig. 5.6(c). This geometry allows us to probe the magnetism in PtSe<sub>2</sub> through vertical transport by passing the charge current between electrodes #2 (graphene) and #3 (Pd). In addition, it allows us to characterize the basic transport properties of monolayer PtSe<sub>2</sub> by utilizing Pd electrodes #3 and #4 in the lateral measurement geometry. We further compare the magneto-transport properties of isolated graphene as well as the graphene/monolayer PtSe<sub>2</sub> heterostructure by relying on electrode pairs #1 & #2 and #2 & #5, respectively. An optical image of the completed device is presented in the bottom panel of Fig. 5.6(c). The transport output was characterized as a function of back-gate voltage ( $V_{BG}$ ), source-drain bias ( $V_{SD}$ ), magnetic field and temperature.



### 5.3. Probing magnetism in atomically thin semiconducting PtSe<sub>2</sub>

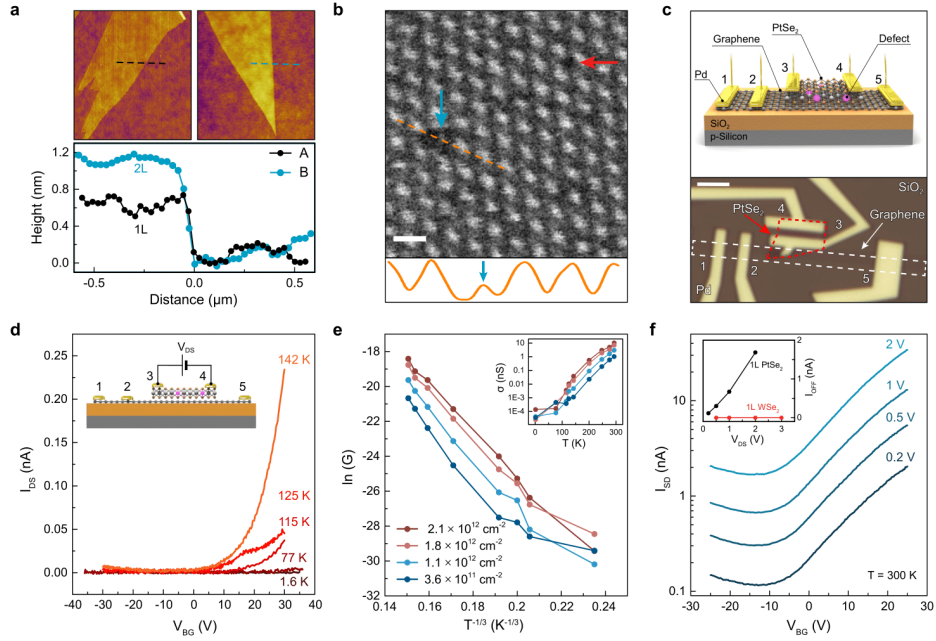


Figure 5.6 – (a) AFM images of mono- and bi-layer PtSe<sub>2</sub>. Color scale of the AFM image is 0-5 nm. Following the dashed lines, a height of  $\sim 0.65$  nm ( $\sim 1.2$  nm) is measured for monolayer (bilayer) PtSe<sub>2</sub>. (b) Raw HAADF image of a bilayer PtSe<sub>2</sub>. Blue (red) arrow shows the site with a missing Pt (Se) atom. Scale bar is 0.5 nm. Bottom panel shows the intensity profile measured along the dashed orange line shown in the STEM image. Blue arrow shows the intensity recorded at the Pt vacancy site. (c) Top panel: device schematics. A few-layer thick PtSe<sub>2</sub> hosting intrinsic defects is transferred on top of monolayer graphene. Both graphene and PtSe<sub>2</sub> are contacted with non-magnetic Pd contacts (80 nm thick). Bottom panel: optical image of a completed device. Scale bar is 3  $\mu$ m. (d)  $V_{BG}$  dependence of  $I_{SD}$  measured at fixed temperature values. Inset shows the device schematic. (e)  $\ln(G)$  vs  $T^{-1/3}$  measured at different doping levels. Inset shows the temperature dependence of device conductance at different doping values. (f) Room temperature  $V_{BG}$  dependence of  $I_{SD}$  measured at fixed  $V_{SD}$  values. Inset compares the  $V_{SD}$  dependence of measured off-state conductance for monolayer PtSe<sub>2</sub> and WSe<sub>2</sub> prepared under the same conditions.

Prior to magnetic field dependent measurements, we first assess the basic charge transport properties of monolayer PtSe<sub>2</sub>. Fig. 5.6(d) shows the  $V_{BG}$  dependence of  $I_{SD}$  measured at temperatures covering the 1.6–142 K range, while maintaining a constant  $V_{SD} = 2$  V. While  $I_{SD}$  is slightly modulated by the application of  $V_{BG}$  due to the semiconducting nature of monolayer PtSe<sub>2</sub>, the device shows a relatively low on-state conductance ( $V_{BG} > -5$  V). The insulating nature of the crystal is unambiguously confirmed by the observed temperature dependence of the conductivity ( $\sigma$ ) measured at fixed carrier concentrations. In the presence of disorder, the electrical transport can be described using the Mott formalism and the variable range hopping (VRH) model which describes the conductivity  $\sigma$  in terms of a characteristic temperature. The observed linear dependence of the  $\ln(\sigma)$  on  $T^{-1/3}$  at different given carrier densities [see Fig. 5.6(e)] supports the 2D VRH nature of charge transport up to room temperature. Such a

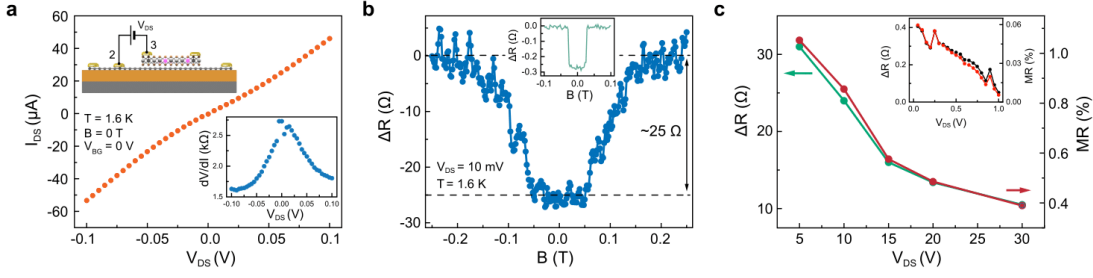


Figure 5.7 – (a) Bias voltage dependence of  $I_{SD}$ . Top inset is the schematics of measurement geometry. Bottom inset is the differential resistance as a function of applied bias. (b) Magnetic field dependence of electrical resistance measured at  $T = 1.6$  K. The observation of a two-plateaus response indicates the presence of antiferromagnetic ground state ordering. Inset shows the magneto-transport measurements for a  $\sim 7$  nm thick metallic PtSe<sub>2</sub>. (c) Bias dependence of change in device resistance as a result of magnetic field and corresponding MR percentage. All measurements are taken at 1.6 K. Inset shows the bias dependence of resistance and MR for a  $\sim 7$  nm thick metallic PtSe<sub>2</sub>.

characteristic temperature dependence has been widely observed in many systems, including defective 2D TMDC monolayers [Han et al., 2010, Radisavljevic and Kis, 2013, Qiu et al., 2013]. In fact, a band-gap of  $\sim 1.2$  eV is expected in monolayer PtSe<sub>2</sub> [Wang et al., 2015a], which in turn should result in a stable off-state over a moderate  $V_{BG}$  range, as previously reported for semiconducting TMDC monolayers [Radisavljevic et al., 2011a, Avsar et al., 2018]. As shown in Fig. 5.6(f), the lack of a clear off-state along with a strong dependence of the off-current on  $V_{SD}$  at room temperature signals the hopping nature of charge transport, and, importantly, further suggests the presence of atomic defects in monolayer PtSe<sub>2</sub> [Qiu et al., 2013]. In order to directly visualize the type of defects in our samples, we relied on Cs-corrected high-resolution transmission electron microscopy imaging. The result obtained from a bilayer PtSe<sub>2</sub> with a low accelerating voltage of 80 kV is shown in Fig. 5.6(b). Consistently with early scanning tunnelling microscopy investigations [Zheng et al., 2019], we observe  $V_{Se}$  and  $V_{Pt}$  defect in ultrathin PtSe<sub>2</sub> films. The concentration of  $V_{Pt}$  defects is found to be  $\sim 9 \times 10^{12} \text{ cm}^{-2}$ . Similarly to bilayer, we observe  $V_{Pt}$  in monolayer as well (not shown here).

After confirming the presence of intrinsic defects in our crystals, we next study the magneto-transport characteristic of our monolayer PtSe<sub>2</sub> sandwiched between the source (graphene) and drain (Pd) electrodes [inset of Fig. 5.7(a)] by utilizing a vertical measurement geometry. A fixed  $V_{SD}$  is applied on PtSe<sub>2</sub> while measuring the dependence of device resistance on the applied magnetic field. As shown in Fig. 5.7(a), the  $I_{SD}$ - $V_{SD}$  curve is nearly linear and symmetric, measured at zero field. As compared to lateral transport measurement given in Fig. 5.6(d), the device resistance under vertical geometry is improved by several orders of magnitude, as a result of the reduced transport pathway. Such a highly conducting response obtained along vertical direction allows us to probe directly the magnetic ordering of monolayer PtSe<sub>2</sub>. To this end, we sweep the out-of-plane magnetic field from  $-0.2$  T to  $0.2$  T while recording the vertical device resistance at  $V_{SD} = 10$  mV. As clearly seen in Fig. 5.7(b), the evolution of the

### 5.3. Probing magnetism in atomically thin semiconducting PtSe<sub>2</sub>

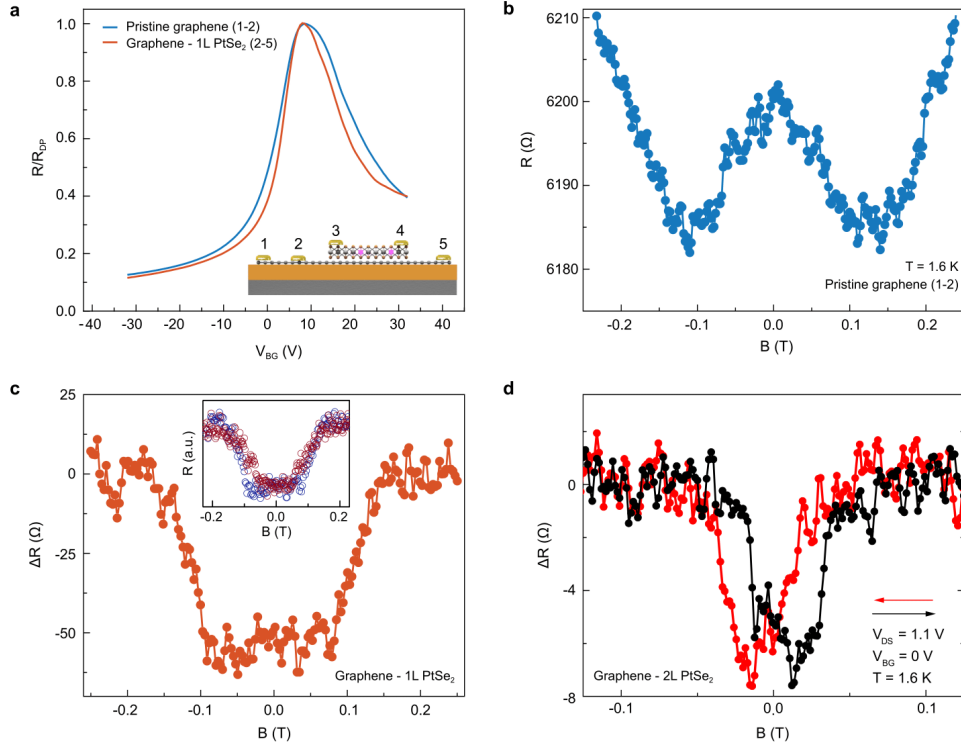


Figure 5.8 – (a)  $V_{\text{BG}}$  dependence of graphene resistance. Red (blue) line represents the device with (without) a monolayer PtSe<sub>2</sub> on top the graphene channel, between the voltage probes. Inset is the schematics of the measurement geometry. (b) Magnetic field dependence of pristine graphene resistance measured at  $T = 1.6$  K. (c) Magnetic field dependence of graphene resistance measured at  $T = 1.6$  K for the device with a monolayer PtSe<sub>2</sub> on the channel. Inset shows the magnetic field response of vertically measured monolayer PtSe<sub>2</sub> (red circles) and laterally measured graphene/monolayer PtSe<sub>2</sub> (blue circles). They have similar coercive fields. (d) Magnetic field dependence of graphene resistance measured at  $T = 1.6$  K for the device with a bilayer PtSe<sub>2</sub> on the graphene channel. Arrows represent magnetic field sweep directions.

resistance in our device with the magnetic field substantially departs from the typical localization response. Indeed, it features plateaus with two different values. As the field is increased, the lower plateau observed in the  $-50 \text{ mT} < B < 50 \text{ mT}$  interval is found to slowly approach the high plateau observed above 150 mT. This two-plateau response is the signature of an antiferromagnetic ground state ordering [Avsar et al., 2019, Klein et al., 2018, Song et al., 2018]. While we find a similar two-plateau response in thicker films of PtSe<sub>2</sub> [inset of Fig. 5.7(b)], the observation of a slow low-to-high plateau switching in monolayer PtSe<sub>2</sub> indicates that the magnetic moments are not fully oriented along the out-of-plane direction, *i.e.* spins could be slightly canted. Similarly to thicker metallic devices, the magneto-resistance percentage is found to be bias-dependent and estimated to be 1% in the low-bias regime, see Fig. 5.7(c).

In order to investigate the impact of magnetic ordering in PtSe<sub>2</sub> on the transport properties of graphene, we characterize the device resistance of graphene with and without PtSe<sub>2</sub> on the channel connecting the source and drain electrodes. Fig. 5.8(a) displays the  $V_{\text{BG}}$  depen-

dences of corresponding device resistances which show nearly identical device characteristics. However, the magnetic field responses of these junctions present striking differences, as shown in Fig. 5.8(b) and (c). While the pristine graphene junction exhibits a conventional weak localization response [Tikhonenko et al., 2008], the junction with the PtSe<sub>2</sub> monolayer shows an antiferromagnetic ordering response [Avsar et al., 2019, Klein et al., 2018, Song et al., 2018]. This difference in the magneto-transport properties is clearly due to the presence of magnetism in PtSe<sub>2</sub> and could be ascribed to two possible origins. One possibility is the back-and-forth hopping of graphene's electrons through the magnetic defect states in PtSe<sub>2</sub> via quantum tunneling, as previously reported in graphene/WS<sub>2</sub> heterostructures [Avsar et al., 2014]. On the other hand, it may be attributed to the interface-induced magnetism by PtSe<sub>2</sub>. This latter possibility is further supported by the nearly identical shapes of the magnetic response of pure PtSe<sub>2</sub> and the graphene/PtSe<sub>2</sub> heterostructure, as shown in the inset of Fig. 5.8(c). Finally, we complement our investigation by replacing monolayer PtSe<sub>2</sub> with bilayer PtSe<sub>2</sub>. We observe a hysteresis loop with minima at  $\pm 15$  mT under backward and forward scans [Fig. 5.8(d)], which is the hallmark of ferromagnetism [Leven and Dumpich, 2005]. The maximum change in the device resistance upon the application of magnetic field is  $\sim 16 \Omega$  and it strongly depends on the applied  $V_{SD}$ . The MR percentage probed by graphene is  $\sim 1\%$  and it is nearly independent of the applied  $V_{BG}$ . Our findings demonstrate that monolayer (bilayer) PtSe<sub>2</sub> exhibits antiferromagnetic (ferromagnetic) ground state ordering, and proximitized graphene electrodes can effectively be used as a sensitive probe to detect such magnetism [Kim et al., 2019].

### 5.3.2 Theoretical results

We here address the physical mechanism underlying the observed effects from a theoretical perspective. As in the case of metallic PtSe<sub>2</sub>, we conclude that lattice imperfections are the origin of the observed layer-dependent magnetism in the semiconducting PtSe<sub>2</sub>. Motivated by the direct observation of Pt vacancies in our transmission electron microscope images shown in Fig. 5.6(b), their indirect inference from our charge transport measurements as well as earlier scanning tunneling microscopy studies [Zheng et al., 2019], we investigate the magnetic properties of mono- and bilayer models of PtSe<sub>2</sub> with platinum vacancy defects by means of first-principles calculations. We stress that the RKKY model does not apply here, due to the semiconducting nature of mono- and bilayer PtSe<sub>2</sub>. For the monolayer case, we find that V<sub>Pt</sub> defect in its fully spin-polarized configuration gives rise to a local magnetic moment of  $4.00 \mu_B$ , which is localized mostly on the six selenium atoms neighboring to the missing Pt atom. We note, however, that the configuration characterized local magnetic moments in the two Se atomic planes oriented antiparallel to each other [see Fig. 5.9(a)] is 35 meV lower in energy than the former. Even though this value is dependent on the density functional adopted, all approximations considered indicate that such defect is energetically more stable in the antiferromagnetic configuration as compared to the ferromagnetic (Table 5.1) or non-magnetic (Table 5.2) one. Overall, this result is at odds with earlier calculations on Pt vacancy defect in monolayer PtSe<sub>2</sub> [Gao et al., 2017], where it was found that such defect induces a

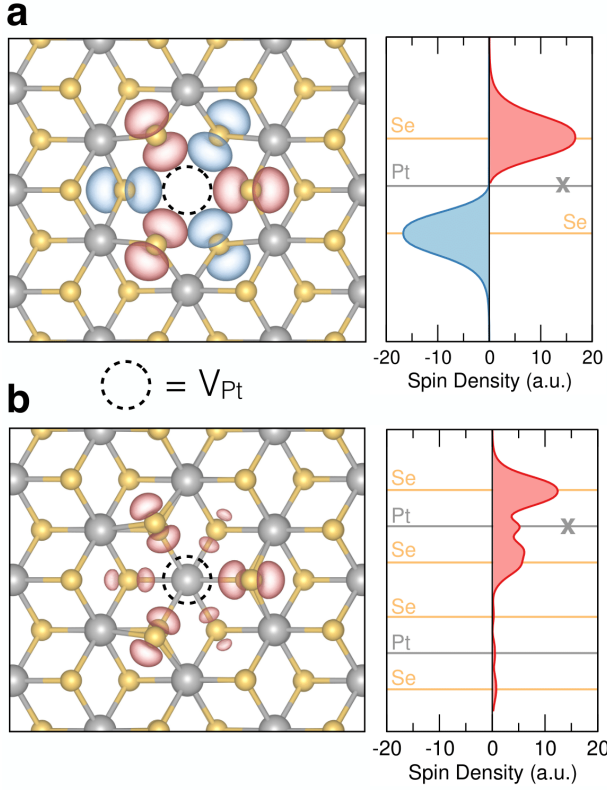


Figure 5.9 – (a) Spin-density distribution at the ground-state configuration of  $V_{\text{Pt}}$  defect in monolayer PtSe<sub>2</sub> calculated from first principles. Grey and orange balls represent Pt and Se atoms, respectively. The red and blue isosurfaces correspond to positive and negative spin densities. The position of the missing Pt atom is marked with a dashed circle. The right panel shows the in-plane averaged spin density as a function of out-of-plane position. (b) Spin-density distribution at the  $V_{\text{Pt}}$  defect in top layer of bilayer PtSe<sub>2</sub> calculated from first principles. Units in panels (a) and (b) agree with each other.

ferromagnetic response accompanied by a local magnetic moment of  $6.00 \mu_{\text{B}}$ . Here, we would like to also note that the Se point defect does not lead to magnetism.

Next, we consider bilayer PtSe<sub>2</sub> model with Pt vacancy in one of the two layers. Contrary to the monolayer case discussed above, for a defective bilayer we could not identify any solution other than the ferromagnetic configuration with a net magnetic moment of  $1.33 \mu_{\text{B}}$ , see Fig. 5.9(b). This value agrees well with the one obtained for  $V_{\text{Pt}}$  defects in thicker metallic PtSe<sub>2</sub> slabs [Avsar et al., 2019]. The reason for this traces back to the existence of the interlayer coupling between the PtSe<sub>2</sub> sheets in the bilayer system. In our previous work [Avsar et al., 2019], we have shown that platinum vacancy defects located at the surfaces of multilayer PtSe<sub>2</sub> act as magnetic centers, while their formation in the inner regions of the thick samples (as well as in the three-dimensional bulk material) does not lead to any local magnetic moment. This observation clearly pinpoints the pivotal role of interlayer interactions in quenching the defect-induced magnetic response in PtSe<sub>2</sub>. In bilayer PtSe<sub>2</sub>, the interlayer coupling affects only one of the two selenium atomic planes. As a result, the defect-induced magnetic moment in this system is reduced ( $1.33 \mu_{\text{B}}$ ) as compared to the fully polarized defect in monolayer PtSe<sub>2</sub> ( $4.00 \mu_{\text{B}}$ ), and, remarkably, the spin density primarily resides on the outmost three selenium atoms in the defective [Fig. 5.9(b)]. Hence, any antiferromagnetic solution can be realized in such a sort of "triangular lattice", due to topological frustration. Overall, our first-principles calculations suggest that platinum vacancy defect yields an antiferro- (ferro-) magnetic order in mono (bi-)layer PtSe<sub>2</sub>, portraying a picture in accord with experiments.

Table 5.1 – Difference in total energy between the ferromagnetic and antiferromagnetic orders of a  $4 \times 4$  supercell of monolayer PtSe<sub>2</sub> hosting a Pt vacancy defect for different exchange-correlation functionals.

Density Functional	$E_{\text{AFM}} - E_{\text{FM}} (\text{wo/ SOC})$	$E_{\text{AFM}} - E_{\text{FM}} (\text{w/ SOC})$
LDA [Ceperley and Alder, 1980]	42	32
PBE [Perdew et al., 1996a]	29	35
PBEsol [Perdew et al., 2008]	3	7
PW91 [Perdew and Wang, 1992]	63	65
revPBE [Zhang and Yang, 1998]	34	44

Table 5.2 – Difference in total energy between the ferromagnetic and non-magnetic solutions of a  $4 \times 4$  supercell of monolayer PtSe<sub>2</sub> hosting a Pt vacancy defect for different exchange-correlation functionals.

Density Functional	$E_{\text{AFM}} - E_{\text{NM}}$
LDA [Ceperley and Alder, 1980]	−8
PBE [Perdew et al., 1996a]	−89
PBEsol [Perdew et al., 2008]	−64
PW91 [Perdew and Wang, 1992]	−27
revPBE [Zhang and Yang, 1998]	−94

### 5.3.3 Methodology

Our calculations were performed under the gradient-corrected, spin-orbit inclusive, semilocal density-functional theory formalism. The energy cutoff for the plane wave basis set is set to 500 eV. The integration over the Brillouin zone is carried out with the equivalent of 12  $k$ -points per unit cell along each periodic direction. During the geometry optimizations, the in-plane lattice constants and interlayer spacing for the bilayer systems were constrained to their experimental values of 3.73 Å and 5.08 Å, respectively, while atomic coordinates were relaxed until each residual component on the Hellmann-Feynman forces was lower than 0.01 eV/Å. We model defective mono and bilayer PtSe<sub>2</sub> by introducing a single Pt vacancy in an otherwise pristine  $4 \times 4$  supercells containing 48 and 96 atoms, respectively. The adopted models host a  $V_{\text{Pt}}$  concentration of  $14 \times 10^{12} \text{ cm}^{-2}$ , very close to our experimental estimate of  $\sim 9 \times 10^{12} \text{ cm}^{-2}$ . A vacuum region 15 Å thick was introduced to separate the periodic images. All calculations were performed with VASP [Kresse and Hafner, 1993, Kresse and Furthmüller, 1996].

## 5.4 Conclusion

In summary, we have unraveled an unexpected magnetic response in both metallic and semiconducting films of PtSe<sub>2</sub>. As far as the metallic films are concerned, our electrical measurements show the existence of either ferromagnetic or anti-ferromagnetic ground state

orderings depending on the number of layers in this ultrathin material. The change in the device resistance upon application of a  $\sim 25$  mT magnetic field is as high as  $400\ \Omega$ , with a magnetoresistance value of 5%. Our first-principles calculations, along with transmission electron microscope imaging, suggest that surface magnetism induced by the presence of Pt vacancies and the RKKY exchange couplings across ultrathin films of  $\text{PtSe}_2$  are responsible for the observed layer-dependent magnetism. In contrast to recently discovered intrinsic ferromagnets [Burch et al., 2018, Gong and Zhang, 2019],  $\text{PtSe}_2$  has some key advantages for immediate research: it is stable without the need for an encapsulation process, it can be easily grown with various scalable methods, and readily isolated from its as-prepared substrate which makes it transferrable onto any arbitrary substrate. Compared to other, intrinsic metallic ferromagnets, however, the currently observed critical temperature in  $\text{PtSe}_2$  is small. We suggest that improvements can be achieved in future experiments by controlling *e.g.* the vacancy concentration (to increase the concentration and total magnitude of the resulting magnetic moment), the crystal thickness (to control the sign of the coupling and the switching fields as discussed above), and the Fermi energy (to modulate the density of states at the Fermi level). Concerning semiconducting  $\text{PtSe}_2$ , on the other hand, we have demonstrated that the defect-induced magnetism is preserved in the ultimate limit of thickness miniaturization. As the crystal is thinned down from bi- to mono-layer, we observe a ferromagnetic-to-antiferromagnetic crossover, a behavior which is opposite to the one observed in the prototypical 2D magnet  $\text{CrI}_3$  [Huang et al., 2017]. Furthermore, we show that graphene can be effectively used to probe the magnetization of semiconducting  $\text{PtSe}_2$  through the proximity effect.

Overall, contrary to the widespread assumption that defects in 2D materials are detrimental to the overall crystal quality, defect engineering could be the key approach for enriching their functionalities by inducing magnetism in air-stable materials. In the case of  $\text{PtSe}_2$ , combining this unexpected magnetism with unique thickness dependent properties could have several applications. For instance, atomically thin semiconducting  $\text{PtSe}_2$  could be exploited as a magnetic substrate for several proximity studies. On the other hand, thicker metallic  $\text{PtSe}_2$  could be integrated into lateral and vertical spin torque devices, tunneling magneto-resistance devices, and spin valve devices for generating spin-polarized charge carriers.





# **Understanding and Manipulating Magnetism in Monolayer CrI<sub>3</sub>**

## **Part II**



## 6 Magnetic Exchange Interactions in Monolayer $\text{CrI}_3$ from Many-Body Wavefunction Calculations

The marked interplay between the crystalline, electronic, and magnetic structure of atomically thin magnets has been regarded as the key feature for designing next-generation magneto-optoelectronic devices. In this respect, a detailed understanding of the microscopic interactions underlying the magnetic response of these crystals is of primary importance. Here, we combine model Hamiltonians with multi-reference configuration interaction wavefunctions to accurately determine the strength of the spin couplings in the prototypical single-layer magnet  $\text{CrI}_3$ . Our calculations identify the (ferromagnetic) Heisenberg exchange interaction  $J = -1.44$  meV as the dominant term, being the inter-site magnetic anisotropies substantially weaker. We also find that single-layer  $\text{CrI}_3$  features an out-of-plane easy axis ensuing from a single-ion anisotropy  $A = -0.10$  meV, and predict  $g$ -tensor in-plane components  $g_{xx} = g_{yy} = 1.90$  and out-of-plane component  $g_{zz} = 1.92$ . In addition, we assess the performance of a dozen widely used density functionals against our accurate correlated wavefunctions calculations and available experimental data, thereby establishing reference results for future first-principles investigations. Overall, our findings offer a firm theoretical ground to recent experimental observations.

This Chapter is adapted from:

M. Pizzochero, R. Yadav and O. V. Yazyev

*Magnetic Exchange Interactions in Monolayer  $\text{CrI}_3$  from Many-Body Wavefunction Calculations*  
2D Materials, in press (2020) [pre-print: arXiv:1911.12150]

My contribution to this work has been designing the project, performing density-functional calculations, analyzing the data, and writing the paper.

## **6.1 Motivation**

Down to the monolayer limit, CrI<sub>3</sub> consists of a honeycomb plane of Cr atoms sandwiched between two planes of I atoms, as shown in Fig. 6.1. Each Cr atom exhibits a six-fold coordination, which gives rise to edge-sharing octahedra. According to a purely ionic argument, the Cr atoms present a formal oxidation state of +3 and a resulting valence electron configuration  $3d^34s^0$ . As a consequence of the crystal field associated with the octahedral environment, a splitting of the  $d$  orbitals into three triply occupied  $t_{2g}$  states and two higher-energy empty  $e_g$  states occurs, the extent of which has not been ascertained yet and will be given in the following. However, on the basis of the Hund's rule, such an electron occupation yields  $S = 3/2$  [Lado and Fernández-Rossier, 2017]. This has been experimentally confirmed in single- and multi-layer CrI<sub>3</sub>, where a magnetization saturation of  $3 \mu_B$  per Cr<sup>3+</sup> ion has been observed [McGuire et al., 2015, Huang et al., 2017].

The scenario mentioned above qualitatively suggests that Cr<sup>3+</sup> ions act as magnetic centers, which interact *via* non-magnetic iodine ligands through the so-called super-exchange coupling theoretically proposed by P.W. Anderson [Anderson, 1950]. On the experimental side, the hysteretic features emerging in magneto-optical Kerr effect (MOKE) measurements of single-layer CrI<sub>3</sub> are the hallmarks of a ferromagnetic spin order [Huang et al., 2017], which, given the Cr-I-Cr bond angle of  $\sim 90^\circ$ , is consistent with the Goodenough-Kanamori rule [Goodenough, 1958, Kanamori, 1959]. Furthermore, such experimental investigations revealed that single-layer CrI<sub>3</sub> displays an out-of-plane easy axis and a critical temperature of 45 K, only slightly lower than its three-dimensional counterpart [Huang et al., 2017].

From the computational point of view, the accurate description of magnetic interactions in monolayer CrI<sub>3</sub> (and, in general, in solids) comes as a challenging task, mainly due to the inherent inadequacy of semilocal density functionals in properly capturing electron-electron interactions. Several approximations have been devised for describing localization effects (*e.g.* Hubbard-corrected or hybrid density functionals), but they invariably rely on adjustable parameters, which in turn are system- and property-dependent and cannot be determined following universal protocols. These limitations can effectively be overcome by relying on many-body wavefunctions, which, though computationally demanding, enable to recover a substantial amount of the correlation energy. In addition, we stress that the nature and strength of numerous magnetic interactions occurring in monolayers of CrI<sub>3</sub> yet remain largely unknown, and their determination is essential in order to provide a detailed comprehension of the intriguing spin physics hosted by this crystal. Here, we report on the first *ab initio* quantum chemistry investigation of magnetic interactions in two-dimensional CrI<sub>3</sub> by carrying out multi-reference configuration interaction calculations. We further exploit such benchmark results to assess the performances of several density-functional approximations. Overall, our work portrays an unprecedentedly accurate picture of the spin interactions in monolayer CrI<sub>3</sub>, which is instrumental in understanding its magnetic properties.

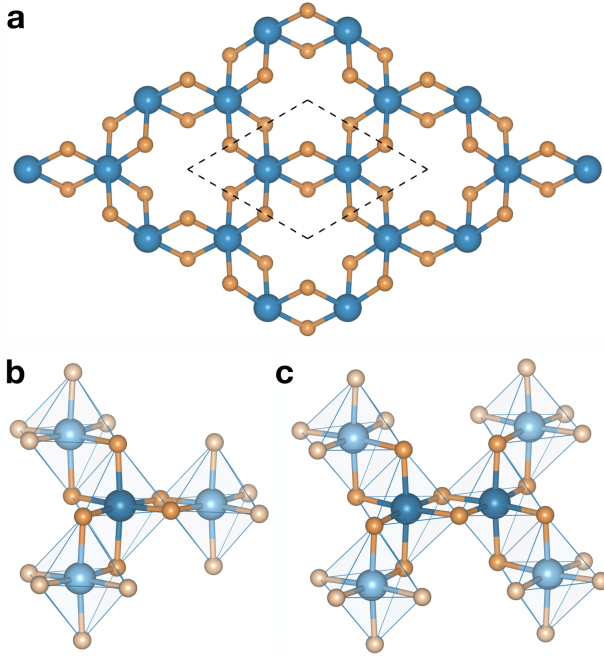


Figure 6.1 – (a) Crystal structure of single-layer  $\text{CrI}_3$ . Blue and orange balls represent chromium and iodine atoms, respectively. The unit cell is indicated with black dashed lines. (b) One-site and (c) two-site finite-size models adopted for the quantum chemistry calculations. The atoms shown in darker (lighter) colors are treated at the correlated (Hartree-Fock) level. The fragments are further embedded in a periodic array of point charges (not shown).

## 6.2 Results and dicussion

### 6.2.1 Spin Hamiltonian from many-body wavefunctions

We consider a generalized, bilinear model Hamiltonian, which captures intra- as well as inter-site exchange interactions between the  $i$ -th and  $j$ -th nearest-neighbor centers with spins  $\vec{S}_i$  and  $\vec{S}_j$ , respectively. Such a Hamiltonian reads

$$\mathcal{H} = J \sum_{i,j} \vec{S}_i \cdot \vec{S}_j + \sum_{i,j} \vec{S}_i \cdot \vec{\Gamma} \cdot \vec{S}_j + \sum_i A S_i^2 + \sum_i \mu_B \vec{B} \cdot \vec{g} \cdot \vec{S}_i + \sum_{i,j} \vec{D} \cdot \vec{S}_i \times \vec{S}_j \quad (6.1)$$

with  $J$  corresponding to the isotropic Heisenberg exchange,  $\vec{\Gamma}$  the symmetric anisotropic tensor,  $A$  the single-ion anisotropy parameters,  $\vec{g}$  the  $g$ -tensor in the Zeeman term that accounts for the interaction of the lattice with the external magnetic field  $\vec{B}$ , and  $\vec{D}$  the antisymmetric Dzyaloshinsky-Moriya interaction parameter. This latter term vanishes due to the  $C_{2h}$  point group of the  $\text{CrI}_3$  lattice and the ensuing inversion symmetry. Assuming a local Kitaev frame according to which the  $z$  axis is perpendicular to the  $\text{Cr}_2\text{I}_2$  plaquette for each Cr-Cr bond [Katukuri et al., 2014, Yadav et al., 2016, Yadav et al., 2018b],  $\vec{\Gamma}$  takes the form

$$\vec{\Gamma} = \begin{pmatrix} 0 & \Gamma_{xy} & -\Gamma_{yz} \\ \Gamma_{xy} & 0 & \Gamma_{yz} \\ -\Gamma_{yz} & \Gamma_{yz} & K \end{pmatrix} \quad (6.2)$$

with  $K$  being the Kitaev parameter.

In order to determine the magnetic interactions contained in Eq. (6.1), we perform many-body wavefunction calculations on carefully chosen embedded model systems. The models consist

## Chapter 6. Magnetic Exchange Interactions in Monolayer CrI<sub>3</sub> from Many-Body Wavefunction Calculations

Table 6.1 – Relative energies of the Cr<sup>3+</sup> 3d<sup>3</sup> multiplet structure obtained with the many-body wavefunction CASSCF and MRCI methods on finite-size model systems. Energies are given in eV.

3d <sup>3</sup> splitting	CASSCF	MRCI
<sup>4</sup> A <sub>2</sub> (t <sub>2g</sub> <sup>3</sup> e <sub>g</sub> <sup>0</sup> )	0.00	0.00
<sup>4</sup> T <sub>2</sub> (t <sub>2g</sub> <sup>2</sup> e <sub>g</sub> <sup>1</sup> )	1.48; 1.49; 1.49	1.62; 1.67; 1.67
<sup>2</sup> E(t <sub>2g</sub> <sup>1</sup> e <sub>g</sub> <sup>2</sup> )	2.34; 2.34	2.22; 2.22
<sup>4</sup> T <sub>2</sub> (t <sub>2g</sub> <sup>2</sup> e <sub>g</sub> <sup>1</sup> )	2.35; 2.42; 2.42	2.50; 2.58; 2.58
<sup>2</sup> T <sub>2</sub> (t <sub>2g</sub> <sup>1</sup> e <sub>g</sub> <sup>2</sup> )	2.45; 2.46; 2.46	2.33; 2.34; 2.34

of a central unit containing either one [Fig. 6.1(b)] or two [Fig. 6.1(c)] edge-sharing octahedra treated at the correlated level, surrounded by the nearest neighbor octahedra, the orbitals of which are frozen at the Hartree-Fock level. To ensure charge neutrality and mimic the periodic environment to which the finite-size model is subjected in the extended system, the fragment is embedded in an array of point charges fitted to reproduce the Madelung ionic potential of the crystalline lattice. We rely on the model shown in Fig. 6.1(b) and Fig. 6.1(c) to determine intra- and inter-site magnetic interactions, respectively. Electron correlation effects in the central unit are described at both the complete-active-space self-consistent-field (CASSCF) as well as multi-reference configuration interaction (MRCI) levels of theory [Helgaker et al., 2000], including spin-orbit interactions. As a first step, multi-configuration reference wavefunctions are constructed for an active space spanned by six electrons in six  $t_{2g}$  levels (that is, 3 at each Cr site). The orbitals are optimized for an average of low-lying septet, quintet, triplet, and singlet states. Next, MRCI calculations are performed including single and double excitations involving the  $d$  ( $t_{2g}$ ) valence shells of Cr<sup>3+</sup> ion and the  $p$  valence shells of the bridging I ligands [Helgaker et al., 2000]. We anticipate that, while inessential for the intra-site magnetic interactions, an MRCI treatment of the electron correlation is crucial to accurately determine the inter-site magnetic parameters due to the important role of the super-exchange coupling, being this effect neglected in the CASSCF wavefunctions. Finally, we quantify the nature and magnitude of the magnetic parameters in CrI<sub>3</sub> by mapping the resulting *ab initio* Hamiltonian onto the model Hamiltonian of Eq. (6.1) through the well-established procedure detailed in Ref. [Bogdanov et al., 2013].

Before moving to spin interactions, we elucidate the electronic structure of the magnetic centers in single-layer CrI<sub>3</sub>. The relative energies of the multiplet structure of the 3d<sup>3</sup> orbitals of the Cr<sup>3+</sup> ion are given in Table 6.1. As discussed above, according to the crystal-field theory, one should expect a singlet ground state for the Cr<sup>3+</sup> ion residing in an octahedral environment. This is confirmed by our correlated wavefunction calculations, which found <sup>4</sup>A<sub>2</sub>(t<sub>2g</sub><sup>3</sup>e<sub>g</sub><sup>0</sup>) to be the lowest-energy configuration. The higher-energy terms <sup>4</sup>T<sub>2</sub>(t<sub>2g</sub><sup>2</sup>e<sub>g</sub><sup>1</sup>) and <sup>2</sup>E(t<sub>2g</sub><sup>1</sup>e<sub>g</sub><sup>2</sup>) can interact with the <sup>4</sup>A<sub>2</sub>(t<sub>2g</sub><sup>3</sup>e<sub>g</sub><sup>0</sup>) ground state in the presence of spin-orbit coupling, inducing a zero-field splitting of the spin quartet into  $m_s = \pm 1/2$  and  $m_s = \pm 3/2$  Kramers doublets, respectively. Our CASSCF results obtained including all 3d orbitals at the Cr site in

the active space indicate that the  ${}^4T_2(t_{2g}^2 e_g^1)$  configuration lies 1.48 – 1.49 eV higher in energy than the  ${}^4A_2$  one. This quantity slightly increases to 1.62 – 1.67 eV at the MRCI level. We notice that the spin-orbit interactions affect the splittings given in Table 6.1 by only  $\sim 0.1$  meV.

The inter- and intra-site magnetic parameters of Eq. (6.1) obtained at both the CASSCF and MRCI levels are listed in Table 6.2. As far as the inter-site interactions are concerned, we find a dominant isotropic Heisenberg exchange  $J = -1.44$  meV, signaling a ferromagnetic ground state of single-layer  $\text{CrI}_3$ , in line with experimental observations [Huang et al., 2017] and earlier theoretical results. Indeed, this value lies in between those previously reported, which range from  $-1.10$  meV to  $-1.63$  meV [Lado and Fernández-Rossier, 2017, Xu et al., 2018a, Torelli and Olsen, 2018]. Such isotropic Heisenberg coupling largely exceeds the anisotropic exchange interactions, being the Kitaev parameter contributing only up to  $-0.08$  meV and off-diagonal anisotropic terms smaller than  $J$  by several orders of magnitude. This finding is at odds with the first-principles results of Ref. [Xu et al., 2018a], in which a Kitaev interaction of magnitude comparable to  $J$  was reported. It is worth noticing that the CASSCF method largely underestimates the inter-site exchange couplings, as compared to the MRCI method. This is especially true for the isotropic Heisenberg exchange, which at the CASSCF level is found to be 0.82 meV lower than that obtained at the MRCI level. This difference points towards (and, to some extent, quantifies) the significant role of the super-exchange channels between the  $\text{Cr}^{3+}$  ions occurring *via* the bridging I ligands in governing the magnetism of single-layer  $\text{CrI}_3$ .

We next discuss intra-site magnetic interactions. Even in the absence of magnetic field, the interplay between the spin-orbit coupling and the crystal field lifts the degeneracy of the electronic ground state for  $S > 1/2$ . The extent of such a zero-field splitting is quantified by the single-ion anisotropy. We derive this quantity by following the effective-Hamiltonian methodology presented in Ref. [Maurice et al., 2009]. In this approach, the mixing of the  ${}^4A_2$  components with the higher-energy states is treated in a perturbative manner, and the spin-orbit wavefunctions related to the high-spin  $t_{2g}^3$  configurations are projected onto the  ${}^4A_2$   $|S, M_s\rangle$  states. We then construct the effective Hamiltonian  $\tilde{H}_{\text{eff}} = \sum_k E_k |\tilde{\psi}_k\rangle \langle \tilde{\psi}_k|$ , where  $\tilde{\psi}_k$  are the ortho-normalized projections of the low-lying quartet wavefunctions with corresponding eigenvalues  $E_k$ . A one-to-one correspondence between  $\tilde{H}_{\text{eff}}$  and the model Hamiltonian  $\tilde{H}_{\text{mod}} = S \cdot \bar{A} \cdot S$  leads to the  $\bar{A}$  tensor, which, upon diagonalization, yields the commonly used axial parameter  $A$  [Maurice et al., 2009]. We obtain  $A = -0.10$  meV, with the magnetic axis lying in the direction normal to the lattice plane. The negative sign of  $A$  indicates that the easy axis of magnetization points along the magnetic axis, in accord with experiments [Huang et al., 2017]. We remark that this value is less than half than that obtained in Ref. [Xu et al., 2018a] by means of density functional theory.

Finally, we quantify the response of the Cr sites to the external magnetic field  $\vec{B}$  through the determination of the  $g$ -tensor appearing in the Zeeman term of the spin Hamiltonian in Eq. (6.1). This quantity can readily be accessed in experiments, *i.e.* electron spin resonance measurements [Saiz et al., 2019]. From the quantum chemistry point of view, the multi-configuration wavefunctions are known to provide an accurate description of the spin-orbit multiplets. This allows one to evaluate the matrix elements of the total magnetic moment

## Chapter 6. Magnetic Exchange Interactions in Monolayer CrI<sub>3</sub> from Many-Body Wavefunction Calculations

Table 6.2 – Magnetic exchange coupling parameters in single-layer CrI<sub>3</sub>: isotropic Heisenberg magnetic exchange ( $J$ ), symmetric anisotropic ( $\Gamma_{xy}$ ,  $\Gamma_{yz}$ , and  $\Gamma_{zx}$ ), and Kitaev ( $K$ ) interactions along with single-ion anisotropy ( $A$ ) and the components of the  $g$ -tensor ( $g_{xx}$ ,  $g_{yy}$ ,  $g_{zz}$ ) calculated by means of CASSCF and MRCI methods.

Magnetic exchange coupling	CASSCF	MRCI
$J$ (meV)	-0.62	-1.44
$K$ (meV)	-0.01	-0.08
$\Gamma_{xy}$ (meV)	$-1.0 \times 10^{-3}$	$-2.3 \times 10^{-3}$
$\Gamma_{yz} = -\Gamma_{zx}$ (meV)	$-2.1 \times 10^{-4}$	$-1.2 \times 10^{-3}$
$A$ (meV)	-0.10	
$g_{xx} = g_{yy}$	1.90	
$g_{zz}$	1.92	

operator  $\hat{\mu} = -\mu_B(g_e\hat{S} + \hat{L})$  in the basis of the multiplet eigenstates, with  $\hat{L}$  and  $\hat{S}$  being the angular momentum and spin operators, whose expectation values are obtained for a given Cr site, and  $g_e$  being the free-electron Landé factor. The Zeeman Hamiltonian can be written in terms of total moment  $\mu$  as  $H_Z = -\hat{\mu} \cdot \vec{B}$ . In order to obtain the  $g$ -tensor, such  $H_Z$  is mapped onto the Zeeman model Hamiltonian presented in Eq. (6.1) through the well-established procedure devised in Refs. [Bolvin, 2006, Chibotaru and Ungur, 2012]. To this end, we rely on an active space that encompasses all the five  $d$  orbitals of Cr (with 3 electrons). We construct the initial wavefunction by averaging over the seven quartets and five doublets listed in Table 6.1. We find an anisotropic  $g$ -tensor, with  $g_{xx} = g_{yy} = 1.90$  and  $g_{zz} = 1.92$ , where the  $x = y$  ( $z$ ) axis lies in the (perpendicular to) the CrI<sub>3</sub> lattice plane.

### 6.2.2 Magnetic interactions from density functional theory

With the accurate many-body wavefunction results at hand, we are in a position to assess the performance of widely used exchange and correlation functionals in describing *selected* magnetic interactions occurring in single-layer CrI<sub>3</sub>. We address by means of first-principles calculations in a periodic setting the isotropic Heisenberg exchange  $J$ , the magnetic anisotropy  $E_{\text{MAE}}$ , and provide an estimate of the Curie temperature ( $T_C$ ), for which the experimental value (45 K) is available. Specifically, we climb the ladder of Density Functional Theory (DFT) by considering the local density approximation using the Ceperley and Alder (CA) parametrization [Ceperley and Alder, 1980], several flavors of the generalized gradient approximation (PBE [Perdew et al., 1996a], PBEsol [Perdew et al., 2008], PW91 [Perdew and Wang, 1992], revPBE [Zhang and Yang, 1998]) and its Hubbard-corrected extension DFT+ $U$  [Dudarev et al., 1998] (with  $1.0 \text{ eV} \leq U \leq 3.0 \text{ eV}$ ), some representative examples of meta generalized gradient approximations (SCAN [Sun et al., 2015], TPSS, and RTPSS [Sun et al., 2011]), and hybrid Fock-exchange/density-functionals, both in their plain (PBE0 [Perdew et al., 1996b]) and range-separated (HSE03 [Heyd et al., 2003] and HSE06 [Krukau et al., 2006]) formalisms.

The main finding of our MRCI investigation is that, among the inter-site interactions listed in



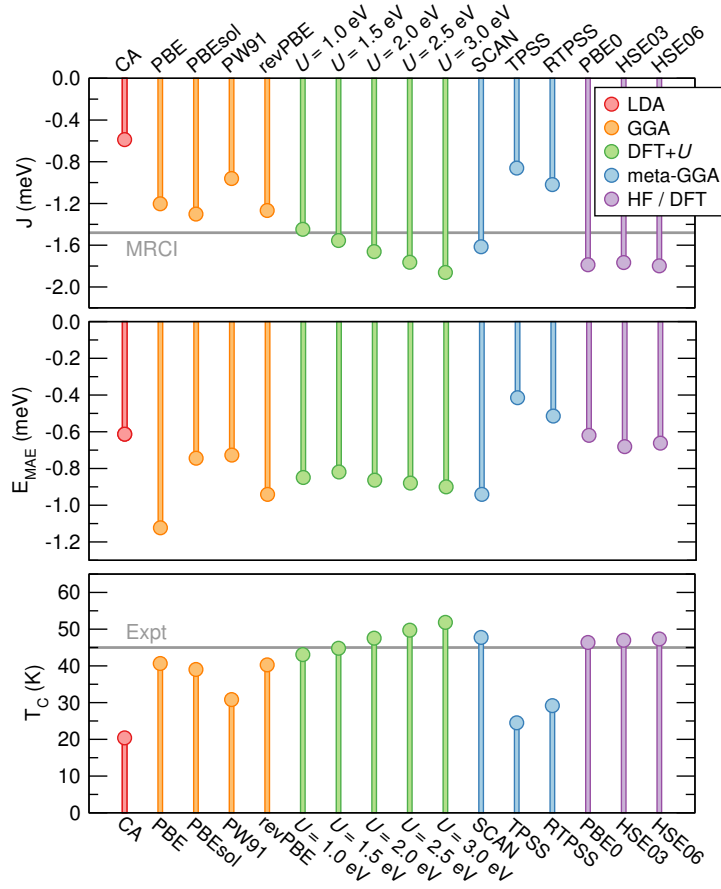


Figure 6.2 – Heisenberg exchange coupling ( $J$ ), magnetocrystalline anisotropy energy ( $E_{\text{MAE}}$ ), and Curie temperature ( $T_C$ ) of single-layer  $\text{CrI}_3$  as determined with several classes of density functionals on a periodic model system. Also shown as horizontal black lines are the value of  $J$  obtained upon mapping the MRCI Hamiltonian onto a pure Heisenberg Hamiltonian as well as the experimental Curie temperature.

Table 6.2, the dominant one is the Heisenberg exchange coupling. This indicates that single-layer  $\text{CrI}_3$  can effectively be described as an *isotropic* Heisenberg magnet. Hence, we map the first-principles results onto the isotropic Heisenberg spin Hamiltonian  $\mathcal{H} = J \sum_{i,j} \vec{S}_i \cdot \vec{S}_j$  by determining  $J$  according to the usual expression [Whangbo et al., 2003]

$$J = \frac{E_{\text{FM}} - E_{\text{AFM}}}{2N_{\text{nn}}S^2} \quad (6.3)$$

where  $E_{\text{FM}}$  ( $E_{\text{AFM}}$ ) is the total energy of the out-of-plane ferromagnetic (antiferromagnetic) phase and  $N_{\text{nn}}$  is the number of the nearest neighbors surrounding the magnetic site. In order to conduct a meaningful comparison between the many-body wavefunction and the density-functional results, we re-map the *ab initio* Hamiltonian onto the isotropic Heisenberg Hamiltonian. We obtain a benchmark value of  $J = -1.48$  meV at the MRCI level, only slightly larger than that obtained on the basis of Eq. (6.1).

The upper panel of Fig. 6.2 compares the values of  $J$  calculated with several density-functional approximations with our MRCI benchmark result. Notwithstanding their sharp differences in treating electron-electron interactions, all considered functionals provide a qualitative agreement with experiments, yielding a ferromagnetic ground state and an accompanying magnetic moment  $\mu = 3 \mu_B$  per  $\text{Cr}^{3+}$  ion [Huang et al., 2017, McGuire et al., 2015]. However,

## Chapter 6. Magnetic Exchange Interactions in Monolayer CrI<sub>3</sub> from Many-Body Wavefunction Calculations

the magnitude of  $J$  largely depends on the adopted approximation. For instance, both CA and (R)TPSS functionals severely underestimate the value of  $J$  when compared with the MRCI result, despite their marked dissimilarities in describing exchange and correlation effects. Though to a lesser extent, an underestimation is observed when adopting the generalized gradient approximations as well. Among the meta-GGA functionals considered here, only SCAN is seen to lead to a satisfactory agreement with the benchmark value. Surprisingly, all hybrid functionals overestimate  $J$  by  $\sim 20\%$ . The best agreement between DFT and MRCI results is achieved with the PBEsol, SCAN or DFT+ $U$  functionals – the latter matching the MRCI calculation upon the introduction of moderate values of Coulomb on-site repulsion (1.0 – 1.5 eV) – as they deviate from the benchmark value by less than 0.2 meV.

Next, we determine the magnetocrystalline anisotropy energy ( $E_{\text{MAE}}$ ) per formula unit as

$$E_{\text{MAE}} = \frac{E(\mu_{\perp}) - E(\mu_{\parallel})}{2} \quad (6.4)$$

with  $E(\mu_{\perp})$  and  $E(\mu_{\parallel})$  being the total energy of single-layer CrI<sub>3</sub>, with the magnetic moment  $\mu$  pointing towards the out-of-plane and in-plane direction, respectively. Our results are overviewed in the middle panel of Fig. 6.2. MOKE investigations revealed that single-layer CrI<sub>3</sub> features an out-of-plane axis, albeit the magnitude of  $E_{\text{MAE}}$  remains undetermined to date. Even though the results of our calculations appear to be spread over a quite broad interval depending on adopted the density-functional, for the ferromagnetic phase we obtain negative magnetocrystalline anisotropy energies irrespectively of the approximation considered. This finding lends support to MOKE observations [Huang et al., 2017], and is further consistent with our many-body wavefunction results concerning the single-ion anisotropy  $A$  and  $g$ -tensor (see Table 6.2). We then examine the spin orientation of the higher-energy antiferromagnetic phase. As compared to the stable ferromagnetic ordering, this configuration is found to exhibit an in-plane axis and a substantially lower magnetocrystalline anisotropy energy, being  $E_{\text{MAE}} = 0.39, 0.90$ , and  $0.70$  meV at the PBE, SCAN and HSE06 levels, respectively.

Finally, we address the Curie temperature of monolayer CrI<sub>3</sub> from first principles and compare the results of our calculations with the experimental value of 45 K. To this end, we rely on the formalism developed in Ref. [Torelli and Olsen, 2018], in which an analytic expression of  $T_C$  in the two-dimensional limit is derived on the basis of a fit to Monte Carlo results achieved on model lattices. In brief, this expression reads as

$$T_C = T_I f\left(\frac{\Delta}{J(2S-1)}\right) \quad (6.5)$$

where  $T_I$  is the critical temperature for the corresponding Ising model  $T_I = S^2 J \tilde{T}_C / k_B$  ( $\tilde{T}_C = 1.52$  in the case of honeycomb lattices),  $\Delta$  accounts for anisotropy parameters  $\Delta = A(2S-1) + BS N_{\text{nn}}$ , with  $A = (\Delta E_{\text{FM}} + \Delta E_{\text{AFM}})/2S^2$  and  $B = (\Delta E_{\text{FM}} - \Delta E_{\text{AFM}})/N_{\text{nn}} S^2$ , with  $\Delta E_{\text{FM}}$  ( $\Delta E_{\text{AFM}}$ ) being the differences in energy between the in-plane and out-of-plane spin configurations in the ferromagnetic (antiferromagnetic) state, and  $f$  is a function of the form  $f(x) = \tanh^{\frac{1}{4}} \left[ \frac{6}{N_{\text{nn}}} \log(1 + \gamma x) \right]$ , where  $\gamma = 0.033$ . Our results are shown in the lower panel of

Fig. 6.2. Similarly to the investigation of  $J$ , we observe that the value of the Curie temperature obtained at the CA and (R)TPSS levels is about halved as compared the experimental benchmark, while it is only slightly underestimated when adopting gradient-corrected functionals, with the exception of the PW91 case. Also, we notice a good performance of both SCAN and DFT+ $U$  functionals. Contrary to the case of  $J$ , however, we remark that hybrid functionals yield an excellent agreement with the experimental  $T_C$ , differing only by  $\sim 2$  K. We suggest that the reason for this traces back to the favorable compensation between the overestimated  $J$  and the underestimated  $E_{\text{MAE}}$ , as both these quantities enter Eq. (6.5). As DFT+ $U$  and SCAN density functionals lead to a superior description of both the Heisenberg exchange coupling and the Curie temperature, it is likely that the resulting magnetocrystalline anisotropy energies should be reliable as well. Hence, we anticipate a  $E_{\text{MAE}} \approx -0.87$  meV for ferromagnetic single-layer  $\text{CrI}_3$ .

### 6.3 Conclusion

In summary, we have combined CASSCF and MRCI calculations with model Hamiltonians to quantify the spin interactions in two-dimensional  $\text{CrI}_3$ . We have found that the inter-site magnetic interactions are primarily dictated by the ferromagnetic Heisenberg exchange coupling  $J = -1.44$  meV, as inter-site magnetic anisotropies  $\tilde{\Gamma}$  play a practically negligible role. Furthermore, our calculations indicate that single-layer  $\text{CrI}_3$  features an out-of-plane easy axis, as confirmed by the determination of single-ion anisotropy  $A = -0.10$  meV,  $g$ -tensor  $g_{xx} = g_{yy} = 1.90$  and  $g_{zz} = 1.92$ , as well as first-principles calculations of the magnetocrystalline anisotropy energy. In addition, we have assessed the performance of various flavors of popular density functionals against our accurate MRCI calculations and available experimental data, and found that DFT+ $U$  (with  $U = 1.0 - 1.5$  eV) and SCAN functionals show an excellent description of exchange interactions. Overall, our work provides firm theoretical ground to recent experimental observations, unveils the magnitude of several magnetic interactions, and establishes reference results for future DFT studies, thereby offering a comprehensive picture of the microscopic spin physics in monolayer  $\text{CrI}_3$ .

### 6.4 Methodology

Many-body wavefunction calculations on finite-size model systems have been carried out with the help of MOLPRO quantum chemistry package [Werner et al., 2012]. For the two-site calculations, all-electron basis functions of quadruple-zeta quality were used for the  $\text{Cr}^{3+}$  ions [Balabanov and Peterson, 2005] in the central unit while the bridging I ligands were described with energy-consistent relativistic pseudopotentials along with quintuple-zeta quality basis sets for their valence shells [Peterson et al., 2006]. The remaining I atoms in the two-octahedra central region were treated with energy-consistent relativistic pseudopotentials along with triple-zeta quality basis sets [Peterson et al., 2006].  $\text{Cr}^{3+}$  ions belonging to the octahedra adjacent to the reference unit were described as closed-shell  $\text{Co}^{3+} t_{2g}^6$  ions, using all-electron triple-zeta basis functions [Balabanov and Peterson, 2005], while for the I ligands belonging

## Chapter 6. Magnetic Exchange Interactions in Monolayer CrI<sub>3</sub> from Many-Body Wavefunction Calculations

---

to these adjacent octahedra which are not shared with the central unit we relied on energy-consistent relativistic pseudopotentials along with double-zeta quality basis sets [Peterson et al., 2006]. As a first step, CASSCF calculations [Helgaker et al., 2000] were carried out for an average of one septet, quintet, triplet, and singlet states, essentially of  $t_{2g}^3 - t_{2g}^3$  character. Since CASSCF calculations also account for super-exchange processes of  $t_{2g}^4 - t_{2g}^2$  type in addition the  $t_{2g}^3 - t_{2g}^3$  direct exchange between nearest neighbors, the corresponding wavefunctions encodes a finite-weight contribution from inter-site excitations of  $t_{2g}^4 - t_{2g}^2$  type. With the CASSCF wavefunctions at hand, we next accounted for single and double excitations from the Cr  $d$  ( $t_{2g}$ ) and bridging I  $p$  valence orbitals through MRCI calculations. One septet, quintet, triplet, and singlet states were considered in the spin-orbit treatment, in both CASSCF and MRCI calculations. Finally, the resulting quantum chemistry total energies associated with one septet, one quintet, one triplet, and one singlet along with their corresponding wavefunctions were mapped onto the effective spin Hamiltonian given in Eq. (6.1) using the procedure detailed in Ref. [Bogdanov et al., 2013]. This involves all sixteen spin-orbit states associated with the different possible couplings between the two nearest neighbors spins. In the case of the one-site calculations, all-electron basis functions of quadruple-zeta quality were used for the Cr<sup>3+</sup> ion [Balabanov and Peterson, 2005] in the reference unit while the I ligands were described using energy-consistent relativistic pseudopotentials along with quadruple-zeta quality basis sets for their valence shells [Peterson et al., 2006]. The transition metal and ligand sites in the nearest-neighbor octahedral units were described analogously to the case of two-site calculations discussed above. The  $g$ -factors and  $A$  were obtained using the wavefunctions optimized for an average of low-lying seven quartets and five doublet states at the CASSCF level.

Density-functional calculations on periodic models have been carried out with the Vienna *Ab Initio* Simulation Package (VASP) [Kresse and Hafner, 1993, Kresse and Furthmüller, 1996]. Spin-orbit coupling was included in all calculations in a self-consistent manner. Electron-core interactions are described with the projector-augmented wave method, while the Kohn-Sham wavefunctions for the valence electrons were expanded in a plane wave basis with a cutoff on the kinetic energy of 500 eV. Integration over the first Brillouin zone was carried out using a mesh of  $15 \times 15$   $k$ -points for all the adopted exchange and correlation functionals but the hybrid ones, where a reduced mesh of  $8 \times 8$   $k$ -points was used. DFT+ $U$  calculations were performed on top of the PBE functional, introducing an increasing amount of Coulomb on-site repulsion  $U$  on the  $d$  shell of Cr atoms following the rotationally invariant scheme proposed by Dudarev [Dudarev et al., 1998]. For each functional and magnetic configuration, we performed geometry optimization by relaxing the atomic coordinates until the maximum component of the Hellmann-Feynman forces was smaller than 0.005 eV/Å while constraining the lattice constant to the experimental value of 6.867 Å. For hybrid functional and quantum chemistry calculations, we rely on the atomic models relaxed at the GGA level. A vacuum region 17 Å thick is included to avoid artificial interactions between periodic images.

## 7 Inducing Magnetic Phase Transitions in Monolayer $\text{CrI}_3$ *via* Lattice Deformations

Atomically thin films of layered chromium triiodide ( $\text{CrI}_3$ ) have recently been regarded as suitable candidates to a wide spectrum of technologically relevant applications, mainly owing to the opportunity they offer to achieve a reversible transition between coexisting in-plane ferro- and out-of-plane antiferro-magnetic orders. However, no routes for inducing such a transition have been designed down to the single-layer limit. Here, we address the magnetic response of monolayer  $\text{CrI}_3$  to in-plane lattice deformations through a combination of isotropic Heisenberg spin Hamiltonians and first-principles calculations. Depending on the magnitude and orientation of the lattice strain exerted, we unveil a series of direction-dependent parallel-to-antiparallel spins crossovers, which yield the emergence of ferromagnetic, Néel antiferromagnetic, zigzag and stripy antiferromagnetic ground states. Additionally, we identify a critical point in the magnetic phase diagram whereby the exchange couplings vanish and the magnetism is quenched. Our work establishes guidelines for extensively tailoring the spin interactions in monolayer  $\text{CrI}_3$  *via* strain engineering, and further expands the magnetically ordered phases which can be hosted in a two-dimensional crystal.

This Chapter is adapted from:

M. Pizzochero & O. V. Yazyev

*Inducing Magnetic Phase Transitions in Monolayer  $\text{CrI}_3$  via Lattice Deformations*

The Journal of Physical Chemistry C 124, 7585 (2020)

My contribution to this work has been designing the project, performing all first-principles calculations, analyzing the data, and writing the paper.

## **7.1 Motivation**

Within the constantly expanding family of two-dimensional magnets, semiconducting thin films of CrI<sub>3</sub> are arguably the most prototypical members. They exhibit a layered crystal structure, in which Cr atoms are located at the corners of in-plane honeycomb networks and reside in edge-sharing octahedra formed by I atoms [McGuire et al., 2015]. As far as the magnetism is concerned, each Cr<sup>3+</sup> ion features effective spin 3/2 [Lado and Fernández-Rossier, 2017], which interacts with neighboring sites through intra-layer (inter-layer) ferromagnetic (antiferromagnetic) exchange couplings, as pinpointed by the evolution of the thickness-dependent hysteretic features reported in recent MOKE experiments [Huang et al., 2017]. The competition between ferro- and antiferro-magnetic couplings in bi- and few-layer CrI<sub>3</sub> allows one to switch between these two phases, thereby tailoring the nature of the magnetic ground state. This has been experimentally accomplished through a broad variety of different techniques, including electrostatic gating [Huang et al., 2018], doping [Jiang et al., 2018a], applied external pressure [Song et al., 2019, Li et al., 2019], off-plane lattice deformations [Thiel et al., 2019], or adjusting the stacking patterns of the layers [Sivadas et al., 2018, Ubrig et al., 2019]. Such an extensive control over the magnetism in atomically thin CrI<sub>3</sub> holds promise for the realization of novel ultrathin magnetoelectronic devices [Wang et al., 2018, Song et al., 2018, Klein et al., 2018].

Down to the single-layer limit, however, the lack of antiferromagnetic interactions across the crystal hinders the realization of any magnetic order other than the ferromagnetic one. In this Chapter, we theoretically investigate the effect of in-plane lattice deformations on the magnetism of monolayer CrI<sub>3</sub>. We unveil a series of magnetic phase transitions arising from the competition between symmetry inequivalent Heisenberg exchange couplings in the distorted lattice, which gives rise to both antiferromagnetic and ferrimagnetic orders, along with a non-magnetic phase. Overall, our findings provide useful guidelines for modulating the magnetic properties of CrI<sub>3</sub> down to the ultimate limit of atomic thickness through strain engineering.

## **7.2 Methodology**

Our first-principles calculations are performed within the spin-polarized Density Functional Theory (DFT) framework, as implemented in VASP [Kresse and Hafner, 1993, Kresse and Furthmüller, 1996]. We adopt the generalized gradient approximation devised by Perdew, Burke and Ernzerhof [Perdew et al., 1996a], and further include a Hubbard correction  $U = 1.5$  eV on the  $d$  orbitals of Cr atoms [Dudarev et al., 1998]. Such an exchange-correlation density functional ensures an excellent description of magnetic properties of monolayer CrI<sub>3</sub> when compared to benchmark multireference wavefunction results [Pizzochero et al., 2020] and available experimental data [Huang et al., 2017, Torelli and Olsen, 2018]. The cutoff on the kinetic energy is set to 400 eV and the Brillouin zone is sampled with a  $12 \times 12$   $k$ -mesh. We determine the exchange couplings between a pair of magnetic Cr<sup>3+</sup> sites through the well-established four-state method for energy mapping analysis detailed in Refs. [Xiang et al., 2011, Xiang et al., 2013]. This approach allows one to determine the exchange coupling between a

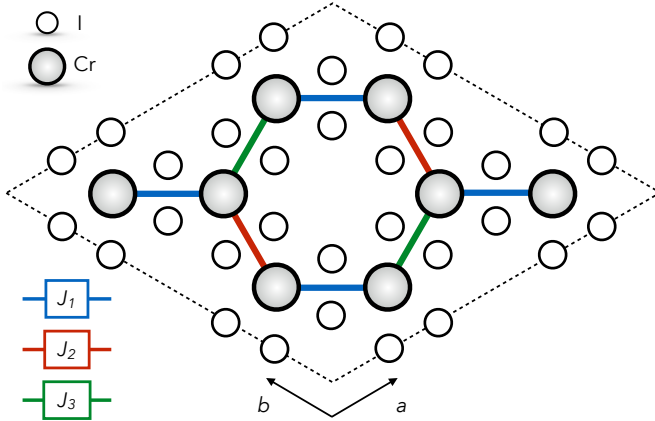


Figure 7.1 – Atomic structure of monolayer  $\text{CrI}_3$ , with white and grey circles representing chromium and iodine atoms, respectively. The  $2 \times 2$  supercell considered in our calculations is indicated with black dashed lines. The three symmetry inequivalent exchange couplings  $J_1$ ,  $J_2$ , and  $J_3$  between  $\text{Cr}^{3+}$  ions are indicated with blue, red, and green solid lines, respectively.

pair of sites without introducing any arbitrary choice on the magnetic configurations of the supercells. For each spin configuration, we optimized the atomic coordinates until the residual Hellmann-Feynman forces acting on each atom converge to  $0.005 \text{ meV/\AA}$ . In order to properly account for all the relevant exchange couplings between the nearest neighbors in the distorted lattice, we consider an atomic model of monolayer  $\text{CrI}_3$  consisting of a  $2 \times 2$  hexagonal supercell containing 32 atoms. For the calculation of the exchange couplings between the second- and third-nearest neighbors, on the other hand, we adopt a  $3 \times 3$  hexagonal supercell containing 72 atoms.

### 7.3 Results and discussion

We start by describing magnetic interactions in unstrained monolayer  $\text{CrI}_3$ . According to our previous quantum chemistry investigation [Pizzochero et al., 2020], the isotropic exchange coupling exceeds inter-site anisotropies in  $\text{CrI}_3$  by several orders of magnitude. This indicates that the *isotropic* Heisenberg Hamiltonian  $\mathcal{H}$  which couples the  $i$ -th and  $j$ -th sites carrying  $S_i$  and  $S_j$  spins, respectively, is a suitable spin model for the description of the magnetic exchange interactions in monolayer  $\text{CrI}_3$  [Lado and Fernández-Rossier, 2017, Pizzochero et al., 2020]. Such a Hamiltonian reads as

$$\mathcal{H} = \frac{J}{2} \sum_{\langle i,j \rangle} \vec{S}_i \cdot \vec{S}_j + \frac{J'}{2} \sum_{\langle\langle i,j \rangle\rangle} \vec{S}_i \cdot \vec{S}_j + \frac{J''}{2} \sum_{\langle\langle\langle i,j \rangle\rangle\rangle} \vec{S}_i \cdot \vec{S}_j \quad (7.1)$$

with  $J$ ,  $J'$  and  $J''$  being the Heisenberg exchange couplings between nearest, second-nearest, and third-nearest neighbors sites. We determine  $J$ ,  $J'$  and  $J''$  to be  $-1.53 \text{ meV}$ ,  $-0.38 \text{ meV}$ , and  $-0.01 \text{ meV}$ , respectively. In line with earlier calculations [Torelli and Olsen, 2018], we note that the inter-site interactions are primarily dictated by the nearest neighbors exchange coupling  $J$ , as the next-nearest neighbors couplings  $J'$  and  $J''$  are substantially weaker and further feature the same sign, thereby ruling out any possible competition between  $J$ ,  $J'$ , and  $J''$  in determining the magnetic ground state. Hence, in the following we restrict our description to

## Chapter 7. Inducing Magnetic Phase Transitions in Monolayer CrI<sub>3</sub> *via* Lattice Deformations

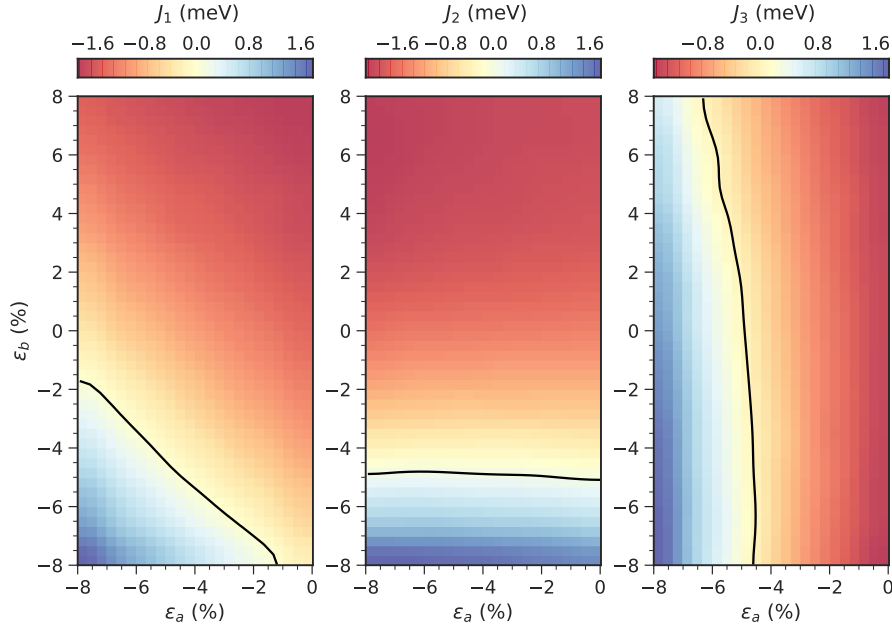


Figure 7.2 – Evolution of  $J_1$  (left panel),  $J_2$  (middle panel), and  $J_3$  (right panel) with the in-plane  $\epsilon_a$  and  $\epsilon_b$  lattice deformations in monolayer CrI<sub>3</sub>. The exchange couplings are defined according to Fig. 7.1. The black lines indicate the boundaries between positive and negative couplings, corresponding to bond-dependent parallel-to-antiparallel spins transitions. The raw data have been smoothed with cubic polynomials for visualization purposes.

nearest neighbors couplings only ( $J' = J'' = 0$  meV), according to which Eq. (7.1) boils down to

$$\mathcal{H} = \frac{J}{2} \sum_{\langle i,j \rangle} \vec{S}_i \cdot \vec{S}_j \quad (7.2)$$

We systematically investigate the effect of lattice deformations on single-layer CrI<sub>3</sub> by introducing in-plane lattice strain along both the  $a$  and  $b$  directions shown in Fig. 7.1. We quantify the relative amount of strain along each direction as  $\epsilon_a = (a - a_0)/a_0$  and  $\epsilon_b = (b - b_0)/b_0$ , with  $a_0 = b_0$  being the experimental equilibrium lattice constant of 13.734 Å in the adopted  $2 \times 2$  supercell. We span an interval of lattice strain  $\epsilon_a = [-8\%, 0\%]$  and  $\epsilon_b = [-8\%, +8\%]$  through a  $9 \times 17$  grid. Upon the introduction of an anisotropic strain (that is,  $\epsilon_a \neq \epsilon_b$ ), the honeycomb lattice on which the Cr<sup>3+</sup> ions reside is subjected to a non-symmetric distortion, which gives rise to the formation of the three inequivalent bonds between the nearest spin-3/2 centers. Such a symmetry breaking, in turn, requires the introduction of three distinct Heisenberg exchange couplings  $J_1$ ,  $J_2$ , and  $J_3$  (see Fig. 7.1) in order to establish the nature of the magnetic ground state. It is clear that these bond-dependent couplings become equivalent by symmetry ( $J_1 = J_2 = J_3$ ) in either the unstrained ( $\epsilon_a = \epsilon_b = 0$ ) or biaxially strained ( $\epsilon_a = \epsilon_b \neq 0$ ) lattice. Overall, the determination of  $J_1$ ,  $J_2$ , and  $J_3$  within the strain grid mentioned above requires over 1800 calculations.

The response of  $J_1$ ,  $J_2$ , and  $J_3$  to lattice deformations is presented in Fig. 7.2. While the strain



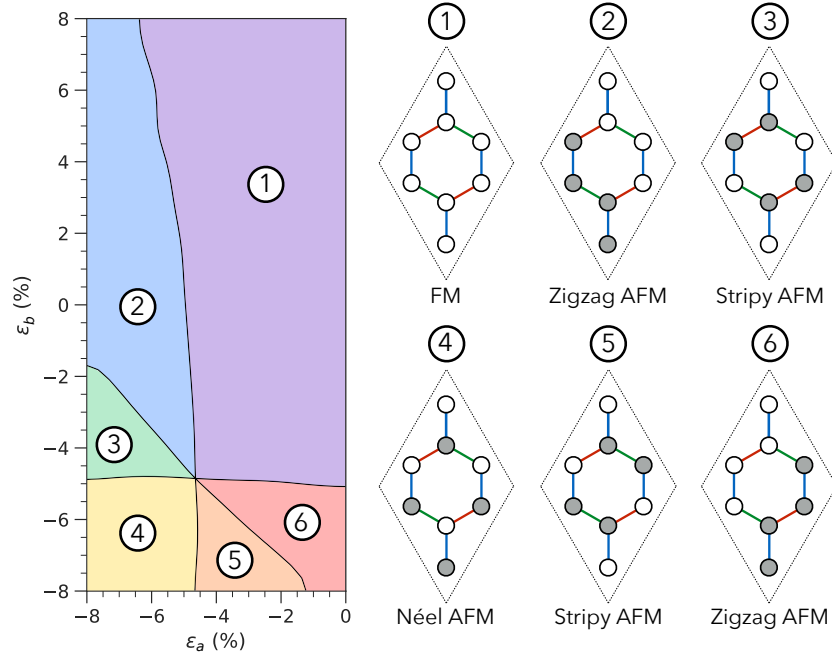


Figure 7.3 – Magnetic phase diagram of monolayer  $\text{CrI}_3$  under in-plane lattice deformations. The spin configurations emerging in the honeycomb network are also shown, with white and black circles representing  $\text{Cr}^{3+}$  ions carrying opposite magnetic moments. Bonds between  $\text{Cr}^{3+}$  ions are color-coded according to Fig. 7.1. Dashed lines indicate the unit cell.

exerted does not affect the of the local magnetic moments carried by the  $\text{Cr}^{3+}$  ions, it is found to have a strong influence on the magnitude and sign of the exchange couplings. On the one hand, tensile strain lowers all of them, hence further strengthening the ferromagnetic phase. On the other hand, lattice compressions are found to increase  $J_1$ ,  $J_2$ , and  $J_3$  and eventually revert their signs, thereby promoting a bond-dependent parallel-to-antiparallel spins transition. Indeed, the amount and direction of the lattice strain which is necessary to promote such a transition largely differ for the three couplings. Specifically, our calculations indicate that an antiparallel orientation of the spins along each pair of  $\text{Cr}^{3+}$  ions occurs at  $(\epsilon_a \lesssim -1.5\%; \epsilon_b \lesssim -1.5\%)$ ,  $(\epsilon_b \lesssim -5\%)$ , and  $(\epsilon_a \lesssim -4.5\%)$  for  $J_1$ ,  $J_2$ , and  $J_3$ , respectively.

Such a pronounced competition between the three Heisenberg exchange couplings induces the emergence of a strain-dependent magnetic ground state in monolayer  $\text{CrI}_3$ . Indeed, six distinct domains can be distinguished in the space spanned by the lattice strain, depending on the (relative) signs of  $J_1$ ,  $J_2$ , and  $J_3$ . The magnetic phase diagram of strained  $\text{CrI}_3$ , along with the spin configurations which are realized upon lattice deformations, are shown Fig. 7.3. In Domains ① and ④, all the exchange couplings feature the same sign, yielding a ferromagnetic or Néel antiferromagnetic ground state, respectively, whereas the other regions exhibit a ferrimagnetic ground state whereby the equality  $\text{sgn}(J_1) = \text{sgn}(J_2) = \text{sgn}(J_3)$  does not hold. Specifically, Domains ② and ⑥ enclose the zigzag antiferromagnetic state, where two exchange couplings are positive and one is negative. An opposite situation, in which two couplings are negative and only one is positive, is observed in Domains ③ and ⑤,

## Chapter 7. Inducing Magnetic Phase Transitions in Monolayer $\text{CrI}_3$ *via* Lattice Deformations

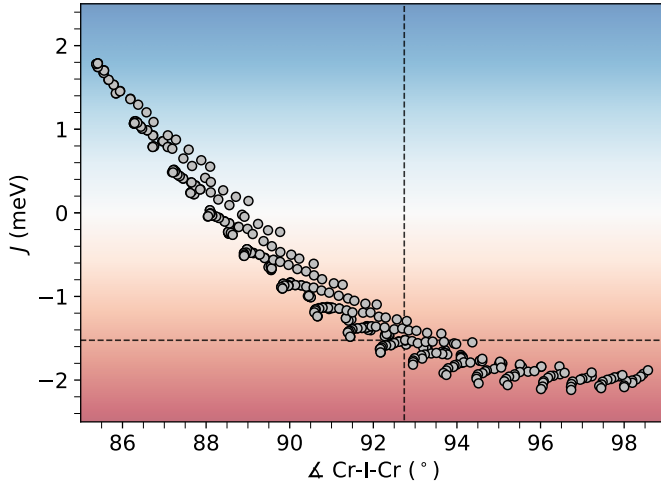


Figure 7.4 – Exchange couplings ( $J$ ) as a function of the metal-ligand-metal bond angle ( $\angle\text{Cr-I-Cr}$ ) in monolayer  $\text{CrI}_3$ . Dashed lines mark the equilibrium values in unstrained  $\text{CrI}_3$ . Background shaded in red and blue colors marks positive and negative values of  $J$ , respectively, indicating a ferromagnetic and antiferromagnetic interaction between nearest-neighbors  $\text{Cr}^{3+}$  ions, respectively.

therefore giving rise to a stripy antiferromagnetic state. It is worth noting that these magnetic phases can be realized within a relatively narrow interval of lattice strain of  $\sim 5\%$  in magnitude – provided that the direction along which the deformation occurs is carefully controlled – thereby highlighting a marked interplay between lattice deformations and magnetic exchange couplings in monolayer  $\text{CrI}_3$ . Indeed, the six strain-induced magnetic transitions encompass all the possible magnetically ordered phases which can be realized on a honeycomb lattice.

Importantly, we remark that the phase diagram shown in Fig. 7.3 displays a singularity located at  $\epsilon_a \approx \epsilon_b \approx -5\%$ . This corresponds to the point in which the domain boundaries intersect, leading to  $J_1 \approx J_2 \approx J_3 \approx 0$ . According to the adopted isotropic Heisenberg spin Hamiltonian, such a critical point signals the absence of any magnetic order. The strain-induced quenching of the isotropic exchange couplings may be exploited to single out the otherwise negligible anisotropic exchange couplings in monolayer  $\text{CrI}_3$  [Pizzochero et al., 2020]. This is of particular interest in the context of Kitaev physics [Kitaev, 2006], which emerges when a large Kitaev-to-Heisenberg coupling ratio is achieved. In our previous work [Pizzochero et al., 2020], we have quantified the Kitaev parameter  $K$  in unstrained monolayer  $\text{CrI}_3$  to be  $-0.08$  meV, resulting in a practically negligible  $K/J$  ratio of 0.06. Under appropriate strain conditions ( $\epsilon_a \approx \epsilon_b \approx -5\%$ ), however, we suggest that the  $K/J$  ratio can be enhanced to a great extent, hence driving monolayer  $\text{CrI}_3$  in the Kitaev spin-liquid phase, provided that  $K$  remains non-vanishing. Indeed, a recent quantum chemistry investigation has demonstrated that compressive biaxial strain substantially increases the magnitude of the ferromagnetic Kitaev coupling in several honeycomb lattices [Yadav et al., 2018a].

Finally, we briefly comment on the dependence of the exchange couplings on the crystal structure. According to the rule proposed by Goodenough [Goodenough, 1958] and Kanamori [Kanamori, 1959], the sign of the exchange coupling in superexchange-dominated magnetic lattices is mainly governed by the metal-ligand-metal angle. Specifically, depending on whether such an angle is close to either  $90^\circ$  or  $180^\circ$ , a parallel or antiparallel spin orientation has to be expected, respectively. Unstrained  $\text{CrI}_3$  complies with this rule [Lado and Fernández-Rossier, 2017], as the bond angle  $\angle\text{Cr-I-Cr} \approx 90^\circ$  is accompanied by  $J < 0$ . In Fig. 7.4,

we present the dependence of the 459 isotropic exchange couplings calculated in this work on the  $\angle\text{Cr-I-Cr}$ . We observe that a ferro- to antiferro-magnetic crossover occurs when the bond angle takes values which are lower than  $88^\circ$ . This is at odds with the Goodenough-Kanamori rule, according to which such a crossover should instead take place when approaching the  $180^\circ$  limit. Overall, our results indicate that the Goodenough-Kanamori rule is not an appropriate guideline to rationalize the magnetism of monolayer  $\text{CrI}_3$  subjected to lattice deformations.

## 7.4 Conclusion

In summary, we have combined model spin Hamiltonians with DFT+ $U$  calculations to address the magnetic response of monolayer  $\text{CrI}_3$  to in-plane lattice deformations. We revealed that, depending on the magnitude and the direction along which the mechanical strain is applied, the ferromagnetic ground state can be driven into either the Néel antiferromagnetic or ferrimagnetic phases, these latter including both stripy and zigzag spin configurations. We identified a critical point emerging at the intersection between the magnetic phase boundaries in the strain space whereby the isotropic Heisenberg exchange couplings vanish, hence quenching any magnetically ordered phase and possibly conferring a central role to the otherwise weak inter-site anisotropies. To conclude, our findings open new viable routes for extensively engineering the magnetism of  $\text{CrI}_3$  through lattice strain down to the ultimate limit of thickness miniaturization.



## 8 Atomic-Scale Defects in the Two-Dimensional Ferromagnet CrI<sub>3</sub> from First Principles

The family of atomically thin magnets holds great promise for a number of prospective applications in magneto-optoelectronics, with CrI<sub>3</sub> arguably being its most prototypical member. However, the formation of defects in this system remains unexplored to date. Here, we investigate native point defects in monolayer CrI<sub>3</sub> by means of first-principles calculations. We consider a large set of intrinsic impurities and address their atomic structure, thermodynamic stability, diffusion and aggregation tendencies as well as local magnetic moments. Under thermodynamic equilibrium, the most stable defects are found to be either Cr or I atomic vacancies along with their complexes, depending on the chemical potential conditions. These defects are predicted to be quite mobile at room and growth temperatures, and to exhibit a strong tendency to agglomerate. In addition, our calculations indicate that deviations from the nominal stoichiometry largely impact the magnetic moments, and the defect-induced lattice distortions can drive local ferromagnetic-to-antiferromagnetic phase transitions. Overall, this work portrays a comprehensive picture of intrinsic point defects in monolayer CrI<sub>3</sub> from a theoretical perspective.

This Chapter is adapted from:

M. Pizzochero

*Atomic-Scale Defects in the Two-Dimensional Ferromagnet CrI<sub>3</sub> from First Principles*

Journal of Physics D: Applied Physics, in press (2019)

DOI: <https://doi.org/10.1088/1361-6463/ab7ca3>

*Invited Article, Special Issue on 2D and Layered Magnetic Materials*

My contribution to this work has been designing the project, performing all first-principles calculations, analyzing the data, and writing the paper.

### 8.1 Motivation

Under thermodynamic equilibrium conditions, the entropic contribution to the overall free energy of a solid is responsible for the ubiquitous presence of defects at finite temperatures. Although disorder often affects the properties of materials in a detrimental manner, in many cases the incorporation of a certain amount of impurities has proven instrumental in expanding the functionalities of the hosting system. This is especially true in ultrathin crystals, where the reduced dimensionality of the lattice enhances the impact of imperfections [Jiang et al., 2019, Susi et al., 2017], as it has been demonstrated *e.g.* for elemental monolayers like graphene [Banhart et al., 2011, Yazyev and Helm, 2007, Bonfanti et al., 2018, Nair et al., 2012, González-Herrero et al., 2016], silicene [Liu et al., 2016a, Pizzochero et al., 2016, Qiu et al., 2015] or phosphorene [Pei et al., 2016, Sharma et al., 2018], as well as transition metal dichalcogenides [Lin et al., 2016, Li et al., 2016a, Pizzochero and Yazyev, 2017, Pizzochero and Yazyev, 2018, Pedramrazi et al., 2019, Avsar et al., 2019]. However, the role of defects in atomically thin magnets remains entirely unexplored to date.

In the following, we investigate the formation of intrinsic defects in monolayer CrI<sub>3</sub> by means of first-principles calculations. We address the atomic structure, thermodynamic stability, diffusion and aggregation tendencies along with the defect-induced magnetic moments of a large set of native impurities, including vacancy, adatom, self-interstitial and antisite defects. Overall, this work offers a theoretical insight into defects formation in monolayer CrI<sub>3</sub> and further lays the foundation for defect engineering in this prototypical two-dimensional magnet.

### 8.2 Methodology

Our first-principles calculations are performed within the spin-polarized density functional theory formalism, as implemented in the the Vienna *Ab Initio* Simulation Package (VASP) [Kresse and Hafner, 1993, Kresse and Furthmüller, 1996]. The exchange and correlation effects are treated under the generalized gradient approximation devised by Perdew, Burke, and Ernzerhof (PBE) [Perdew et al., 1996a]. In the case of pristine and defective supercells of CrI<sub>3</sub>, this functional is supplemented with an on-site Coulomb repulsion term  $U = 1.5$  eV acting on the  $d$  shell of Cr atoms [Dudarev et al., 1998]. The resulting PBE+ $U$  density functional was shown to provide an excellent description of the magnetic properties of monolayer CrI<sub>3</sub>, as demonstrated by the comparison with higher-level many-body wavefunction results and available experimental data [Pizzochero et al., 2020, Huang et al., 2017, Torelli and Olsen, 2018].

Electron-core interactions are described through the projector-augmented wave method, while the Kohn-Sham wavefunctions for the valence electrons are expanded in a plane wave basis with a cutoff on the kinetic energy of 400 eV. The integration over the first Brillouin zone is carried out using the equivalent of  $12 \times 12$   $k$ -points per unit cell. The atomic coordinates are optimized until the maximum component of the Hellmann-Feynman forces are smaller than 0.02 eV/Å, while constraining the lattice constant to the experimental value of 6.867

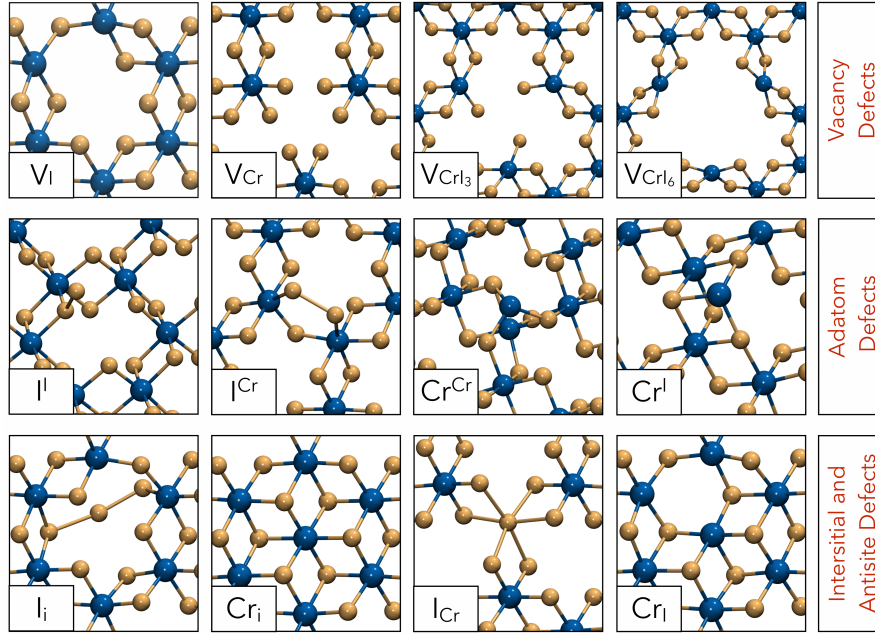


Figure 8.1 – Atomic structure of the point defects in monolayer  $\text{CrI}_3$  considered in this work. Blue and orange balls represent Cr and I atoms, respectively.

Å. The saddle points for the determination of the energy barriers are located with the help of the climbing-image nudged elastic band method [Henkelman et al., 2000]. Specifically, we have optimized under the appropriate constraints the intermediate image between the initial and the final states until forces converged to  $0.04 \text{ eV}/\text{\AA}$ . Similarly to our previous work [Pizzochero et al., 2020], magnetic exchange interactions have been calculated following the well-established four-state method for energy-mapping analysis [Xiang et al., 2013, Xiang et al., 2011]. We model defective lattices by introducing point defects in otherwise pristine  $4 \times 4$  hexagonal supercells of monolayer  $\text{CrI}_3$  containing 128 atoms. A vacuum region  $17 \text{ \AA}$  thick is included to avoid artificial interactions between periodic replicas.

### 8.3 Results and discussion

We start by examining the stability of native defects in monolayer  $\text{CrI}_3$ . We consider a broad set of different point defects, the atomic structure of which is shown in Fig. 8.1. The investigated defects belong to three classes, namely (i) vacancy defects, including atomic vacancies ( $V_I$  or  $V_{Cr}$ ) along with their complexes  $V_{CrI_3}$  and  $V_{CrI_6}$ , (ii) adatom defects, consisting of excess atoms located on top of either chromium ( $I^{Cr}$  and  $Cr^{Cr}$ ) or iodine lattice site ( $I^I$  and  $Cr^I$ ), and (iii) antisite ( $Cr_I$  and  $I_{Cr}$ ) or self-interstitial ( $Cr_i$  and  $I_i$ ) defects, depending on whether the extra Cr and I atoms are sitting in an occupied or unoccupied site, respectively.

Under thermodynamic equilibrium, the quantity of primary interest in governing the relative stability of defects is their formation energy ( $E_{\text{form}}$ ). Given that  $\text{CrI}_3$  is a binary system, in most cases the introduction of intrinsic defects is accompanied by a deviation from the nominal

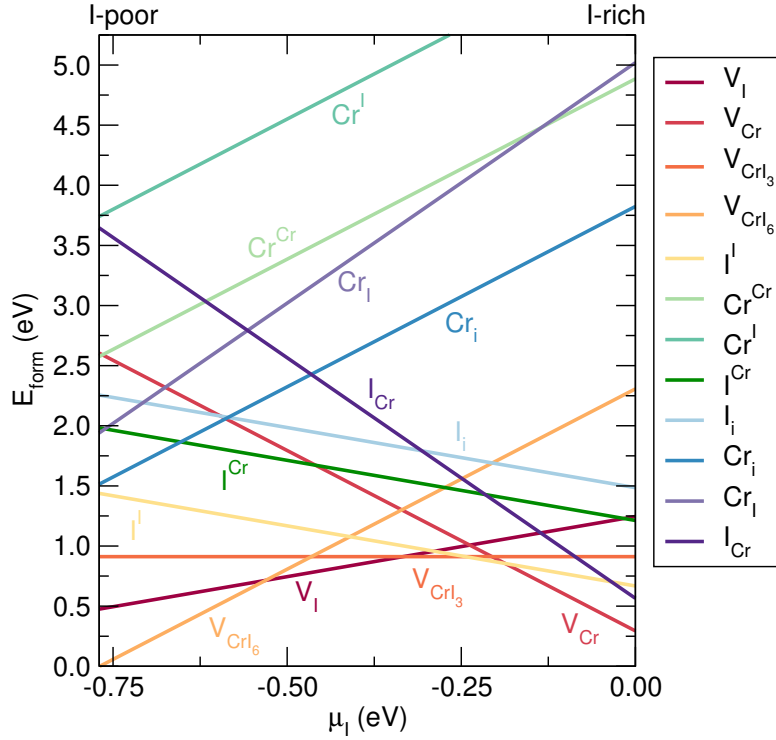


Figure 8.2 – Formation energy ( $E_{\text{form}}$ ) of the point defects shown in Fig. 8.1 as a function of the iodine chemical potential ( $\mu_{\text{I}}$ ).

stoichiometry, thereby rendering  $E_{\text{form}}$  dependent on chemical potentials of the constituent elements. For charge-neutral defects at zero Kelvin and standard pressure, the formation energy takes the form

$$E_{\text{form}}(\mu) = E_{\text{defect}} - E_{\text{host}} - \sum_i n_i \mu_i \quad (8.1)$$

with  $E_{\text{defect}}$  and  $E_{\text{host}}$  being the total energies of the defective and pristine supercell, respectively,  $n_i$  the number of atoms that one has to add to or remove from the lattice in order to create the defect, and  $\mu_i$  the corresponding chemical potential. As is customary, we assume that Cr and I are in thermal equilibrium with monolayer CrI<sub>3</sub> through to the expression

$$\mu_{\text{CrI}_3} = \mu_{\text{Cr}} + 3\mu_{\text{I}}. \quad (8.2)$$

The relevant interval of chemical potential in which defect formation energies are physically meaningful spans the energy range in which monolayer CrI<sub>3</sub> remains stable against the decomposition into its elemental constituents. These are taken to be the lowest-energy phases of these chemical elements, namely the bcc Cr crystal and the isolated I<sub>2</sub> molecule. Within this formalism, the range of stability of monolayer CrI<sub>3</sub> is  $-0.77 \text{ eV} < \mu_{\text{I}} < 0 \text{ eV}$ .

In Fig. 8.2, we overview the formation energy of the point defects shown in Fig. 8.1 as a function of the I chemical potential. Although the relative stability of the defects is largely ruled by the chemical potential, our calculations reveal that either atomic vacancies or their complexes



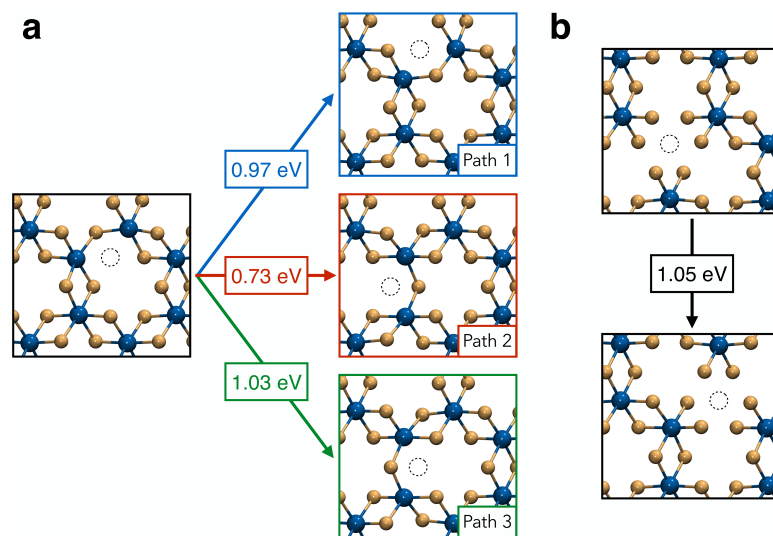


Figure 8.3 – Energy barriers to diffuse to neighboring sites for (a) I and (b) Cr vacancy defects. The defect site is marked with a black dashed circle.

exhibit the lowest formation energies. Specifically, I-rich conditions promote the formation of  $V_{Cr}$  and  $V_{CrI_3}$  defects, whereas I-poor conditions enhance the stability of  $V_I$  and  $V_{CrI_6}$  ones. This result demonstrates that, when thermodynamic equilibrium prevails, monolayer  $CrI_3$  is likely to exhibit a sub-stoichiometric composition.

As far as the metastable defects are concerned, we found that I adatoms display lower formation energies than Cr adatoms over the entire range of chemical potential. However, while the binding of an extra I atom on top of an I site is more stable than on top of a Cr site by 0.55 eV, the opposite behavior is observed for an extra Cr atom, being  $Cr^{Cr}$  lower in energy than  $Cr^I$  by 1.15 eV. Differently from adatom defects, the relative stability of self-interstitials is dominated by the chemical potential conditions. In fact, the  $I_I$  defect remains the most stable self-interstitial defect only under I-rich conditions, as approaching I-poor conditions stabilizes the formation of the  $Cr_I$  defect. It is worth noticing that, while excess I atoms incorporate into monolayer  $CrI_3$  as adatom defects (*i.e.*,  $I^I$  is more stable than  $I_I$  by 0.82 eV), excess Cr atoms should instead be accommodated in the lattice as self-interstitials (*i.e.*,  $Cr_I$  is more stable than  $Cr^{Cr}$  by 1.06 eV). The relative stability of antisites is also governed by chemical potential conditions, as I-rich (I-poor) conditions stabilize the  $I_{Cr}$  ( $Cr_I$ ) defect. We notice that the formation energy of both the antisite defects considered is larger than the sum of the formation energy of an isolated vacancy and an isolated adatom by 0.40 eV and 0.05 eV for  $I_{Cr}$  and  $Cr_I$  defects, respectively. This indicates that vacant sites enhance the reactivity of the lattice as compared to the pristine areas of the monolayer.

We now turn our attention to the mobility of atomic vacancies. As we discussed above, these defects exhibit the lowest formation energy in a quite broad range of chemical potential and further constitutes the building blocks for the also stable vacancy complexes  $V_{CrI_3}$  and  $V_{CrI_6}$ . In Fig. 8.3(a), we give the energy barriers for a  $V_I$  to diffuse to the three nearest neighboring

## Chapter 8. Atomic-Scale Defects in the Two-Dimensional Ferromagnet CrI<sub>3</sub> from First Principles

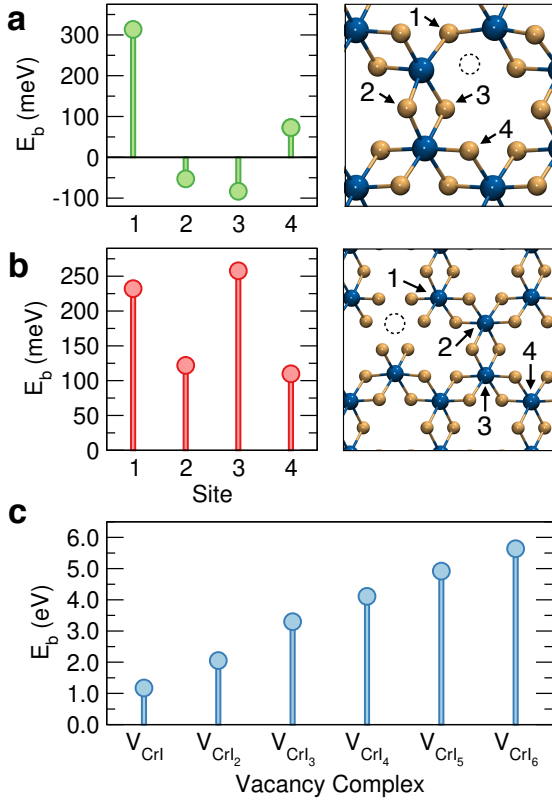


Figure 8.4 – Agglomeration energy ( $E_b$ ) of a pair of (a) I and (b) Cr vacancy defects. The site at which the first vacancy is located is indicated with a black dashed circle. (c) Agglomeration energy of vacancy complexes  $V_{CrI_x}$ , with  $x = 1, 2, \dots, 6$ .

I sites. Specifically, we consider diffusion processes to either the I atom bridging the same (path 1) or the nearest (paths 2 and 3) pair of Cr atoms between which  $V_I$  is introduced. We found that  $V_I$  features a diffusion barrier in the 0.73 – 1.03 eV range, depending on the path considered, with path 2 being the most energetically favorable. Furthermore, we determine the energy barrier for a  $V_{Cr}$  defect to diffuse to the nearest equivalent to be 1.05 eV, as we show in Fig. 8.3(b). We estimate the diffusion coefficient  $D$  of vacancy defects as

$$D = d^2 \nu \exp \left[ -\frac{E_{\text{barr}}}{k_B T} \right] \quad (8.3)$$

with  $E_{\text{barr}}$  being the energy barrier for vacancy defects to diffuse (see Fig. 8.3),  $T$  the considered temperature,  $k_B$  the Boltzmann constant,  $d$  the hopping distance and  $\nu$  the vibrational frequency, typically in the order of  $10^{12} \text{ s}^{-1}$ . Notice that, in the above expression, a negligible change in entropy between the initial and the transition states is assumed. At  $T = 300 \text{ K}$ , we find  $D \approx 10^{-15} \text{ cm}^2 \text{ s}^{-1}$  for  $V_I$  (along the favorable path 2) and  $D \approx 10^{-21} \text{ cm}^2 \text{ s}^{-1}$  for  $V_{Cr}$ . These diffusion coefficients increase to  $D \approx 10^{-11} \text{ cm}^2 \text{ s}^{-1}$  and  $D \approx 10^{-15} \text{ cm}^2 \text{ s}^{-1}$ , respectively, at  $T = 450 \text{ K}$ , *i.e.* the temperature at which molecular-beam epitaxy experiments are carried out [Li et al., 2020a], hence indicating a certain degree of mobility of these defects under epitaxial growth conditions.

Next, we investigate the tendency of vacancy defects to aggregate. To this end, we quantify the agglomeration energy  $E_b$  of a given defect complex  $AB$ , formed upon clustering of the

Table 8.1 – Difference in local magnetic moments between pristine and defective monolayers  $\text{CrI}_3$  ( $\Delta\mu$ ), the latter hosting the point defects shown in Fig. 8.1.

Point Defect	$\Delta\mu$ ( $\mu_B$ )	Point Defect	$\Delta\mu$ ( $\mu_B$ )
$V_I$	1.00	$\text{Cr}^{\text{Cr}}$	6.00
$V_{\text{Cr}}$	−6.00	$\text{Cr}^{\text{I}}$	6.00
$V_{\text{CrI}_3}$	−3.00	$\text{Cr}_i$	1.00
$V_{\text{CrI}_6}$	0.00	$I_i$	6.00
$I^{\text{I}}$	1.00	$I_{\text{Cr}}$	−5.00
$I^{\text{Cr}}$	1.00	$\text{Cr}_I$	7.00

otherwise spatially separated  $A$  and  $B$  defects, by comparing their formation energies as

$$E_b = E_{\text{form}}(A) + E_{\text{form}}(B) - E_{\text{form}}(AB). \quad (8.4)$$

According to this expression, positive (negative) values of  $E_b$  point towards an energetically favorable (unfavorable) tendency of defects to aggregate. In Figs. 8.4(a) and (b), we show the agglomeration energies to form a secondary vacancy defect at several lattice sites neighboring the first missing atom. For the I divacancies case shown in Fig. 8.4(a), we find that, depending on the site considered, the introduction of a secondary  $V_I$  can be either energetically favorable (sites 1 and 4) or unfavorable (sites 2 and 3), with the agglomeration energy attaining its maximum upon formation of a secondary I vacancy at site 1. This is in contrast with the formation of a second  $V_{\text{Cr}}$  shown in Fig. 8.4(b), whereby  $E_b$  remains positive at all sites investigated. In particular, we observe that the formation of a Cr divacancy defect is more stable when involving two Cr atoms bridged by the same pair of I ligands (that is, sites 1 and 3).

In order to understand the stability of the vacancy complexes  $V_{\text{CrI}_3}$  and  $V_{\text{CrI}_6}$ , we calculate their agglomeration energy with respect to isolated Cr and I vacancies. Specifically, we remove an increasing amount of I atoms residing in the first coordination shell of a  $V_{\text{Cr}}$  defect, therefore giving rise to a family of  $V_{\text{CrI}_x}$  defects, with  $x = 1, 2, \dots, 6$ . Our results are given in Fig. 8.4(c). For all considered  $V_{\text{CrI}_x}$  complexes, we find a substantial aggregation tendency, with  $E_b$  in the of 1 – 6 eV energy interval and monotonically increasing by  $\sim 1$  eV for each subsequent I atom removed. These values are at least one order of magnitude larger than those found for I and Cr divacancies. We suggest that such a marked tendency of I vacancies to agglomerate around a  $V_{\text{Cr}}$  defect is at the origin of the thermodynamic stability of  $V_{\text{CrI}_3}$  and  $V_{\text{CrI}_6}$  observed in Fig. 8.2.

Finally, we discuss the effect of point defects on the magnetism of  $\text{CrI}_3$ . Table 8.1 lists the difference in magnetic moments between pristine (*i.e.*,  $3 \mu_B$  per  $\text{Cr}^{3+}$  ion, in accord with experiments [Huang et al., 2017]) and defective lattice, this latter hosting the defects shown in Fig. 8.1. Remarkably, we notice that all defects but  $V_{\text{CrI}_6}$  affect the magnetism of monolayer  $\text{CrI}_3$ , thereby suggesting that deviations from the nominal stoichiometry are likely to be accompanied by an alteration of the local magnetic moments. Specifically,  $V_I$  and  $V_{\text{Cr}}$  defects lead to a  $\Delta\mu$  of  $-1.00 \mu_B$  and  $6.00 \mu_B$ , respectively, while the  $\Delta\mu$  associated with the  $V_{\text{CrI}_3}$  complex is  $-3.00 \mu_B$ . Excess Cr or I atoms, whether as adatom or self-interstitial defects,

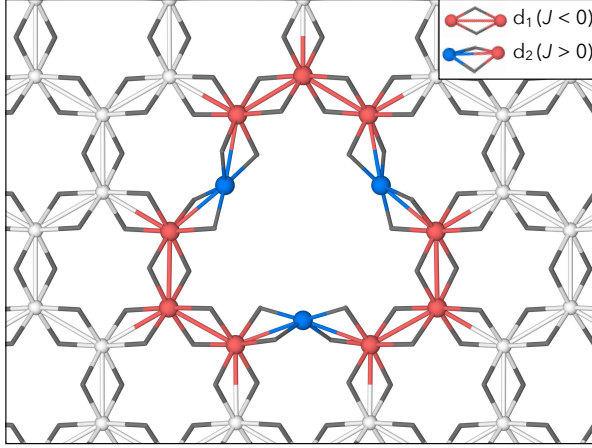


Figure 8.5 – Atomic and magnetic structure of the  $V_{\text{CrI}_6}$  defect in monolayer  $\text{CrI}_3$ . Blue and red balls represent Cr sites carrying opposite magnetic moments. Also given are the  $d_1$  and  $d_2$  bonds in the vicinity of the defect, along which a ferromagnetic and antiferromagnetic coupling is predicted, respectively.

change the intrinsic magnetic moments by  $6.00 \mu_B$  and  $1.00 \mu_B$ , respectively, while antisite  $\text{I}_{\text{Cr}}$  ( $\text{Cr}_\text{I}$ ) defect induces a larger  $\Delta\mu$  of  $-5.00 \mu_B$  ( $7.00 \mu_B$ ).

Point defects lead to local distortions of the atomic structure of monolayer  $\text{CrI}_3$ , possibly affecting the magnetic exchange interactions in their vicinity. In a recent work [Pizzochero and Yazyev, 2020], it has been shown that lattice deformations can modulate the magnetic ground state of monolayer  $\text{CrI}_3$  to a large extent, with a ferro-to-antiferromagnetic crossover taking place upon the reduction of the Cr-I-Cr bond angle below  $\sim 88^\circ$ . Among the thermodynamically stable defects which form in monolayer  $\text{CrI}_3$  (see Fig. 8.2),  $V_{\text{CrI}_6}$  is the one inducing the most substantial lattice distortion. Indeed, it gives rise to two structurally inequivalent Cr-Cr bonds, which correspond to the  $d_1$  (with  $d_{\text{Cr-Cr}} = 3.92 \text{ \AA}$  and  $\angle \text{Cr-I-Cr} = 92^\circ$ ) and  $d_2$  (with  $d_{\text{Cr-Cr}} = 3.69 \text{ \AA}$  and  $\angle \text{Cr-I-Cr} = 85^\circ$ ) bonds schematically depicted in Fig. 8.5. These structural parameters have to be compared with those of pristine  $\text{CrI}_3$ , *i.e.*  $d_{\text{Cr-Cr}} = 3.96 \text{ \AA}$  and  $\angle \text{Cr-I-Cr} = 93^\circ$ , for which a Heisenberg exchange coupling  $J = -1.44 \text{ meV}$  has been reported [Pizzochero et al., 2020].

We assess the role of  $V_{\text{CrI}_6}$  defect and the ensuing local distortion of the atomic structure on the magnetism of monolayer  $\text{CrI}_3$  by determining the Heisenberg exchange couplings along the two inequivalent Cr-Cr bonds. While the exchange coupling associated with the  $d_1$  bond ( $J = -1.34 \text{ meV}$ ) is found to be almost unchanged w.r.t. the pristine monolayer, a weak and antiferromagnetic coupling ( $J = 0.08 \text{ meV}$ ) emerges along the  $d_2$  bond, hence revealing a local magnetic-phase transition driven by the defect-induced lattice distortion. Overall, this finding paves the way towards defect-engineering of monolayer  $\text{CrI}_3$ , in which antiferromagnetic domains embedded in a ferromagnetic matrix may be realized through structural deformations caused by impurities [Wang et al., 2020].

## 8.4 Conclusion

In summary, we have carried out extensive first-principles calculations to investigate the formation of native defects in the prototypical two-dimensional magnet  $\text{CrI}_3$ . Depending

on the chemical potential conditions, we have identified mobile  $V_I$  and  $V_{Cr}$  species along with their complexes  $V_{CrI_3}$  and  $V_{CrI_6}$  as the most stable defects, these latter emerging as a consequence of the strong agglomeration tendency. Our results indicate that, under thermodynamic equilibrium, monolayer  $CrI_3$  should exhibit a sub-stoichiometric nature, which in turn is found to affect the magnetic moments and Heisenberg exchange couplings locally. To conclude, our findings pinpoint a marked intertwining between atomic-scale disorder and magnetism in monolayer  $CrI_3$ .



# Revisiting Two *Classics* in Chemistry

## Part III





## 9 Picture of the Wet Electron: A Localized Transient State in Liquid Water

A transient state of the excess electron in liquid water preceding the development of the solvation shell, the so-called wet electron, has been invoked to explain spectroscopic observations, yet its binding energy and atomic structure have remained highly elusive. Here, we carry out hybrid functional molecular dynamics to unveil the ultrafast solvation mechanism leading to the hydrated electron. In the pre-hydrated regime, the electron is found to repeatedly switch between a *quasi*-free electron state in the conduction band and a localized state with a binding energy of 0.26 eV, which we assign to the wet electron. This transient state self-traps in a region of the liquid which extends up to  $\sim 4.5$  Å and involves a severe disruption of the hydrogen-bond network. Our picture provides an unprecedented view on the nature of the wet electron, which is instrumental to understand the properties of this fundamental species in liquid water.

This Chapter is adapted from:

M. Pizzochero, F. Ambrosio and A. Pasquarello

*Picture of the Wet Electron: A Localized Transient State in Liquid Water*

Chemical Science 10, 7442 (2019)

My contribution to this work has been performing first-principles and molecular dynamics calculations, analyzing the data, and writing the paper.

### 9.1 Motivation

Since its very first discovery more than fifty years ago [Hart and Boag, 1962], the hydrated electron has been the focus of a seamless and intensive experimental [Schwarz, 1991, Tauber and Mathies, 2003, Paik et al., 2004, Emde et al., 1998, Silva et al., 1998, Bragg et al., 2004] and theoretical [Ambrosio et al., 2017, Uhlig et al., 2012, Turi, 2015, Marsalek et al., 2012, Boero et al., 2003, Rossky and Schnitker, 1988, Larsen et al., 2010, Turi and Madarász, 2011, Larsen et al., 2011] research effort. Besides the fundamental interest in understanding the response of liquid water to an excess charge, this species is relevant to numerous applications, including its role, *e.g.* as a reducing agent in synthetic chemistry or in inducing mutagenic lesions in DNA [Herbert and Coons, 2017, Siefertmann and Abel, 2011]. It is now well-established that, under thermodynamic equilibrium conditions, the hydrated electron is accommodated in a *quasi*-spherical electrophilic cavity with a radius of  $\sim 1.8$  Å formed upon the re-arrangement of about five water molecules [Ambrosio et al., 2017, Turi and Rossky, 2012, Wilhelm et al., 2019, Holden et al., 2019]. It occupies a *s*-like ground state within the band gap of the solvent [Herbert and Coons, 2017, Tang et al., 2010], from which it can be excited to *p*-like states through optical transitions of  $\sim 1.7$  eV [Hart and Boag, 1962]. Notwithstanding the large body of studies on the hydrated electron, the atomistic mechanism leading to its formation and the nature of its precursors have remained poorly understood.

On the experimental side, there is widespread consensus that two transient precursor states precede the formation of the hydrated electron, namely (i) the *quasi*-free electron and (ii) the wet electron [Nordlund et al., 2007, Migus et al., 1987, Long et al., 1990, Laenen et al., 2000]. The latter is a short-lived state, which is thought to form upon the trapping of the excess electron ( $e_{\text{aq}}$ ) at defective water molecule sites [Mozumder, 1988], likely where broken hydrogen bonds are present possibly due to thermal fluctuations of the solvent [Migus et al., 1987, Nordlund et al., 2007]. When the trapping is ineffective, the  $e_{\text{aq}}$  remains within the conduction states of the aqueous solvent, giving rise to a *quasi*-free electron delocalized over distances of  $\sim 40$  Å [Palianov et al., 2014, Savolainen et al., 2014]. Building on spectroscopic observations, the following dynamics for the formation of the hydrated electron have been tentatively invoked [Nordlund et al., 2007]. First, immediately after injection into liquid water,  $e_{\text{aq}}$  effectively acts as a *quasi*-free electron. Next, it traps at a broken hydrogen-bond site leading to the formation of the solvation shell of the equilibrated  $e_{\text{aq}}$ , with the entire process being accompanied by a continuous shrinking of the localization length [Savolainen et al., 2014]. Though plausible, this experimentally inferred mechanism remains vague and many issues need to be clarified. For instance, a thorough knowledge of the energetics and atomic structure of the wet electron is fully missing, including the degree of perturbation to the hydrogen-bond network required to trap the excess charge. In particular, it remains to be ascertained whether a "trap-seeking" or "trap-digging" mechanism is operative [Bartczak and Pernal, 2001], the latter being analogous to the self-trapping polaron. Moreover, it is an open question whether the wet electron steadily collapses into the hydrated one right after trapping [Nordlund et al., 2007], or rather undergoes a sequence of trapping and subsequent detrapping processes [Assel et al., 1999].

Earlier theoretical investigations did not succeed in distinguishing the two above mentioned

precursor species in bulk water and their interplay. Molecular dynamics simulations carried out on bulk water systems identified suitable trapping sites and further estimated their concentration and lifetime distributions [Turi et al., 2006, Bartczak and Pernal, 2001, Schnitker et al., 1986, Motakabbir and Rossky, 1989, Skorobogatiy et al., 2005]. However, the large number of molecules involved in such calculations required the use of simplified classical interactions, by which the electronic structure of the solvent is not explicitly accounted for. On the other hand, *ab initio* simulations are well-known to be routinely affordable only on a small number of molecules and have been used in this context to study the properties of the wet electron by attaching an extra charge to a small water cluster composed of very few molecules [Webster et al., 1991, Kim et al., 1996]. However, the minimal model adopted casts doubt on the extent to which it can be representative of the more complex bulk liquid water system.

Here, we perform *ab initio* molecular dynamics simulations of a realistic model of bulk water to elucidate the nature of the excess electron in the early stages of the solvation process. For the very first time, we determine its energy level and the accompanying structural features before the thermodynamic equilibrium is established. Overall, our findings shed new light on the elusive wet electron and offer an appealing theoretical picture to the interpretation of experimental observations.

## 9.2 Computational model

We model the excess electron in liquid water by adding one extra negative charge to a periodically repeated cubic cell containing 128 water molecules at the experimental density. The electronic structure is described through a hybrid functional that reproduces the experimental band gap of liquid water and partially suppresses the self-interaction error. The functional is supplemented with nonlocal van der Waals interactions, which ensure that the structural properties of liquid water and its mass density are properly reproduced. The adopted functional has been extensively benchmarked and successfully used in the case of the hydrated electron [Ambrosio et al., 2017]. Here, we perform adiabatic molecular dynamics simulations. This approach admittedly neglects electron scattering processes on the basis that the trapping of the wet electron has been measured to occur on the hundred femtosecond time scale [Migus et al., 1987], while the time of electron thermalization is estimated to be an order of magnitude faster, thus leading to an effective decoupling of the two physical processes [Mozumder, 1988]. Reported energy values correspond to averages between occupied and unoccupied single-particle energy levels, to ensure optimal compliance with the generalized Koopmans' theorem [Perdew et al., 1982].

## 9.3 Results

### 9.3.1 Energetics and dynamics of excess electrons

We monitor the molecular dynamics simulation of the extra electron by following the evolution in time of its energy level. For a representative trajectory, the first picosecond of the solvation

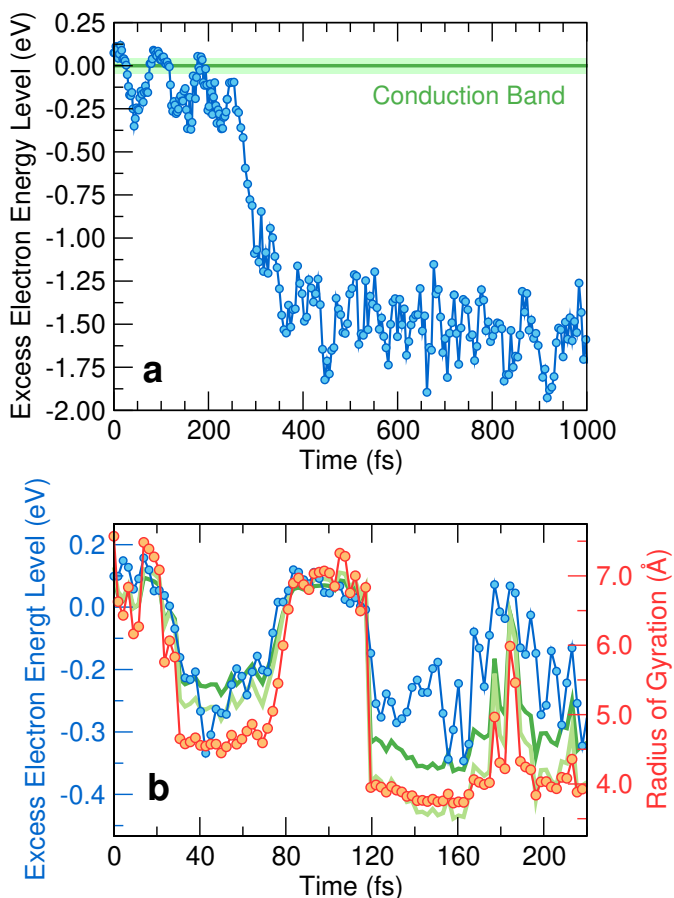


Figure 9.1 – (a) Time evolution of the energy level of the excess electron. The average of the conduction band minimum (horizontal green line) with the shaded area representing the standard deviation of its distribution has been obtained from a simulation of neat water. The energies are referred to this average value. (b) Magnification of the first 220 fs of the evolution together with the corresponding radius of gyration of the excess electron. Energy levels obtained from the particle-in-a-box and the hydrogen-like atom models proposed in Ref. [Jacobson and Herbert, 2011] are also shown as light and dark green lines, respectively.

dynamics is shown in Fig. 9.1(a). Because of the abrupt transition at 275 fs, two regimes can easily be distinguished in accord with experiment [Migus et al., 1987]. First, we identify the fully hydrated regime (after  $\sim 275$  fs), in which the one-particle level remains approximately constant and is pinned deep in the band gap of liquid water. The energy level at  $\sim -1.6$  eV in Fig. 9.1(a) can be reconciled with the experimental vertical ionization energy (VIE) at 3.2-3.6 eV [Tang et al., 2010, Shreve et al., 2010], considering the position of the conduction band w.r.t. the vacuum level ( $V_0 = -0.7$ -1.0 eV, [Ambrosio et al., 2017, Ambrosio et al., 2018]), the finite-size effect (0.7 eV, [Ambrosio et al., 2017]), and subsequent residual relaxation. In Fig. 9.2(a), we illustrate the relative charge density and recognize the well-known configuration of the hydrated electron consisting of a spherical-like distribution coordinated on average by five water molecules [Ambrosio et al., 2017]. Next, we focus on the pre-solvated regime (before  $\sim 275$  fs), in which the energy level of the excess electron oscillates in the vicinity of the continuum of the conduction states. In Fig. 9.2(b), the charge density in correspondence of the first minimum of the energy level (at  $\sim 40$  fs) is given. This is a trapped state in which the charge density is localized, albeit over an extended area which includes several water molecules. At variance, when the energy level occurs in the conduction band, the excess charge is found to be delocalized over the full simulation cell (not shown here). Overall, a picture emerges in which the hydrated  $e_{aq}$  is preceded by a pre-solvated regime with quite

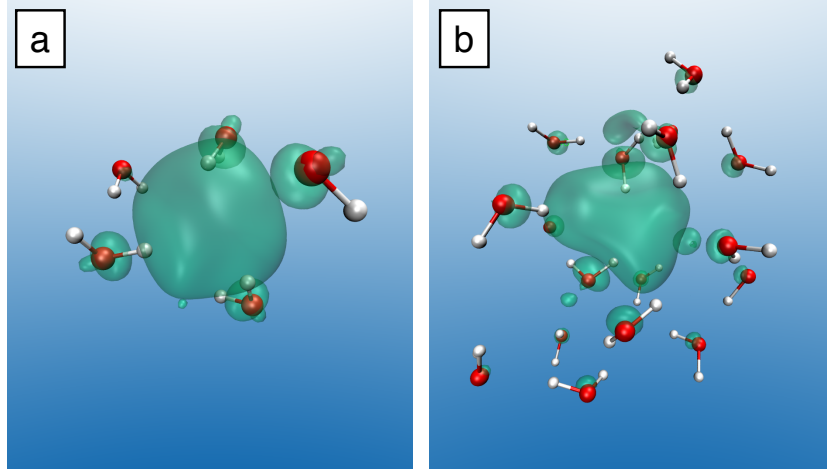


Figure 9.2 – Charge density of (a) the hydrated and (b) the wet electron. The same probability density of 55% is shown in the two cases. For clarity, only the water molecules in the vicinity of the localized electron are shown.

distinct dynamical, energetic, and structural properties.

We analyze in more detail the two distinct precursors among which the pre-hydrated electron switches like in a two-state system dynamics [cf. Fig. 9.1(b)]. The energy levels of these two states lie either at or slightly below the conduction band edge. To gain insight into their spatial extension, we determine their radius of gyration. As shown in Fig. 9.1(b), the energy level of the excess electron strongly correlates with the radius of gyration, thereby indicating that it is largely ruled by localization effects. Such a correlation has been quantified in a previous work [Jacobson and Herbert, 2011], in which two simple yet effective models connecting the energy level of the excess electron  $E$  with its radius of gyration  $R_{\text{gyr}}$  have been proposed, *i.e.* the particle-in-a-box model ( $E_{\text{PIB}}$ ) and the hydrogen-like atom model ( $E_{\text{hydrogenic}}$ ). In atomic units, such relations read

$$E_{\text{PIB}} = \frac{3(\pi^2 - 6)E_h}{8(R_{\text{gyr}}/a_0)^2} \quad (9.1)$$

$$E_{\text{hydrogenic}} = \frac{9E_h}{8(R_{\text{gyr}}/a_0)^2} \quad (9.2)$$

Through the above equations, we have estimated the energy levels of the excess electron in the early-time dynamics based on the radius of gyration. The corresponding energies are given in Fig. 9.1(b), in which a nice agreement between the models and the explicit first-principles calculation can be observed.

For pre-hydrated states with energy levels in the continuum, we find an average radius of gyration of  $\sim 7.5$  Å. This value corresponds to half the size of our simulation cell (15.64 Å), further supporting their delocalized character. We recognize these states as being *quasi*-free electron precursors. Their radii of gyration have recently been estimated to be  $\sim 40$  Å [Savolainen et al., 2014], consistent with a fully delocalized charge density in our simulation

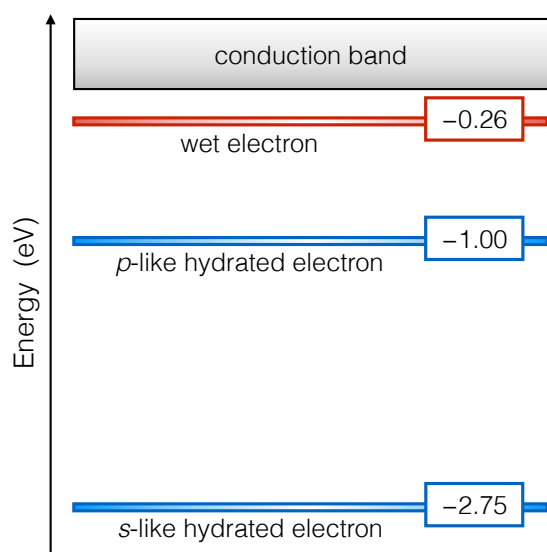


Figure 9.3 – Energy levels of the wet and the hydrated electrons with respect to the conduction band of liquid water.

cell. For pre-hydrated states with energy levels deeper in the band gap, we remark that their radii of gyration assume well-defined values for periods of about 50 fs, suggesting a distinctive character for these transient states. Their radii of gyration are  $\sim 4.5$  Å, slightly larger than the radius of gyration of the hydrated electron (2.5 Å) [Ambrosio et al., 2017]. This signals the formation of a trapped state with a localized charge distribution that we assign to the experimentally observed wet electron [Migus et al., 1987, Assel et al., 1999, Nordlund et al., 2007].

We obtain the binding energy of the wet electron by averaging the energy level of the pre-hydrated state over the time interval in which the radius of gyration is smaller than 4.5 Å. We find that its energy level lies at 0.26 eV below the bottom of the conduction band edge. In Fig. 9.3, this energy level is compared with the  $s$ -like and  $p$ -like levels of the hydrated electron, which fall at 2.75 and 1.00 eV [Ambrosio et al., 2017], respectively. On the basis of these binding energies, we exclude that the wet electron is a close relative of the excited  $p$ -like state of the hydrated electron, as proposed in the literature [Long et al., 1990, Wang et al., 2008a, Webster et al., 1991]. This is further supported by the fact that the cavity of the hydrated electron is not yet formed upon the creation of the wet electron. The remarkably low binding energy of the wet electron emphasizes the distinct nature of this precursor with respect to the hydrated one. In fact, in previous non-adiabatic one-electron simulations [Webster et al., 1991], it has been postulated that the wet electron could be associated with an excited localized  $p$ -like state that survives for over 1 ps well above the vacuum level. In order to address this possibility, we have carried out time-dependent density functional theory calculations for the wet electron configurations and inspected the oscillator strengths over an excitation energy window of  $\sim 1$  eV. In this range, we do not detect any strong transition to a localized  $p$ -like state and verify that the final states are delocalized.

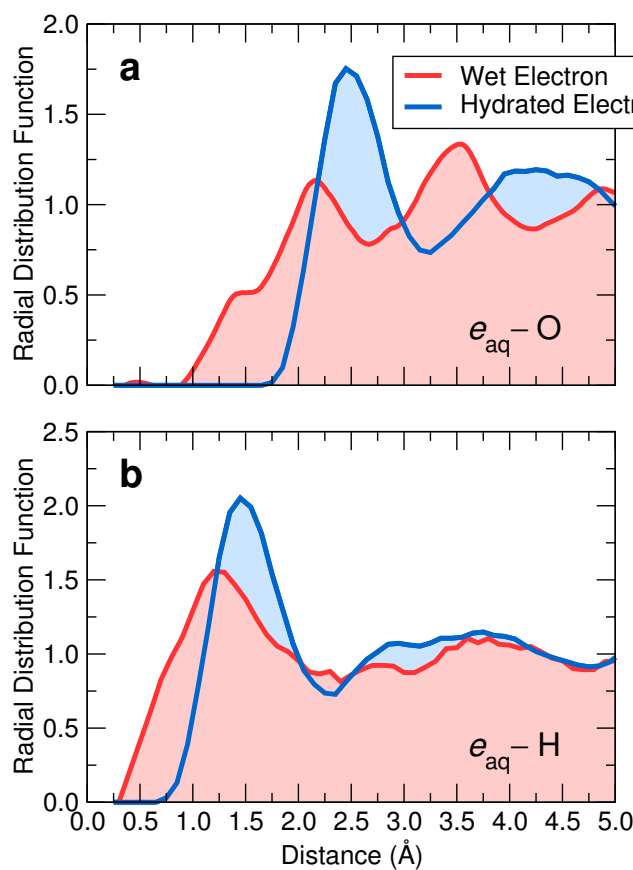


Figure 9.4 – Radial distribution functions of (a) oxygen and (b) hydrogen atoms with respect to the center of the excess electron for the wet (red) and the hydrated (blue) electron.

### 9.3.2 Atomic structure of the wet electron

Following our identification of the wet electron, we analyze its structural properties. To locate the center of its charge density, we first consider the average position of the electron wave function. Then, we determine the radial distribution functions of oxygen [ $g_O(r)$ ] and hydrogen [ $g_H(r)$ ] atoms with respect to this center. These functions are given in Fig. 9.4, where they are compared with those of the fully hydrated case. For the wet electron, we remark that  $g_H(r)$  starts developing at lower radii than  $g_O(r)$ , indicating that an electrostatic preference is already operative in this case. Furthermore, the cavity associated with the wet electron is significantly smaller than that obtained for the hydrated electron, as can be inferred from the principal peaks in  $g_O(r)$  and  $g_H(r)$ , which are shifted towards smaller distances. We gain further insight into the size of the electron cavity through an analysis based on Voronoi volumes. Our investigation yields an average Voronoi volume around the wet electron of  $20.50 \text{ \AA}^3$ , thereby clearly indicating that its cavity is smaller than that of the fully hydrated electron ( $23.96 \text{ \AA}^3$ , [Ambrosio et al., 2017]).

In the case of the hydrated electron, the first peak in  $g_O(r)$  matches the extent of the charge density as given by the radius of gyration ( $2.5 \text{ \AA}$ ). [Ambrosio et al., 2017] At variance, for the wet

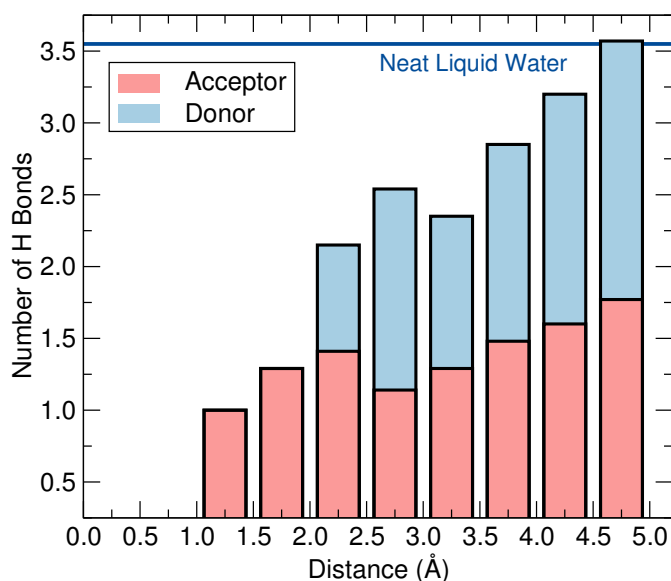


Figure 9.5 – Number of hydrogen bonds per water molecule as a function of the distance from the wet electron center. Red-shaded (blue-shaded) areas indicate the contributions of acceptor (donor) type to the total number of H bonds. The horizontal line marks the average number of hydrogen bonds per water molecule in neat liquid water.

electron, the radius of gyration ( $\sim 4.5$  Å) extends well beyond the position of the first O peak (2.1 Å), indicating that the charge density is not fully accommodated within the cavity, consistently with its display in Fig. 9.2(b). Overall, the distribution functions of the wet electron appear less structured. To understand the role of the disorder in shaping such cavities, we estimate the degree of distortion through the deviation of the flattening  $f$  of the involved ellipsoid from the perfect spherical symmetry expected for a  $s$ -like ground state ( $f = 0$ ). We calculate the flattening by taking the major (minor) semi-axis as the longest (shortest) distance between H pairs coordinating the excess electron. On average, we find  $f = 0.58$  for the wet electron, noticeably larger than for the fully hydrated electron ( $f = 0.25$ , [Ambrosio et al., 2017]).

Next, we address the physical origin of the trapping of the wet electron. Based on spectroscopic evidence, it has been suggested that this species forms at a broken hydrogen bond [Nordlund et al., 2007]. To examine this possibility, we compare the hydrogen-bond network in the vicinity of the wet electron with that of neat liquid water. As a definition of a hydrogen bond, we rely on a well-established geometrical criterion [Schwegler et al., 2000, Luzar and Chandler, 1996], which consists in assuming that two water molecules are hydrogen-bonded when the interatomic distance between their oxygen atoms is smaller than 3.50 Å and their corresponding O-H $\cdots$ O bond angle larger than 140°. For neat water, we find the number of H bonds per molecule to be 3.55, in close agreement with the estimate of 3.58 derived from experimental data [Soper et al., 1997]. In Fig. 9.5, we show the number of H bonds as a function of distance from the wet electron center. At large distances, the bulk value is recovered, but the number of H bonds strongly decreases when approaching the wet electron. More specifically, at the shortest distances this number is found to be more than halved compared to that of neat liquid water and remains perturbed up to  $\sim 4.5$  Å, consistent with the radius of gyration of the wet electron. Hence, the water molecules are more loosely bonded in the region over which the charge density extends. Since the wet electron does not affect the local water density, we attribute this property to ultrafast librational motions of the water



molecules, which take place on the same time scale as the formation of the wet electron [Emde et al., 1998, Silva et al., 1998, Nordlund et al., 2007]. Further analysis of hydrogen bonds in terms of donor and acceptor types reveals that only acceptor-type hydrogen bonds occur at distances smaller than 2.0 Å from the wet electron. As can be seen in Fig. 9.4(b), this radius englobes the full first peak in the  $g_H(r)$ , which hence results from an orientation of the water molecules towards the negative charge density. Overall, the adopted criterion leads to about two H atoms oriented towards the negative charge center and up to six broken hydrogen bonds in the region of the wet electron. These results indicate that the wet electron impacts the structure of liquid water both by reorienting the water molecules in the immediate vicinity of its center and by weakening the water network over a region corresponding to the extension of its charge density. It is worth noticing in this context that such a disruption of the hydrogen bond network is a feature that the wet and hydrated electron have in common [Jacobson and Herbert, 2010, Wilhelm et al., 2019]. This allows us to further clarify the mechanism leading to the formation of the hydrated electron. In fact, we suggest that the role of the wet electron as a precursor is to locally break the hydrogen bond network in liquid water, in order to "prepare" a suitable site where the subsequent equilibration towards the hydrated electron can occur.

## 9.4 Discussion and conclusion

We here discuss our findings in the light of available experimental observations. On the basis of spectroscopic measurements [Nordlund et al., 2007], a mechanism has been postulated, in which the initially delocalized excess electron acquires a localized character upon trapping in a transient state before collapsing into the hydrated electron. Our simulations qualitatively support this mechanism but additionally reveal the underlying dynamics. Indeed, the wet electron is not found to decay steadily into its hydrated form, but rather undergoes repeatedly trapping and subsequent detrapping before the thermodynamic equilibrium prevails (cf. Fig. 9.1). The first evidence pointing to the wet electron consists in a state absorbing in the near infrared (0.9-1.6 eV) [Migus et al., 1987]. With our assignment of the wet electron to a state lying at 0.26 eV below the conduction band together with the assumption of an electron affinity of 0.8–1.0 eV for liquid water [Ambrosio et al., 2017, Ambrosio et al., 2018], this brings us to ascribe the observed absorption to transitions involving final states above the vacuum level. Concerning the atomic structure, we have confirmed that broken hydrogen-bond sites play a role in the conversion of the *quasi*-free electron to the wet electron state, as has previously been surmised [Nordlund et al., 2007]. However, our simulations indicate that a "trap-digging" process is at the origin of the formation of the wet electron, thus ruling out its description in terms of pre-existing trapping sites, as widely assumed so far [Nordlund et al., 2007, Migus et al., 1987, Mozumder, 1988, Bartczak and Pernal, 2001, Turi et al., 2006, Schnitker et al., 1986, Motakabbir and Rossky, 1989]. This can be inferred from the development of the wide region around the wet electron in which the hydrogen-bond network is perturbed, which is unlikely to ensue from a thermal fluctuation of the neat liquid. In addition, we remark that a simulation of neat water of similar size and duration does not yield energy levels as deep as 0.26 eV (cf. Fig. 9.1), while it reproduces properly the experimental estimate of the

number of hydrogen bonds per molecule. As far as the involved time scales are concerned, one distinguishes the one pertaining to the trapping of the *quasi*-electron into the wet electron state and the one associated with the formation of the hydrated electron. Migus *et al.* assigned lifetimes of 110 and 240 fs to these respective processes, but a consensual assessment is still lacking and reported timescales range from 50 to 500 fs for both processes [Wang et al., 2008a]. This order of magnitude is consistent with the evolution in our model (cf. Fig. 9.1).

In conclusion, we carried out a comprehensive investigation of the pre-hydrated excess electron through hybrid functional molecular dynamics simulations. Before the collapse into the hydrated structure, the excess electron is found to alternate between a *quasi*-free state and a localized state with a binding energy of 0.26 eV. In the latter state, the hydrogen-bond network is severely disrupted over a large region of 4.5 Å, corresponding to the extension of the electron charge density. We identified this state as the so-called wet electron, providing a picture in accord with experimental observations.

### 9.5 Methodology

We use the spin-polarized PBE0( $\alpha$ ) hybrid functional [Perdew et al., 1996b], with a fraction of Fock exchange  $\alpha$  set to 0.40, which yields a Kohn-Sham band gap of 8.8 eV for liquid water in accord with experimental and theoretical estimates [Chen et al., 2016]. There is ample evidence in the literature concerning the reliability of hybrid functionals similar to the one used in this work for the treatment of aqueous systems [Todorova et al., 2006, Zhang et al., 2011, DiStasio et al., 2014, Gaiduk et al., 2018]. The van der Waals interactions are described through the nonlocal rVV10 functional [Vydrov and Van Voorhis, 2010, Sabatini et al., 2013], in which the parameter  $b$  is set to 5.3 to correctly reproduce the experimental mass density of liquid water [Ambrosio et al., 2016]. We take advantage of the implementation provided in the CP2K suite of codes [Lippert et al., 1997]. The core-valence interactions are described through Goedecker-Teter-Hutter pseudopotentials and the valence electron wave functions are expanded in a triple- $\zeta$  polarized (TZP) basis. The charge density is expanded in a plane-wave basis set defined by a cutoff of 800 Ry. Our molecular dynamics are performed in the Born-Oppenheimer scheme, in which the electrons are constantly thermalized to the ground state. The equations of motion are integrated with the Verlet algorithm and a time step of 0.48 fs. The simulation is started from an equilibrated configuration of neat liquid water [Ambrosio et al., 2016]. We carry out molecular dynamics runs in the  $NVT$  ensemble, in which the temperature is maintained at 350 K to ensure a frank diffusive motion via the use of a Nosé-Hoover thermostat [Nosé, 1984, Hoover, 1985]. We also perform four additional runs in the  $NVE$  ensemble and find equivalent physical properties for the wet electron (now shown here), ruling out any effect associated to the thermostat. We do not explicitly include quantum nuclear motions, but their effect on the band-gap renormalization are accounted for by the choice of the fraction  $\alpha$  [Ambrosio et al., 2017]. The adopted methodology is the same as that used in Ref. [Ambrosio et al., 2017], in which an excellent description was achieved for the fully hydrated electron as far as the VIE, the  $s \rightarrow p$  transition, the thermodynamic redox level, and the radius of gyration are concerned. This allows us to compare our results for the wet

electron in a consistent manner with those of the hydrated one. To check finite-size effects, we additionally carry out a simulation of the wet electron in a cell containing 64 water molecules, and find that its energy level does not depend on the supercell size within less than 20 meV.



## 10 To Bend or Not to Bend, the Dilemma of Multiple Bonds

Beyond the second row of the periodic table, the nature of the multiple bonds between the elements of the main groups remains yet elusive, and "non-classical" bonding schemes are often invoked for their description. Here, focusing on group 14, we perform an accurate modeling of the Si-Si and C-C double bonds, including electron correlation effects. We show that Si=Si bonds are "classical" and closely resemble the C=C ones, being similarly subjected to a sort of tug of war in which the  $\sigma$  bond favors distortion and the  $\pi$  bond opposes to it. The essential difference between Si and C boils down to the size of their valence shells, which determines the  $\pi$ -bending stiffness. In carbon, such a stiffness is large because, upon bending, the atomic  $s$  orbitals interfere destructively with the  $p$  ones. In silicon, the  $s$  shell is smaller than the  $p$  one, the bending stiffness is reduced and the  $\pi$  bonds typically succumb, distort, and weaken. Electron correlation plays a major role in this context, since  $\pi$  bonds are far from their molecular orbital limit. Hence, we further show that, upon weakening the effective repulsion between  $\pi$  electrons, one may remove any structural instability, strengthen the  $\pi$  bonds, and turn Si into a closer relative of C than it is used to be.

This Chapter is adapted from:

M. Pizzochero, M. Bonfanti and R. Martinazzo

*To Bend or Not to Bend, the Dilemma of Multiple Bonds*

Physical Chemistry Chemical Physics 21, 26342 (2019) [pre-print: chemrxiv.8066747.v1]

*Selected as 2019 PCCP HOT Article*

Reproduced by permission of the PCCP Owner Societies

My contribution to this work has been performing density-functional calculations of extended systems, analyzing the data, and writing the paper.

## 10.1 Motivation

Carbon is doubtlessly a truly unique element in the periodic table as it gives rise to an incomparably large library of molecules and extended architectures, ranging from 3D diamond to 2D graphene, from 1D nanotubes to 0D fullerenes. Among all the chemical elements, it is the only one that can stably form either  $sp^3$  or  $sp^2$  or  $sp$  bonds. This extraordinary chemical flexibility is at the heart of the existence of life in its known forms [Katsnelson, 2007] and the very same ability to form stable, highly conjugated structures appears to be crucial for the extraordinarily high efficiency of several photo-induced processes in biosystems [Jang and Mennucci, 2018].

Moving down along the group IV of the periodic table, one can readily notice that neither silicon nor its heavier congeners share much of the peculiar chemistry of carbon, despite they have the same attitude to form four chemical bonds. In striking contrast with carbon, already Si is well-known to preferentially form three-dimensional  $sp^3$  structures [Wen et al., 2010], and to be quite reluctant to  $\pi$  bonds. Several simple  $X_2Y_4$  molecules ( $X$  = group 14 element) prefer an unusual, "double bridged" structure rather than forming a double bond between the two  $X$ 's (a tendency that increases when moving down the group [Trinquier and Barthelat, 1990]) and, most often, double bonds in *pseudo*-olefins and derivatives are found to be *weaker* than a single bond (*e.g.*, the energy needed to break  $H_2SiSiH_2$  into two  $SiH_2$  fragments,  $\approx 60 \text{ kcal mol}^{-1}$ , is much smaller than the average Si-Si bond energy,  $\approx 95 \text{ kcal mol}^{-1}$ ), consistently with Carter-Goddard's theory [Carter and Goddard, 1986]. In spite of these oddities, several structures containing double [Davidson and Lappert, 1973, West et al., 1981] and triple [Sekiguchi et al., 2004, Sekiguchi et al., 2006] bonds between higher group 14 elements – as well as trisilalenes [Ishida et al., 2003], and exotic aromatic [Abersfelder et al., 2010] and antiaromatic [Suzuki et al., 2011] rings – have been realized and the celebrated "Double Bond Rule" disproved (today, almost all group 13-16 elements are known to be able to form doubly bonded species [Power, 1999, Fischer and Power, 2010]). Si-Si double bonds may feature rather unique structures [Wang et al., 2008b] that have no analogue in carbon chemistry, and are currently being investigated for integration in carbon  $\pi$ -electronic systems, owing to their high potential for applications [Matsuo and Hayakawa, 2018]. Even Si monolayers, known as silicene, have been identified in a *quasi* free-standing form [De Crescenzi et al., 2016], in full analogy with graphene which can be freely suspended [Meyer et al., 2007] or laid down on several substrates with little or no interaction, *e.g.* SiC(0001) [de Heer et al., 2011], Ni(111) after Au intercalation [Varykhalov et al., 2008] but also graphite [Li et al., 2009].

Notwithstanding their formal analogy with unsaturated carbon, the above mentioned low-coordinated structures are far from being " $sp^2$ ", thereby challenging chemical intuition on how they stand. In fact, they typically appear distorted at the multiple bonds, a feature that is known as "*trans*-bending" in silenes, disilenes and higher group analogues, and "buckling" in silicene [Vogt et al., 2012] and germanene [Davila et al., 2014]. How seemingly just a curiosity it may be, such a distortion draws a clear dividing line between C and the other group 14 elements, and likely underlies the most striking difference between them: the former exists as a bulk layered crystal (graphite), while neither silicon nor its higher congeners do. In fact, theoretical modelling shows that silicene multilayers develop strong interlayer bonds that

ultimately lead to four-coordinated structures [Wen et al., 2010]. Several explanations have been invoked for the description of the structural distortion at multiple bonds in Si and Ge, ranging from  $\sigma - \pi$  mixing and coordinate-dative bonds between (singlet) *pseudo*-carbenes in molecules [Trinquier and Malrieu, 1987, Malrieu and Trinquier, 1989, Trinquier and Malrieu, 1990, Jacobsen and Ziegler, 1994, Karni et al., 2009] up to  $\pi$  capability [Zhang et al., 2002] and *pseudo* Jahn-Teller distortion [Jose and Datta, 2012, Molina et al., 2015] in one- and two-dimensional systems. However, none of them settles this issue convincingly, applies equally well to finite-sized and extended systems and accounts, *e.g.*, for the effects of electronegative and/or  $\pi$ -donating substituents.

Here, we introduce a unified description of multiple bonding on the basis of an accurate, "classical"  $\sigma + \pi$  model, and single out the main ingredients governing distortion at multiple bonds. Our findings show that (i) a  $\sigma - \pi$  separation is yet relevant for distorted bonds, and a classical picture consisting of two inequivalent bonds (one  $\sigma$  and one  $\pi$ -like) is adequate in most situations; (ii) the equilibrium molecular structure is determined by a delicate interplay between a distorting  $\sigma$  force and a resisting  $\pi$  one, (iii) electron correlation plays a subtle role in that it tunes the strength of the  $\pi$  bond and its bending stiffness. Furthermore, the difference between carbon and silicon is traced back to atomic-like properties, albeit in a counter-intuitive way: the *larger* interaction between valence orbitals in C – which arises from the similar size of the *s* and *p* valence shells – determines a *greater* weakening of the  $\pi$  bond upon distortion (*i.e.*, a larger bending stiffness), because *s* and *p* orbitals interfere *destructively* in forming the  $\pi$  bond. This establishes a direct connection between the unusual atomic properties of second-row elements, due to the presence of poorly screened *p* valence orbitals [Pyykkö, 1979, Kutzelnigg, 1984], and their unique chemistry. The idea that the  $\sigma$  and the  $\pi$  electrons act oppositely in determining the equilibrium structure is not new and has been long scrutinized, especially in connection with the bond alternating distortion in conjugated and aromatic molecules [Shaik et al., 2001]. Following early observations by Longuet-Higgins and Salem [H. C. Longuet-Higgins and L. Salem, 1959], extensive theoretical and experimental investigations have convincingly established that the  $\pi$ -bonds are always distortive w.r.t. bond alternation, and it is thus only the presence of a  $\sigma$  resistance that makes bond-equalized structures like benzene possible [Shaik et al., 2001]. In the context of *trans*-bending – where  $\sigma$  bonds are distortive and  $\pi$  ones resistive – application of *ab initio* Valence Bond theory to several triply bonded binary systems  $H_nX \equiv YH_m$  [Danovich et al., 2002, Ploshnik et al., 2011], already proved that bending determines a strengthening of the  $\sigma$  bonds and a weakening of the (in plane)  $\pi$  ones. Our modeling provides an insight into this behavior and singles out the main factors governing distortion, that is the geometry-dependent hybridization, the hopping energy (or transfer integral) between the hybrid orbitals, and the electron repulsion in the hybrids forming the  $\pi$ -like bond.

In this Chapter, after describing the computational methods used in this work, we present our  $\sigma + \pi$  model, pinpoint the main ingredients responsible for *trans*-bending and critically examine alternative ways of binding. Finally, we extend our findings to group 14 layered materials and draw conclusions.

## 10.2 Methodology

Density Functional Theory (DFT) was used throughout to investigate the energetics of both molecular and extended systems. For molecules, all-electron density functional theory calculations were performed using the popular B3LYP hybrid functional to describe exchange-correlation effects and the Pople's 6-31++G\*\* atomic-orbital basis-set to expand the Kohn-Sham orbitals, in a spin-unrestricted framework. Calculations were performed with the Gaussian16 code [Frisch et al., 2016] using tight convergence criteria for both the electronic and the geometric optimizations. Generalized internal coordinates were employed to perform the constrained geometry optimizations, for example, for computing the bending potentials (see below).

For extended systems, spin-polarized first-principles calculations were performed within the plane-wave PAW approach, as implemented in the ABINIT code [Gonze et al., 2009, Gonze et al., 2016]. The JTH PAW dataset [Jollet et al., 2014] and the bare PBE GGA-functional [Perdew et al., 1996a] were used throughout, except when investigating layered crystals, for which the van der Waals D3 correction proposed by Grimme [Grimme et al., 2010] and based on the Becke-Johnson method [Becke and Johnson, 2006] was added. A rather high plane-wave cutoff ( $\geq 20$  Ha) was chosen to ensure tight convergence of the electronic energy w.r.t. the real-space mesh and integrations over the Brillouin zone were performed using a  $30 \times 30 \times 1$  (3) Monkhorst-Pack  $k$ -grids for monolayers (multilayers), introducing a large vacuum region of 20 Å when necessary, and adopting tight convergence criteria on forces in the geometry optimization runs ( $< 0.001$  eV/Å). We further performed DFT+ $\bar{U}$  calculations (we use  $\bar{U}$  instead of the popular  $U$  to distinguish it from the Coulomb energy of the Hubbard model described below) using the Hubbard term inside the PAW sphere only, in its fully rotationally invariant form with double-counting correction in the fully localized limit [Anisimov et al., 1991, Liechtenstein et al., 1995], as described in Ref. [Amadon et al., 2008]. For comparison, all calculations were also performed with norm-conserving pseudopotentials [Troullier and Martins, 1991], using the same PBE functional above and either a plane-wave (ABINIT) or an atom-centered basis set of double- $\zeta$  *plus* polarization quality (SIESTA [Soler et al., 2002]), yielding very similar results.

## 10.3 Results and discussion

### 10.3.1 A simple $\sigma + \pi$ model

We assess here the reliability of a "classical"  $\sigma + \pi$  bonding scheme in describing the chemical bond in a  $Y_2X=XY_2$  molecule, where Y is a substituent and X a group 14 element, see Fig. 10.1(a). The case of a triple bond can be handled similarly but will not be considered here. We focus on planar and *trans*-bent configurations of  $C_{2h}$  symmetry, and assume that the X atoms form a  $\pi$ -like bond and three non-bent  $\sigma$  bonds using hybrid orbitals  $sp^\tau$  (for X-Y) and  $sp^\mu$  (for X-X). According to Coulson's directionality theorem, the hybridization indexes  $\tau$  and  $\mu$  are given by the spatial arrangement of the ligands around each X atom, and fully determine the nature of the atomic states involved in  $\pi$ -bonding, *i.e.*, the  $sp^\lambda$  hybrids forming the angle



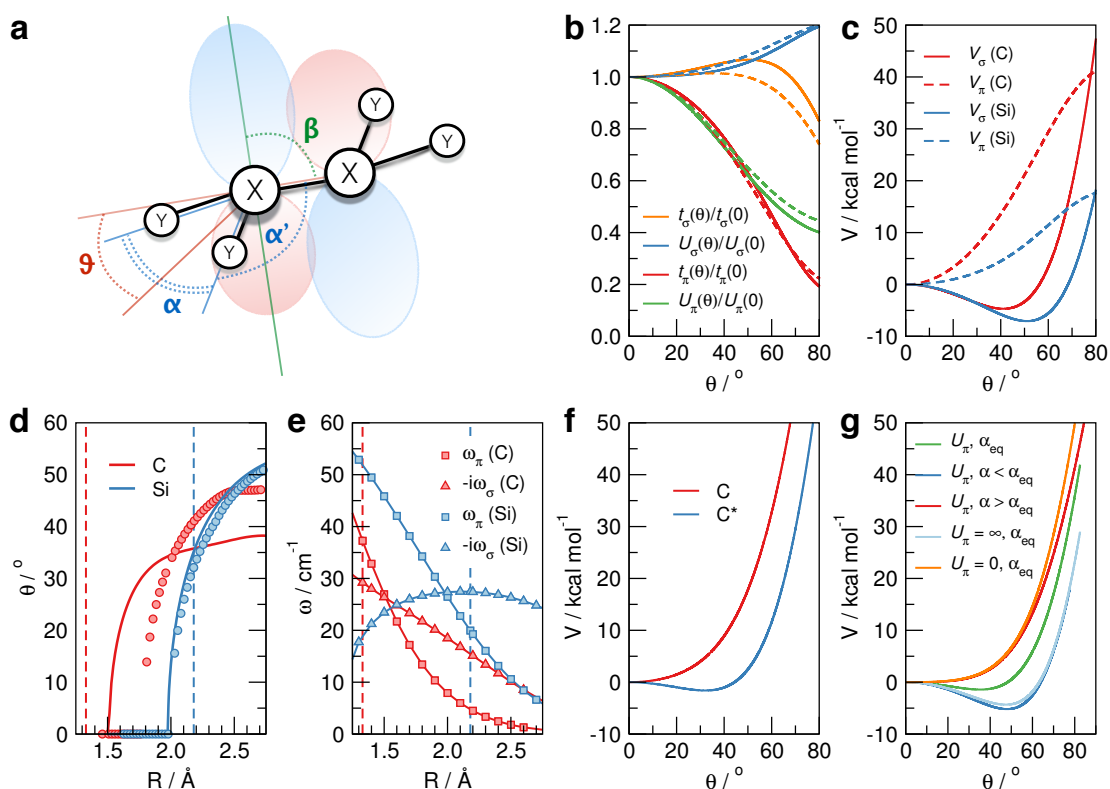


Figure 10.1 – (a) Schematics of the  $Y_2X=XY_2$  model described in the main text, showing the bond angles  $\alpha = \angle YXY$  and  $\alpha' = \angle YXX$ , the pyramidalization angle  $\theta$  and the  $sp^\lambda$  hybrid orbitals forming the  $\pi$  bond, along with the angle  $\beta$  that they make with the  $XX$  axis. (b) Behavior of the effective hopping ( $t$ ) and Coulomb ( $U$ ) energies for the  $\pi$  and the  $\sigma$  bonds, as indicated, as functions of the pyramidalization angle. Solid lines for  $X = \text{Si}$  and dashed lines for  $X = \text{C}$ . Values refer to the equilibrium  $XX$  distances and  $YXY$  angles found in disilene and ethylene,  $[(R, \alpha) = (2.18 \text{ \AA}, 111.67^\circ)$  for  $X=\text{Si}$  and  $(1.33 \text{ \AA}, 116.50^\circ)$  for  $X=\text{C}$ ]. (c) The  $\pi$ - (dashed lines) and  $\sigma$ - (solid lines) bending potentials in disilene (blue) and ethylene (red). (d) Pyramidalization angle in disilene (blue solid line) and ethylene (red solid line). Also reported are the results of first-principles calculations (symbols) where, consistently with the model, structures were optimized for each  $XX$  distance at a fixed angle  $\alpha$ . Vertical bars mark the equilibrium  $X-X$  bond length in the two molecules. (e)  $\pi$ -bending stiffness (squares) and  $\sigma$ -bending moment (triangles), color coded as in (c). (f) Total bending potential for real ethylene (red) and for a fictitious ethylene with a reduced  $ss(\sigma)$  hopping (blue). (g) Total bending potential in disilene, for different values of the  $\text{HSiH}$  angle (mimicking the effect of  $Y$ 's electronegativity) and of the  $\pi$  "on site" Coulomb energy (mimicking the effect of  $\pi$ -donor and  $\pi$ -acceptor species).

$\beta$  with the  $XX$  axis [Fig. 10.1(a)]. Pyramidalization occurs when  $\alpha'$  takes a value smaller than  $\pi - \alpha/2$  and is generally quantified by the pyramidalization angle  $\theta$  shown in Fig. 10.1(a). We vary  $\alpha'$  at constant  $\alpha$  since in this way the  $sp^\tau$  hybrids remain unchanged upon bending and the strength of the  $XY$  bonds does not affect the pyramidalization energetics.

We describe bonding as independently provided by the  $\sigma$  and  $\pi$ -like contributions. For simplicity, the bond obtained in this way is termed  $\pi$ -like since it reduces to a true  $\pi$  bond in planar configurations (but notice that no  $\sigma - \pi$  one-electron mixing picture applies here because we deal with interacting electrons), and write the binding energy as  $E_{\sigma+\pi} = E_{\sigma} + E_{\pi} - \nu(R)$ , where  $E_{\sigma}$ ,  $E_{\pi}$  are the  $\sigma$ ,  $\pi$  electronic terms and  $\nu(R)$  is a short-range potential that accounts for the repulsion between the X ion cores. By construction,  $E_{\sigma+\pi}$  is referenced to the *triplet* state of the fragments. When  $XY_2$  has a singlet ground-state the true binding energy  $E_{BE}$  must account for the promotion energy needed to excite the fragments into their triplet state, *i.e.*,  $E_{BE} = E_{\sigma+\pi} - \Sigma E_{TS}$  where  $E_{TS} = E_T - E_S$  is the triplet-singlet separation energy of each fragment, and  $\Sigma$  stands for their sum ( $\Sigma E_{TS} \equiv 2E_{TS}$  in the symmetric case considered here). It is then clear that no  $\sigma + \pi$  bonding scheme can be conceived when  $\Sigma E_{TS} > E_{\sigma+\pi}$  [Malrieu and Trinquier, 1989, Trinquier and Malrieu, 1987]. In turn,  $E_{\sigma}$  and  $E_{\pi}$  are obtained separately from a (non-orthogonal) two-electron two-state Hubbard model, which is a simple, analytically solvable, correlated model in which binding is determined by the competition between a *hopping energy*  $t$  and the "*on-site*" *Coulomb energy*  $U$ , typically subsumed in the ratio  $U/|t|$ . For our  $\sigma + \pi$  model, the effective hoppings are between  $sp^{\mu}$  ( $sp^{\lambda}$ ) hybrids for the  $\sigma$  ( $\pi$ ) bond, and can be expressed in terms of atomic orbital (AO) contributions known as Slater-Koster parameters [Slater and Koster, 1954]. Likewise, the bare on-site Coulomb energy can be approximately expressed in terms of AO contributions and hybridization indexes, and screening can be described by a classical dielectric constant that is a weighted sum of  $s$  and  $p$  contributions. We used the first-principles based Slater-Koster parameters given in Refs. [Porezag et al., 1995, Frauenheim et al., 1995] for C-C and Si-Si, respectively, and obtained the bare Coulomb energies from bielectronic integrals on Slater-type AOs. We further obtained the AO screening constants from available results for graphene and silicene [Wehling et al., 2011] and from the triplet-singlet separation energies in methylene and sylilene. For further technical details concerning our model, the reader is addressed to Ref. [Pizzochero et al., 2019b].

Fig. 10.1(b) shows the behavior of the effective hopping and Coulomb energies upon bending. The X-X distance and the HXH angle were fixed at their equilibrium value in  $H_2XXH_2$ , namely  $(R, \alpha) = (2.18 \text{ \AA}, 111.67^\circ)$  for X=Si and  $(1.33 \text{ \AA}, 116.50^\circ)$  for X=C. For both C and Si the  $\sigma$  bonds are close to the molecular orbital limit ( $U_{\sigma}/t_{\sigma} \approx 1$  at  $\theta = 0$ ), while the  $\pi$  bonds depart significantly from such limit ( $U_{\pi}/t_{\pi} \approx 4.5 - 4.6$  at  $\theta = 0$ ). Upon distortion the increase of  $\sigma$  hopping is accompanied by a decrease of the  $\pi$  one for both Si and C. This is due to the increase of the hybridization index in  $sp^{\mu}$  and its decrease in  $sp^{\lambda}$ . The corresponding energy variations are reported in Fig. 10.1(c), where the separate  $\sigma$  and  $\pi$  bending potentials  $V_{\nu}(R, \theta) - V_{\nu}(R, 0)$  ( $\nu = \sigma, \pi$ ) are shown for both C and Si. Fig. 10.1(c) makes evident a stronger weakening of the  $\pi$  bond for C and a larger strengthening of the  $\sigma$  one for Si, with the net result that for C the behavior of the  $\pi$  bond dominates the energetics and the equilibrium structure is planar [red curve in Fig. 10.1(f)], while the opposite holds for Si and the structure is *trans*-bent [green curve in Fig. 10.1(g)]. For the latter, we find that  $E_{\pi}$  is about 17% smaller than its value at  $\theta = 0$  and  $E_{\sigma}$  about 4% larger.

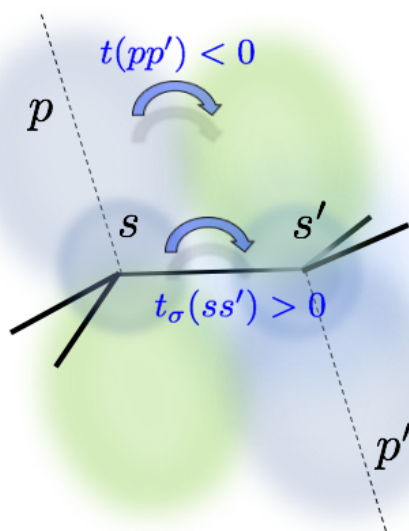


Figure 10.2 – Main orbital interactions contributing to the  $\pi$ -bending stiffness. When the molecule *trans*-bends  $ss'$  hopping becomes possible and competes with the  $pp'$  one, thereby reducing the magnitude of the interaction between the hybrid  $|s\rangle + \sqrt{\lambda}|p\rangle$  of one X atom and the hybrid  $|s'\rangle + \sqrt{\lambda}|p'\rangle$  of the other X atom. Here,  $|p\rangle$  and  $|p'\rangle$  are  $p$  orbitals directed along the pyramidal axes (dashed lines), for a  $C_{2h}$  configuration of  $Y_2XXY_2$ .

Importantly, a detailed analysis of the energetics reveals that the comparatively larger  $ss(\sigma)$  hopping energy for C plays a pivotal role in this context. Upon bending, the hopping between  $s$  orbitals competes with the  $pp(\pi)$  one and weakens the  $\pi$ -like bond, see Fig. 10.2. Had C a smaller  $ss(\sigma)$  hopping energy, ethylene too would take a *trans*-bent equilibrium structure [Fig. 10.1(f)]. Given the higher importance of  $s-s$  hopping in carbon is due to the similar size of its  $s$  and  $p$  shells, – a unique feature of the second-row elements which reflects the poor screening experienced by the lowest-energy orbitals of each angular momentum (*i.e.*  $1s, 2p, 3d, 4f$ , etc.) [Pyykkö, 1979, Kutzelnigg, 1984] – this finding establishes a direct connection between the atomic properties and the tendency of  $p$ -block second-row elements to form ideal multiply bonded structures. Note that a widespread argument, often invoked to explain the Double Bond Rule, relates the above atomic properties to the (length and) strength of  $\pi$  bonds [Kutzelnigg, 1984] but does not actually explain why the *distorting tendency* increases considerably beyond the second row.

### 10.3.2 Influence of the bond length

The relative weight of the  $\sigma$  and  $\pi$  contributions changes when varying the internuclear distance  $R$ , mainly because the  $\pi$  bond is more sensitive than the  $\sigma$  one to the  $U/t$  ratio and weakens faster when increasing  $R$ . As a consequence, pyramidalization diminishes (and eventually vanishes) when compressing the bond, while increases upon stretching. This is shown in Fig. 10.1(d), where we study the behavior of the equilibrium pyramidalization angle at different X-X distances, along with the results of first-principles calculations for  $H_2XXH_2$  species in which, consistently with the model, structural optimizations were performed for each XX distance at a fixed  $\angle HXH$  angle. The related Fig. 10.1(e) shows the "bending stiffness" and the "bending moment". These are the force constants of the  $\pi$  and  $\sigma$  bending potentials at  $\theta = 0$ , hence a property of the ideal  $\sigma$  and  $\pi$  bonds, here conveniently expressed in terms of frequency of motion of a hydrogen point mass.

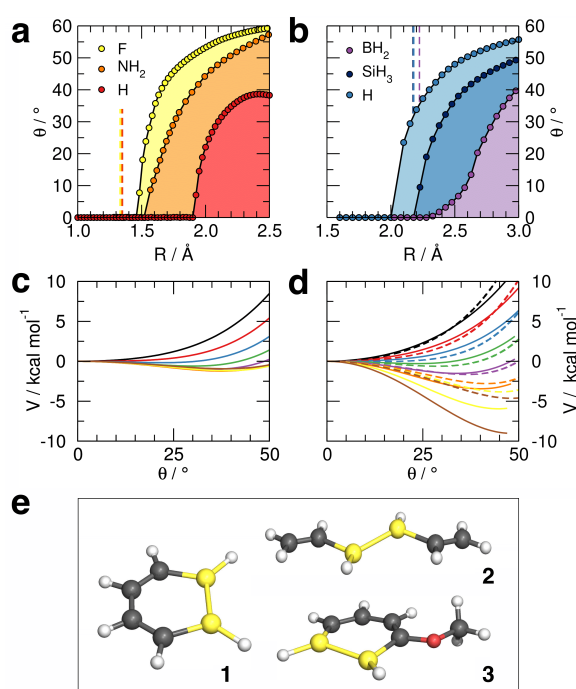


Figure 10.3 – (a) Pyramidalization angle for a stretched C-C  $\pi$  bond, with different substituents,  $\text{Y}=\text{H}$ ,  $\text{NH}_2$  and  $\text{F}$ , as indicated. Vertical bars mark the equilibrium position. (b) Same as in (a) for a Si-Si  $\pi$  bond and  $\text{Y}=\text{H}$ ,  $\text{SiH}_3$  and  $\text{BH}_2$ . Panels (c,d): Bending potentials in  $\text{H}_2\text{C}=\text{CH}_2$  (c) and  $\text{H}_2\text{Si}=\text{SiH}_2$  (d), at fixed X-X internuclear distance ( $R=1.8\text{--}2.5$  Å in steps of 0.1 Å, in black, red, blue, green, purple, orange, yellow and maroon, respectively). Also shown as dashed lines in panel (d) the results of our  $\sigma + \pi$  model. (e) Optimized structure of some conjugated Si-containing molecule with a flat (1) and a distorted (2, 3) Si=Si unit. Black, yellow, white and red balls for C, Si, H and O, respectively.

As is evident from Fig. 10.1(d), the model predicts, and the first-principles calculations confirm, that ethylene does undergo pyramidalization if stretched enough and, on the other hand, disilene does flatten when properly compressed. For ethylene, the quantitative prediction of the transition from a planar to a *trans*-bent structure is hampered by the rather flat energetics [see Fig. 10.3(c)], but for disilene the agreement with first-principles results is remarkable, especially in light of the simplicity of the model.

### 10.3.3 Substituent effects

Our model only describes the double bond between two X atoms, but can qualitatively account for different Y species. Fig. 10.1(g) shows the effect of the angle  $\alpha = \angle \text{YSiY}$  on the pyramidalization energetics. According to Bent's rule such a change can be induced in the (equilibrium) bending angle  $\alpha$  by changing the electronegativity of Y, the larger the electronegativity the smaller the angle is. Y's electronegativity is seen to increase the tendency to distortion, and this occurs because of an increased distortion force exerted by the  $\sigma$  bond and, to a lesser extent, a reduced resistance of the  $\pi$  one. Fig. 10.1(f) also mimics the effect of  $\pi$ -donating ( $\pi$ -acceptor) species, which are expected to increase (decrease) the role of the Coulomb repulsion in the  $\pi$  bond, hence to reduce (increase) the  $\pi$  resistance to distort. Notice that the case  $U_\pi = 0$  corresponds to a purely tight-binding (Hückel) description of the  $\pi$  bond, and this is seen to be unable to capture *trans*-bending.

Figs. 10.3(a,b) show the pyramidalization in  $\text{Y}_2\text{C}=\text{CY}_2$  ( $\text{Y}=\text{H}$ ,  $\text{NH}_2$  and  $\text{F}$ ) and in  $\text{Y}_2\text{Si}=\text{SiY}_2$  ( $\text{Y}=\text{H}$ ,  $\text{SiH}_3$  and  $\text{BH}_2$ ), as described by first-principles calculations.  $\pi$ -donating groups like  $-\text{NH}_2$  are seen to favor pyramidalization of the  $\pi$  centers, and to "anticipate" the transition

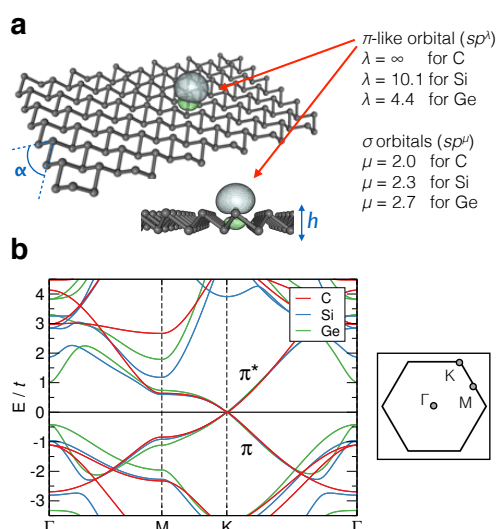


Figure 10.4 – (a) Optimized silicene structure with key geometrical parameters (the valence angle  $\alpha$  and the buckling height  $h$ ) and an iso-surface of the  $\pi$ -like  $sp^\lambda$  hybrid orbital determined from the lattice structure. Also given are the hybridization indexes for the  $\pi$ -like and the  $\sigma$  orbitals, for C, Si and Ge. (b) Band structures of graphene, silicene and germanene at their equilibrium geometries (energies are referenced to the Fermi energy and given in units of  $t$ , as obtained from the Fermi velocity at the  $K$  point,  $t = 2.8$ ,  $1.1$  and  $1.0$  eV for C, Si and Ge, respectively). The inset shows the Brillouin zone of the honeycomb lattice with its high symmetry points.

to a *trans*-bent distorted configuration w.r.t. to  $\pi$  neutral substituents, see Fig. 10.3(a). On the other hand,  $\pi$ -accepting groups such as  $-\text{BH}_2$  act in the opposite way and "delay" such distortion, see Fig. 10.3(b). Similar effects arise under resonance, and make the Si=Si unit planar in disilabenzene [Fig. 10.3(e), 1], and *trans*-bent once  $\pi$ -doped by, e.g.,  $-\text{OCH}_3$  [Fig. 10.3(e), 3]. Conjugation is not enough to remove *trans*-bending, since triene 2 in Fig. 10.3(e) is not flat. Finally, Figs. 10.3(c) and (d) report the pyramidalization energetics in ethylene and disilene, and highlight the differences between C and Si. Fig. 10.3(d) further shows that our model model describes *trans*-bending in disilene quite accurately.

### 10.3.4 Elemental 2D and layered crystals

Next, we consider two group 14 2D crystals beyond graphene [Novoselov et al., 2004], namely silicene [Vogt et al., 2012] and germanene [Davila et al., 2014]. Their chemistry and their preparation have been recently reviewed by Hartman and Sofer [Hartman and Sofer, 2019], who have also pointed out the potentials of their derivatives. Here, the focus is on their atomic structure and physical properties, since they offer a suitable paradigm to compare the diverse chemical bonding of group IV elements arranged in a stable, low-coordinated lattice [Fig. 10.4(a)].

The above mentioned 2D crystals share the same band structure, characterized by two dispersing  $\pi$ -like bands crossing each other at the Fermi level, the so-called Dirac cones, which are symmetric to a large extent w.r.t. the Fermi energy [that is, the  $e$ - $h$  symmetry [Castro Neto et al., 2009], see Fig. 10.4(b)]. They have though rather different crystal structures. Of the three, only graphene is planar, the other two being substantially buckled, with a buckling height of  $0.53 \text{ \AA}$  in silicene and  $0.71 \text{ \AA}$  in germanene, see Fig. 10.4(a). As a consequence, with the exception of graphene, the  $\pi$  cloud of these materials is built from  $sp^\lambda$  hybrids with non-vanishing  $s$ -weight and their  $\sigma$  backbone has more  $p$  character than expected.

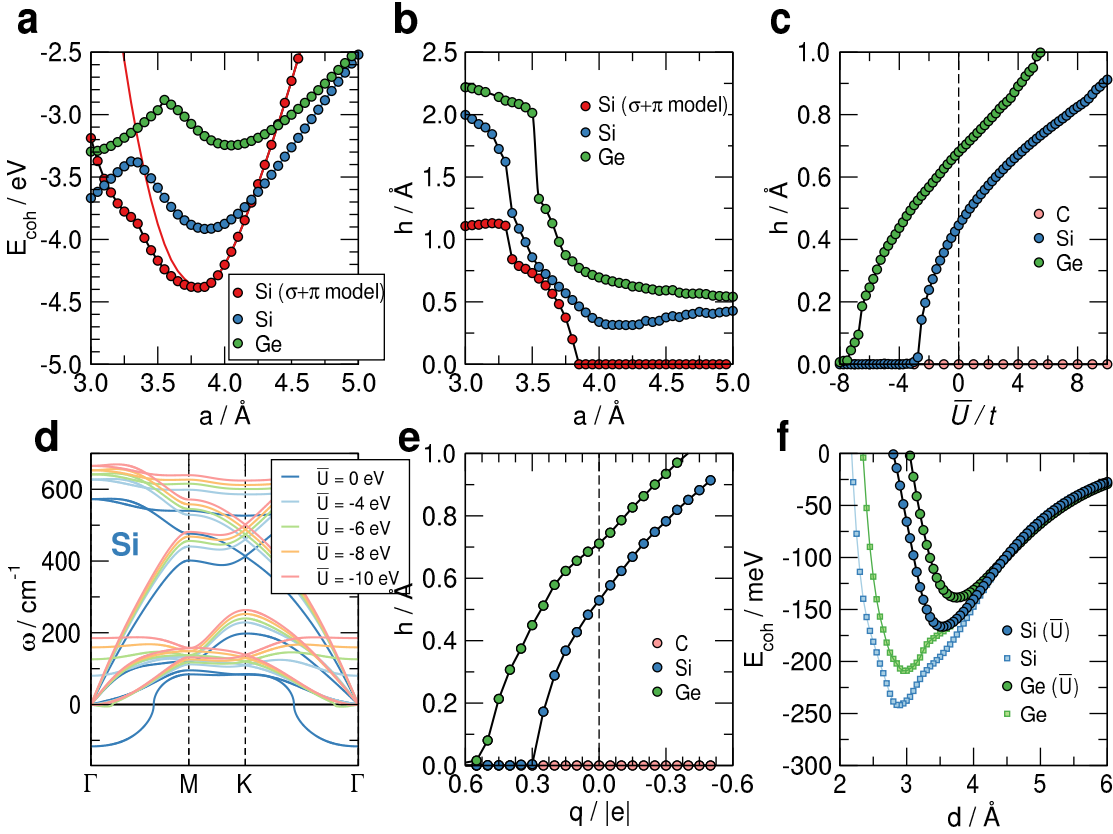


Figure 10.5 – (a) Cohesive energy (per atom) *vs.* lattice constant for silicene and germanene (blue and green circles, respectively), along with the results of the  $\sigma + \pi$  model for silicene (red symbols for the lowest energy structure, red line for the flat layer). (b) Behavior of the buckling height for the cases considered in (a). (c) Evolution of buckling height with  $\bar{U}/t$  for C, Si and Ge monolayers, as indicated. (d) Phonon dispersion of a planar silicene model with  $\bar{U} = 0$  eV (blue lines) and for  $\bar{U} < 0$  as indicated. Imaginary frequencies are shown as negative. For the labels of the indicated special  $k$ -points see the inset of Fig. 10.4(b). (e) Buckling height for C, Si and Ge monolayers as a function of the doping charge per atom. (f) Interaction energy (per atom) *vs.* interlayer spacing  $d$  in flat, Bernal-stacked Si (blue) and Ge (green) multilayers, for  $\bar{U} = 0$  eV (light squares) and for  $\bar{U} = -15$  eV (circles). In the latter cases the flat arrangements are stable down to  $d \approx 3.0$  \AA.

In the remainder of this Section, we exploit the findings described above in periodic first-principles calculations and artificially modify the effective  $e$ - $e$  repulsion by working in the framework of Hubbard-corrected Density Functional Theory (DFT+ $\bar{U}$ ) [Anisimov et al., 1991, Anisimov et al., 1996, Anisimov et al., 1997, Dudarev et al., 1998, Himmetoglu et al., 2014]. DFT+ $\bar{U}$  is an effective method to cope with the over-delocalization problem of semilocal density functionals, and it offers the opportunity of carrying out *in silico* experiments with electron correlation effects. This can be simply accomplished by varying the Hubbard energy  $\bar{U}$  on the valence  $p$  orbitals, in such a way to either enhance ( $\bar{U} > 0$ ) or reduce ( $\bar{U} < 0$ ) the Coulomb repulsion between  $\pi$  electrons.

Fig. 10.5 summarizes our main findings. Panels (a) and (b) show, respectively, the cohesive energy and the bucking height of the optimized Si and Ge honeycomb structures at a varying lattice constant, in the region appropriate for the ‘low-buckled’ monolayers [see Fig. 10.5(b) for  $a$  in the range 3.5-4.5 Å]. Also shown are the results of a  $\sigma + \pi$  model of silicene developed similarly to that described above, which is seen to describe low-buckled Si monolayers reasonably well. Panel (c) shows the influence of the electron correlation on buckling, and proves that a reduced Coulomb repulsion between  $\pi$  electrons drives both silicene and germanene towards a planar geometry. Panel (d) presents the phonon dispersion of silicene for decreasing values of  $\bar{U}$ . Two effects are readily noticed: firstly, alleviation of the Coulomb repulsion removes the dynamical instability associated to silicon atoms involved in an ideal  $sp^2$  hybridization; secondly, the decrease of  $\bar{U}$  enhances the lattice stiffening, as evidenced by the frequency blueshift. Overall, the results shown in panels (c) and (d) of Fig. 10.5 generalize our previous finding that a decreased  $U/t$  ratio stabilizes the  $\pi$  bond against pyramidalization.

We further doped the 2D crystals (without adding any Hubbard correction) with either positive or negative charges, in order to confirm that the above structural distortions are ruled by electron correlation. This resembles the experimental situation where the crystal is placed on top of a dielectric material and electrostatically gated. Both graphene, silicene and germanene have rather symmetric  $\pi/\pi^*$  bands, with the same number of levels above and below the neutrality point [*i.e.*, the above mentioned  $e$ - $h$  symmetry, Fig. 10.4(b)]. Whether such one-electron feature dominates the electronic structure, the effect of the doping charge is the same irrespective of its sign. On the contrary, whether  $e$ - $e$  repulsion plays any role, such a role is emphasized by electrons and reduced by holes. Fig. 10.5(e) shows that this is indeed the case, at least for Si and Ge. Graphene structure, on the other hand, is again found to be structurally insensitive to charge doping. This does not mean that correlation does not play any role in graphene, only that it is not as important as for its congeners. Indeed, at a closer look, graphene chemistry *does* depend on the sign of the charge injected [Huang et al., 2011, Pizzochero et al., 2015].

There exist several interesting artificial structures that can be envisaged when modifying the Coulomb repulsion between  $\pi$  electrons. Among them, we focus here on 3D crystals and on the intriguing possibility of a stable van der Waals stacking of planar monolayers, *i.e.*, of the hypothetical *silicite* and *germanite*. This is a non-trivial issue, since it not obvious that structurally stable flat monolayers remain stable against *interlayer*  $\sigma(pp)$  bonding and do not collapse into a  $sp^3$ -like structure. We find that structurally stable *layered* structures do form for both Si and Ge, though at values of  $\bar{U}$  smaller than those required to make the corresponding monolayers flat, see Fig. 10.5(f). The cohesive energies of these “artificially correlated” materials are found to be 167 and 139 meV/atom for Si and Ge, respectively. These are significantly larger than that in graphite (54 meV/atom according to experiments [Zacharia et al., 2004] and to our calculations), in line with the three-fold increase of the atomic polarizability when moving from carbon to Si and Ge [Pyykkö, 1979, Kutzelnigg, 1984].

### 10.4 Conclusion

Double bonds between carbon and silicon atoms are prototypical examples of second- and higher-row multiple bonds. Their geometrical structure results from a delicate balance between distorting and restoring forces, of  $\sigma$  and  $\pi$  origin respectively. In carbon, the  $\pi$ -bending stiffness is unusually large – mainly because its  $s$  and  $p$  valence shells have similar size – and the double bonds are flat. In silicon, it is smaller and the bonds bend, *weakening* their  $\pi$  component and *strengthening* the  $\sigma$  one. Hence,  $\pi$  bonds in Si feature a more pronounced "radical" character than their C counterparts, and display a rather different chemistry [West, 1987, Patai et al., 2001]. However,  $\pi$  bonds are largely ruled by electron correlation effects, *i.e.*, the "on-site" Coulomb repulsion that shapes the Heitler-London correlations. Reducing the repulsion between  $\pi$  electrons may stabilize the ideal planar structures, and make Si behaving in closer analogy with C.



## 11 Concluding Remarks

Over a decade after the groundbreaking isolation of graphene [Novoselov et al., 2004], the field of two-dimensional materials keeps attracting a lively interest across diverse disciplines, owing to the exciting opportunities it offers to unravel exotic physical phenomena as well as to conceive and realize prospective applications. Not only new members continuously enrich the library of atomically thin crystals [Mounet et al., 2018], but additionally an ever-growing number of effective strategies for the modulation of their functionalities is devised, including defect- and crystalline phase-engineering [Susi et al., 2017, Lin et al., 2014], a careful control over the atomic thickness [Ciarrocchi et al., 2018] along with the realization of van der Waals architectures with desired features [Novoselov et al., 2016, Cavassilas et al., 2018], or even the manipulation of the mutual rotation angle in multilayer films [Cao et al., 2018b, Cao et al., 2018a], to mention but a few. Overall, 2D materials hold great promise for the realization of next-generation devices in a broad spectrum of applications, ranging from flexible optoelectronics [Wang et al., 2012] to magnetism [Gong and Zhang, 2019]. Yet, many challenges remain to be faced in order to translate the unique features of 2D materials into potential technologies. In this Thesis, we made progress by theoretically investigating various aspects concerning the physics of inorganic 2D materials, with a particular emphasis on the structural disorder and magnetic order in atomically thin molybdenum disulfide ( $\text{MoS}_2$ ), platinum diselenide ( $\text{PtSe}_2$ ), and chromium triiodide ( $\text{CrI}_3$ ).

In Part I of this Thesis, we have studied the formation of point defects in the different polymorphs of transition metal dichalcogenides by means of density functional theory calculations. We have considered  $\text{MoS}_2$ , the most representative group VI dichalcogenide, and examined the formation of disorder under two experimentally relevant situations, namely thermodynamic equilibrium and electron beam irradiation. As a first step, we have addressed the thermodynamic stability of a large set of intrinsic point defects. Our calculations suggested that native impurities exhibit significantly lower formation energies in the  $1T'$  phase compared to the  $2H$  phase, thereby indicating that the  $1T'$  polymorph is more susceptible to host lattice imperfections. Furthermore, we have revealed that, in both polymorphs, the metastable metal adatom and antisite defects induce local magnetic moments, hence identifying the type of defects that may be responsible for the experimentally observed ferromagnetism in irradiated  $\text{MoS}_2$  [Mathew et al., 2012] as well as other group VI dichalcogenides [Guguchia et al., 2018]. Next,

we have investigated the response of  $1T'$ -MoS<sub>2</sub> to the electron beam irradiation. The range of electron beam energies required to image the sample *without* inducing any knock-on damage, as well as detailed guidelines for the controlled creation of vacancy defects in the electron microscope has been discussed on the basis of *ab initio* molecular dynamics simulations. Importantly, we have predicted the beam-driven formation of vacancy line defects in  $1T'$ -MoS<sub>2</sub>. Even though line defects in the semiconducting  $2H$  phase of transition metal dichalcogenides have extensively been created in the electron microscope [Komsa et al., 2013] and represent a suitable platform for achieving a nearly complete spin polarization of charge carriers [Pulkin and Yazyev, 2016], their effect on the electronic properties of the semi-metallic  $1T'$  phase remains an open issue to be addressed in future studies. Finally, we have presented a joint experimental and theoretical work on defect-induced magnetism in otherwise non-magnetic PtSe<sub>2</sub>, in collaboration with the group of Prof. Andras Kis at EPFL. Magneto-transport measurements revealed an unexpected magnetic response, the nature of which is ruled by the atomic thickness of the crystal. Specifically, it was found that semiconducting mono- and bi-layer exhibit an antiferro- and ferro-magnetic response, while thicker metallic samples (consisting of a ten of layers) display a layer-dependent ferro- or antiferromagnetic order in an odd or even multilayers, respectively. Furthermore, the magnetism is quenched when approaching the three-dimensional bulk limit, hence pinpointing a pronounced interplay between lattice dimensionality and magnetism in PtSe<sub>2</sub>. Our first-principles calculations, supported by their direct visualization in the electron microscope, have associated the observed magnetism with the presence of Pt vacancy defects along with their distance-dependent exchange interactions. Considering the ubiquitous presence of defects in ultrathin materials, our findings expand the range of 2D magnets into materials that would otherwise be overlooked. Notwithstanding the conceptual advance in the context of defect engineering, the observed critical temperature of a few Kelvin is small for any practical applications. In this regard, we suggest that improvements can be made by carefully controlling the concentration and spatial distribution of vacancies, as it can be achieved upon electron or ion beam exposure [Krasheninnikov and Nordlund, 2010]. In particular, we suggest that theory may play a crucial role in predicting the most effective arrangements of Pt vacancies in raising the Curie/Néel temperature, *e.g.* by determining the magnetic exchange couplings of such Pt vacancies in defects clusters, and subsequently estimating the critical temperature according to the formalism developed in Ref. [Torelli and Olsen, 2018] in the two-dimensional limit.

In Part II, we have moved from structural disorder to intrinsic magnetic order in atomically thin crystals by considering monolayer CrI<sub>3</sub>, the most archetypical 2D magnet. We have provided a detailed understanding of the microscopic spin interactions and designed a viable route to manipulate them. Given that density functional approximations often lack an accurate description of electron correlation effects which are at the origin of the emergence of magnetically ordered phases, we have obtained an unprecedentedly accurate description of the magnetic exchange interactions in CrI<sub>3</sub> through a combination of generalized Heisenberg spin Hamiltonians with many-body wavefunction calculations at the multi-reference configuration interaction level of theory. Our investigation has indicated that magnetic exchange interactions are primarily dominated by the ferromagnetic Heisenberg coupling  $J = -1.44$

---

meV, being off-diagonal and Kitaev anisotropies contributing only up to  $-0.08$  meV. This result is in sharp contrast with recent experimental investigations of *bulk*  $\text{CrI}_3$  [Lee et al., 2020], where a large Kitaev-to-Heisenberg ratio was reported. In agreement with experiments [Huang et al., 2017, Saiz et al., 2019], however, monolayer  $\text{CrI}_3$  is found to possess an out-of-plane easy axis ensuing from a single-ion anisotropy  $A = -0.10$  meV, and  $g$ -tensor featuring in-plane components  $g_{xx} = g_{yy} = 1.90$  and out-of-plane component  $g_{zz} = 1.92$ . Overall, these results offer a theoretical ground to recent experiments, and further lay the foundation for future quantum mechanical investigation based on model spin Hamiltonians, *e.g.* through exact diagonalization techniques. Next, we relied on these reference values to assess the performance of a dozen density functionals in describing the magnetic interactions in monolayer  $\text{CrI}_3$ . We have found that the PBE functional supplemented with an on-site Coulomb repulsion  $U = 1.50$  eV yields an excellent description of  $J$  and Curie temperature when compared to quantum chemistry and experimental results, at a reasonably low computational coast. We have then used such an optimal functional to study the effect of mild lattice deformations on the magnetism of monolayer  $\text{CrI}_3$ . Depending on the magnitude and direction of the strain exerted, we have revealed a series of magnetic phase transitions from the ferromagnetic state to Néel antiferromagnetic as well as ferrimagnetic states, the latter including both stripy and zigzag spin configurations. Furthermore, we have identified a critical point in the strain space in which the isotropic Heisenberg couplings vanish, and suggested that this region may be suitable to single out the otherwise weak anisotropic inter-site coupling as a consequence of the enhancement of the Heisenberg-to-Kitaev coupling ratio, possibly driving monolayer  $\text{CrI}_3$  into the quantum spin liquid phase. To the best of our knowledge, our work proposes the very first strategy to induce magnetic phase transitions in the ultimate limit of atomic thickness in  $\text{CrI}_3$ , and further expands the magnetically ordered phases which can be hosted in a 2D magnet. Finally, we have briefly overviewed the formation of native defects in  $\text{CrI}_3$  and found that, when thermodynamic equilibrium prevails, this material should exhibit a sub-stoichiometric composition due to the large stability of vacancy defects and their complexes. These predictions have partly been confirmed in later experiments [Li et al., 2020b], where the formation of an iodine-deficient phase of monolayer  $\text{CrI}_3$  was observed upon thermal annealing. Furthermore, we have shown that defects can affect the local magnetic moment of  $\text{Cr}^{3+}$  ions, thereby indicating a marked intertwining between atomic-scale disorder and magnetic order in monolayer  $\text{CrI}_3$ .

In Part III, we have revisited two long-standing yet poorly understood issues in physical chemistry in the light of modern first-principles methodologies. These include (i) the mechanism underlying the formation of hydrated electrons in liquid water, in collaboration with Prof. Alfredo Pasquarello at EPFL and (ii) the nature of multiple bonds between higher main group elements of the periodic table, in collaboration with Prof. Rocco Martinazzo at the University of Milan. In addition to the fundamental interest in understanding the response of liquid water to an excess electron, last decades have witnessed considerable interest in the hydrated electron due to its ubiquitous role in many biological and chemical processes, most notably DNA damage in living organisms. We have addressed its pre-hydration dynamics by performing hybrid-functional molecular dynamics simulations and time-dependent density functional

theory calculations on a realistic model system. We have revealed a competition between two distinct pre-solvated species, *i.e.* a delocalized quasi-free state in the conduction band of the solvent and a localized state in the band gap with a binding energy of 0.26 eV, which we have assigned to the long-sought wet electron. This wet electron is found to self-trap in a region of the liquid which extends up to 4.5 Å and involves a severe disruption of the hydrogen-bond network, hence behaving in analogy with polarons in crystalline lattices. This work provides for the first time an atomistic view on the nature of the wet electron, which is instrumental in understanding the properties of this fundamental state in liquid water. Next, we have established a unified picture of the double bond, ruling out the main ingredients which confer to carbon its well-known chemical flexibility. In fact, while unsaturated carbon compounds are stable and display a planar geometry, multiple bonds between Si and Ge atoms are fragile and invariably exhibit structural distortions, an effect which is known as *trans*-bending in silenes and buckling in elemental group IV 2D materials like silicene and germanene. We have shown that the atomic structure of both Si=Si and C=C bonds result from a compromise between the tendency of the  $\sigma$  bonds to cause a structural distortion and the  $\pi$  bond tendency to restore planarity. The essential difference between Si and C stems from the relative size of their valence shells, which determines the  $\pi$ -bending stiffness. At odds with carbon, in silicon the *s* shell is smaller than the *p* one, and the reduced bending stiffness is at the origin of the observed deviation of the  $\pi$  bonds from the ideal  $sp^2$  case. In this regard, the Coulomb repulsion  $U$  between the  $\pi$  electron pushes the  $\pi$  bonds away from their molecular orbital (or band-like) limit. Hence, upon artificially weakening  $U$  between  $\pi$  electrons, one may remove any structural distortion, and make unsaturated silicon compounds acting in analogy with carbon compounds.

To conclude, this Thesis mainly reported on an interdisciplinary investigation of atomically thin crystals, including native and engineered defects in transition metal dichalcogenides, magnetic exchange interactions in monolayers of chromium triiodide along with their control through lattice deformations, as well as a detailed understanding of the nature of multiple bonds between group IV monolayers like graphene, silicene, and germanene. In addition to the works which have been presented in great detail, we would like to mention that other relevant findings have been achieved during the doctoral studies, including the investigation of the structural and electronic properties of monolayer MoSe<sub>2</sub> epitaxially grown on either GaAs(111) [ACS Nano 11, 6355 (2017)] or *h*-BN [ACS Nano 12, 11161 (2018)], in collaboration with the group of Prof. Andras Kis at EPFL, the creation and manipulation of topological domain boundaries in the quantum spin Hall insulator 1T'-WSe<sub>2</sub> [Nano Letters 19, 5634 (2019)], in collaboration with the group of Prof. Michael Crommie at the University of California at Berkeley, as well as the pressure-induced crystalline- and electronic-phase transitions in layered group IV transition metal dichalcogenides [Nature Communications, submitted (2020)], in collaboration with the group of Prof. Ana Akrap at the University of Fribourg.

## Bibliography

- [Abersfelder et al., 2010] Abersfelder, K., White, A. J. P., Rzepa, H. S., and Scheschkewitz, D. (2010). A tricyclic aromatic isomer of hexasilabenzene. *Science*, 327:564.
- [Amadon et al., 2008] Amadon, B., Jollet, F., and Torrent, M. (2008).  $\gamma$  and  $\beta$  cerium: LDA+U calculations of ground-state parameters. *Physical Review B*, 77:155104.
- [Ambrosio et al., 2018] Ambrosio, F., Guo, Z., and Pasquarello, A. (2018). Absolute energy levels of liquid water. *The Journal of Physical Chemistry Letters*, 9:3212.
- [Ambrosio et al., 2016] Ambrosio, F., Miceli, G., and Pasquarello, A. (2016). Structural, dynamical, and electronic properties of liquid water: A hybrid functional study. *The Journal of Physical Chemistry B*, 120:7456.
- [Ambrosio et al., 2017] Ambrosio, F., Miceli, G., and Pasquarello, A. (2017). Electronic levels of excess electrons in liquid water. *The Journal of Physical Chemistry Letters*, 8:2055.
- [Anderson, 1950] Anderson, P. W. (1950). Antiferromagnetism. Theory of superexchange interaction. *Physical Review*, 79:350.
- [Anisimov et al., 1997] Anisimov, V. I., Aryasetiawan, F., and Lichtenstein, A. I. (1997). First-principles calculations of the electronic structure and spectra of strongly correlated systems: The LDA+U method. *Journal of Physics: Condensed Matter*, 9:767.
- [Anisimov et al., 1996] Anisimov, V. I., Elfimov, I. S., Hamada, N., and Terakura, K. (1996). Charge-ordered insulating state of  $\text{Fe}_3\text{O}_4$  from first-principles electronic structure calculations. *Physical Review B*, 54:4387.
- [Anisimov et al., 1991] Anisimov, V. I., Zaanen, J., and Andersen, O. K. (1991). Band theory and Mott insulators: Hubbard U instead of Stoner I. *Physical Review B*, 44:943.
- [Ansari et al., 2019] Ansari, L., Monaghan, S., McEvoy, N., Coileáin, C. Ó., Cullen, C. P., Lin, J., Siris, R., Stimpel-Lindner, T., Burke, K. F., Mirabelli, G., Duffy, R., Caruso, E., Nagle, R. E., Duesberg, G. S., Hurley, P. K., and Gity, F. (2019). Quantum confinement-induced semimetal-to-semiconductor evolution in large-area ultra-thin  $\text{PtSe}_2$  films grown at 400 °C. *npj 2D Materials and Applications*, 3:33.

## Bibliography

---

- [Assel et al., 1999] Assel, M., Laenen, R., and Laubereau, A. (1999). Retrapping and solvation dynamics after femtosecond UV excitation of the solvated electron in water. *The Journal of Chemical Physics*, 111:6869.
- [Ataca and Ciraci, 2011] Ataca, C. and Ciraci, S. (2011). Functionalization of single-layer MoS<sub>2</sub> honeycomb structures. *The Journal of Physical Chemistry C*, 115:13303.
- [Avsar et al., 2020] Avsar, A., Cheon, C.-Y., Pizzochero, M., Tripathi, M., Ciarrocchi, A., Yazyev, O. V., and Kis, A. (2020). Probing magnetism in atomically thin semiconducting PtSe<sub>2</sub>. *submitted to Nature Communications*.
- [Avsar et al., 2019] Avsar, A., Ciarrocchi, A., Pizzochero, M., Unuchek, D., Yazyev, O. V., and Kis, A. (2019). Defect induced, layer-modulated magnetism in ultrathin metallic PtSe<sub>2</sub>. *Nature Nanotechnology*, 14:674.
- [Avsar et al., 2018] Avsar, A., Marinov, K., Marin, E. G., Iannaccone, G., Watanabe, K., Taniguchi, T., Fiori, G., and Kis, A. (2018). Reconfigurable diodes based on vertical WSe<sub>2</sub> transistors with van der Waals bonded contacts. *Advanced Materials*, 30:1707200.
- [Avsar et al., 2014] Avsar, A., Tan, J. Y., Taychatanapat, T., Balakrishnan, J., Koon, G. K. W., Yeo, Y., Lahiri, J., Carvalho, A., Rodin, A. S., O'Farrell, E. C. T., Eda, G., Castro Neto, A. H., and Özyilmaz, B. (2014). Spin-orbit proximity effect in graphene. *Nature Communications*, 5:4875.
- [Balabanov and Peterson, 2005] Balabanov, N. B. and Peterson, K. A. (2005). Systematically convergent basis sets for transition metals. I. All-electron correlation consistent basis sets for the 3d elements Sc - Zn. *The Journal of Chemical Physics*, 123:064107.
- [Balog et al., 2010] Balog, R., Jorgensen, B., Nilsson, L., Andersen, M., Rienks, E., Bianchi, M., Fanetti, M., Laegsgaard, E., Baraldi, A., Lizzit, S., Sljivancanin, Z., Basenbacher, F., Hammer, B., Pedersen, T. G., Hofmann, P., and Hornekaer, L. (2010). Bandgap opening in graphene induced by patterned hydrogen adsorption. *Nature Materials*, 9:315.
- [Banhart, 1999] Banhart, F. (1999). Irradiation effects in carbon nanostructures. *Reports on Progress in Physics*, 62:1181.
- [Banhart et al., 2011] Banhart, F., Kotakoski, J., and Krashenninnikov, A. V. (2011). Structural defects in graphene. *ACS Nano*, 5:26.
- [Bartczak and Pernal, 2001] Bartczak, W. M. and Pernal, K. (2001). Potential traps for an excess electron in liquid water: The trap lifetime distributions. *Research on Chemical Intermediates*, 27:891.
- [Becke and Johnson, 2006] Becke, A. D. and Johnson, E. R. (2006). A simple effective potential for exchange. *The Journal of Chemical Physics*, 124:221101.
- [Bengtsson, 1999] Bengtsson, L. (1999). Dipole correction for surface supercell calculations. *Physical Review B*, 59:12301.

- [Boero et al., 2003] Boero, M., Parrinello, M., Terakura, K., Ikeshoji, T., and Liew, C. C. (2003). First-principles molecular-dynamics simulations of a hydrated electron in normal and supercritical water. *Physical Review Letters*, 90:226403.
- [Bogdanov et al., 2013] Bogdanov, N. A., Maurice, R., Rousochatzakis, I., van den Brink, J., and Hozoi, L. (2013). Magnetic state of pyrochlore  $\text{Cd}_2\text{Os}_2\text{O}_7$  emerging from strong competition of ligand distortions and longer-range crystalline anisotropy. *Physical Review Letters*, 110:127206.
- [Bolvin, 2006] Bolvin, H. (2006). An alternative approach to the g-matrix: Theory and applications. *ChemPhysChem*, 7:1575.
- [Bonfanti et al., 2018] Bonfanti, M., Achilli, S., and Martinazzo, R. (2018). Sticking of atomic hydrogen on graphene. *Journal of Physics: Condensed Matter*, 30:283002.
- [Born and Oppenheimer, 1927] Born, M. and Oppenheimer, J. R. (1927). Zur Quantentheorie der Molekeln. *Annalen der Physik*, 389:457.
- [Bostwick et al., 2009] Bostwick, A., McChesney, J. L., Emtsev, J. V., Seyller, T., Horn, K., Kevan, S. D., and Rotenberg, E. (2009). Quasiparticle transformation during a metal-insulator transition in graphene. *Physical Review Letters*, 103:056404.
- [Boys and Bernardi, 1970] Boys, S. and Bernardi, F. (1970). The calculation of small molecular interactions by the differences of separate total energies. Some procedures with reduced errors. *Molecular Physics*, 19:553.
- [Bragg et al., 2004] Bragg, A. E., Verlet, J. R. R., Kammrath, A., Cheshnovsky, O., and Neumark, D. M. (2004). Hydrated electron dynamics: From clusters to bulk. *Science*, 306:669.
- [Bunjaku and Luisier, 2019] Bunjaku, T. and Luisier, M. (2019). Thermal properties of disordered  $\text{Li}_x\text{MoS}_2$ : An ab initio study. *Physical Review Materials*, 3:034001.
- [Burch et al., 2018] Burch, K. S., Mandrus, D., and Park, J.-G. (2018). Magnetism in two-dimensional van der Waals materials. *Nature*, 563:47.
- [Calandra, 2013] Calandra, M. (2013). Chemically exfoliated single-layer  $\text{MoS}_2$ : Stability, lattice dynamics, and catalytic adsorption from first principles. *Physical Review B*, 88:245428.
- [Cao et al., 2016] Cao, D., Shu, H. B., Wu, T. Q., Jiang, Z. T., Jiao, Z. W., Cai, M. Q., and Hu, W. Y. (2016). First-principles study of the origin of magnetism induced by intrinsic defects in monolayer  $\text{MoS}_2$ . *Applied Surface Science*, 361:199.
- [Cao et al., 2018a] Cao, Y., Fatemi, V., Demir, A., Fang, S., Tomarken, S. L., Luo, J. Y., Sanchez-Yamagishi, J. D., Watanabe, K., Taniguchi, T., Kaxiras, E., Ashoori, R. C., and Jarillo-Herrero, P. (2018a). Correlated insulator behaviour at half-filling in magic-angle graphene superlattices. *Nature*, 556:80.

## Bibliography

---

- [Cao et al., 2018b] Cao, Y., Fatemi, V., Fang, S., Watanabe, K., Taniguchi, T., Kaxiras, E., and Jarillo-Herrero, P. (2018b). Unconventional superconductivity in magic-angle graphene superlattices. *Nature*, 556:43.
- [Carter and Goddard, 1986] Carter, E. A. and Goddard, W. A. (1986). Relation between singlet-triplet gaps and bond energies. *The Journal of Physical Chemistry*, 90:998.
- [Castro Neto, 2001] Castro Neto, A. H. (2001). Charge density wave, superconductivity, and anomalous metallic behavior in 2D transition metal dichalcogenides. *Physical Review Letters*, 86:4382.
- [Castro Neto et al., 2009] Castro Neto, A. H., Guinea, F., Peres, N. M. R., Novoselov, K. S., and Geim, A. K. (2009). The electronic properties of graphene. *Review of Modern Physics*, 81:109.
- [Cavassilas et al., 2018] Cavassilas, N., Logoteta, D., Lee, Y., Michelini, F., Lannoo, M., Bescond, M., and Luisier, M. (2018). Dual-gated WTe<sub>2</sub>/MoSe<sub>2</sub> van der Waals tandem solar cells. *The Journal of Physical Chemistry C*, 122:28545.
- [Ceperley and Alder, 1980] Ceperley, D. M. and Alder, B. J. (1980). Ground state of the electron gas by a stochastic method. *Physical Review Letters*, 45:566.
- [Chen et al., 2016] Chen, W., Ambrosio, F., Miceli, G., and Pasquarello, A. (2016). Ab initio electronic structure of liquid water. *Physical Review Letters*, 117:186401.
- [Chhowalla et al., 2013] Chhowalla, M., Shin, H. S., Eda, G., Li, L.-J., Loh, K. P., and Zhang, H. (2013). The chemistry of two-dimensional layered transition metal dichalcogenide nanosheets. *Nature Chemistry*, 5:263.
- [Chibotaru and Ungur, 2012] Chibotaru, L. F. and Ungur, L. (2012). Ab initio calculation of anisotropic magnetic properties of complexes. I. Unique definition of pseudospin Hamiltonians and their derivation. *The Journal of Chemical Physics*, 137:064112.
- [Chow et al., 2015] Chow, P. K., Jacobs-Gedrim, R. B., Gao, J., Lu, T.-M., Yu, B., Terrones, H., and Koratkar, N. (2015). Defect-induced photoluminescence in monolayer semiconducting transition metal dichalcogenides. *ACS Nano*, 9:1520.
- [Ciarrocchi et al., 2018] Ciarrocchi, A., Avsar, A., Ovchinnikov, D., and Kis, A. (2018). Thickness-modulated metal-to-semiconductor transformation in a transition metal dichalcogenide. *Nature Communications*, 9:919.
- [Clark et al., 2019] Clark, O. J., Mazzola, F., Feng, J., Sunko, V., Marković, I., Bawden, L., Kim, T. K., King, P. D. C., and Bahramy, M. S. (2019). Dual quantum confinement and anisotropic spin splitting in the multivalley semimetal PtSe<sub>2</sub>. *Physical Review B*, 99:045438.
- [Danovich et al., 2002] Danovich, D., Ogliaro, F., Karni, M., Apeloig, Y., Cooper, D. L., and Shaik, S. (2002). Silynes (RCSiR') and disilynes (RSiSiR'): Why are less bonds worth energetically more? *Angewandte Chemie International Edition*, 40:4023.



- [Davidson and Lappert, 1973] Davidson, P. J. and Lappert, M. F. (1973). Stabilisation of metals in a low co-ordinative environment using the bis(trimethylsilyl)methyl ligand; coloured Sn ii and Pb II alkyls,  $M[CH(SiMe_3)_2]_2$ . *Journal of the Chemical Society, Chemical Communications*, page 317.
- [Davila et al., 2014] Davila, M. E., Xian, L., Cahangirov, S., Rubio, A., and Le Lay, G. (2014). Germanene: A novel two-dimensional germanium allotrope akin to graphene and silicene. *New Journal of Physics*, 16:095002.
- [De Crescenzi et al., 2016] De Crescenzi, M., Berbezier, I., Scarselli, M., Castrucci, P., Abbarchi, M., Ronda, A., Jardali, F., Park, J., and Vach, H. (2016). Formation of silicene nanosheets on graphite. *ACS Nano*, 10:11163.
- [de Heer et al., 2011] de Heer, W. A., Berger, C., Ruan, M., Sprinkle, M., Li, X., Hu, Y., Zhang, B., Hankinson, J., and Conrad, E. (2011). Large area and structured epitaxial graphene produced by confinement controlled sublimation of silicon carbide. *Proceedings of the National Academy of Sciences of the United States of America*, 108:16900.
- [DiStasio et al., 2014] DiStasio, R. A., Santra, B., Li, Z., Wu, X., and Car, R. (2014). The individual and collective effects of exact exchange and dispersion interactions on the ab initio structure of liquid water. *The Journal of Chemical Physics*, 141:084502.
- [Donarelli et al., 2013] Donarelli, M., Bisti, F., Perrozzi, F., and Ottaviano, L. (2013). Tunable sulfur desorption in exfoliated  $MoS_2$  by means of thermal annealing in ultra-high vacuum. *Chemical Physics Letters*, 588:198.
- [Dudarev et al., 1998] Dudarev, S. L., Botton, G. A., Savrasov, S. Y., Humphreys, C. J., and Sutton, A. P. (1998). Electron-energy-loss spectra and the structural stability of nickel oxide: An LSDA+U study. *Physical Review B*, 57:1505.
- [Duerloo et al., 2014] Duerloo, K.-A. N., Li, Y., and Reed, E. J. (2014). Structural phase transitions in two-dimensional Mo- and W-dichalcogenide monolayers. *Nature Communications*, 5:4214.
- [Eda et al., 2012] Eda, G., Fujita, T., Yamaguchi, H., Voiry, D., Chen, M., and Chhowalla, M. (2012). Coherent atomic and electronic heterostructures of single-layer  $MoS_2$ . *ACS Nano*, 6:7311.
- [Eda et al., 2011] Eda, G., Yamaguchi, H., Voiry, D., Fujita, T., Chen, M., and Chhowalla, M. (2011). Photoluminescence from chemically exfoliated  $MoS_2$ . *Nano Letters*, 11:5111.
- [Elias et al., 2009] Elias, D. C., Nair, R. R., Mohiuddin, T. M. G., Morozov, S. V., Blake, P., Halsall, M. P., Ferrari, A. C., Boukhvalov, D. W., Katsnelson, M. I., Geim, A. K., and Novoselov, K. S. (2009). Control of graphene's properties by reversible hydrogenation: Evidence for graphane. *Science*, 323:610.

## Bibliography

---

- [Emde et al., 1998] Emde, M. F., Baltuška, A., Kummrow, A., Pshenichnikov, M. S., and Wiersma, D. A. (1998). Ultrafast librational dynamics of the hydrated electron. *Physical Review Letters*, 80:4645.
- [Enyashin et al., 2011] Enyashin, A. N., Yadgarov, L., Houben, L., Popov, I., Weidenbach, M., Tenne, R., Bar-Sadan, M., and Seifert, G. (2011). New route for stabilization of 1T-WS<sub>2</sub> and MoS<sub>2</sub> phases. *The Journal of Physical Chemistry C*, 115:24586.
- [Esfahani et al., 2015] Esfahani, D. N., Leenaerts, O., Sahin, H., Partoens, B., and Peeters, F. M. (2015). Structural transitions in monolayer MoS<sub>2</sub> by lithium adsorption. *The Journal of Physical Chemistry C*, 119:10602.
- [Fan et al., 2014] Fan, X.-L., Yang, Y., Xiao, P., and Lau, W.-M. (2014). Site-specific catalytic activity in exfoliated MoS<sub>2</sub> single-layer polytypes for hydrogen evolution: Basal plane and edges. *Journal of Materials Chemistry A*, 2:20545.
- [Fei et al., 2017] Fei, Z., Palomaki, T., Wu, S., Zhao, W., Cai, X., Sun, B., Nguyen, P., Finney, J., Xu, X., and Cobden, D. H. (2017). Edge conduction in monolayer WTe<sub>2</sub>. *Nature Physics*, 13:677.
- [Fischer and Power, 2010] Fischer, R. C. and Power, P. P. (2010).  $\pi$ -bonding and the lone pair effect in multiple bonds involving heavier main group elements: Developments in the new millennium. *Chemical Reviews*, 110:3877.
- [Frauenheim et al., 1995] Frauenheim, T., Weich, F., Köhler, T., Uhlmann, S., Porezag, D., and Seifert, G. (1995). Density-functional-based construction of transferable nonorthogonal tight-binding potentials for Si and SiH. *Physical Review B*, 52:11492.
- [Frindt, 1966] Frindt, R. F. (1966). Single crystals of MoS<sub>2</sub> several molecular layers thick. *Journal of Applied Physics*, 37:1928.
- [Frisch et al., 2016] Frisch, M. J., Trucks, G. W., Schlegel, H. B., Scuseria, G. E., Robb, M. A., Cheeseman, J. R., Scalmani, G., Barone, V., Petersson, G. A., Nakatsuji, H., Li, X., Caricato, M., Marenich, A. V., Bloino, J., Janesko, B. G., Gomperts, R., Mennucci, B., Hratchian, H. P., Ortiz, J. V., Izmaylov, A. F., Sonnenberg, J. L., Williams-Young, D., Ding, F., Lipparini, F., Egidi, F., Goings, J., Peng, B., Petrone, A., Henderson, T., Ranasinghe, D., Zakrzewski, V. G., Gao, J., Rega, N., Zheng, G., Liang, W., Hada, M., Ehara, M., Toyota, K., Fukuda, R., Hasegawa, J., Ishida, M., Nakajima, T., Honda, Y., Kitao, O., Nakai, H., Vreven, T., Throssell, K., Montgomery, Jr., J. A., Peralta, J. E., Ogliaro, F., Bearpark, M. J., Heyd, J. J., Brothers, E. N., Kudin, K. N., Staroverov, V. N., Keith, T. A., Kobayashi, R., Normand, J., Raghavachari, K., Rendell, A. P., Burant, J. C., Iyengar, S. S., Tomasi, J., Cossi, M., Millam, J. M., Klene, M., Adamo, C., Cammi, R., Ochterski, J. W., Martin, R. L., Morokuma, K., Farkas, O., Foresman, J. B., and Fox, D. J. (2016). Gaussian16 Revision a.03. Gaussian Inc. Wallingford CT.
- [Gaiduk et al., 2018] Gaiduk, A. P., Gustafson, J., Gygi, F., and Galli, G. (2018). First-principles simulations of liquid water using a dielectric-dependent hybrid functional. *The Journal of Physical Chemistry Letters*, 9:3068.

- [Gao et al., 2015] Gao, G., Jiao, Y., Ma, F., Jiao, Y., Waclawik, E., and Du, A. (2015). Charge mediated semiconducting-to-metallic phase transition in molybdenum disulfide monolayer and hydrogen evolution reaction in new 1T' phase. *The Journal of Physical Chemistry C*, 119:13124.
- [Gao et al., 2017] Gao, J., Cheng, Y., Tian, T., Hu, X., Zeng, K., Zhang, G., and Zhang, Y.-W. (2017). Structure, stability, and kinetics of vacancy defects in monolayer PtSe<sub>2</sub>: A first-principles study. *ACS Omega*, 2:8640.
- [Garcia et al., 2014] Garcia, A., Raya, A. M., Mariscal, M. M., Esparza, R., Herrera, M., Molina, S. I., Scavello, G., Galindo, P. L., Jose-Yacaman, M., and Ponce, A. (2014). Analysis of electron beam damage of exfoliated MoS<sub>2</sub> sheets and quantitative HAADF-STEM imaging. *Ultramicroscopy*, 146:33.
- [Gibertini et al., 2019] Gibertini, M., Koperski, M., Morpurgo, A. F., and Novoselov, K. S. (2019). Magnetic 2D materials and heterostructures. *Nature Nanotechnology*, 14:408.
- [Goloveshkin et al., 2015] Goloveshkin, A. S., Lenenko, N. D., Zaikovskii, V. I., Golub, A. S., Korlyukov, A. A., and Bushmarinov, I. S. (2015). Ridges and valleys on charged 1T-MoS<sub>2</sub> sheets guiding the packing of organic cations. *RSC Advances*, 5:19206.
- [Gong and Zhang, 2019] Gong, C. and Zhang, X. (2019). Two-dimensional magnetic crystals and emergent heterostructure devices. *Science*, 363:706.
- [González et al., 2016] González, C., Biel, B., and Dappe, Y. J. (2016). Theoretical characterisation of point defects on a MoS<sub>2</sub> monolayer by scanning tunnelling microscopy. *Nanotechnology*, 27:105702.
- [González-Herrero et al., 2016] González-Herrero, H., Gómez-Rodríguez, J. M., Mallet, P., Moaied, M., Palacios, J. J., Salgado, C., Ugeda, M. M., Veuillen, J.-Y., Yndurain, F., and Brihuega, I. (2016). Atomic-scale control of graphene magnetism by using hydrogen atoms. *Science*, 352:437.
- [Gonze et al., 2009] Gonze, X., Amadon, B., Anglade, P.-M., Beuken, J.-M., Bottin, F., Boulanger, P., Bruneval, F., Caliste, D., Caracas, R., Côté, M., Deutsch, T., Genovese, L., Ghosez, P., Giantomassi, M., Goedecker, S., Hamann, D., Hermet, P., Jollet, F., Jomard, G., Leroux, S., Mancini, M., Mazevet, S., Oliveira, M., Onida, G., Pouillon, Y., Rangel, T., Rignanese, G.-M., Sangalli, D., Shaltaf, R., Torrent, M., Verstraete, M., Zerah, G., and Zwanziger, J. (2009). ABINIT: First-principles approach to material and nanosystem properties. *Computer Physics Communications*, 180:2582.
- [Gonze et al., 2016] Gonze, X., Jollet, F., Abreu Araujo, E., Adams, D., Amadon, B., Applencourt, T., Audouze, C., Beuken, J.-M., Bieder, J., Bokhanchuk, A., Bousquet, E., Bruneval, F., Caliste, D., Côté, M., Dahm, F., Da Pieve, F., Delaveau, M., Di Gennaro, M., Dorado, B., Espejo, C., Geneste, G., Genovese, L., Gerossier, A., Giantomassi, M., Gillet, Y., Hamann, D., He, L., Jomard, G., Laflamme Janssen, J., Le Roux, S., Levitt, A., Lherbier, A., Liu, F., Lukačević, I.,

## Bibliography

---

- Martin, A., Martins, C., Oliveira, M., Poncé, S., Pouillon, Y., Rangel, T., Rignanese, G.-M., Romero, A., Rousseau, B., Rubel, O., Shukri, A., Stankovski, M., Torrent, M., Van Setten, M., Van Troeye, B., Verstraete, M., Waroquiers, D., Wiktor, J., Xu, B., Zhou, A., and Zwanziger, J. (2016). Recent developments in the ABINIT software package. *Computer Physics Communications*, 205:106.
- [Goodenough, 1958] Goodenough, J. B. (1958). An interpretation of the magnetic properties of the perovskite-type mixed crystals  $\text{La}_{1-x}\text{Sr}_x\text{CoO}_{3-\lambda}$ . *Journal of Physics and Chemistry of Solids*, 6:287.
- [Grimme et al., 2010] Grimme, S., Antony, J., Ehrlich, S., and Krieg, H. (2010). A consistent and accurate ab initio parametrization of density functional dispersion correction (DFT-D) for the 94 elements H-Pu. *The Journal of Chemical Physics*, 132:154104.
- [Guguchia et al., 2018] Guguchia, Z., Kerelsky, A., Edelberg, D., Banerjee, S., von Rohr, F., Scullion, D., Augustin, M., Scully, M., Rhodes, D. A., Shermadini, Z., Luetkens, H., Shengelaya, A., Baines, C., Morenzoni, E., Amato, A., Hone, J. C., Khasanov, R., Billinge, S. J. L., Santos, E., Pasupathy, A. N., and Uemura, Y. J. (2018). Magnetism in semiconducting molybdenum dichalcogenides. *Science Advances*, 4:eaat3672.
- [H. C. Longuet-Higgins and L. Salem, 1959] H. C. Longuet-Higgins and L. Salem (1959). The alternation of bond lengths in long conjugated chain molecules. *Proceedings of the Royal Society of London. Series A. Mathematical and Physical Sciences*, 251:172.
- [Hamann et al., 1979] Hamann, D. R., Schlüter, M., and Chiang, C. (1979). Norm-conserving pseudopotentials. *Physical Review Letters*, 43:1494.
- [Han et al., 2010] Han, M. Y., Brant, J. C., and Kim, P. (2010). Electron transport in disordered graphene nanoribbons. *Physical Review Letters*, 104:056801.
- [Hardy et al., 2015] Hardy, W. J., Chen, C.-W., Marcinkova, A., Ji, H., Sinova, J., Natelson, D., and Morosan, E. (2015). Very large magnetoresistance in  $\text{Fe}_{0.28}\text{TaS}_2$  single crystals. *Physical Review B*, 91:054426.
- [Hart and Boag, 1962] Hart, E. J. and Boag, J. W. (1962). Absorption spectrum of the hydrated electron in water and in aqueous solutions. *Journal of the American Chemical Society*, 84:4090.
- [Hartman and Sofer, 2019] Hartman, T. and Sofer, Z. (2019). Beyond graphene: Chemistry of Group 14 graphene analogues: Silicene, germanene, and stanene. *ACS Nano*, 13:8566.
- [Helgaker et al., 2000] Helgaker, T., Jørgensen, P., and Olsen, J. (2000). *Molecular Electronic-Structure Theory*. John Wiley & Sons.
- [Henkelman et al., 2000] Henkelman, G., Uberuaga, B. P., and Jónsson, H. (2000). A climbing image nudged elastic band method for finding saddle points and minimum energy paths. *The Journal of Chemical Physics*, 113:9901.

- [Herbert and Coons, 2017] Herbert, J. M. and Coons, M. P. (2017). The hydrated electron. *Annual Review of Physical Chemistry*, 68:447.
- [Heyd et al., 2003] Heyd, J., Scuseria, G. E., and Ernzerhof, M. (2003). Hybrid functionals based on a screened Coulomb potential. *The Journal of Chemical Physics*, 118:8207.
- [Himmetoglu et al., 2014] Himmetoglu, B., Floris, A., de Gironcoli, S., and Cococcioni, M. (2014). Hubbard-corrected DFT energy functionals: The LDA+U description of correlated systems. *International Journal of Quantum Chemistry*, 114:14.
- [Hohenberg and Kohn, 1964] Hohenberg, P. and Kohn, W. (1964). Inhomogeneous electron gas. *Physical Review*, 136:B864.
- [Holden et al., 2019] Holden, Z. C., Rana, B., and Herbert, J. M. (2019). Analytic gradient for the qm/mm-ewald method using charges derived from the electrostatic potential: Theory, implementation, and application to ab initio molecular dynamics simulation of the aqueous electron. *The Journal of Chemical Physics*, 150:144115.
- [Hong et al., 2015] Hong, J., Hu, Z., Probert, M., Li, K., Lv, D., Yang, X., Gu, L., Mao, N., Feng, Q., Xie, L., Zhang, J., Wu, D., Zhang, Z., Jin, C., Ji, W., Zhang, X., Yuan, J., and Zhang, Z. (2015). Exploring atomic defects in molybdenum disulphide monolayers. *Nature Communications*, 6:6293.
- [Hoover, 1985] Hoover, W. G. (1985). Canonical dynamics: Equilibrium phase-space distributions. *Physical Review A*, 31:1695.
- [Huang et al., 2018] Huang, B., Clark, G., Klein, D. R., MacNeill, D., Navarro-Moratalla, E., Seyler, K. L., Wilson, N., McGuire, M. A., Cobden, D. H., Xiao, D., Yao, W., Jarillo-Herrero, P., and Xu, X. (2018). Electrical control of 2D magnetism in bilayer CrI<sub>3</sub>. *Nature Nanotechnology*, 13:544.
- [Huang et al., 2017] Huang, B., Clark, G., Navarro-Moratalla, E., Klein, D. R., Cheng, R., Seyler, K. L., Zhong, D., Schmidgall, E., McGuire, M. A., Cobden, D. H., Yao, W., Xiao, D., Jarillo-Herrero, P., and Xu, X. (2017). Layer-dependent ferromagnetism in a van der Waals crystal down to the monolayer limit. *Nature*, 546:270.
- [Huang et al., 1994] Huang, F., Kief, M. T., Mankey, G. J., and Willis, R. F. (1994). Magnetism in the few-monolayers limit: A surface magneto-optic Kerr-effect study of the magnetic behavior of ultrathin films of Co, Ni, and Co-Ni alloys on Cu(100) and Cu(111). *Physical Review B*, 49:3962.
- [Huang et al., 2011] Huang, L. F., Ni, M. Y., Zhang, G. R., Zhou, W. H., Li, Y. G., Zheng, X. H., and Zeng, Z. (2011). Modulation of the thermodynamic, kinetic, and magnetic properties of the hydrogen monomer on graphene by charge doping. *The Journal of Chemical Physics*, 135:064705.

## Bibliography

---

- [Ishida et al., 2003] Ishida, S., Iwamoto, T., Kabuto, C., and Kira, M. (2003). A stable silicon-based allene analogue with a formally sp-hybridized silicon atom. *Nature*, 421:725.
- [Jacobsen and Ziegler, 1994] Jacobsen, H. and Ziegler, T. (1994). Nonclassical double bonds in ethylene analogs: Influence of Pauli repulsion on trans bending and  $\pi$ -bond strength. A density functional study. *Journal of the American Chemical Society*, 116:3667.
- [Jacobson and Herbert, 2010] Jacobson, L. D. and Herbert, J. M. (2010). A one-electron model for the aqueous electron that includes many-body electron-water polarization: Bulk equilibrium structure, vertical electron binding energy, and optical absorption spectrum. *The Journal of Chemical Physics*, 133:154506.
- [Jacobson and Herbert, 2011] Jacobson, L. D. and Herbert, J. M. (2011). Theoretical characterization of four distinct isomer types in hydrated-electron clusters, and proposed assignments for photoelectron spectra of water cluster anions. *Journal of the American Chemical Society*, 133:19889.
- [Jang and Mennucci, 2018] Jang, S. J. and Mennucci, B. (2018). Delocalized excitons in natural light-harvesting complexes. *Reviews of Modern Physics*, 90:035003.
- [Jiang et al., 2019] Jiang, J., Xu, T., Lu, J., Sun, L., and Ni, Z. (2019). Defect engineering in 2D materials: Precise manipulation and improved functionalities. *Research*, page 4641739.
- [Jiang et al., 2018a] Jiang, S., Li, L., Wang, Z., Mak, K. F., and Shan, J. (2018a). Controlling magnetism in 2D CrI<sub>3</sub> by electrostatic doping. *Nature Nanotechnology*, 13:549.
- [Jiang et al., 2018b] Jiang, S., Shan, J., and Mak, K. F. (2018b). Electric-field switching of two-dimensional van der Waals magnets. *Nature Materials*, 17:406.
- [Jollet et al., 2014] Jollet, F., Torrent, M., and Holzwarth, N. (2014). Generation of projector augmented-wave atomic data: A 71 element validated table in the XML format. *Computer Physics Communications*, 185:1246.
- [Jones, 2015] Jones, R. O. (2015). Density functional theory: Its origins, rise to prominence, and future. *Reviews of Modern Physics*, 87:897.
- [Jose and Datta, 2012] Jose, D. and Datta, A. (2012). Understanding of the buckling distortions in silicene. *The Journal of Physical Chemistry C*, 116:24639.
- [Kanamori, 1959] Kanamori, J. (1959). Superexchange interaction and symmetry properties of electron orbitals. *Journal of Physics and Chemistry of Solids*, 10:87.
- [Karni et al., 2009] Karni, M., Apeloig, Y., Kapp, J., and Schleyer, P. v. R. (2009). Theoretical aspects of compounds containing Si, Ge, Sn and Pb. In *The Chemistry of Organic Silicon Compounds. Vol. 3 PATAI'S Chemistry of Functional Groups*. John Wiley & Sons.

- [Karthikeyan et al., 2019] Karthikeyan, J., Komsa, H.-P., Batzill, M., and Krasheninnikov, A. V. (2019). Which transition metal atoms can be embedded into two-dimensional molybdenum dichalcogenides and add magnetism? *Nano Letters*, 19:4581.
- [Kasuya, 1956] Kasuya, T. (1956). A Theory of Metallic Ferro- and Antiferromagnetism on Zener's Model. *Progress of Theoretical Physics*, 16:45.
- [Katagiri et al., 2016] Katagiri, Y., Nakamura, T., Ishii, A., Ohata, C., Hasegawa, M., Katsumoto, S., Cusati, T., Fortunelli, A., Iannaccone, G., Fiori, G., Roche, S., and Haruyama, J. (2016). Gate-tunable atomically thin lateral MoS<sub>2</sub> Schottky junction patterned by electron beam. *Nano Letters*, 16:3788.
- [Katsnelson, 2007] Katsnelson, M. I. (2007). Graphene: Carbon in two dimensions. *Materials Today*, 10:20.
- [Katukuri et al., 2014] Katukuri, V. M., Nishimoto, S., Yushankhai, V., Stoyanova, A., Kandpal, H., Choi, S., Coldea, R., Rousochatzakis, I., Hozoi, L., and van den Brink, J. (2014). Kitaev interactions between  $j = 1/2$  moments in honeycomb Na<sub>2</sub>IrO<sub>3</sub> are large and ferromagnetic: Insights from ab initio quantum chemistry calculations. *New Journal of Physics*, 16:013056.
- [KC et al., 2014] KC, S., Longo, R. C., Addou, R., Wallace, R. M., and Cho, K. (2014). Impact of intrinsic atomic defects on the electronic structure of MoS<sub>2</sub> monolayers. *Nanotechnology*, 25:375703.
- [Kim et al., 1996] Kim, K. S., Park, I., Lee, S., Cho, K., Lee, J. Y., Kim, J., and Joannopoulos, J. D. (1996). The nature of a wet electron. *Physical Review Letters*, 76:956.
- [Kim et al., 2019] Kim, M., Kumaravadivel, P., Birkbeck, J., Kuang, W., Xu, S. G., Hopkinson, D. G., Knolle, J., McClarty, P. A., Berdyugin, A. I., Ben Shalom, M., Gorbachev, R. V., Haigh, S. J., Liu, S., Edgar, J. H., Novoselov, K. S., Grigorieva, I. V., and Geim, A. K. (2019). Micromagnetometry of two-dimensional ferromagnets. *Nature Electronics*, 2:457.
- [Kitaev, 2006] Kitaev, A. (2006). Anyons in an exactly solved model and beyond. *Annals of Physics*, 321:2.
- [Klein et al., 2018] Klein, D. R., MacNeill, D., Lado, J. L., Soriano, D., Navarro-Moratalla, E., Watanabe, K., Taniguchi, T., Manni, S., Canfield, P., Fernández Rossier, J., and Jarillo-Herrero, P. (2018). Probing magnetism in 2D van der Waals crystalline insulators via electron tunneling. *Science*, 360:1218.
- [Kohn and Sham, 1965] Kohn, W. and Sham, L. J. (1965). Self-consistent equations including exchange and correlation effects. *Physical Review*, 140:A1133.
- [Komsa et al., 2012] Komsa, H.-P., Kotakoski, J., Kurasch, S., Lehtinen, O., Kaiser, U., and Krasheninnikov, A. V. (2012). Two-dimensional transition metal dichalcogenides under electron irradiation: Defect production and doping. *Physical Review Letters*, 109:035503.

## Bibliography

---

- [Komsa and Krasheninnikov, 2015] Komsa, H.-P. and Krasheninnikov, A. V. (2015). Native defects in bulk and monolayer MoS<sub>2</sub> from first principles. *Physical Review B*, 91:125304.
- [Komsa et al., 2013] Komsa, H.-P., Kurasch, S., Lehtinen, O., Kaiser, U., and Krasheninnikov, A. V. (2013). From point to extended defects in two-dimensional MoS<sub>2</sub>: Evolution of atomic structure under electron irradiation. *Physical Review B*, 88:035301.
- [Krasheninnikov and Nordlund, 2010] Krasheninnikov, A. V. and Nordlund, K. (2010). Ion and electron irradiation-induced effects in nanostructured materials. *Journal of Applied Physics*, 107:071301.
- [Kresse and Furthmüller, 1996] Kresse, G. and Furthmüller, J. (1996). Efficient iterative schemes for ab initio total-energy calculations using a plane-wave basis set. *Physical Review B*, 54:11169.
- [Kresse and Hafner, 1993] Kresse, G. and Hafner, J. (1993). Ab initio molecular dynamics for liquid metals. *Physical Review B*, 47:558.
- [Kresse and Joubert, 1999] Kresse, G. and Joubert, D. (1999). From ultrasoft pseudopotentials to the projector augmented-wave method. *Physical Review B*, 59:1758.
- [Kretschmer et al., 2017] Kretschmer, S., Komsa, H.-P., Bøggild, P., and Krasheninnikov, A. V. (2017). Structural transformations in two-dimensional transition-metal dichalcogenide MoS<sub>2</sub> under an electron beam: Insights from first-principles calculations. *The Journal of Physical Chemistry Letters*, 8:3061.
- [Krukau et al., 2006] Krukau, A. V., Vydrov, O. A., Izmaylov, A. F., and Scuseria, G. E. (2006). Influence of the exchange screening parameter on the performance of screened hybrid functionals. *The Journal of Chemical Physics*, 125:224106.
- [Kutzelnigg, 1984] Kutzelnigg, W. (1984). Chemical bonding in higher main group elements. *Angewandte Chemie International Edition*, 23:272.
- [Lado and Fernández-Rossier, 2017] Lado, J. L. and Fernández-Rossier, J. (2017). On the origin of magnetic anisotropy in two dimensional CrI<sub>3</sub>. *2D Materials*, 4:035002.
- [Laenen et al., 2000] Laenen, R., Roth, T., and Laubereau, A. (2000). Novel precursors of solvated electrons in water: Evidence for a charge transfer process. *Physical Review Letters*, 85:50.
- [Larsen et al., 2010] Larsen, R. E., Glover, W. J., and Schwartz, B. J. (2010). Does the hydrated electron occupy a cavity? *Science*, 329:65.
- [Larsen et al., 2011] Larsen, R. E., Glover, W. J., and Schwartz, B. J. (2011). Response to Comments on “Does the hydrated electron occupy a cavity?”. *Science*, 331:1387.



- [Lee et al., 2020] Lee, I., Utermohlen, F. G., Weber, D., Hwang, K., Zhang, C., van Tol, J., Goldberger, J. E., Trivedi, N., and Hammel, P. C. (2020). Fundamental spin interactions underlying the magnetic anisotropy in the Kitaev ferromagnet  $\text{CrI}_3$ . *Physical Review Letters*, 124:017201.
- [Leven and Dumpich, 2005] Leven, B. and Dumpich, G. (2005). Resistance behavior and magnetization reversal analysis of individual Co nanowires. *Physical Review B*, 71:064411.
- [Li et al., 2009] Li, G., Luican, A., and Andrei, E. Y. (2009). Scanning tunneling spectroscopy of graphene on graphite. *Physical Review Letters*, 102:176804.
- [Li et al., 2016a] Li, H., Tsai, C., Koh, A. L., Cai, L., Contryman, A. W., Fragapane, A. H., Zhao, J., Han, H. S., Manoharan, H. C., Abild-Pedersen, F., Nørskov, J. K., and Zheng, X. (2016a). Activating and optimizing  $\text{MoS}_2$  basal planes for hydrogen evolution through the formation of strained sulphur vacancies. *Nature Materials*, 15:48.
- [Li et al., 2020a] Li, P., Wang, C., Zhang, J., Chen, S., Guo, D., Ji, W., and Zhong, D. (2020a). Single-layer  $\text{CrI}_3$  grown by molecular beam epitaxy. *arXiv:1912.02559*.
- [Li et al., 2020b] Li, P., Wang, C., Zhang, J., Chen, S., Guo, D., Ji, W., and Zhong, D. (2020b). Single-layer  $\text{CrI}_3$  grown by molecular beam epitaxy. *arXiv:1912.02559*.
- [Li et al., 2019] Li, T., Jiang, S., Sivadas, N., Wang, Z., Xu, Y., Weber, D., Goldberger, J. E., Watanabe, K., Taniguchi, T., Fennie, C. J., Mak, K. F., and Shan, J. (2019). Pressure-controlled interlayer magnetism in atomically thin  $\text{CrI}_3$ . *arXiv:1905.10905*.
- [Li et al., 2016b] Li, Y., Duerloo, K.-A. N., Wauson, K., and Reed, E. J. (2016b). Structural semiconductor-to-semimetal phase transition in two-dimensional materials induced by electrostatic gating. *Nature Communications*, 7:10671.
- [Liechtenstein et al., 1995] Liechtenstein, A. I., Anisimov, V. I., and Zaanen, J. (1995). Density-functional theory and strong interactions: Orbital ordering in Mott-Hubbard insulators. *Physical Review B*, 52:5467.
- [Lin et al., 2014] Lin, Y.-C., Dumcenco, D. O., Huang, Y.-S., and Suenaga, K. (2014). Atomic mechanism of the semiconducting-to-metallic phase transition in single-layered  $\text{MoS}_2$ . *Nature Nanotechnology*, 9:391.
- [Lin et al., 2016] Lin, Z., Carvalho, B. R., Kahn, E., Lv, R., Rao, R., Terrones, H., Pimenta, M. A., and Terrones, M. (2016). Defect engineering of two-dimensional transition metal dichalcogenides. *2D Materials*, 3:022002.
- [Lippert et al., 1997] Lippert, G., Hutter, J., and Parrinello, M. (1997). A hybrid gaussian and plane wave density functional scheme. *Molecular Physics*, 92:477.
- [Liu et al., 2016a] Liu, H., Feng, H., Du, Y., Chen, J., Wu, K., and Zhao, J. (2016a). Point defects in epitaxial silicene on  $\text{Ag}(111)$  surfaces. *2D Materials*, 3:025034.

## Bibliography

---

- [Liu and Guo, 2015] Liu, L. and Guo, J. (2015). Assessment of performance potential of MoS<sub>2</sub>-based topological insulator field-effect transistors. *Journal of Applied Physics*, 118:124502.
- [Liu et al., 2016b] Liu, X., Balla, I., Bergeron, H., and Hersam, M. C. (2016b). Point defects and grain boundaries in rotationally commensurate MoS<sub>2</sub> on epitaxial graphene. *The Journal of Physical Chemistry C*, 120:20798.
- [Long et al., 1990] Long, F. H., Lu, H., and Eisenthal, K. B. (1990). Femtosecond studies of the presolvated electron: An excited state of the solvated electron? *Physical Review Letters*, 64:1469.
- [Lopez-Sanchez et al., 2013] Lopez-Sanchez, O., Lembke, D., Kayci, M., Radenovic, A., and Kis, A. (2013). Ultrasensitive photodetectors based on monolayer MoS<sub>2</sub>. *Nature Nanotechnology*, 8:497.
- [Lu et al., 2017] Lu, A. K. A., Pourtois, G., Luisier, M., Radu, I. P., and Houssa, M. (2017). On the electrostatic control achieved in transistors based on multilayered MoS<sub>2</sub>: A first-principles study. *Journal of Applied Physics*, 121:044505.
- [Luzar and Chandler, 1996] Luzar, A. and Chandler, D. (1996). Effect of environment on hydrogen bond dynamics in liquid water. *Physical Review Letters*, 76:928.
- [Mak et al., 2010] Mak, K. F., Lee, C., Hone, J., Shan, J., and Heinz, T. F. (2010). Atomically thin MoS<sub>2</sub>: A new direct-gap semiconductor. *Physical Review Letters*, 105:136805.
- [Mak et al., 2019] Mak, K. F., Shan, J., and Ralph, D. C. (2019). Probing and controlling magnetic states in 2D layered magnetic materials. *Nature Reviews Physics*, 1:646.
- [Malrieu and Trinquier, 1989] Malrieu, J. P. and Trinquier, G. (1989). Trans-bending at double bonds. Occurrence and extent. *Journal of the American Chemical Society*, 111:5916.
- [Manzeli et al., 2017] Manzeli, S., Ovchinnikov, D., Pasquier, D., Yazyev, O. V., and Kis, A. (2017). 2D transition metal dichalcogenides. *Nature Reviews Materials*, 2:17033.
- [Marsalek et al., 2012] Marsalek, O., Uhlig, F., VandeVondele, J., and Jungwirth, P. (2012). Structure, dynamics, and reactivity of hydrated electrons by ab initio molecular dynamics. *Accounts of Chemical Research*, 45:23.
- [Martinazzo et al., 2010] Martinazzo, R., Casolo, S., and Tantardini, G. F. (2010). Symmetry-induced band-gap opening in graphene superlattices. *Physical Review B*, 81:245420.
- [Mathew et al., 2012] Mathew, S., Gopinadhan, K., Chan, T. K., Yu, X. J., Zhan, D., Cao, L., Rusydi, A., Breese, M. B. H., Dhar, S., Shen, Z. X., Venkatesan, T., and Thong, J. T. L. (2012). Magnetism in MoS<sub>2</sub> induced by proton irradiation. *Applied Physics Letters*, 101:102103.
- [Matsuo and Hayakawa, 2018] Matsuo, T. and Hayakawa, N. (2018).  $\pi$ -electron systems containing Si=Si double bonds. *Science and Technology of Advanced Materials*, 19:108.

- [Maurice et al., 2009] Maurice, R., Bastardis, R., Graaf, C. d., Suaud, N., Mallah, T., and Guihéry, N. (2009). Universal theoretical approach to extract anisotropic spin Hamiltonians. *Journal of Chemical Theory and Computation*, 5:2977.
- [McGuire et al., 2015] McGuire, M. A., Dixit, H., Cooper, V. R., and Sales, B. C. (2015). Coupling of crystal structure and magnetism in the layered, ferromagnetic insulator  $\text{CrI}_3$ . *Chemistry of Materials*, 27:612.
- [Mermin and Wagner, 1966] Mermin, N. D. and Wagner, H. (1966). Absence of ferromagnetism or antiferromagnetism in one- or two-dimensional isotropic Heisenberg models. *Physical Review Letters*, 17:1133.
- [Meyer et al., 2007] Meyer, J. C., Geim, A. K., Katsnelson, M. I., Novoselov, K. S., Booth, T. J., and Roth, S. (2007). The structure of suspended graphene sheets. *Nature*, 446:60.
- [Migus et al., 1987] Migus, A., Gauduel, Y., Martin, J. L., and Antonetti, A. (1987). Excess electrons in liquid water: First evidence of a prehydrated state with femtosecond lifetime. *Physical Review Letters*, 58:1559.
- [Molina et al., 2015] Molina, B., Soto, J., and Castro, J. (2015). Pseudo Jahn-Teller effect in the decasilanaphthalene molecule: Towards the origin of the buckling in silicene. *Chemical Physics*, 460:97.
- [Monkhorst and Pack, 1976] Monkhorst, H. J. and Pack, J. D. (1976). Special points for Brillouin-zone integrations. *Physical Review B*, 13:5188.
- [Motakabbir and Rossky, 1989] Motakabbir, K. A. and Rossky, P. J. (1989). On the nature of pre-existing states for an excess electron in water. *Chemical Physics*, 129:253.
- [Mounet et al., 2018] Mounet, N., Gibertini, M., Schwaller, P., Campi, D., Merkys, A., Marrazzo, A., Sohler, T., Castelli, I. E., Cepellotti, A., Pizzi, G., and Marzari, N. (2018). Two-dimensional materials from high-throughput computational exfoliation of experimentally known compounds. *Nature Nanotechnology*, 13:246.
- [Mozumder, 1988] Mozumder, A. (1988). Conjecture on electron trapping in liquid water. *International Journal of Radiation Applications and Instrumentation. Part C. Radiation Physics and Chemistry*, 32:287.
- [Nair et al., 2012] Nair, R. R., Sepioni, M., Tsai, I.-L., Lehtinen, O., Keinonen, J., Krasheninnikov, A. V., Thomson, T., Geim, A. K., and Grigorieva, I. V. (2012). Spin-half paramagnetism in graphene induced by point defects. *Nature Physics*, 8:199.
- [Najmaei et al., 2015] Najmaei, S., Yuan, J., Zhang, J., Ajayan, P., and Lou, J. (2015). Synthesis and defect investigation of two-dimensional molybdenum disulfide atomic layers. *Accounts of Chemical Research*, 48:31.
- [Noh et al., 2014] Noh, J.-Y., Kim, H., and Kim, Y.-S. (2014). Stability and electronic structures of native defects in single-layer  $\text{MoS}_2$ . *Physical Review B*, 89:205417.

## Bibliography

---

- [Nordlund et al., 2007] Nordlund, D., Ogasawara, H., Bluhm, H., Takahashi, O., Odelius, M., Nagasono, M., Pettersson, L. G. M., and Nilsson, A. (2007). Probing the electron delocalization in liquid water and ice at attosecond time scales. *Physical Review Letters*, 99:217406.
- [Nosé, 1984] Nosé, S. (1984). A unified formulation of the constant temperature molecular dynamics methods. *The Journal of Chemical Physics*, 81:511.
- [Novoselov et al., 2004] Novoselov, K. S., Geim, A. K., Morozov, S. V., Jiang, D., Zhang, Y., Dubonos, S. V., Grigorieva, I. V., and Firsov, A. A. (2004). Electric field effect in atomically thin carbon films. *Science*, 306:666.
- [Novoselov et al., 2005] Novoselov, K. S., Jiang, D., Schedin, F., Booth, T. J., Khotkevich, V. V., Morozov, S. V., and Geim, A. K. (2005). Two-dimensional atomic crystals. *Proceedings of the National Academy of Sciences of the United States of America*, 102:10451.
- [Novoselov et al., 2016] Novoselov, K. S., Mishchenko, A., Carvalho, A., and Castro Neto, A. H. (2016). 2D materials and van der Waals heterostructures. *Science*, 353:461.
- [Paik et al., 2004] Paik, D. H., Lee, I.-R., Yang, D.-S., Baskin, J. S., and Zewail, A. H. (2004). Electrons in finite-sized water cavities: Hydration dynamics observed in real time. *Science*, 306:672.
- [Palianov et al., 2014] Palianov, P., Martin, P., Quéré, F., and Pommeret, S. (2014). Ultrafast formation of hydrated electrons in water at high concentration: Experimental evidence of the free electron. *Journal of Experimental and Theoretical Physics*, 118:489.
- [Pandey et al., 2016] Pandey, M., Rasmussen, F. A., Kuhar, K., Olsen, T., Jacobsen, K. W., and Thygesen, K. S. (2016). Defect-tolerant monolayer transition metal dichalcogenides. *Nano Letters*, 16:2234.
- [Parr and Yang, 1994] Parr, R. G. and Yang, W. (1994). *Density-Functional Theory of Atoms and Molecules*. Oxford University Press.
- [Patai et al., 2001] Patai, S., Rappoport, Z., and Apeloig, Y. (2001). *The chemistry of organic silicon compounds*. John Wiley & Sons.
- [Pauli, 1925] Pauli, W. (1925). über den Zusammenhang des Abschlusses der Elektronengruppen im Atom mit der Komplexstruktur der Spektren. *Zeitschrift für Physik*, 31:765.
- [Pedramrazi et al., 2019] Pedramrazi, Z., Herbig, C., Pulkin, A., Tang, S., Phillips, M., Wong, D., Ryu, H., Pizzochero, M., Chen, Y., Wang, F., Mele, E. J., Shen, Z.-X., Mo, S.-K., Yazyev, O. V., and Crommie, M. F. (2019). Manipulating topological domain boundaries in the single-layer quantum spin Hall insulator 1T'-WSe<sub>2</sub>. *Nano Letters*, 19:5634.
- [Pei et al., 2016] Pei, J., Gai, X., Yang, J., Wang, X., Yu, Z., Choi, D.-Y., Luther-Davies, B., and Lu, Y. (2016). Producing air-stable monolayers of phosphorene and their defect engineering. *Nature Communications*, 7:10450.

- [Perdew et al., 1996a] Perdew, J. P., Burke, K., and Ernzerhof, M. (1996a). Generalized gradient approximation made simple. *Physical Review Letters*, 77:3865.
- [Perdew et al., 1996b] Perdew, J. P., Ernzerhof, M., and Burke, K. (1996b). Rationale for mixing exact exchange with density functional approximations. *The Journal of Chemical Physics*, 105:9982.
- [Perdew et al., 1982] Perdew, J. P., Parr, R. G., Levy, M., and Balduz, J. L. (1982). Density-functional theory for fractional particle number: Derivative discontinuities of the energy. *Physical Review Letters*, 49:1691.
- [Perdew et al., 2008] Perdew, J. P., Ruzsinszky, A., Csonka, G. I., Vydrov, O. A., Scuseria, G. E., Constantin, L. A., Zhou, X., and Burke, K. (2008). Restoring the density-gradient expansion for exchange in solids and surfaces. *Physical Review Letters*, 100:136406.
- [Perdew and Wang, 1992] Perdew, J. P. and Wang, Y. (1992). Accurate and simple analytic representation of the electron-gas correlation energy. *Physical Review B*, 45:13244.
- [Peterson et al., 2006] Peterson, K. A., Shepler, B. C., Figgen, D., and Stoll, H. (2006). On the spectroscopic and thermochemical properties of ClO, BrO, IO, and their anions. *The Journal of Physical Chemistry A*, 110:13877.
- [Pi et al., 2019] Pi, L., Li, L., Liu, K., Zhang, Q., Li, H., and Zhai, T. (2019). Recent progress on 2D noble-transition-metal dichalcogenides. *Advanced Functional Materials*, 29:1904932.
- [Pizzochero, 2020] Pizzochero, M. (2020). Atomic-scale defects in the two-dimensional ferromagnet CrI<sub>3</sub> from first principles. *Journal of Physics D: Applied Physics*, in press, DOI: <https://doi.org/10.1088/1361-6463/ab7ca3>.
- [Pizzochero et al., 2019a] Pizzochero, M., Ambrosio, F., and Pasquarello, A. (2019a). Picture of the wet electron: A localized transient state in liquid water. *Chemical Science*, 10:7442.
- [Pizzochero et al., 2016] Pizzochero, M., Bonfanti, M., and Martinazzo, R. (2016). Hydrogen on silicene: like or unlike graphene? *Physical Chemistry Chemical Physics*, 18:15654.
- [Pizzochero et al., 2019b] Pizzochero, M., Bonfanti, M., and Martinazzo, R. (2019b). To bend or not to bend, the dilemma of multiple bonds. *Physical Chemistry Chemical Physics*, 21:26342.
- [Pizzochero et al., 2015] Pizzochero, M., Leenaerts, O., Partoens, B., Martinazzo, R., and Peeters, F. M. (2015). Hydrogen adsorption on nitrogen and boron doped graphene. *Journal of Physics: Condensed Matter*, 27:425502.
- [Pizzochero et al., 2020] Pizzochero, M., Yadav, R., and Yazyev, O. V. (2020). Magnetic exchange interactions in monolayer CrI<sub>3</sub> from many-body wavefunction calculations. *2D Materials*, in press, pre-print: arXiv:1911.12150.

## Bibliography

---

- [Pizzochero and Yazyev, 2017] Pizzochero, M. and Yazyev, O. V. (2017). Point defects in the 1T' and 2H phases of single-layer MoS<sub>2</sub>: A comparative first-principles study. *Physical Review B*, 96:245402.
- [Pizzochero and Yazyev, 2018] Pizzochero, M. and Yazyev, O. V. (2018). Single-layer 1T'-MoS<sub>2</sub> under electron irradiation from ab initio molecular dynamics. *2D Materials*, 5:025022.
- [Pizzochero and Yazyev, 2020] Pizzochero, M. and Yazyev, O. V. (2020). Inducing magnetic phase transitions in monolayer CrI<sub>3</sub> via lattice deformations. *The Journal of Physical Chemistry C*, 124:7585.
- [Ploshnik et al., 2011] Ploshnik, E., Danovich, D., Hiberty, P. C., and Shaik, S. (2011). The nature of the idealized triple bonds between principal elements and the  $\sigma$  origins of trans-bent geometries – A valence bond study. *Journal of Chemical Theory and Computation*, 7:955.
- [Porezag et al., 1995] Porezag, D., Frauenheim, T., Köhler, T., Seifert, G., and Kaschner, R. (1995). Construction of tight-binding-like potentials on the basis of density-functional theory: Application to carbon. *Physical Review B*, 51:12947.
- [Power, 1999] Power, P. P. (1999).  $\pi$ -bonding and the lone pair effect in multiple bonds between heavier main group elements. *Chemical Reviews*, 99:3463.
- [Pulkin and Yazyev, 2016] Pulkin, A. and Yazyev, O. V. (2016). Spin- and valley-polarized transport across line defects in monolayer MoS<sub>2</sub>. *Physical Review B*, 93:041419.
- [Pulkin and Yazyev, 2017] Pulkin, A. and Yazyev, O. V. (2017). Robustness of the quantum spin Hall insulator phase in monolayer 1T' transition metal dichalcogenides. *Journal of Electron Spectroscopy and Related Phenomena*, 219:72.
- [Pyykkö, 1979] Pyykkö, P. (1979). On the interpretation of "secondary periodicity" in the periodic system. *Journal of Chemical Research, Synopses*, page 380.
- [Qian et al., 2014] Qian, X., Liu, J., Fu, L., and Li, J. (2014). Quantum spin Hall effect in two-dimensional transition metal dichalcogenides. *Science*, 346:1344.
- [Qiu et al., 2013] Qiu, H., Xu, T., Wang, Z., Ren, W., Nan, H., Ni, Z., Chen, Q., Yuan, S., Miao, F., Song, F., Long, G., Shi, Y., Sun, L., Wang, J., and Wang, X. (2013). Hopping transport through defect-induced localized states in molybdenum disulphide. *Nature Communications*, 4:2642.
- [Qiu et al., 2015] Qiu, J., Fu, H., Xu, Y., Oreshkin, A. I., Shao, T., Li, H., Meng, S., Chen, L., and Wu, K. (2015). Ordered and reversible hydrogenation of silicene. *Physical Review Letters*, 114:126101.
- [Radisavljevic and Kis, 2013] Radisavljevic, B. and Kis, A. (2013). Mobility engineering and a metal-insulator transition in monolayer MoS<sub>2</sub>. *Nature Materials*, 12:815.

- [Radisavljevic et al., 2011a] Radisavljevic, B., Radenovic, A., Brivio, J., Giacometti, V., and Kis, A. (2011a). Single-layer MoS<sub>2</sub> transistors. *Nature Nanotechnology*, 6:147.
- [Radisavljevic et al., 2011b] Radisavljevic, B., Whitwick, M. B., and Kis, A. (2011b). Integrated circuits and logic operations based on single-layer MoS<sub>2</sub>. *ACS Nano*, 5:9934.
- [Raffone et al., 2016] Raffone, F., Ataca, C., Grossman, J. C., and Cicero, G. (2016). MoS<sub>2</sub> enhanced T-phase stabilization and tunability through alloying. *The Journal of Physical Chemistry Letters*, 7:2304.
- [Rettig and Trotter, 1987] Rettig, S. J. and Trotter, J. (1987). Refinement of the structure of orthorhombic sulfur,  $\alpha$ -S<sub>8</sub>. *Acta Crystallographica Section C*, 43:2260.
- [Rosky and Schnitker, 1988] Rosky, P. J. and Schnitker, J. (1988). The hydrated electron: Quantum simulation of structure, spectroscopy, and dynamics. *The Journal of Physical Chemistry*, 92:4277.
- [Ruderman and Kittel, 1954] Ruderman, M. A. and Kittel, C. (1954). Indirect exchange coupling of nuclear magnetic moments by conduction electrons. *Physical Review*, 96:99.
- [Sabatini et al., 2013] Sabatini, R., Gorni, T., and de Gironcoli, S. (2013). Nonlocal van der Waals density functional made simple and efficient. *Physical Review B*, 87:041108.
- [Saiz et al., 2019] Saiz, C. L., McGuire, M. A., Hennadige, S. R. J., van Tol, J., and Singamaneni, S. R. (2019). Electron spin resonance properties of CrI<sub>3</sub> and CrCl<sub>3</sub> single crystals. *MRS Advances*, page 1.
- [Savolainen et al., 2014] Savolainen, J., Uhlig, F., Ahmed, S., Hamm, P., and Jungwirth, P. (2014). Direct observation of the collapse of the delocalized excess electron in water. *Nature Chemistry*, 6:697.
- [Schnitker et al., 1986] Schnitker, J., Rosky, P. J., and Kenney-Wallace, G. A. (1986). Electron localization in liquid water: A computer simulation study of microscopic trapping sites. *The Journal of Chemical Physics*, 85:2986.
- [Schwarz, 1991] Schwarz, H. A. (1991). Enthalpy and entropy of formation of the hydrated electron. *The Journal of Physical Chemistry*, 95:6697.
- [Schwegler et al., 2000] Schwegler, E., Galli, G., and Gygi, F. (2000). Water under pressure. *Physical Review Letters*, 84:2429.
- [Sekiguchi et al., 2006] Sekiguchi, A., Ichinohe, M., and Kinjo, R. (2006). The chemistry of disilyne with a genuine Si-Si triple bond: Synthesis, structure, and reactivity. *Bulletin of the Chemical Society of Japan*, 79:825.
- [Sekiguchi et al., 2004] Sekiguchi, A., Kinjo, R., and Ichinohe, M. (2004). A stable compound containing a silicon-silicon triple bond. *Science*, 305:1755.

## Bibliography

---

- [Seok et al., 2017] Seok, J., Lee, J.-H., Cho, S., Ji, B., Kim, H. W., Kwon, M., Kim, D., Kim, Y.-M., Oh, S. H., Kim, S. W., Lee, Y. H., Son, Y.-W., and Yang, H. (2017). Active hydrogen evolution through lattice distortion in metallic MoTe<sub>2</sub>. *2D Materials*, 4:025061.
- [Shaik et al., 2001] Shaik, S., Shurki, A., Danovich, D., and Hiberty, P. C. (2001). A different story of  $\pi$ -delocalization – The distortivity of  $\pi$ -electrons and its chemical manifestations. *Chemical Reviews*, 101:1501.
- [Sharma et al., 2018] Sharma, A., Wen, B., Liu, B., Myint, Y. W., Zhang, H., and Lu, Y. (2018). Defect engineering in few-layer phosphorene. *Small*, 14:1704556.
- [Shirodkar and Waghmare, 2014] Shirodkar, S. N. and Waghmare, U. V. (2014). Emergence of ferroelectricity at a metal-semiconductor transition in a 1T monolayer of MoS<sub>2</sub>. *Physical Review Letters*, 112:157601.
- [Sholl and Steckel, 2009] Sholl, D. and Steckel, J. A. (2009). *Density Functional Theory: A Practical Introduction*. John Wiley & Sons.
- [Shreve et al., 2010] Shreve, A. T., Yen, T. A., and Neumark, D. M. (2010). Photoelectron spectroscopy of hydrated electrons. *Chemical Physics Letters*, 493:216.
- [Shu et al., 2016] Shu, H., Li, Y., Niu, X., and Wang, J. (2016). Greatly enhanced optical absorption of a defective MoS<sub>2</sub> monolayer through oxygen passivation. *ACS Applied Materials & Interfaces*, 8:13150.
- [Siefermann and Abel, 2011] Siefermann, K. R. and Abel, B. (2011). The hydrated electron: A seemingly familiar chemical and biological transient. *Angewandte Chemie International Edition*, 50:5264.
- [Silva et al., 1998] Silva, C., Walmhout, P. K., Yokoyama, K., and Barbara, P. F. (1998). Femtosecond solvation dynamics of the hydrated electron. *Physical Review Letters*, 80:1086.
- [Sivadas et al., 2018] Sivadas, N., Okamoto, S., Xu, X., Fennie, C. J., and Xiao, D. (2018). Stacking-dependent magnetism in bilayer CrI<sub>3</sub>. *Nano Letters*, 18:7658.
- [Sivek et al., 2016] Sivek, J., Sahin, H., Partoens, B., and Peeters, F. M. (2016). Giant magnetic anisotropy in doped single layer molybdenum disulfide and fluorographene. *Journal of Physics: Condensed Matter*, 28:195301.
- [Skorobogatiy et al., 2005] Skorobogatiy, M., Park, I., and Joannopoulos, J. (2005). The nature of a floating electron. *Computational Materials Science*, 32:96.
- [Slater and Koster, 1954] Slater, J. C. and Koster, G. F. (1954). Simplified LCAO method for the periodic potential problem. *Physical Review*, 94:1498.
- [Soler et al., 2002] Soler, J. M., Artacho, E., Gale, J. D., García, A., Junquera, J., Ordejón, P., and Sánchez-Portal, D. (2002). The SIESTA method for ab initio order-N materials simulation. *Journal of Physics: Condensed Matter*, 14:2745.



- [Song et al., 2018] Song, T., Cai, X., Tu, M. W.-Y., Zhang, X., Huang, B., Wilson, N. P., Seyler, K. L., Zhu, L., Taniguchi, T., Watanabe, K., McGuire, M. A., Cobden, D. H., Xiao, D., Yao, W., and Xu, X. (2018). Giant tunneling magnetoresistance in spin-filter van der Waals heterostructures. *Science*, 360:1214.
- [Song et al., 2019] Song, T., Fei, Z., Yankowitz, M., Lin, Z., Jiang, Q., Hwangbo, K., Zhang, Q., Sun, B., Taniguchi, T., Watanabe, K., McGuire, M. A., Graf, D., Cao, T., Chu, J.-H., Cobden, D. H., Dean, C. R., Xiao, D., and Xu, X. (2019). Switching 2D magnetic states via pressure tuning of layer stacking. *arXiv:1905.10860*.
- [Soper et al., 1997] Soper, A. K., Bruni, F., and Ricci, M. A. (1997). Site-site pair correlation functions of water from 25 to 400 °C: Revised analysis of new and old diffraction data. *The Journal of Chemical Physics*, 106:247.
- [Splendiani et al., 2010] Splendiani, A., Sun, L., Zhang, Y., Li, T., Kim, J., Chim, C.-Y., Galli, G., and Wang, F. (2010). Emerging photoluminescence in monolayer MoS<sub>2</sub>. *Nano Letters*, 10:1271.
- [Sun et al., 2011] Sun, J., Marsman, M., Csonka, G. I., Ruzsinszky, A., Hao, P., Kim, Y.-S., Kresse, G., and Perdew, J. P. (2011). Self-consistent meta-generalized gradient approximation within the projector-augmented-wave method. *Physical Review B*, 84:035117.
- [Sun et al., 2015] Sun, J., Ruzsinszky, A., and Perdew, J. P. (2015). Strongly constrained and appropriately normed semilocal density functional. *Physical Review Letters*, 115:036402.
- [Susi et al., 2017] Susi, T., Kepaptsoglou, D., Lin, Y.-C., Ramasse, Q. M., Meyer, J. C., Suenaga, K., and Kotakoski, J. (2017). Towards atomically precise manipulation of 2D nanostructures in the electron microscope. *2D Materials*, 4:042004.
- [Suzuki et al., 2011] Suzuki, K., Matsuo, T., Hashizume, D., Fueno, H., Tanaka, K., and Tamao, K. (2011). A planar rhombic charge-separated tetrasilacyclobutadiene. *Science*, 331:1306.
- [Szabo and Ostlund, 1996] Szabo, A. and Ostlund, N. S. (1996). *Modern Quantum Chemistry. Introduction to Advanced Electronic Structure Theory*. Dover.
- [Szabò et al., 2015] Szabò, A., Rhyner, R., and Luisier, M. (2015). Ab initio simulation of single- and few-layer MoS<sub>2</sub> transistors: Effect of electron-phonon scattering. *Physical Review B*, 92:035435.
- [Tang et al., 2017] Tang, S., Zhang, C., Wong, D., Pedramrazi, Z., Tsai, H.-Z., Jia, C., Moritz, B., Claassen, M., Ryu, H., Kahn, S., Jiang, J., Yan, H., Hashimoto, M., Lu, D., Moore, R. G., Hwang, C.-C., Hwang, C., Hussain, Z., Chen, Y., Ugeda, M. M., Liu, Z., Xie, X., Devereaux, T. P., Crommie, M. F., Mo, S.-K., and Shen, Z.-X. (2017). Quantum spin Hall state in monolayer 1T'-WTe<sub>2</sub>. *Nature Physics*, 13:683.
- [Tang et al., 2010] Tang, Y., Shen, H., Sekiguchi, K., Kurahashi, N., Mizuno, T., Suzuki, Y.-I., and Suzuki, T. (2010). Direct measurement of vertical binding energy of a hydrated electron. *Physical Chemistry Chemical Physics*, 12:3653.

## Bibliography

---

- [Tao et al., 2014] Tao, P., Guo, H., Yang, T., and Zhang, Z. (2014). Strain-induced magnetism in MoS<sub>2</sub> monolayer with defects. *Journal of Applied Physics*, 115:054305.
- [Tauber and Mathies, 2003] Tauber, M. J. and Mathies, R. A. (2003). Structure of the aqueous solvated electron from resonance raman spectroscopy: Lessons from isotopic mixtures. *Journal of the American Chemical Society*, 125:1394.
- [Thiel et al., 2019] Thiel, L., Wang, Z., Tschudin, M. A., Rohner, D., Gutiérrez-Lezama, I., Ubrig, N., Gibertini, M., Giannini, E., Morpurgo, A. F., and Maletinsky, P. (2019). Probing magnetism in 2D materials at the nanoscale with single-spin microscopy. *Science*, 364:973.
- [Tikhonenko et al., 2008] Tikhonenko, F. V., Horsell, D. W., Gorbachev, R. V., and Savchenko, A. K. (2008). Weak localization in graphene flakes. *Physical Review Letters*, 100:056802.
- [Todorova et al., 2006] Todorova, T., Seitsonen, A. P., Hutter, J., Kuo, I.-F. W., and Mundy, C. J. (2006). Molecular dynamics simulation of liquid water: Hybrid density functionals. *The Journal of Physical Chemistry B*, 110:3685.
- [Torelli and Olsen, 2018] Torelli, D. and Olsen, T. (2018). Calculating critical temperatures for ferromagnetic order in two-dimensional materials. *2D Materials*, 6:015028.
- [Torelli et al., 2019] Torelli, D., Thygesen, K. S., and Olsen, T. (2019). High throughput computational screening for 2D ferromagnetic materials: The critical role of anisotropy and local correlations. *2D Materials*, 6:045018.
- [Trinquier and Barthelat, 1990] Trinquier, G. and Barthelat, J. C. (1990). Structures of X<sub>2</sub>F<sub>4</sub>, from carbon to lead. Unsaturation through fluorine bridges in Group 14. *Journal of the American Chemical Society*, 112:9121.
- [Trinquier and Malrieu, 1987] Trinquier, G. and Malrieu, J. P. (1987). Nonclassical distortions at multiple bonds. *Journal of the American Chemical Society*, 109:5303.
- [Trinquier and Malrieu, 1990] Trinquier, G. and Malrieu, J. P. (1990). Trans bending at double bonds: Scrutiny of various rationales through valence-bond analysis. *The Journal of Physical Chemistry*, 94:6184.
- [Troullier and Martins, 1991] Troullier, N. and Martins, J. L. (1991). Efficient pseudopotentials for plane-wave calculations. *Physical Review B*, 43:1993.
- [Tuckerman, 2002] Tuckerman, M. E. (2002). Ab initio molecular dynamics: Basic concepts, current trends and novel applications. *Journal of Physics: Condensed Matter*, 14:1297.
- [Turi, 2015] Turi, L. (2015). Hydrated electrons in water clusters: Inside or outside, cavity or noncavity? *Journal of Chemical Theory and Computation*, 11:1745.
- [Turi and Madarász, 2011] Turi, L. and Madarász, Á. (2011). Comment on “Does the hydrated electron occupy a cavity?”. *Science*, 331:1387.

- [Turi et al., 2006] Turi, L., Madarász, A., and Rossky, P. J. (2006). Excess electron localization sites in neutral water clusters. *The Journal of Chemical Physics*, 125:014308.
- [Turi and Rossky, 2012] Turi, L. and Rossky, P. J. (2012). Theoretical studies of spectroscopy and dynamics of hydrated electrons. *Chemical Reviews*, 112:5641.
- [Ubrig et al., 2019] Ubrig, N., Wang, Z., Teyssier, J., Taniguchi, T., Watanabe, K., Giannini, E., Morpurgo, A. F., and Gibertini, M. (2019). Low-temperature monoclinic layer stacking in atomically thin  $\text{CrI}_3$  crystals. *2D Materials*, 7:015007.
- [Ugeda et al., 2018] Ugeda, M. M., Pulkin, A., Tang, S., Ryu, H., Wu, Q., Zhang, Y., Wong, D., Pedramrazi, Z., Martin-Recio, A., Chen, Y., Wang, F., Shen, Z.-X., Mo, S.-K., Yazyev, O. V., and Crommie, M. F. (2018). Observation of topologically protected states at crystalline phase boundaries in single-layer  $\text{WSe}_2$ . *Nature Communications*, 9:3401.
- [Uhlig et al., 2012] Uhlig, F., Marsalek, O., and Jungwirth, P. (2012). Unraveling the complex nature of the hydrated electron. *The Journal of Physical Chemistry Letters*, 3:3071.
- [Van de Walle and Neugebauer, 2004] Van de Walle, C. G. and Neugebauer, J. (2004). First-principles calculations for defects and impurities: Applications to III-nitrides. *Journal of Applied Physics*, 95:3851.
- [Vanderbilt, 1990] Vanderbilt, D. (1990). Soft self-consistent pseudopotentials in a generalized eigenvalue formalism. *Physical Review B*, 41:7892.
- [Varykhalov et al., 2008] Varykhalov, A., Sánchez-Barriga, J., Shikin, A. M., Biswas, C., Vescovo, E., Rybkin, A., Marchenko, D., and Rader, O. (2008). Electronic and magnetic properties of quasifreestanding graphene on Ni. *Physical Review Letters*, 101:157601.
- [Verlet, 1967] Verlet, L. (1967). Computer "experiments" on classical fluids. I. Thermodynamical properties of Lennard-Jones molecules. *Physical Review*, 159:98.
- [Vogt et al., 2012] Vogt, P., De Padova, P., Quaresima, C., Avila, J., Frantzeskakis, E., Asensio, M. C., Resta, A., Ealet, B., and Le Lay, G. (2012). Silicene: Compelling experimental evidence for graphenelike two-dimensional silicon. *Physical Review Letters*, 108:155501.
- [Voiry et al., 2015] Voiry, D., Mohite, A., and Chhowalla, M. (2015). Phase engineering of transition metal dichalcogenides. *Chemical Society Reviews*, 44:2702.
- [Vydrov and Van Voorhis, 2010] Vydrov, O. A. and Van Voorhis, T. (2010). Nonlocal van der Waals density functional: The simpler the better. *The Journal of Chemical Physics*, 133:244103.
- [Wang et al., 2008a] Wang, C.-R., Luo, T., and Lu, Q.-B. (2008a). On the lifetimes and physical nature of incompletely relaxed electrons in liquid water. *Physical Chemistry Chemical Physics*, 10:4463.

## Bibliography

---

- [Wang et al., 2012] Wang, Q. H., Kalantar-Zadeh, K., Kis, A., Coleman, J. N., and Strano, M. S. (2012). Electronics and optoelectronics of two-dimensional transition metal dichalcogenides. *Nature Nanotechnology*, 7:699.
- [Wang et al., 2020] Wang, R., Su, Y., Yang, G., Zhang, J., and Zhang, S. (2020). Bipolar doping by intrinsic defects and magnetic phase instability in monolayer CrI<sub>3</sub>. *Chemistry of Materials*, 32:1545.
- [Wang et al., 2016a] Wang, S., Lee, G.-D., Lee, S., Yoon, E., and Warner, J. H. (2016a). Detailed atomic reconstruction of extended line defects in monolayer MoS<sub>2</sub>. *ACS Nano*, 10:5419.
- [Wang et al., 2015a] Wang, Y., Li, L., Yao, W., Song, S., Sun, J. T., Pan, J., Ren, X., Li, C., Okunishi, E., Wang, Y.-Q., Wang, E., Shao, Y., Zhang, Y. Y., Yang, H.-T., Schwier, E. F., Iwasawa, H., Shimada, K., Taniguchi, M., Cheng, Z., Zhou, S., Du, S., Pennycook, S. J., Pantelides, S. T., and Gao, H.-J. (2015a). Monolayer PtSe<sub>2</sub>, a new semiconducting transition-metal-dichalcogenide, epitaxially grown by direct selenization of Pt. *Nano Letters*, 15:4013.
- [Wang et al., 2008b] Wang, Y., Xie, Y., Wei, P., King, R. B., Schaefer, H. F., Schleyer, P. V. R., and Robinson, G. H. (2008b). A stable silicon(0) compound with a Si=Si double bond. *Science*, 321:1069.
- [Wang et al., 2016b] Wang, Y., Zhang, K., and Xie, G. (2016b). Remarkable suppression of thermal conductivity by point defects in MoS<sub>2</sub> nanoribbons. *Applied Surface Science*, 360:107.
- [Wang et al., 2018] Wang, Z., Gutiérrez-Lezama, I., Ubrig, N., Kroner, M., Gibertini, M., Taniguchi, T., Watanabe, K., Imamoglu, A., Giannini, E., and Morpurgo, A. F. (2018). Very large tunneling magnetoresistance in layered magnetic semiconductor CrI<sub>3</sub>. *Nature Communications*, 9:2516.
- [Wang et al., 2015b] Wang, Z., Tang, C., Sachs, R., Barlas, Y., and Shi, J. (2015b). Proximity-induced ferromagnetism in graphene revealed by the anomalous Hall effect. *Physical Review Letters*, 114:016603.
- [Webster et al., 1991] Webster, F. J., Schnitker, J., Friedrichs, M. S., Friesner, R. A., and Rossky, P. J. (1991). Solvation dynamics of the hydrated electron: A nonadiabatic quantum simulation. *Physical Review Letters*, 66:3172.
- [Wehling et al., 2011] Wehling, T. O., Siasoglu, E., Friedrich, C., Lichtenstein, A. I., Katsnelson, M. I., and Blugel, S. (2011). Strength of effective Coulomb interactions in graphene and graphite. *Physical Review Letters*, 106:236805.
- [Wen et al., 2010] Wen, X.-D., Cahill, T. J., and Hoffmann, R. (2010). Exploring Group 14 structures: 1D to 2D to 3D. *Chemistry: A European Journal*, 16:6555.
- [Werner et al., 2012] Werner, H. J., Knowles, P. J., Knizia, G., Manby, F. R., and Schütz, M. (2012). Molpro: A general-purpose quantum chemistry program package. *WIREs Computational Molecular Science*, 2:242.

- [West, 1987] West, R. (1987). Chemistry of the silicon-silicon double bond. *Angewandte Chemie International Edition*, 26:1201.
- [West et al., 1981] West, R., Fink, M. J., and Michl, J. (1981). Tetramesityldisilene, a stable compound containing a silicon-silicon double bond. *Science*, 214:1343.
- [Whangbo et al., 2003] Whangbo, M.-H., Koo, H.-J., and Dai, D. (2003). Spin exchange interactions and magnetic structures of extended magnetic solids with localized spins: Theoretical descriptions on formal, quantitative and qualitative levels. *Journal of Solid State Chemistry*, 176:417.
- [Wilhelm et al., 2019] Wilhelm, J., VandeVondele, J., and Rybkin, V. V. (2019). Dynamics of the bulk hydrated electron from many-body wave-function theory. *Angewandte Chemie International Edition*, 58:3890.
- [Xiang et al., 2013] Xiang, H., Lee, C., Koo, H.-J., Gong, X., and Whangbo, M.-H. (2013). Magnetic properties and energy-mapping analysis. *Dalton Transactions*, 42:823.
- [Xiang et al., 2011] Xiang, H. J., Kan, E. J., Wei, S.-H., Whangbo, M.-H., and Gong, X. G. (2011). Predicting the spin-lattice order of frustrated systems from first principles. *Physical Review B*, 84:224429.
- [Xie et al., 2017] Xie, L., Liao, M., Wang, S., Yu, H., Du, L., Tang, J., Zhao, J., Zhang, J., Chen, P., Lu, X., Wang, G., Xie, G., Yang, R., Shi, D., and Zhang, G. (2017). Graphene-contacted ultrashort channel monolayer MoS<sub>2</sub> transistors. *Advanced Materials*, 29:1702522.
- [Xu et al., 2018a] Xu, C., Feng, J., Xiang, H., and Bellaiche, L. (2018a). Interplay between Kitaev interaction and single ion anisotropy in ferromagnetic CrI<sub>3</sub> and CrGeTe<sub>3</sub> monolayers. *npj Computational Materials*, 4:57.
- [Xu et al., 2018b] Xu, H., Han, D., Bao, Y., Cheng, F., Ding, Z., Tan, S. J. R., and Loh, K. P. (2018b). Observation of gap opening in 1T' phase MoS<sub>2</sub> nanocrystals. *Nano Letters*, 18:5085.
- [Yadav et al., 2016] Yadav, R., Bogdanov, N. A., Katukuri, V. M., Nishimoto, S., van den Brink, J., and Hozoi, L. (2016). Kitaev exchange and field-induced quantum spin-liquid states in honeycomb  $\alpha$ -RuCl<sub>3</sub>. *Scientific Reports*, 6:37925.
- [Yadav et al., 2018a] Yadav, R., Rachel, S., Hozoi, L., van den Brink, J., and Jackeli, G. (2018a). Strain- and pressure-tuned magnetic interactions in honeycomb Kitaev materials. *Physical Review B*, 98:121107.
- [Yadav et al., 2018b] Yadav, R., Ray, R., Eldeeb, M. S., Nishimoto, S., Hozoi, L., and van den Brink, J. (2018b). Strong effect of hydrogen order on magnetic Kitaev interactions in H<sub>3</sub>LiIr<sub>2</sub>O<sub>6</sub>. *Physical Review Letters*, 121:197203.
- [Yao et al., 2017] Yao, W., Wang, E., Huang, H., Deng, K., Yan, M., Zhang, K., Miyamoto, K., Okuda, T., Li, L., Wang, Y., Gao, H., Liu, C., Duan, W., and Zhou, S. (2017). Direct observation

## Bibliography

---

- of spin-layer locking by local Rashba effect in monolayer semiconducting PtSe<sub>2</sub> film. *Nature Communications*, 8:14216.
- [Yazyev and Helm, 2007] Yazyev, O. V. and Helm, L. (2007). Defect-induced magnetism in graphene. *Physical Review B*, 75:125408.
- [Yazyev and Kis, 2015] Yazyev, O. V. and Kis, A. (2015). MoS<sub>2</sub> and semiconductors in the flatland. *Materials Today*, 18:20.
- [Yazyev et al., 2007] Yazyev, O. V., Tavernelli, I., Rothlisberger, U., and Helm, L. (2007). Early stages of radiation damage in graphite and carbon nanostructures: A first-principles molecular dynamics study. *Physical Review B*, 75:115418.
- [Ye et al., 2016] Ye, G., Gong, Y., Lin, J., Li, B., He, Y., Pantelides, S. T., Zhou, W., Vajtai, R., and Ajayan, P. M. (2016). Defects engineered monolayer MoS<sub>2</sub> for improved hydrogen evolution reaction. *Nano Letters*, 16:1097.
- [Yim et al., 2016] Yim, C., Lee, K., McEvoy, N., O'Brien, M., Riazimehr, S., Berner, N. C., Cullen, C. P., Kotakoski, J., Meyer, J. C., Lemme, M. C., and Duesberg, G. S. (2016). High-performance hybrid electronic devices from layered PtSe<sub>2</sub> films grown at low temperature. *ACS Nano*, 10:9550.
- [Yosida, 1957] Yosida, K. (1957). Magnetic properties of Cu-Mn alloys. *Physical Review*, 106:893.
- [Zacharia et al., 2004] Zacharia, R., Ulbricht, H., and Hertel, T. (2004). Interlayer cohesive energy of graphite from thermal desorption of polyaromatic hydrocarbons. *Physical Review B*, 69:155406.
- [Zan et al., 2013] Zan, R., Ramasse, Q. M., Jalil, R., Georgiou, T., Bangert, U., and Novoselov, K. S. (2013). Control of radiation damage in MoS<sub>2</sub> by graphene encapsulation. *ACS Nano*, 7:10167.
- [Zhang et al., 2011] Zhang, C., Donadio, D., Gygi, F., and Galli, G. (2011). First principles simulations of the infrared spectrum of liquid water using hybrid density functionals. *Journal of Chemical Theory and Computation*, 7:1443.
- [Zhang et al., 2017] Zhang, K., Yan, M., Zhang, H., Huang, H., Arita, M., Sun, Z., Duan, W., Wu, Y., and Zhou, S. (2017). Experimental evidence for type-II Dirac semimetal in PtSe<sub>2</sub>. *Physical Review B*, 96:125102.
- [Zhang et al., 2002] Zhang, R., Lee, S., Law, C.-K., Li, W.-K., and Teo, B. K. (2002). Silicon nanotubes: Why not? *Chemical Physics Letters*, 364:251.
- [Zhang et al., 2016] Zhang, W., Guo, H. T., Jiang, J., Tao, Q. C., Song, X. J., Li, H., and Huang, J. (2016). Magnetism and magnetocrystalline anisotropy in single-layer PtSe<sub>2</sub>: Interplay between strain and vacancy. *Journal of Applied Physics*, 120:013904.

- [Zhang and Yang, 1998] Zhang, Y. and Yang, W. (1998). Comment on “Generalized gradient approximation made simple”. *Physical Review Letters*, 80:890.
- [Zhao et al., 2017a] Zhao, X., Kotakoski, J., Meyer, J. C., Sutter, E., Sutter, P., Krasheninnikov, A. V., Kaiser, U., and Zhou, W. (2017a). Engineering and modifying two-dimensional materials by electron beams. *MRS Bulletin*, 42:667.
- [Zhao et al., 2016] Zhao, Y., Qiao, J., Yu, P., Hu, Z., Lin, Z., Lau, S. P., Liu, Z., Ji, W., and Chai, Y. (2016). Extraordinarily strong interlayer interaction in 2D layered PtS<sub>2</sub>. *Advanced Materials*, 28:2399.
- [Zhao et al., 2017b] Zhao, Y., Qiao, J., Yu, Z., Yu, P., Xu, K., Lau, S. P., Zhou, W., Liu, Z., Wang, X., Ji, W., and Chai, Y. (2017b). High-electron-mobility and air-stable 2D layered PtSe<sub>2</sub> FETs. *Advanced Materials*, 29:1604230.
- [Zheng et al., 2019] Zheng, H., Choi, Y., Baniasadi, F., Hu, D., Jiao, L., Park, K., and Tao, C. (2019). Visualization of point defects in ultrathin layered 1T-PtSe<sub>2</sub>. *2D Materials*, 6:041005.
- [Zheng et al., 2015] Zheng, H., Yang, B., Wang, H., Chen, Z., and Yan, Y. (2015). Strain induced modulation to the magnetism of antisite defects doped monolayer MoS<sub>2</sub>. *Journal of Magnetism and Magnetic Materials*, 386:155.
- [Zhou et al., 2013] Zhou, W., Zou, X., Najmaei, S., Liu, Z., Shi, Y., Kong, J., Lou, J., Ajayan, P. M., Yakobson, B. I., and Idrobo, J.-C. (2013). Intrinsic structural defects in monolayer molybdenum disulfide. *Nano Letters*, 13:2615.





# Michele Pizzochero

## Curriculum Vitæ

Institute of Physics  
EPFL  
Station 3, CH-1015  
Lausanne, Switzerland  
Office: PH H2 434  
☎ +39 346 2413261  
☎ +41 21 69 30308  
✉ [michele.pizzochero@epfl.ch](mailto:michele.pizzochero@epfl.ch)  
skype: michele.pizzochero



## Personal Information

Name Michele Pizzochero  
Born Crema (Italy), December 19, 1991  
Citizenship Italian (EU)

## Education

2016 – 2020 **Ph.D.** in **Physics**, École Polytechnique Fédérale de Lausanne (EPFL), Switzerland.  
2013 – 2015 **M.Sc.** in **Chemistry**, University of Milan, Italy, *Final Grade: 110/110 with honors.*  
2010 – 2013 **B.Sc.** in **Chemistry**, University of Milan, Italy, *Final Grade: 110/110.*

## Experience

### Research

02/2016 – present **École Polytechnique Fédérale de Lausanne (EPFL)**, Switzerland, *Research Assistant.*  
Chair of Computational Condensed Matter Physics, Prof. Oleg V. Yazyev | Institute of Physics  
10/2014 – 01/2016 **University of Milan**, Italy, *Research Intern.*  
Chemical Dynamics Theory Group, Prof. Rocco Martinazzo | Dept. of Chemistry  
07/2014 – 09/2014 **Universiteit Antwerpen**, Belgium, *Research Intern.*  
Condensed Matter Theory, Profs. François M. Peeters and Bart Partoens | Dept. of Physics  
06/2013 – 08/2013 **Technische Universität Kaiserslautern**, Germany, *Research Intern.*  
Lab. of Engineering Thermodynamics, Profs. Martin T. Horsch and Hans Hasse | Dept. of Engineering

### Teaching Activity

2019 **Electronic Structure Methods in Condensed Matter Physics**, TA, Various Lecturers, EPFL.  
2016, 2018, 2019 **Computational Physics III**, TA, with Prof. O. V. Yazyev, EPFL.  
2017 **Solid State Physics II**, TA, with Prof. O. V. Yazyev, EPFL.  
2016 **Computer Simulations of Physical Systems**, Expert, with Prof. A. Pasquarello, EPFL.  
2017, 2018 **General Physics I: Mechanics**, TA, with Prof. S. Bréchet, EPFL.  
2014 **Organic Chemistry**, TA, with Prof. A. Bassoli, University of Milan.

### Professional Service

06/2021 **Organizer**, *First-Principles Modelling of Defects in Solids: Charges Meet Lattices*, ETH Zürich.  
Co-organizing a 3-day workshop to be held at ETH Zurich in July 2021.  
Website: <https://sites.google.com/view/defects-in-solids/>  
07/2019 **Organizer**, *Advanced Electronic Structure Methods in Condensed Matter Physics*, EPFL.  
Co-organized and chaired an international Summer School featuring 15+ invited speakers and 110+ participants.  
Website: <https://sites.google.com/view/eth-electronic-structure-2019>  
2016 – 2019 **Organizer**, *MARVEL Junior Seminars*, EPFL.  
Co-organized a series of 52 seminars in materials science given by junior researchers from Swiss institutions.  
Website: <http://nccr-marvel.ch/outreach/education-and-training/marvel-junior-seminars>

since 2016 **Reviewer for Scientific Journals**, 33+ Manuscripts Reviewed.

- ACS Nano
- Journal of Physics: Condensed Matter
- Physical Chemistry Chemical Physics
- Materials Research Express
- Electronic Structure
- ACS Sustainable Chemistry & Engineering
- 2D Materials
- Energy & Environmental Science
- Superlattices and Microstructures
- Computational Materials Science
- Nanotechnology
- ...

## Grants, Recognitions and Awards

- 2020 **Outstanding Reviewer** for *Materials Research Express*.  
2020 **Swiss National Science Foundation**, Postdoctoral Fellowship at Harvard University (USA).  
2019 **Article Featured** in **2019 Hot PCCP collection**, Pizzochero *et al*, *Phys. Chem. Chem. Phys.* (2019).  
2019 **Pauli Center, ETH Board, EPFL and MARVEL**, Fundings for organizing a Workshop.  
2018 **ETH Board, EPFL and MARVEL**, Fundings for organizing a Summer School.  
2018 **Outstanding Reviewer** for *Journal of Physics: Condensed Matter*.  
2017 **Best Poster Award, 2nd place**, Flatlands Beyond Graphene 2017 conference.  
2016 **Istituto Lombardo Accademia di Scienza e Lettere**, Award for the Master Thesis.  
2015 **Italian Supercomputing Center (CINECA)**, Principal Investigator of a computational grant.  
2013 **Deutscher Akademischer Austauschdienst (DAAD)**, RISE Fellowship.  
2012 **University of Milan**, Scholarship to top-ranked students in Chemistry.  
2011 **University of Milan**, Scholarship to top-ranked students in Chemistry.

## Research Interests

- Quantum theory of materials
- Point and extended defects in solids
- First-principles and molecular dynamics calculations
- 2D and layered crystals
- Magnetic interactions in solids
- Quantum transport at the nanoscale

## Skills

### Computer Skills

OS Unix/Linux, Mac OS, Windows  
Editors L<sup>A</sup>T<sub>E</sub>X, Beamer, Office Package  
DFT Codes Vasp, Siesta/Transiesta, CP2K

### Language Skills

English Fluent  
French Fluent  
Italian Native

## Scientific Contributions

### Peer-Reviewed Publications

\*first theoretical author in experimental-theoretical papers ‡corresponding author #contributed equally

- [15] E. Martino, D. Santos-Cottin, F. Le Martelé, K. Semeniuk, M. Pizzochero,\* K. Cernevics, S. Klotz, L. Delbes, B. Baptiste, F. Capitani, H. Berger, O.V. Yazyev, A. Akrap

*Pressure-driven structural phase transition and band-gap collapse in layered semiconductors 1T-ZrX<sub>2</sub>*  
In preparation

- [14] A. Avsar,# C.-C. Yeon,# M. Pizzochero,#,\* M. Tripathi, A. Ciarrocchi, O. V. Yazyev, and A. Kis

*Probing magnetism in atomically thin semiconducting PtSe<sub>2</sub>*  
Submitted to Nature Communications, (2020)

- [13] M. Pizzochero‡

*Atomic-scale defects in the two-dimensional ferromagnet CrI<sub>3</sub> from first principles*  
Journal of Physics D: Applied Physics, in press (2020)

- [12] M. Pizzochero‡ and O. V. Yazyev

*Inducing magnetic phase transitions in monolayer CrI<sub>3</sub> via lattice deformations*  
The Journal of Physical Chemistry C 124, 7585 (2020)

- [11] M. Pizzochero,<sup>‡</sup> R. Yadav, and O. V. Yazyev  
*Magnetic exchange interactions in monolayer  $\text{CrI}_3$  from many-body wavefunction calculations*  
2D Materials, in press (2020)
- [10] M. Pizzochero, M. Bonfanti, and R. Martinazzo  
*To bend or not to bend, the dilemma of multiple bonds*  
Physical Chemistry Chemical Physics 21, 26342 (2019)
- [9] Z. Pedramrazi, C. Herbig, A. Pulkin, S. Tang, M. Philips, D. Wong, H. Ryu, M. Pizzochero, Y. Chen, F. Wang, E. J. Mele, Z. X. Shen, S.-K. Mo, O. V. Yazyev, and M. F. Crommie  
*Manipulating topological domain boundaries in the single-layer quantum spin Hall insulator  $1T'$ - $\text{WSe}_2$*   
Nano Letters 19, 5634 (2019)
- [8] M. Pizzochero,<sup>‡</sup> F. Ambrosio, and A. Pasquarello  
*Picture of the wet electron: A localized transient state in liquid water*  
Chemical Science 10, 7442 (2019)
- [7] A. Avsar, A. Ciarrocchi, M. Pizzochero,\* D. Unuchek, O. V. Yazyev, and A. Kis  
*Defect induced, layer-modulated magnetism in ultrathin metallic  $\text{PtSe}_2$*   
Nature Nanotechnology 14, 674 (2019)
- [6] M. W. Chen, H. K. Kim, C. Bernard, M. Pizzochero,\* J. Zaldivar Fernandez, J. I. Pascual, M. M. Ugeda, O. V. Yazyev, T. Greber, J. Osterwalder, O. Renault, and A. Kis  
*Electronic properties of transferable atomically-thin  $\text{MoSe}_2/\text{h-BN}$  heterostructures grown on  $\text{Rh}(111)$*   
ACS Nano 12, 11161 (2018)
- [5] M. Pizzochero<sup>‡</sup> and O. V. Yazyev  
*Single-layer  $1T'$ - $\text{MoS}_2$  under electron irradiation from ab initio molecular dynamics*  
2D Materials 5, 025022 (2018)
- [4] M. Pizzochero<sup>‡</sup> and O. V. Yazyev  
*Point defects in the  $1T'$  and  $2H$  phases of single-layer  $\text{MoS}_2$ : A comparative first-principles study*  
Physical Review B 96, 245402 (2017)
- [3] M. W. Chen, D. Ovchinnikov, S. Lazar, M. Pizzochero,\* M. B. Whitwick, A. Surrente, M. Baranowski, O. Lopez-Sanchez, P. Gillet, P. Plochocka, O. V. Yazyev, and A. Kis  
*Highly-oriented atomically thin ambipolar  $\text{MoSe}_2$  grown by molecular beam epitaxy*  
ACS Nano 11, 6355 (2017)
- [2] M. Pizzochero, M. Bonfanti, and R. Martinazzo  
*Hydrogen on silicene: like or unlike graphene?*  
Physical Chemistry Chemical Physics 18, 15654 (2016)
- [1] M. Pizzochero, O. Leenaerts, B. Partoens, R. Martinazzo, and F. M. Peeters  
*Hydrogen adsorption on boron and nitrogen doped graphene*  
Journal of Physics: Condensed Matter 27, 425502 (2015)

### Selected Talks

- Sept. 2019 Title: *Defects in solids and liquids: A theorist's journey*  
University of Milan (IT), Host: Prof. Rocco Martinazzo
- Aug. 2019 Title: *Picture of the wet electron: A localized transient state in liquid water*  
Swiss Physical Society Annual Meeting 2019, University of Zurich (CH)
- Jul. 2019 Title: *To bend or not to bend? Correlation effects in low-dimensional silicon*  
Theory Meets Experiment in Low-Dimensional Structures with Correlated Electrons, Prague (CZ)
- Mar. 2019 Title: *Point defects in  $1T'$ - $\text{MoS}_2$  from first principles*

APS March Meeting, Boston MA (USA)

- Feb. 2019 Title: *To bend or not to bend? The dilemma of the double bond*  
MARVEL Seminars, EPFL, Lausanne (CH)
- Jul. 2018 Title: *Intrinsic and engineered point defects in two-dimensional 1T'-MoS<sub>2</sub>*  
Physics of Defects in Solids: Quantum Mechanics Meets Topology, ICTP, Trieste (IT)
- Jun. 2018 Title: *Intrinsic and engineered point defects in two-dimensional 1T'-MoS<sub>2</sub>*  
2D Materials Explored via Scanning Probe Microscopy, San Sebastian (ES)
- Aug. 2017 Title: *Exploring point defects in 1T' and 2H crystalline phases of single-layer MoS<sub>2</sub>*  
Swiss Physical Society Annual Meeting 2017, Geneva (CH)
- Oct. 2015 Title: *On the adsorption of hydrogen atoms on silicene: unlike graphene*  
University College London (UK), Host: Prof. Angelos Michaelides
- Aug. 2013 Title: *Graphene and its chemical functionalization: electronic structure and properties*  
DAAD Meeting, Cologne University of Applied Sciences (DE)

## Selected Research Highlights and Press Releases

*Picture of the wet electron: a localized transient state in liquid water*, Chem. Sci. (2019)

- *Illuminating the "wet" electron*  
EPFL Press Release, <https://actu.epfl.ch/news/illuminating-the-wet-electron/>
- *Hybrid functional molecular dynamics give unprecedented view on the nature of the wet electron*  
MARVEL Research Highlight, <http://nccr-marvel.ch/highlights/2019-06wetelectron>

*Defect induced, layer modulated magnetism in ultrathin metallic PtSe<sub>2</sub>*, Nat. Nanotechnol. (2019)

- *A new 2D magnet draws future devices closer*  
EPFL Press Release, [news.epfl.ch/news/a-new-2d-magnet-draws-future-devices-closer](https://news.epfl.ch/news/a-new-2d-magnet-draws-future-devices-closer)  
Science Daily, [www.sciencedaily.com/releases/2019/06/190617110546.htm](http://www.sciencedaily.com/releases/2019/06/190617110546.htm)  
Phys.org, [phys.org/news/2019-06-d-magnet-future-devices-closer.html](http://phys.org/news/2019-06-d-magnet-future-devices-closer.html)  
Azom.com, [www.azom.com/news.aspx?newsID=51440](http://www.azom.com/news.aspx?newsID=51440)
- *Behind the paper: Defect induced, layer modulated magnetism in ultrathin metallic PtSe<sub>2</sub>*  
Nature Research Device and Materials Engineering, [devicematerialscommunity.nature.com](https://devicematerialscommunity.nature.com)
- *Scientists Discover 2D Magnetic Material For Spintronic Devices*  
Pioneering Minds, [pioneeringminds.com/](http://pioneeringminds.com/)
- *'Defective' 2D material turns out to be magnetic*  
Materials Today, [www.materialstoday.com/nanomaterials/news/](http://www.materialstoday.com/nanomaterials/news/)
- *New Metallic, Air-Stable 2D Magnet that can be Integrated into Spintronic Devices*  
Nano Werk, <https://www.nanowerk.com/nanotechnology-news2/newsid=52996.php>